ADVANCED ELECTRICAL MACHINE DESIGN
FOR
AZIMUTHING ELECTRICAL PODDED PROPULSOR

CHU KIN HEY

SCHOOL OF ELECTRICAL AND ELECTRONIC ENGINEERING

2017

ADVANCED ELECTRICAL MACHINE DESIGN FOR AZIMUTHING ELECTRICAL PODDED PROPULSOR

CHU KIN HEY

School of Electrical and Electronic Engineering

A thesis submitted to the Nanyang Technological University
in partial fulfillment of the requirement for the degree of
Doctor of Philosophy

2017

Acknowledgement

This work was performed at the School of Electrical & Electronic Engineering (EEE), Power Electronics and Drives division at Nanyang Technological University (NTU) in Singapore and Electrical Power And Control Systems (EPACS) at Advanced Technological Centre (ATC), Rolls-Royce (RR) Singapore Pte. Ltd. The research work was funded by Economic Development Board (EDB), Singapore, and partly NTU and RR, under the Industrial Ph.D. Programme (IPP).

I am very grateful to be offered the research scholarship and the fine opportunity to work with the best professionals in my research area.

I would like to express my deepest gratitude and appreciation to my university supervisor, Associate Professor Dr. Tseng King Jet, for his invaluable guidance and encouragement throughout all phases of the research program. I am grateful to Associate Professor Dr. Josep Pou for his insightful discussions and his help in times of difficulty. I am also thankful to my industrial supervisor, Dr. Amit Gupta for his support during this work.

I would like to express my sincere thanks to Shanmukha Ramakrishna for his many invaluable technical advices and discussions, and for his friendship. Without them, my work would have been much more difficult to accomplish. I would also like to thank Michael Zagrodnik for his interesting discussions and valuable advices.

I wish to express my thanks to my stakeholders at Rolls Royce UK, Dr. Ellis Chong of EPACS and John Cullen of Strategic Research Centre (SRC) for their support. I would also like to thank Dr. Bicky Bhangu for his advices during the early stages of my research work.

Special thanks to Merugu Siva Rama Krishna for his help in my experiment setup and to Ashish Deshpande for his guidance with my simulations. My thanks to laboratory staff at EEE, Lim Kim Peow for his help with the lab equipment.

Last but not least, I express my deepest gratitude and love to my family for their unconditional support and encouragement during these years.

Table of Contents

List of Figures

List of Tables

Nomenclature

Letters

A_c	Cross-sectional area of the magnet or bolts	m^2
ac	Specific electric loading	A/m
A_f	Cross-sectional area of field winding strip	m^2
A_{cond}	Cross-sectional area of conductor	m^2
A_g	Air-gap area per pole	m^2
A_h	Cross-sectional area of medium	m^2
A_m	Magnet pole face area	m^2
A_s	Cross-sectional area of stator conductor	m^2
A_{sp}	Stator pole area	m^2
AT_{ad}	Direct-axis armature MMF	A
AT_{ag}	Air-gap MMF	A
AT_{fl}	Ampere-turns at full-load	A
AT_{fo}	No-load ampere-turns per pole	A
AT_{m1}	Fundamental magnetizing MMF	A
AT_{nl}	Total no-load MMF at rated voltage	A
AT_p	MMF of rotor pole	A
AT_{tooth}	MMF of stator tooth	A
AT_{yr}	MMF of rotor yoke	A
AT_{ys}	MMF of stator yoke	A
b_v	Width of ventilation duct	–
B_{av}	Specific magnetic loading	Tesla
B_d	Magnetic flux density in magnet under demagnetization	Wb/m^2
B_m	Magnet flux density	Wb/m^2
B_{m1}	Fundamental maximum flux density component in machine core	Wb/m^2
B_{mt}	Magnetic flux density due to influence of field excitation	Wb/m^2
B_{pole}	Flux density in pole body	Wb/m^2
B_{rad}	Radial flux density	Wb/m^2
B_{tan}	Tangential flux density	Wb/m^2
B_{tnar}	Flux density in the narrow end of stator tooth	Wb/m^2
B_{tooth}	Flux density in stator teeth	Wb/m^2
B_{yr}	Flux density in rotor yoke	Wb/m^2
B_{ys}	Flux density in stator yoke	Wb/m^2
c	Constant	–
CF_i	Iron loss correction factor	–
C_o	Machine output coefficient	–
C_p	Specific heat capacity	J/kg/K
D	Internal diameter of the stator	m

D_{bar}	Diameter of damper bar	m
D_o	Outer diameter of stator	m
D_r	Outer diameter of rotor	m
D_{shaft}	Diameter of rotor shaft	m
E	Refer to Figure 3-12(a)	m
$\bar{E}_g$	Internal generated voltage phasor	p.u.
F	Refer to Figure 3-12(a)	m
f	Electrical frequency	Hz
F_{rad}	Radial components of magnetic forces per unit area	N/m^2
F_{tan}	Tangential components of magnetic forces per unit area	N/m^2
g	Air-gap length at centre of pole face	m
$\mathbf{G}$	Thermal conductance square matrix	–
h'	Height per stand	m
h_1	Height occupied by insulated conductor in slot	m
h_2	Space above conductor and below wedge	m
h_3	Height of wedge	m
h_4	Height of lip	m
H_{bottom}	Magnetic field strength at bottom of rotor pole	A/m
h_{buck}	Height of field winding buckling space	m
h_c	Height of field conductor	m
h_f	Height of the field coil	m
h_{fi}	Height of the insulation per field conductor	m
h_{pole}	Height of rotor pole	m
h_{slot}	Slot depth	m
H_{tooth}	Magnetic field strength at stator tooth	A/m
H_{top}	Magnetic field strength at top of rotor pole	A/m
H_{yr}	Magnetic field strength at rotor yoke	A/m
h_{yr}	Height of rotor yoke	m
H_{ys}	Magnetic field strength at stator yoke	A/m
h_{ys}	Height of stator yoke	m
i	Refer to equation 5.13	–
I_{bar}	Damper bar current	A
I_f	Field current	A
I_m	Magnetizing current	A
I_{ph}	Phase current	A
$I_{s\text{-}c}$	Phase short-circuit current	A
J_{bar}	Current density in damper bars	A/m^2
J_f	Field winding current density	A/m^2
J_s	Current density of armature windings	A/m^2
k_{ad}	Armature-reaction flux coefficient	–
K_{ag}	Air-gap coefficient	–
$K_{cc\text{-}duct}$	Carter's coefficient for ventilation ducts	–
$K_{cc\text{-}slot}$	Carter's coefficient for stator slots	–
K_{dav}	Average eddy current loss factor	–

K_{dn}	Distribution factor of stator windings	–
K_{gap}	Gap contraction factor	–
K_i	Stacking factor of electrical steel material	–
K_{pn}	Pitch factor of stator windings	–
K_s	Leakage factor	–
K_w	Winding factor of stator windings	–
K_{w1}	Fundamental winding factor	–
L	Stack length of machine steel core	m
l_{ag}	Air-gap length	m
l_f	Length of field winding	m
l_h	Length of body in heat flow direction	m
l_m	Magnet thickness	m
l_{pole}	Axial length of pole body	m
l_{yr}	Length of magnetic path of rotor yoke	m
l_{ys}	Length of magnetic path in stator yoke	m
m	Number of phases	–
M	Number of repeated winding arrangement	–
m_{bar}	Mass of damper bar	kg
m_c	Mass of a PM or pole	kg
MLT_a	Mean length of turn of armature winding	m
MLT_f	Mean length of turn of the field coil	m
m_s	Mass of stator core	kg
m_t	Total mass of teeth on stator	kg
n	Harmonic number	–
N	Number of conductor layers	–
N_{bar}	Number of damper bars	–
NI	Ampere-turns of field winding	A
n_{rotor}	Rotational speed of rotor shaft	rpm
n_s	Synchronous rotational speed	r.p.s
N_{slot}	Total number of stator slots	–
n_{ss}	Stator slot harmonics	–
n_v	Number of ventilation ducts	–
$\mathbf{P}$	Vector containing the power losses in each node	–
p	Number of poles	–
P_c	Losses in a damper bar	W
pc	Permeance coefficient	–
P_{cuf}	Field winding copper loss	W
P_{cus}	Total copper loss in stator	W
P_{fw}	Friction and windage losses	W
P_i	Iron loss in teeth	W
p_m	Magnet permeance	Wb/A
P_{ms}	Iron loss per kg in stator core	kg
P_{mt}	Iron loss per kg in tooth	W/kg
$\mathrm{P_o}$	Power output	kW
P_{out}	Rated output power	W
P_s	Stator core iron loss	W

P_{stray}	Stray losses	W
P_t	Total losses of machine at rated load	W
P_{ti}	Total iron losses	W
q	Slot per pole per phase	–
r_1	Radius at edge of the rotor pole end plate	m
r_2	Radius of mean path of field winding copper strip at edge of the pole end plate	m
R_{ac}	Phase resistance of armature winding	p.u.
R_{bar}	Resistance of damper bar	Ohms
r_c	Radius of curvature	m
R_{cd}	Conduction thermal resistance	K/W
R_{cv}	Convection thermal resistance	K/W
R_f	Resistance of each field coil	Ohms
R	Reluctance through which the flux φ_g passes	A/Wb
R_g	Air-gap reluctance	A/Wb
$R_{n,n}$	Thermal resistances	K/W
R_{ph}	Resistance per phase of the stator winding	Ohms
R_{pho}	Resistance per phase of conductors in overhang	Ohms
R_{phs}	Resistance per phase of conductors in slots	Ohms
r_y	Mean radius of stator yoke	m
S	Machine apparent output power	kVA
SCR	Short-Circuit Ratio	–
t_1	Radial thickness of coil insulation	m
T_{cog}	Cogging torque	Nm
T_f	Number of field winding turns	–
T_{ph}	Number of turns per phase of stator winding	–
T_{Shaft}	Shaft output torque	Nm
$\bar{V}_{ph}$	Phase voltage phasor	p.u.
V	Terminal voltage	Volts
V_f	Voltage per field coil	Volts
W	Rated power	W
w_{cs}	Width of conductor	m
w_c	Width of rotor coil strip	m
W_p	Weight of stator teeth	kg
w_{pole}	Width of pole body	m
w_s	Width of slot	m
w_{so}	Width of slot opening	m
W_t	Total weight of the stator comprised of teeth, windings and insulation weights	kg
w_{tooth}	Width of stator tooth	m
W_y	Weight of stator yoke	kg
X_{ad}	Direct axis armature reaction reactance	p.u.
X_{aq}	Quadrature axis armature reaction reactance	p.u.
X_D	Unsaturated direct-axis synchronous reactance	p.u.
X_d	Direct-axis Synchronous reactance	Ohms

x_l	Stator leakage reactance	Ohms
X_l	Stator leakage reactance	p.u.
x_m	Magnetizing reactance	Ohms
X_m	Magnetizing reactance	p.u.
X_Q	Unsaturated quadrature-axis synchronous reactance	p.u.
X_q	Quadrature axis synchronous reactance	Ohms
y	Stator coil pitch in terms of number of slots	–
z	Mode number	–
Z_{slot}	Number of conductors per slot	–

Symbols

$L_o\lambda_o$	Overhang leakage factor	–
α_h	Convection coefficient	–
λ_h	Thermal conductivity	W/(m·K)
λ_s	Permeance of stator open slots	–
μ_0	Permeability of free space	H/m
μ_r	Relative permeability of recoil line	–
ρ_{cu}	Electrical resistivity of copper	Ohm·m
ρ_d	Direct-axis reduction factor	–
ρ_s	Density of the material	kg/m^3
σ_c	Stresses due to centrifugal force	N/m^2
τ_c	Coil pitch in fractions	–
τ_p	Pole arc	m
τ_{pr}	Rotor pole pitch	m
τ_{ps}	Pole pitch in terms of number of slots	–
τ_{rot}	Ratio of pole arc length to pole pitch length	–
τ_s	Slot pitch	m
τ	Pole pitch	m
φ	Flux per pole	Wb
φ_g	Magnet flux crossing the air-gap	Wb
φ_{lp}	Leakage flux of pole bodies	Wb
φ_{ls}	Leakage flux of poles shoes	Wb
φ_{ml}	Leakage factor of magnet flux	–
Δ	Refer to equation 5.10	–
Δ_{dr}	Shift of a single pole pair	m
$\mathbf{\Delta T}$	Temperature rise vector	–
$\Delta \mathrm{T}$	Temperature rise of the damper bars	K
Δt	Elapsed time	s
Δ_z	Refer to equation 5.12	–
$\in$	Young's modulus of elasticity of stator material	N/m^2
$\propto$	Refer to equation 3.62	–
γ	Refer to Figure 3-12(a)	Degrees

θ	Mechanical angular position of the rotor	rad
ω_c	Mechanical angular speed	rad/s
η	Percentage efficiency of machine	%

Abbreviations

2D	Two-dimensional
3D	Three-dimensional
ABB	ASEA Brown Boveri
AC	Alternating current
BEP	Break-even point
BLSM	Brushless excited synchronous machines
DC	Direct current
DFE	Diode front end
EMF	Electromotive force
FEA	Finite element analysis
FEM	Finite element method
FFT	Fast Fourier transform
HESM	Hybrid excited synchronous machine
HTS	High temperature superconducting
IFEP	Integrated full electric propulsion
IGBT	Insulated-gate bipolar transistor
IM	Induction motor
IMO	International marine organization
MMF	Magnetomotive force
NdFeB	Neodymium iron boron
NPC	Neutral point clamped
OCC	Open circuit characteristic
p.u.	Per unit
PM	Permanent magnet
PMSM	Permanent magnet synchronous machines
POC	Proof of concept
REE	Rare earth elements
RPM, rpm	Revolution per minute
r.p.s	Revolution per second
RR	Rolls-Royce
SmCo	Samarium cobalt
SR	Switched reluctance
THD	Total harmonic distortion
VSI-PWM	Pulse-width-modulation voltage source inverter
WFSM	Wound field synchronous machine

Abstract

At present, energy efficiency, operational reliability and cost savings are some of the most important factors regarding electrical systems in marine business industry. Regulations such as the International Marine Organization (IMO) Tier III impose a tougher limit to global warming emissions than before. The permanent magnet synchronous machines (PMSMs) are great contenders for electrical machine propulsion. They are highly efficient, lightweight and compact. However, due to the high cost of rare earth elements (REE), PMSM is substantially more costly than most machines of other topologies. Unfortunately, no readily available substitute exists for most REE.

In the doctoral thesis, a study of hybrid excitation synchronous machine (HESM) is presented. HESMs are synchronous machines, where the total rotor field excitation is produced by the simultaneous action of electrical and permanent magnet (PM) excitation. This study contributes a more efficient alternative for the brushless excited synchronous machine (BLSM) which meets all the requirements for azimuthing podded propulsion.

A literature review was conducted to understand the trends in the podded propulsor market and electrical machines topologies suitable for marine propulsion. The HESM was found to be a potential alternative to the BLSM. An overview of published HESM designs is given from a standpoint of complexity of design, energy efficiency, cost, manufacturability, etc. The feasibility study narrowed down the possible designs of HESM for traction/propulsion applications.

Based on analytical methods, a program was written for the preliminary calculations of the machine dimensions and its main parameters. The design is refined using Ansys-RMxprt software followed by finite element method (FEM) software, Ansys-Maxwell. Throughout the stages, the machine designs were optimized. Electromagnetic simulations are applied to the final machine designs to obtain design parameters, electromagnetic forces and machine characteristics. Thermal analyses and economy studies are also performed. A benchmark 5MW BLSM is developed to replicate the existing electric machine used in the application.

Two variants of HESMs are developed, one of them with additional armature reaction compensation capability. The performances of the HESMs were found to be superior to that of the BLSM.

An experiment was carried out to verify the armature reaction compensation technique. Two commercially available 12.5kVA, 4-pole wound field synchronous machines were used. One of the machines is modified to incorporate magnets on one edge of each pole. The other machine is left unmodified to act as a benchmark for the experiment. The experimental results along with FEM simulations show improvements to the machine performance brought about by the proposed technique.

Efficiency of electrical machines tends to increase with their sizes. Therefore, there is a power rating limit to which the benefit of higher efficiency can be achieved by this technology. However, when used in low power applications as in this case, the increase in machine efficiency can be quite substantial. Limited by economy, this technology is most feasible for the azimuthing podded propulsor at power levels where the application of PMSM is too expensive and BLSM is not sufficiently energy efficient.

Chapter 1 – Introduction

1.1 Motivation

Since the 1970s, permanent magnet (PM) material technology has improved significantly. The rare earth magnets, such as samarium cobalt (SmCo) and neodymium iron boron (NdFeB) have become popular due to their greater power density, high coercively and linearity of demagnetization curves [1]. Used as the main excitation source in permanent magnet synchronous machines (PMSM), they provide high energy efficiency as most losses are only generated on the stator. As a result, applications of PMSM gained popularity in the industry.

Rare earth materials are fundamental to many nations' economic growth, as well as maintaining and improving quality of life. In recent years, global demand for rare earth magnets has increased. International concerns about the threat of future supply shortages and the adverse environmental impacts from rare earth mining grew [2][3]. Many companies and institutions have begun research to reduce rare earth elements from their products such as computers and electrical motors [4]. The United States Department of Energy has begun funding research to find substitutes for rare earth metals in PM technology. The Advanced Research Projects Agency-Energy (ARPA-E) has introduce a Rare Earth Alternatives in Critical Technologies (REACT) program which started in 2011 [5].

However, no readily available substitute exists for most rare earth elements (REE) [6]. According to Figure 1-1 below, the REEs neodymium, dysprosium and terbium essential for high quality NbFeB magnets are under the most critical status in the near future.

China is currently the top global producer of REEs. In 2011, China produced over 95% of the world's rare earth supply which comprised of the entire world's heavy rare earths production [6]. China has also imposed export quotas on REE production which caused an increase in their price between 2005 and 2011 [2]. With China's near voidance of competition from other REE producers, prices of REE are not expected to decline in the near future [7]. Figure 1-2 shows the estimated world production of rare earth oxides from 1985 to 2014.

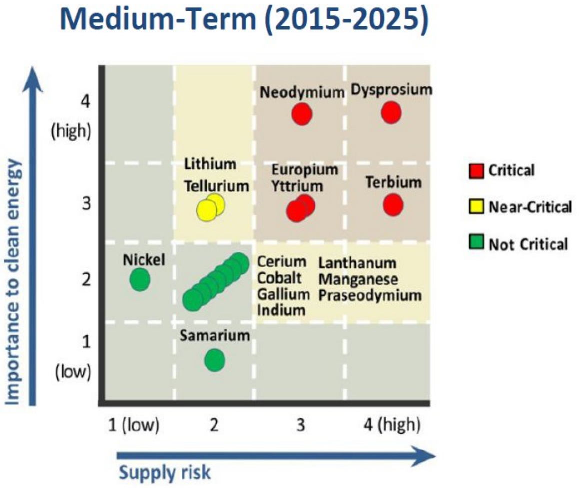

Figure 1-1 Supply risk of REEs for low carbon technology [2]

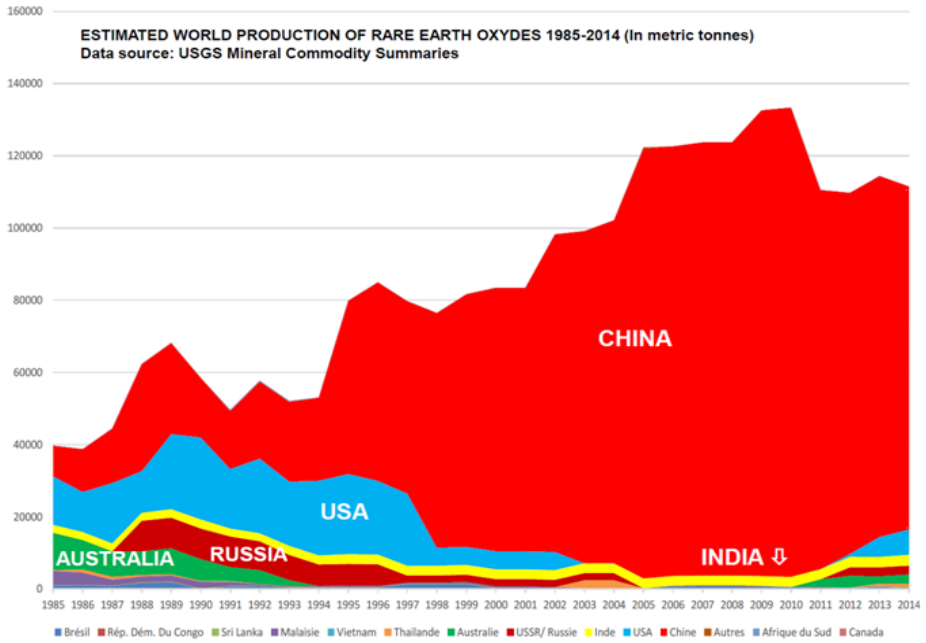

Figure 1-2 China has been the top global producer of REEs since mid-1990s [8]

A marine vessel may travel thousands of miles each year. Improving the efficiency of the propulsion system would mean huge financial savings to the company. There is a growing pressure to reduce global warming emissions. International Marine Organization (IMO) Tier

III regulations will come into effect by year 2016 which will impose a much tougher limit than Tier II [9]. Rare-earth permanent magnet machines offers superior efficiency over other conventional machines topologies reducing emissions.

In this project, the hybrid excited synchronous machine (HESM) topology for podded propulsor is proposed. The novel electrical machine design aims to improve the performance of the existing pod propulsion machine without over-reliance on rare-earth magnets whilst keeping cost low. Based on literature review, the HESM topology has shown potential as a traction/propulsion drive. It can reduce PM material usage and provides more flux controllability compared to PMSM. At the same time, it can deliver higher efficiency over traditional-excited synchronous machine. For podded propulsion application, PM motors are built only for lower power ratings (up to approx. 4.5 MW) due to their lack of economy and brushless excited synchronous machines (BLSM) are very efficient for power ratings above 10 MW. This presents a new opportunity for a new machine topology study within this range of power ratings.

1.2 Objectives

The main objective is to develop an advanced electrical machine architecture that improves the operation efficiency and reliability of the azimuthing electrical podded propulsor. For this purpose, a comprehensive study with specific objectives is implemented and summarized as follows:

1) Explore possible electrical machine architectures for the podded propulsion. Analyze their technical advantages and disadvantages and find an acceptable solution to the problem.

2) Investigate the state-of-the-art in several aspects of design ideas, construction and principle of operation for different types of HESM.

3) Design benchmark BLSM and HESM using analytical methods and obtain their parameters and performances.

4) Optimization of BLSM and HESM designs using finite element analysis (FEA).

5) Investigation of BLSM and HESM performances using FEA for their comparison study.

6) Experimental verification of the concept of armature reaction compensation technique.

1.3 Main contributions of research work

The main contributions of this thesis are the following:

1) The thesis presents an overview of the trends in marine electrical systems and the azimuthing podded propulsion system.

2) The thesis presents a literature review of electrical machine topologies and HESMs in terms of their classifications, operation principles, constructions and their suitability for the podded propulsion.

3) The thesis provides the electromagnetic design, procedure and performance analyses of the BLSM and HESMs using both analytical methods and FEM software. Critical design considerations, methodologies, and implementation for podded propulsion are covered. An analytical design program and a V-curves program have been written for this purpose.

4) The thesis has introduced a progressive magnet air-gap design for the HESM and also a magnet retainment system (both inventions have been included in a patent idea). The thesis shows the feasibility of the HESMs for podded propulsion. Their main

constraints are presented. Main performance comparisons between the machines such as torque, waveform harmonics, energy efficiency, thermal and costs are carried out.

5) The thesis demonstrates the technique of armature reaction compensation and verifies its concept through laboratory tests. The experimental results are compared to the simulated results.

1.4 Patent and Publication

Patent:

Title: Armature reaction compensated salient-pole hybrid excited synchronous machine.
Date of submission: 15th April 2016 (Rolls-Royce IP Department)
Current status: Invention idea accepted. Patent drafting work in progress.
Authors: Kin Hey Chu, Ellis Chong, Shanmukha Ramakrishna, Amit Kumar Gupta, and King Jet Tseng.

Publication:

IECON 2017 - 43rd Annual Conference of the IEEE Industrial Electronics Society:
Title: Salient Pole Wound Field Synchronous Machine for Marine Propulsors with Outboard Drives- Analysis and Design
Status: Submitted
Date of submission: 24/03/2017
Authors: K.H. Chu, J. Pou, A.K. Gupta, and Ramakrishna S

1.5 Organisation of the thesis

This doctoral thesis consists of seven chapters, the structure and contents are organized as follows:

Chapter 1 introduces the overview of the background problems, motivation and objective for this research work.

Chapter 2 provides the technical overview and trends in the field of electrical marine propulsion. A feasibility study of published HESM designs is given.

Chapter 3 deals with the major design calculations, procedure and concepts of the BLSM and HESMs. The analytical design calculations are performed by an iterative program to find the most suitable machine dimensions. Following that, Ansys-RMxprt software is used to obtain more accurate machine designs and parameters.

Chapter 4 describes the major design improvements implemented on the BLSM and the two variants of HESMs. Design optimizations were carried out using finite element modelling software, Ansys-Maxwell.

Chapter 5 investigates and compares the performances and parameters of the BLSM and HESMs using Ansys-Maxwell software.

Chapter 6 introduces the test machines and the experimental setup to verify the operation principle of armature reaction compensation. It also presents the experimental results and their comparison with FEA results.

Chapter 7 discusses the scientific contributions of the research work and the suggestions on future work.

Chapter 2 – Literature Review on Hybrid Excitation Synchronous Machines Considering Azimuthing Podded Propulsor Application

2.1 Introduction

Hybrid excitation synchronous machines, also known as double excitation synchronous machines, utilize simultaneous action of two different excitation sources [10]. They are namely a PM excitation and a direct current (DC) field winding excitation. A PM field provides the main excitation flux while DC excitation operates either strengthening or weakening the air-gap flux distribution. These give them the combined advantages of PM excited machines and conventional wound field synchronous machines.

An overview of marine electrical systems, azimuthing podded propulsion systems, machine topology selection and the literature review of HESM will be covered in this chapter.

2.2 Introduction to marine electrical systems and the azimuthing podded propulsor

Since the 1980's, electric ship propulsion has made a strong comeback [5]. By around middle 1990's, electric motors were already having a firm foothold in marine propulsion market and many companies offered different solutions for electric propulsion [11]. Many operations on marine vessels require electricity. Having all of the engines to produce electricity instead of dividing between electric generation and propulsion reduces the number of engine units. This in turn reduces capital and maintenance costs.

2.2.1 Integrated full electric propulsion (IFEP)

Integrated full electric propulsion (IFEP) typically consist of a set of prime movers (diesel engines and gas turbines) mechanically coupled to electrical power generators which feed the propeller motors through electronic converters. The reason to have both types of prime movers is that while gas turbines are much lower in weight and size, they are efficient only at rated power, whereas diesel engines have higher efficiency over a wider power range. Gas turbines are also quieter with fewer vibrations. Figures 2-1 and 2-2 illustrate the infrastructure of the IFEP.

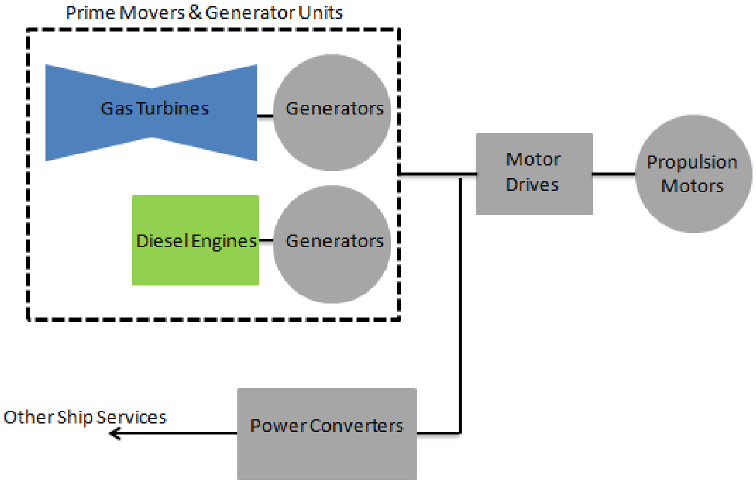

Figure 2-1 Main structure of an integrated full electric propulsion (IFEP) system

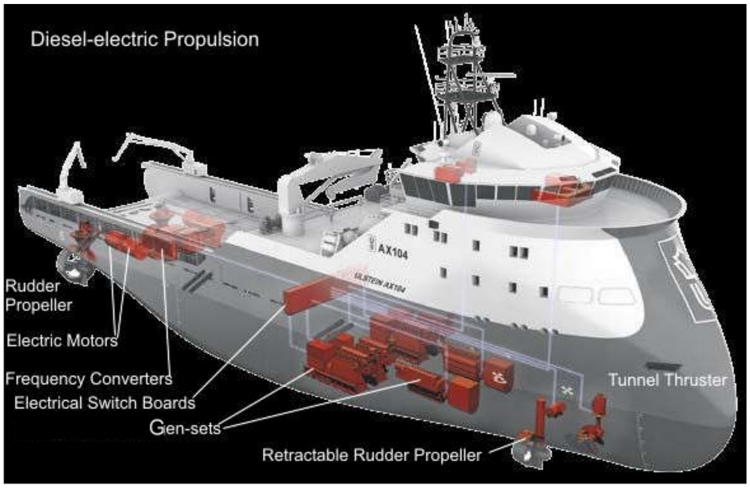

Figure 2-2 The electric propulsion systems generally include a power plant, switchboards, transformers, frequency converters and electric motors [12]

Compared to traditional diesel engine propulsion, which has relatively low power to weight ratio and takes up too much space due to the long propeller shaft, IFEP allows an optimised ship design with low noise and vibration. Fuel consumption is also improved as electric propulsion can produce high efficiency at any speeds. Moreover, carbon emissions from gas turbines are also lower, reducing the environmental impact. Figure 2-3 shows and compares the space occupied in a marine vessel by different propulsion architectures. An example of a recent Podded IFEP is the RMS Queen Mary 2 transatlantic ocean liner.

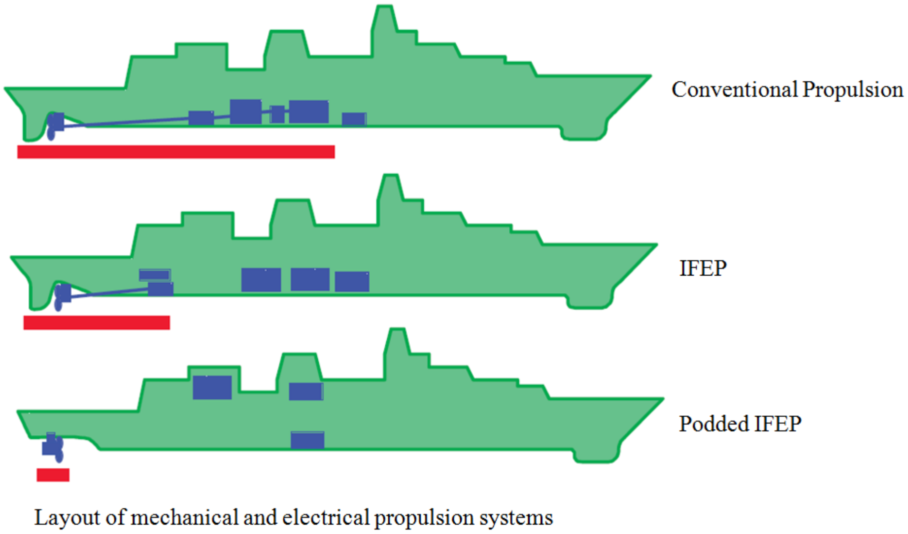

Figure 2-3 Comparison between different propulsion architectures [13]

2.2.2 Azimuthing podded propulsor market

The main manufacturers of the pod market are ASEA Brown Boveri (ABB) and Rolls-Royce (RR) where they produce the Azipod® and Mermaid® pod respectively. The pod unit is situated under the hull of the vessel; it contains the electric motor which is directly connected to the propeller. It can rotate 360 degrees and doubles as a rudder to steer the ship, giving it improved manoeuvrability. With the absence of the gearbox in a direct-drive system, higher efficiency, lower noise and vibration can be achieved. The pod unit can be operated in a pulling or pushing configuration. Placing in a pulling configuration helps to avoid cavitation formation, vibration and noise, increasing efficiency and lifespan. The Azipod entered service in 1990 on service vessel Seili, while the first Mermaid pods were delivered to Millennium ships in 1998 [11]. The demand for podded propulsions is expected to grow into a potential market in the future [14]. Applications of the podded propulsor include cruise liners, tankers, icebreakers, offshore drill rigs, and naval vessels, and many more. Figures 2-4 and 2-5 show the Mermaid pods on the RMS Queen Mary 2 cruise liner and a simplified podded propulsor unit respectively.

Figure 2-4 The RMS Queen Mary 2 cruise liner has four 21.5MW Mermaid pods. While rear twin pods can rotate 360 degrees, the front pods are fixed [15]

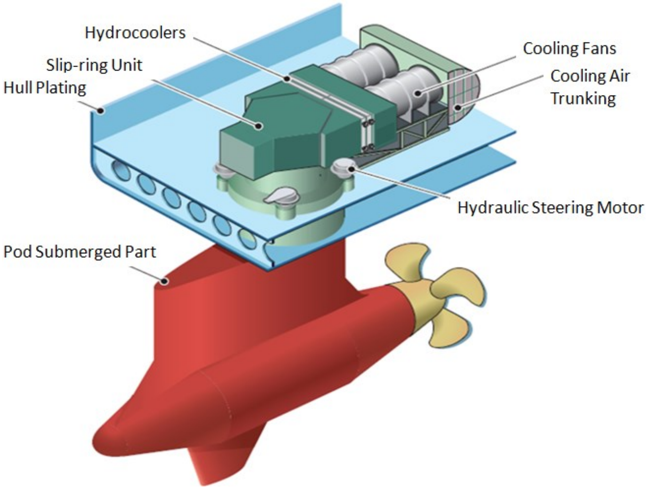

Figure 2-5 A podded propulsor unit [16]

The electric motor can either be an induction motor (IM) or a brushless wound field synchronous motor (BLSM) [16]. For high power applications, the BLSM is most common because of its high efficiency and ease of control. The BLSM gets more economical as its size increases. IM is better suited for smaller propulsion systems and rugged purposes such as icebreaker [17]. The motor runs at low speed at high torque.

Both companies offer their podded propulsion system in three different variants of i) Podded propulsion for ships, ii) Ice breaking classes and iii) High thrust and dynamic positioning. Power ratings of the pods range from to 1.3 to 22MW for ABB and 4 to 27MW for RR, depending on its variant [18][19].

Permanent magnet synchronous machines podded propulsion systems are however available in the lower power range [20][21]. They have lower losses than the IM and BLSM due to absence of active windings in the rotor. Losses in the magnets and rotor are small.

2.2.3 Motor characteristics of pods

The requirements for podded propulsor machines are quite unique compared to conventional synchronous machines found in power plants and hydroelectric generation plants. The desired motor characteristics beginning with the most important point are:

(i) High reliability – Avoid costly repairs, downtime and dry docking.
(ii) Small outer diameter or high power density – High hydrodynamic efficiency.
(iii) Low capital, running and maintenance cost – Cost attractive and competitive.
(iv) Low losses and high power factor in electric machine – High system efficiency.
(v) Integration of a number of auxiliary services – e.g. Fault-monitoring systems. Propulsion unit offered as a complete system package.
(vi) Low noise and vibrations – Quiet operation for passenger comfort in cruise liners and minimise detection in naval ships.
(vii) Weight of machine (i.e. minimum kg/kVA)– Optimium use and selection of materials of construction, ease of transport and installation.

For fault tolerant capability, some pod motors use two independent set of windings (half motor). Each set of windings is connected to a separate power converter. In the event that one breaks down, the motor can still run at a lower rating [22][23][24]. Figure 2-6 shows the schematics of a Mermaid pod system for RMS Queen Mary 2 cruise liner. The stator is shrink-fitted in the pod housing for cooling by surrounding sea water. Therefore, air cooling cubicle can be compact.

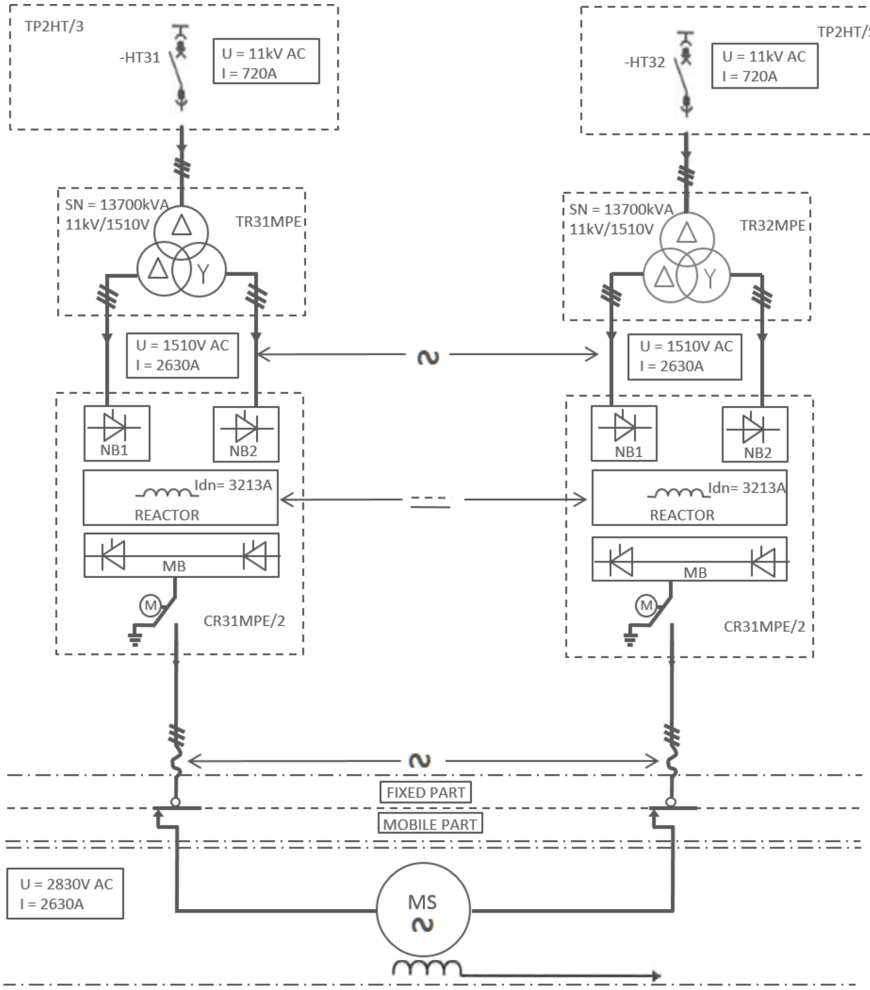

Figure 2-6 Schematics of a Mermaid pod system for RMS Queen Mary 2 cruise liner [23]

2.2.4 Power converter and drive

The power converter for the podded propulsor is a pulse-width-modulation voltage source inverter (VSI-PWM). Flexible ranges of output voltage and output power levels are achievable to meet the requirements of the customer. Driven by vector control, it gives accuracy, flexibility along with high performance. It has low switching losses, low motor Total Harmonic Distortion (THD) and can drive the motor at very low frequency at full torque [25]. The drives are water cooled [22][26]. Figure 2-7 shows a PWM 3-level 12-pulse diode front end (DFE) neutral point clamped (NPC) inverter using press pack insulated-gate bipolar transistor (IGBT). However, high switching frequency of the VSI-PWM can result in bearing currents which damage bearings.

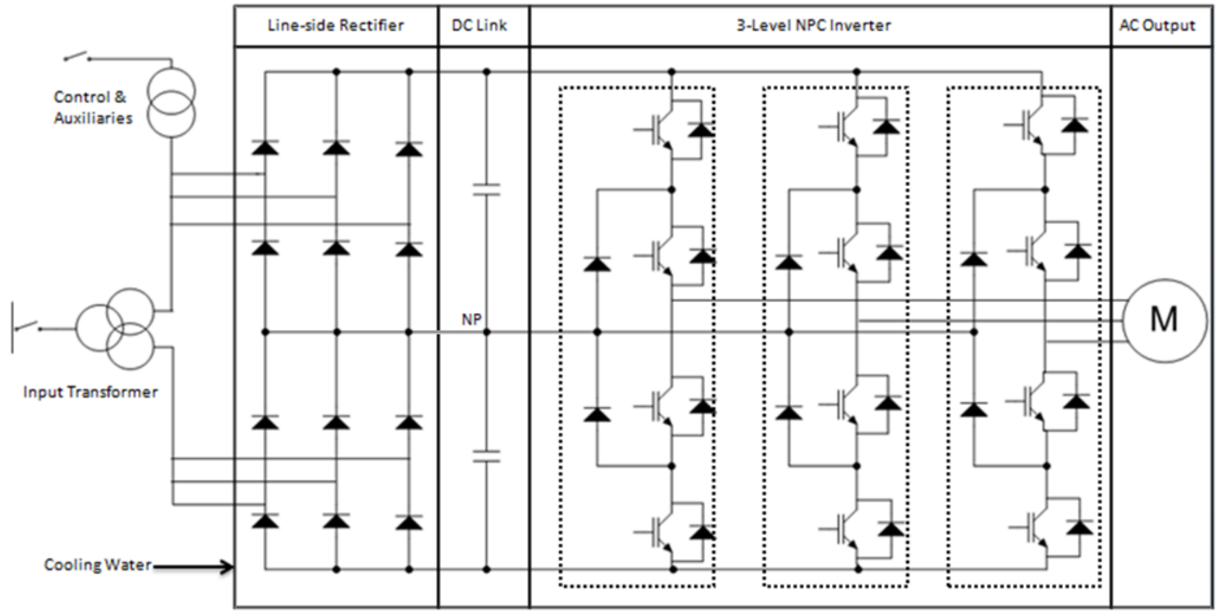

Figure 2-7 PWM 3-level 12-pulse diode front end (DFE) neutral point clamped (NPC) inverter using press pack IGBT

2.3 Electrical machine topologies, current trends and suitability for marine propulsion applications

This section covers briefly on the three main machine construction, their characteristics and inherited advantages and disadvantages. The choice of the hybrid excited synchronous machine construct for the podded propulsor will then be decided based on their merits.

2.3.1 Choice of machine configuration: radial/ axial / transverse flux construction

There are three main mechanical constructions of electrical machines. They are radial, axial and transverse flux machine configurations. Radial flux machines are the most commonly used and easiest to manufacture due to their mature establishments in current industries. Torque is generated in the regions of the air-gap through interaction of stator current and magnetic flux which travels radially from rotor to stator. With our application in mind, comparisons of radial flux machine configuration between the two others are as follows:

2.3.1.1 Radial vs. axial construction

Axial flux machines characteristically have a short length but a large diameter and may be constructed with different length to diameter ratios. Magnetic flux passes axially from the rotor disc to its stator. The main advantage of using axial flux machine is that its torque is proportional to its radius cubed.

For our application, the radial flux machine has clear advantages [27]:

- It inherently has a more rugged rotor.
- It is easier to cool. Stator windings can be better cooled through the outer casing which is in direct contact with surrounding water. Rotor can also be hollowed for coolants to flow.
- Easy arrangement of damper windings.
- Straightforward adjustment of rotor inertia.

However, some of its weaker points are [28]:

- Having a more complex structure
- More difficult for maintenance.
- Lower power to weight ratio.
- Surface-mounted magnets on rotor more exposed to centrifugal forces.

2.3.1.2 Radial vs. transverse construction

Transverse flux machines inherently have good fault-tolerant capability due to having high inductance which limits the current during a fault. However, they are difficult to manufacture, not suitable for wide constant power speed ratio and suffer from low power factor. It also utilises rotor discs as in axial flux machines. Magnet flux passes both radially and axially from rotor to stator [29]. RR has previously built and tested a 2MW transverse flux machine for marine propulsion. The prototype suffered from a range of problems including a low power factor of 0.7 [30][31].

Advantages of radial flux machines over transverse flux machines are [1]:

- Cheaper and easier to manufacture.
- Higher power factor at various loads.
- More suitable for wide constant power speed ratio. Marine propulsion sometimes require up to 10% of flux weakening operation.

Disadvantages are [1]:

- Lower inherited fault-tolerant capability.
- Lower torque density and higher copper losses.
- Lower pole count versus winding count.
- Competition for space between electric and magnetic loading limiting torque production.

2.4 Review and comparison of selected published HESM topologies

From the previous section, it is concluded that the radial flux machine configuration is best suited for azimuthing marine propulsors. Therefore, the axial and transverse flux machine constructions are not considered in the following review. A range of designs based on their excitation methods are selected to be mentioned in the following section.

2.4.1 Classification of HESM excitations

There are generally two ways to classify HESM excitations [32]:

1) Series and parallel excitation:

This describes the interaction of PM and field excitation flux in the magnetic circuit. In series excitation, flux from excitation windings has to pass through the permanent magnets. Its flux regulation is distributed uniformly and a higher efficiency in wide speed range operation than parallel configuration [33]. However, rare-earth permanent magnets material has a low relative permeability about unity. As a result, flux control capability with series excitation is less effective.

In parallel excitation, excitation windings flux works in parallel with the PM flux without crossing through PM material. Therefore, it has a better flux regulation capability than series configuration. However, it has a more complex design structure [34]. Figure 2-8 illustrates the operating principles of series and parallel excitation.

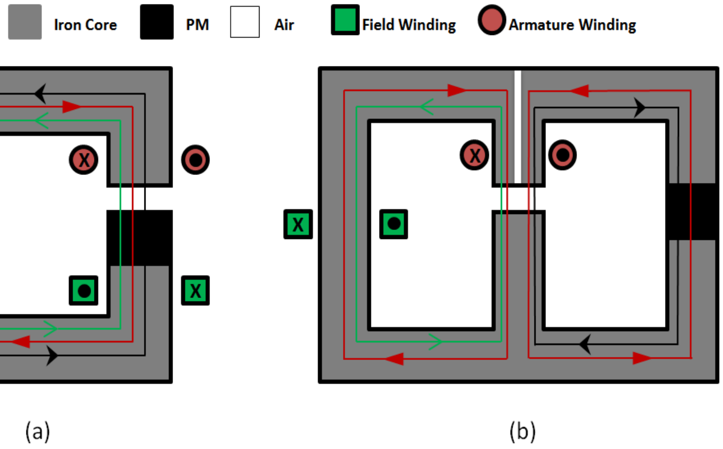

Figure 2-8 Operating principles of a series HESM (a) and a parallel HESM (b), Red lines denote armature excitation flux while black and green lines refer to PM and field excitation flux respectively

2) Location of field excitation windings in the machine:

Field excitation windings can be located either on the stator, rotor or mixed (i.e. both) [35]. To improve reliability both excitations should be on the stator which is a non-moving part. This can allow less protective measures, ease of analysis and manufacturing, and higher speed capability. However, this point mainly depends on the design and requirements of the electrical machine.

In the next section, selected HESM constructions will be reviewed and assessed, with a final comparison among the designs in the view of determining a preferred topology for the application.

2.4.2 Advantages and disadvantages of HESM

Every machine topology has their pros and cons. While HESM inherits the advantages of both PMSM and wound field synchronous machine (WFSM), it also inherits their disadvantages. Table 2-1 shows a list of them.

Table 2-1 Comparison of HESM, PMSM and WFSM properties

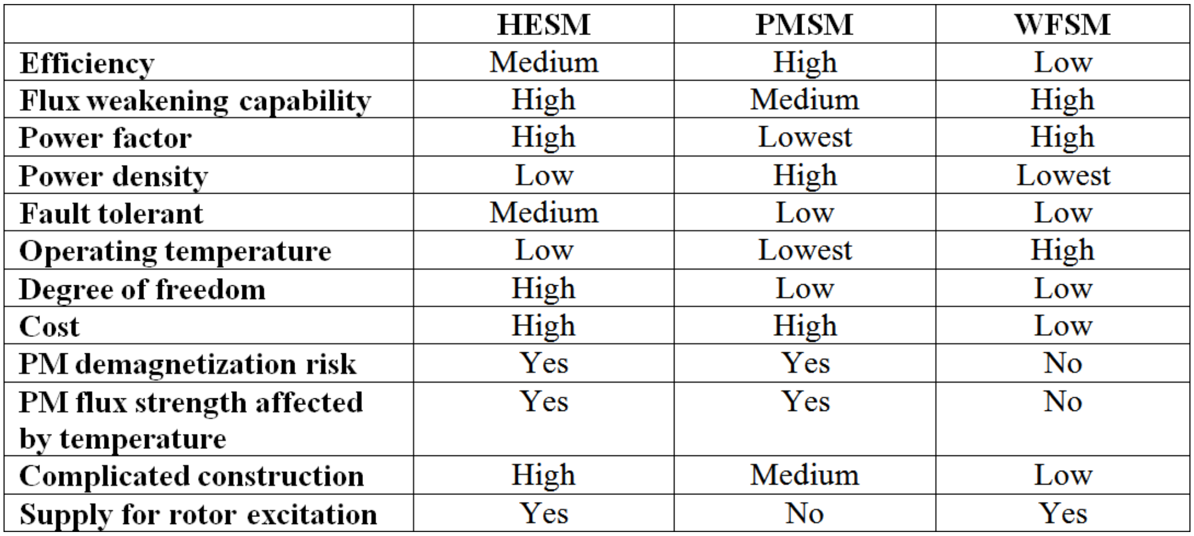

	HESM	PMSM	WFSM
Efficiency	Medium	High	Low
Flux weakening capability	High	Medium	High
Power factor	High	Lowest	High
Power density	Low	High	Lowest
Fault tolerant	Medium	Low	Low
Operating temperature	Low	Lowest	High
Degree of freedom	High	Low	Low
Cost	High	High	Low
PM demagnetization risk	Yes	Yes	No
PM flux strength affected by temperature	Yes	Yes	No
Complicated construction	High	Medium	Low
Supply for rotor excitation	Yes	No	Yes

2.4.3 Review of published HESM topologies

2.4.3.1 Hybrid excitation synchronous machine (HESM)

Naoe and Fukami proposed a two-pole prototype machine of 0.75kVA, 200V and 60Hz in 2001 shown in Figure 2-9. The machine has a conventional synchronous machine stator and a tandem two-part rotor. One part of the rotor has PM excitation while the other part has wound field excitation. They are separated by an axial air-gap. Therefore, both parts of the rotor are magnetically independent of each other due to the flux produced by the field current not passing the PM because of its large reluctance. Hence, a low magnetomotive force (MMF) from the field winding can alter the air-gap flux [36].

A prototype was made and tested. Figure 2-10 shows the flux regulation of the HESM. The fluxes of PM and wound field are indicated by dotted lines and the overall air-gap flux is the sum of the both. Figure 2-11 (a) shows that the overall induced electromotive force (EMF) has a wide control range by adjusting field current and (b) the induced EMF waveform on the stator is sinusoidal having a RMS voltage of 163V at a field current of 1 A [36].

Table 2-2 Advantages and disadvantages of the HESM

Advantages	Disadvantages
i) Simple construction [36]. ii) Ease of control of air-gap flux by adjusting field current [36]. iii) No limit to no. of poles [36]. iv) Easy to obtain machine parameters for flux control [36].	i) Require slip ring and brushes which greatly reduces reliability and increases maintenance cost [36]. ii) Uneven torque on shaft when winding field current is not at 2A which produce an EMF of 200V at 3600 rpm (Rated).*

Note: [ ] - Reported in literature, * - Deduction by author

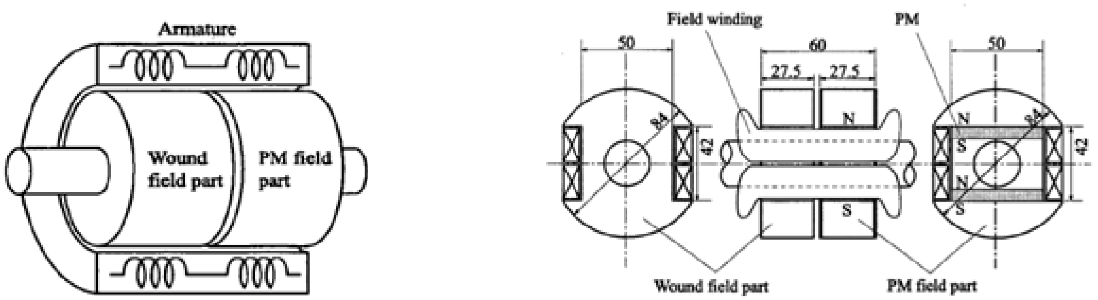

(a) (b)

Figure 2-9 (a) Structure of the proposed HESM and (b) cross section of the HESM [36]

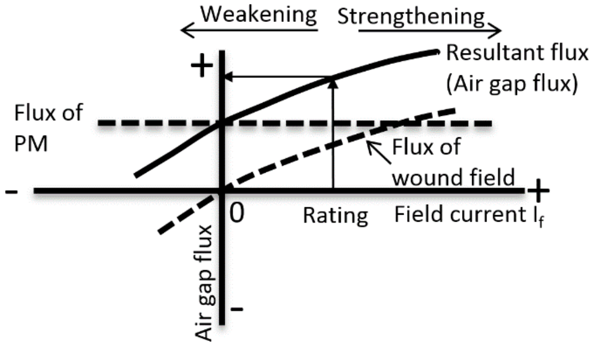

Figure 2-10 Field regulation schematic [36]

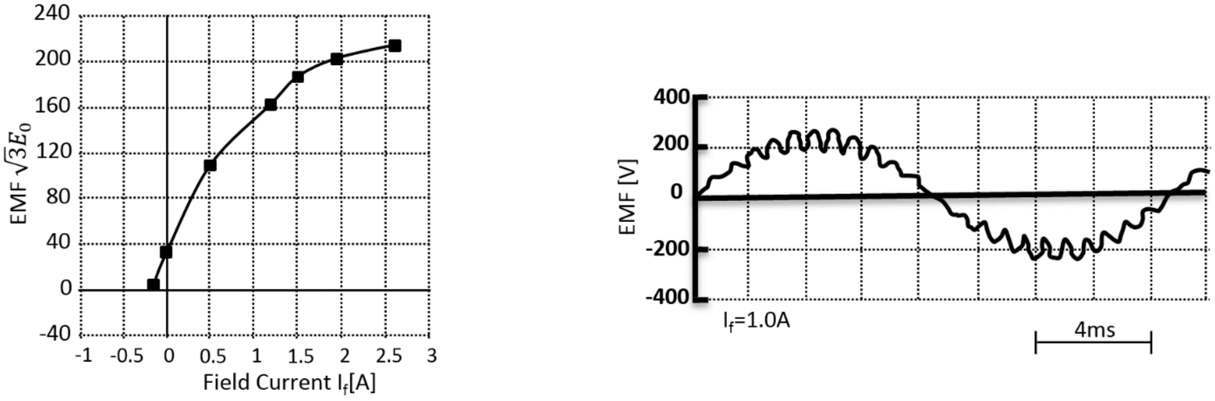

(a) (b)

Figure 2-11 (a) Open-circuit magnetization curve and (b) back-EMF waveform [36]

2.4.3.2 Dual-stator hybrid excited synchronous generator (DSHESG)

In 2007, Liu et al published a paper on a novel dual-stator hybrid excited synchronous claw-pole generator (DSHESG). It is specially designed for wind power generation applications [37].

The main structure of the DSHESG seen in Figure 2-12 comprises of permanent magnets, claw-poles, outer stator, inner stator and field windings. The phase angles of back-EMF in the two stators are consistent. Inner stator can increases output voltage and power density significantly. The total induced back-EMF is contributed by the EMFs induced on the inner stator by PMs and outer stator by PMs and field windings. Both magnetic circuits are in parallel. Output voltage can be maintained a constant value regardless of rotational speed by adjusting the field winding current [37]. Figure 2-13 shows the outer and inner stator winding distribution, where the outer stator winding is distributed, skewed and short-pitched and the inner stator has concentrated windings [38].

A prototype of the generator is also fabricated to test against FEA simulations. Both of the results match closely. Figure 2-14 shows the trapezoidal waveform of a phase back-EMF and experimental result of three-phase voltage waveform. The amplitude of induced back-EMF in outer winding and inner winding is about 100V and 23V respectively, with sums up to about 130V. Figure 2-15 shows the effect flux regulation on the voltage output at no-load [38].

Table 2-3 Advantages and disadvantages of the DSHESG

Advantages	Disadvantages
i) Good field controllability [37]. ii) Air-gap flux easily controlled [37]. iii) Higher output voltage and power density due to inner stator [37]. iv) Reduces leakage flux problems [37]. v) Low demagnetization risk*	i) Slip-ring and brushes required for flux strengthening and weakening.* ii) Machine assembly is complex.*

Note: [ ] - Reported in literature, * - Deduction by author

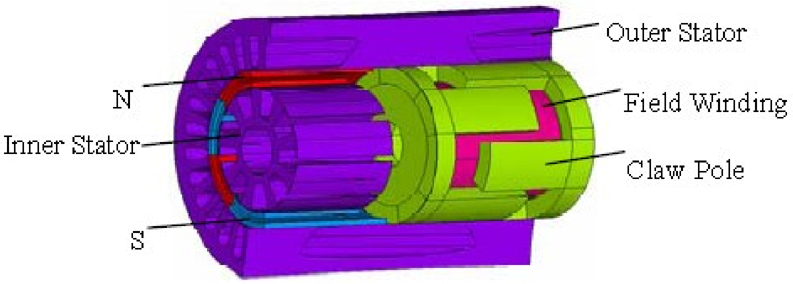

Figure 2-12 Structure of DSHESG [37]

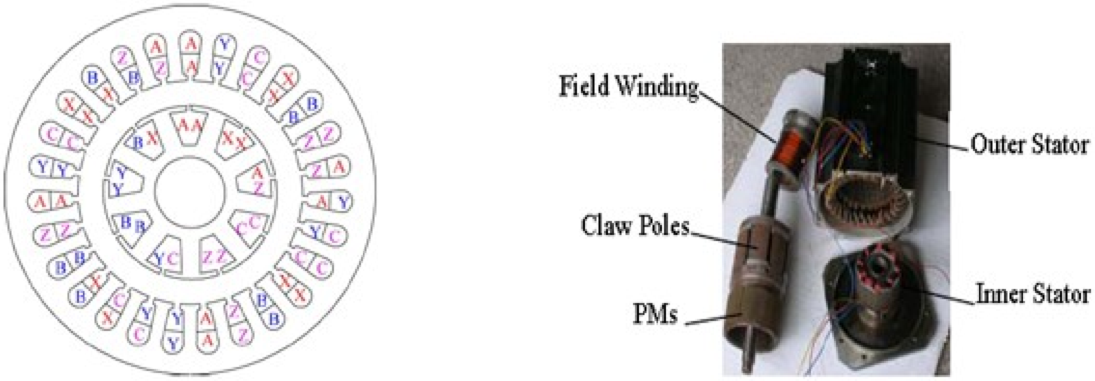

(a) (b)

Figure 2-13 (a) Layout of outer and inner stator windings [38] and (b) prototype of DSHESG [37]

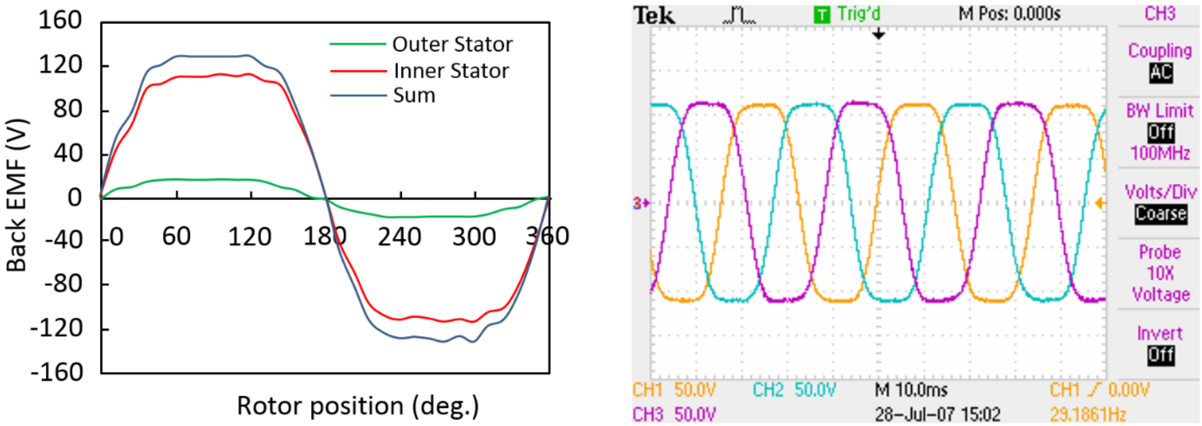

(a) (b)

Figure 2-14 (a) Trapezoidal waveform of a phase back-EMF and (b) experimental result of three-phase voltage waveform [37]

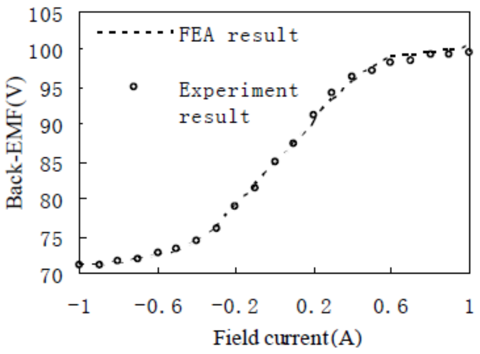

Figure 2-15 Effect of flux regulation on voltage at no-load [37]

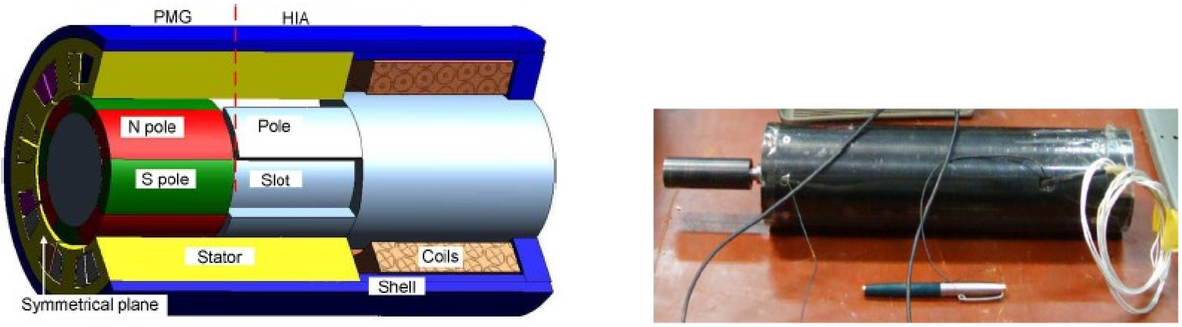

(a) (b)

Figure 2-16 (a) Diagram of the HESG showing the machine structure [39] and (b) prototype [40]

Another tandem rotor concept comes from Fu and Zou in 2008 shown in Figure 2-16. The HESG machine combines a surface-mounted PM rotor and a switched reluctance (SR) rotor. The switched-reluctance rotor has an excitation coil that induces its teeth to be either north or south pole. The PM and the SR rotors are separated from each other by an axial air-gap forming a magnetically parallel circuit. This feature is used to strengthen or weaken the magnetic flux on the rotor. The generator can operate at speed between 2000 rpm and 9000rpm [39].

2.4.3.3 Synchronous/permanent magnet hybrid AC machine (SynPM)

In 1998, Luo and Lipo proposed the synchronous/permanent magnet hybrid AC machine (SynPM). As shown in Figure 2-17, the machine consists of four PM and two wound field excitation poles on its rotor. The PM poles are the main source of air-gap flux while the excitation poles regulate the air-gap flux distribution. Each phase winding on the stator is formed by connecting three coils in series which comes under the influence of the two PM poles and one excitation pole. This allows the back-EMF to be adjustable in each phase [41].

The principle of operation of the SynPM is shown in Figures 2-18 to 2-20. As seen, there are three operating modes i.e. flux strengthening, flux weakening and no excitation, which corresponds to positive current flow, negative current flow and zero current flow. The magnitudes of total EMFs induced due to the flux regulation are three and two times more for positive and zero current flow respectively than for negative current flow. Flux distribution in the machine is also shown for each case [41].

This machine can find both application as a generator and motor [41]. No prototype has been built for this machine.

Table 2-4 Advantages and disadvantages of the SynPM

Advantages	Disadvantages
i) Increased reliability, machine operational even if excitation windings are out of service [41].	i) Requires slip-rings and brushes [41]. ii) For high speed operation, high flux density in stator core due to flux weakening

ii) High speed operation with field weakening capability [41]. iii) High efficiency [41]. iv) High power density [41]. v) Simple machine structure.*	may cause iron loss [41]. iii) Torque pulsations and vibrations produced due to space and time harmonic components by the combination of four pole and two pole flux and field weakening with the six pole flux of the armature reaction [41].

Note: [ ] - Reported in literature, * - Deduction by author

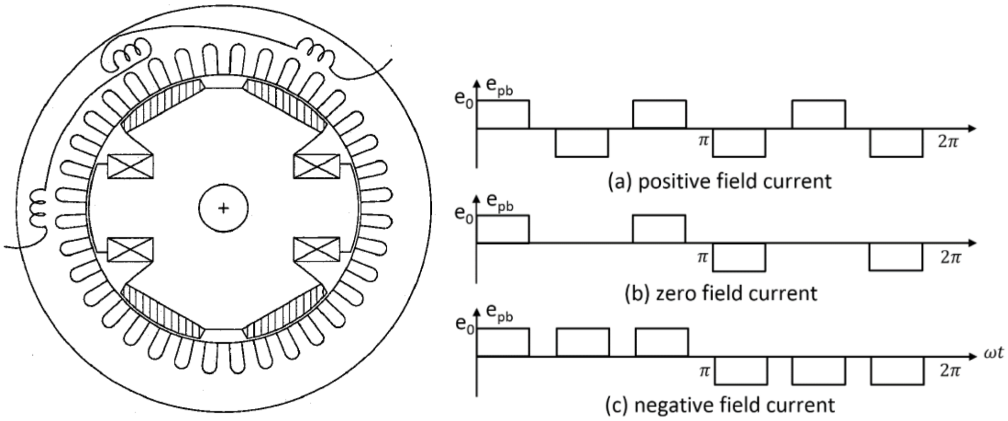

(a) positive field current

(b) zero field current

(c) negative field current

Figure 2-17 Structure of the SynPM machine and back-EMF waveforms of a phase belt winding for different excitation current direction [41]

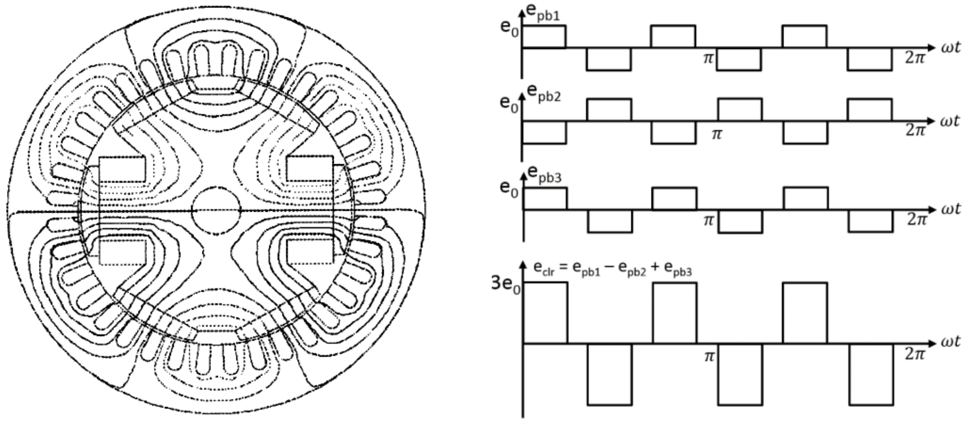

Figure 2-18 Flux distribution and back-EMF of machine with full positive excitation current [41]

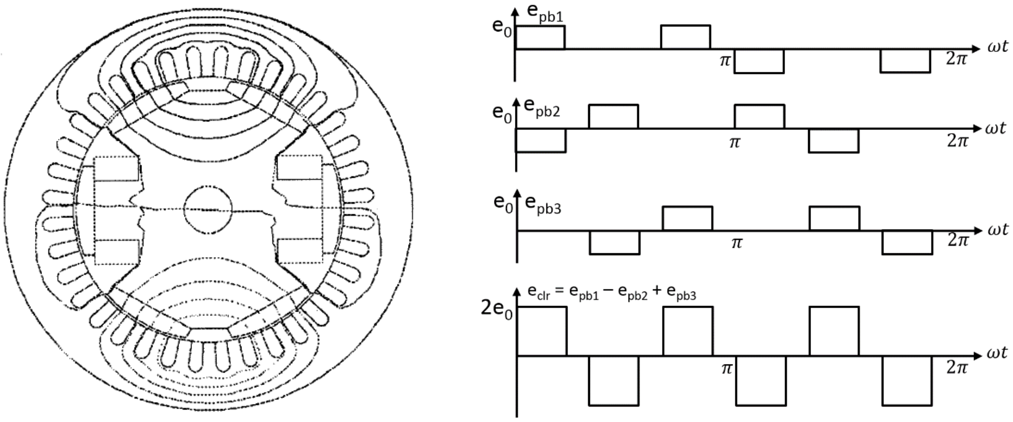

Figure 2-19 Flux distribution and back-EMF of machine with zero excitation current [41]

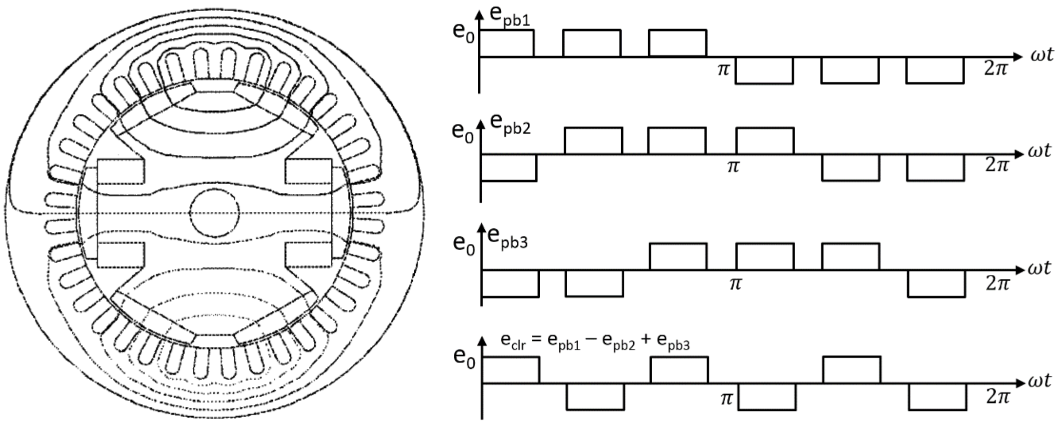

Figure 2-20 Flux distribution and back-EMF of machine with full negative excitation current [41]

2.4.3.4 Series double excited synchronous machine (SDESM)

In 2006, Fodorean et al presented a series double excited synchronous machine for electric vehicle traction shown in Figure 2-21. Due to this application, the machine will operate at optimum efficiency under a given partial loading which would be quite difficult to achieve by other machine topologies [33]. The machine rotor has four poles with surface-mounted PMs and DC field winding. Field winding excitation flux can be strengthened or weaken by DC excitation current via slip-rings and brushes. In motoring mode, the machine is able to gain in speed through flux weakening whilst reducing the iron losses almost by three times [42]. The publication did not illustrate the output voltage waveform, however from Figure 2-22 (a), it can be seen that the air-gap waveform is quite square-ish compared to conventional synchronous machines. Therefore, one can deduce the output voltage waveform contains a number of harmonics.

A 5.5kW prototype has been built. Figure 2-22 (b) and 2-23 (a) shows the output voltage under flux strengthening and weakening mode respectively. The SDESM is able to produce the desired performance in terms of torque, speed power factor and efficiency in generating and motoring mode for both experimental and FEA simulation [42].

Table 2-5 Advantages and disadvantages of the SDESM

Advantages	Disadvantages
i) Simple construction. [33] ii) Reduced iron losses in wide speed operation. [33] iii) Wide speed range of 2.8:1 for motoring mode. [33] iv) Good flux weakening capability. [33]	i) Require slip-rings and brushes. [33] ii) Requires a lot of PM material.*

Note: [ ] - Reported in literature, * - Deduction by author

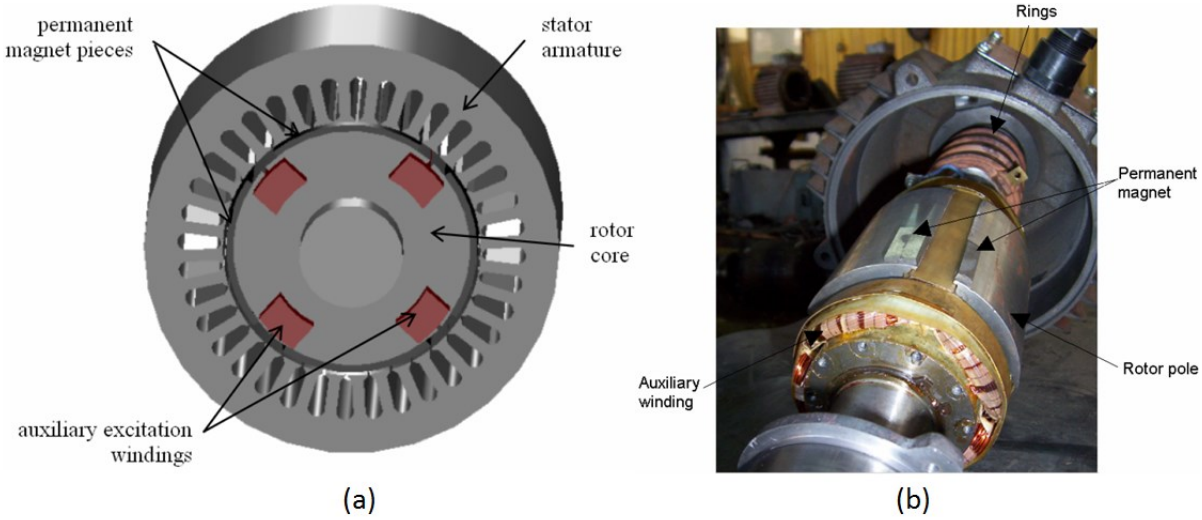

Figure 2-21 (a) Machine structure and (b) rotor of the SDESM [42]

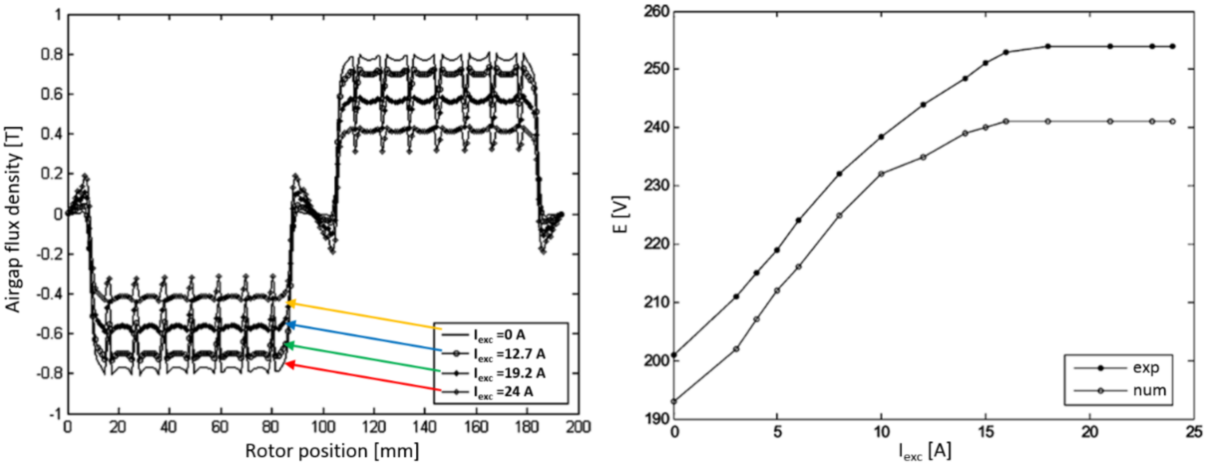

(a) (b)

Figure 2-22 Flux-strengthening mode: (a) FEM simulation results on the air-gap flux and (b) back-EMF for different values of excitation current [33]

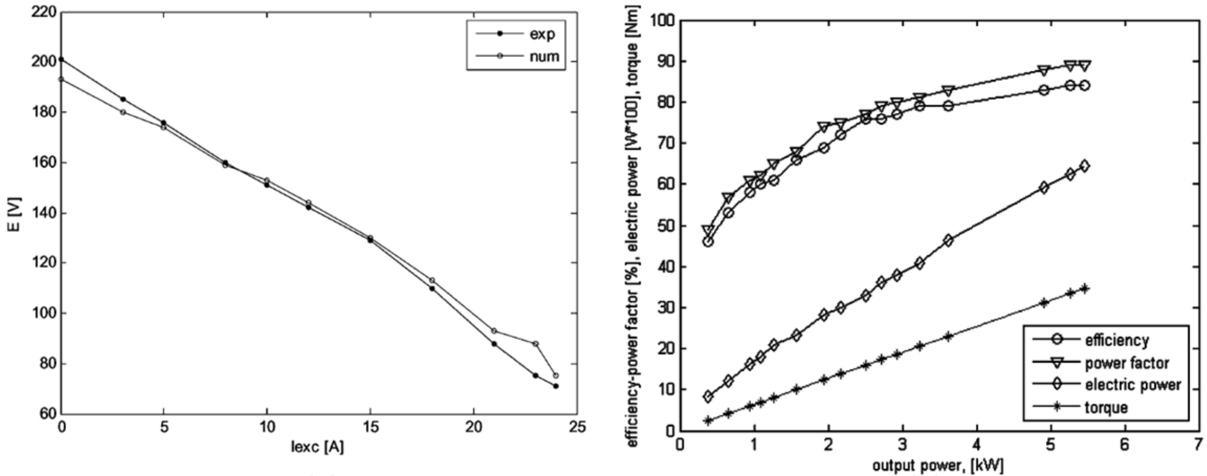

(a) (b)

Figure 2-23 (a) Back-EMF for different values of excitation current in flux-weakening mode and (b) SDESM performance in motor mode [33]

2.4.3.5 Hybrid excitation synchronous generator (HESG)

In 2012, Kamiev et al proposed 3 different designs of hybrid excitation synchronous generator (HESG) for marine diesel genset. They are a) 6-2 HESG, b) 4-4 HESG and 8-8 HESG shown in Figure 2-24 respectively. The former digit indicates the number of PM poles while the latter digit indicates the number of electrically excited poles. All of the machines have 4 pole-pairs regardless of the field excitation poles. They also share the same stator.

The main function of the excitation poles is to compensate armature reaction when generator is supplying inductive loads [34].

The main requirements of alternating current (AC) island operations are meeting a peak torque of 160% rated torque, voltage variations within ±10% of rated voltage, supplying inductive loads having power factor of 0.8, parallel operation and sustaining a short-circuit current of 300% rated current for 2 seconds [34].

In the literature, the machines performances are simulated and compared. Each machine is rated at 500kW. The 4-4 HESG is chosen as the most suitable HESG for the application. Table 4-5 shows their respective performance based on FEM simulations [34]:

Table 2-6 Performances of different HESG configurations

Performance at rated operation	**6-2 HESG**	**4-4 HESG**	**8-8 HESG**
Efficiency at rated power (%)	96.16	97.05	96.71
Rated field excitation current (A)	42	15.75	18.25
Power density (kW/m3)	1995	1904	1802
Turns per excitation pole	500	500	280
d-axis inductance	Medium	Highest	Lowest
Armature reaction compensation distribution	Asymmetrical	Asymmetrical	Symmetrical
Structural integrity issue	No	No	Yes
Magnetic circuit of both sources	Series	Series	Series

The 4-4 HESG has the highest efficiency, lowest rated field excitation current, good power density, better control and distribution of air-gap flux out of the three machine designs. It should be also note that 4-4 HESG has the lowest PM mass thereby reducing material cost. However, 4-4 HESG has the lowest power density without field excitation. Figure 2-25 shows the voltage waveforms for 4-4 HESG and 8-8 HESG compared to a traditional synchronous generator. Both voltage waveforms from hybrid machines appear to be more sinusoidal than the traditional SG voltage waveform with 4-4 HESG having the best

waveform. At the time of writing, no prototype has been built. A 55kW prototype is being planned [34].

Table 2-7 Advantages and disadvantages of the HESGs

Advantages	Disadvantages
i) Good air-gap flux controllability [34]. ii) High power generation efficiency comparable to PMSM efficiency [34]. iii) Easy of manufacture [34]. iv) Low harmonic contents due to sinusoidal air-gap flux distribution [43]. v) Fault tolerant: can operate without excitation poles but on a lower voltage [34]. vi) Simple and rugged machine structure.*	i) Slip rings and brushes [34].

Note: [ ] - Reported in literature, * - Deduction by author

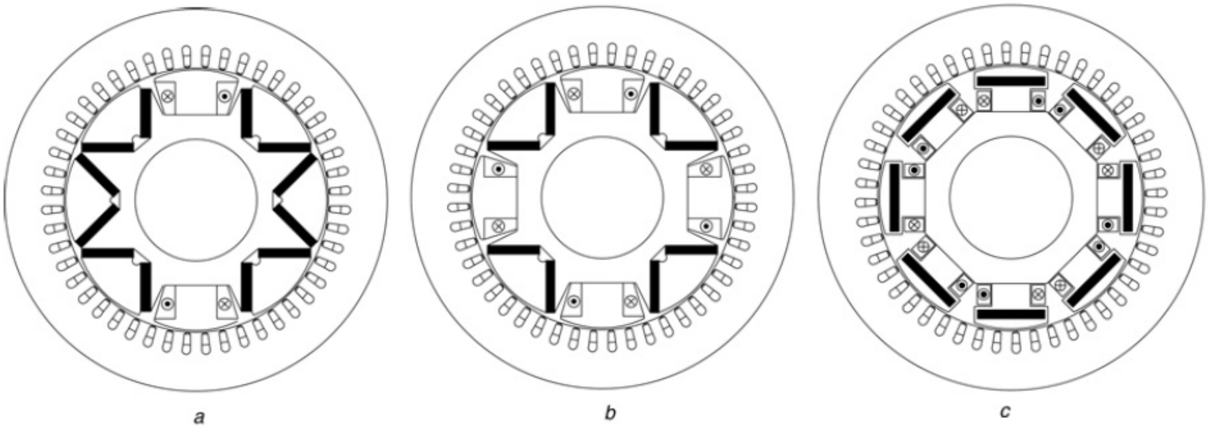

Figure 2-24 Structures of the HESGs: a) 6-2 HESG, b) 4-4 HESG and c) 8-8 HESG [34]

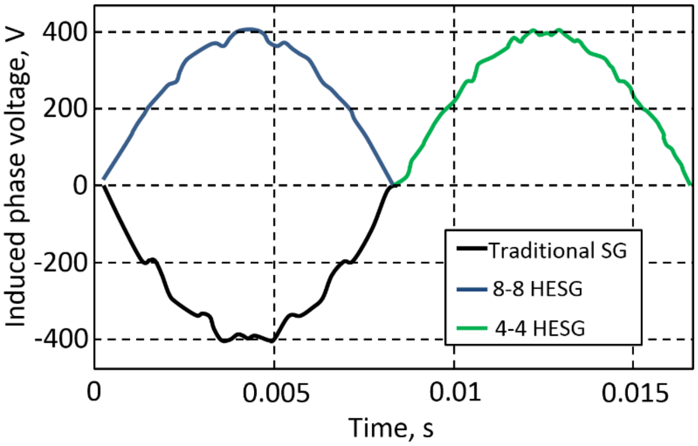

Figure 2-25 Comparison of half-cycle induced phase voltages of SGs with different excitations [34]

2.4.3.6 Consequent-pole permanent-magnet machine (CPPM)

In 2001, Tapia et al presented a consequent-pole permanent-magnet machine (CCPM). The 8-pole machine comprises of surface PM excitation and variable flux excitation via a DC field winding located circumferentially in the centre of the stator. As seen in Figure 2-26, each pole on the rotor is divided into two sections, each section consist of a PM or an iron core alternately placed with respect to the poles adjacent, forming a interleaved pattern. Polarities of the PMs are placed alternately and they are radially magnetized [44].

The stator has two axially adjacent tooth sections with a conventional three-phase AC winding. The DC field winding is located in between the tooth sections. When there is no field excitation, the flux in the machine is only due to PMs. Attracted by opposite PM polarity, the flux travels as the leftmost rotor in Figure 2-27(a) [44].

When field winding is excited such that the flux produced is added to the direction of the PM flux; flux from the PMs and the fields are in tangential. This magnetizing effect increases the flux per pole as shown in Figure 2-27(a) [45]. When field winding current flows in an opposite direction as to the magnetizing effect, flux from the field windings subtract the flux from the PM. The total flux per pole decreases and flux crosses the stator yoke axially giving a demagnetizing effect as shown in Figure 2-27(b) [45].

A 3kW prototype has been tested and experimental results agree with the simulation results. The voltage waveforms with different field excitations are shown in Figure 2-28(b). Both the old and improved machines have similar back-EMF waveforms [45].

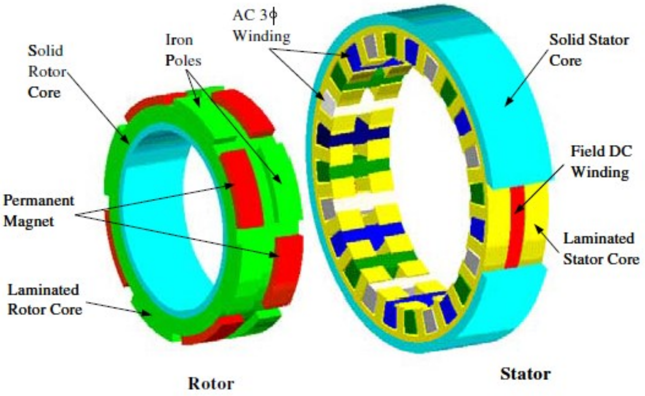

Figure 2-26 Structure of the CPPM machine [46]

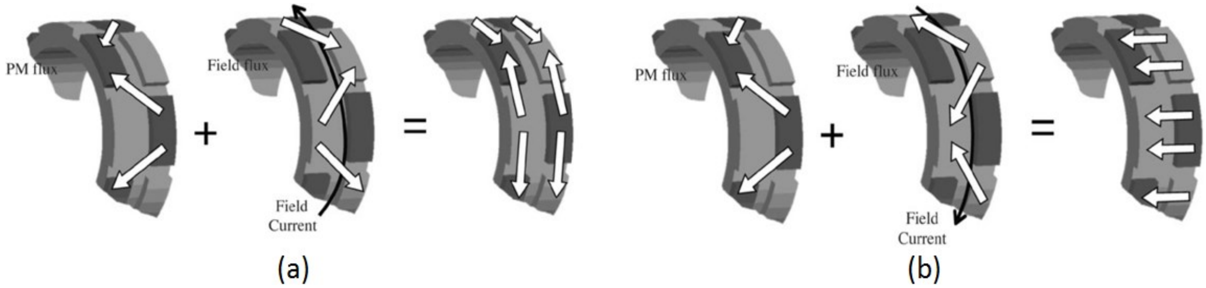

Figure 2-27 (a) Magnetizing effect and (b) demagnetizing effect of the field flux [45]

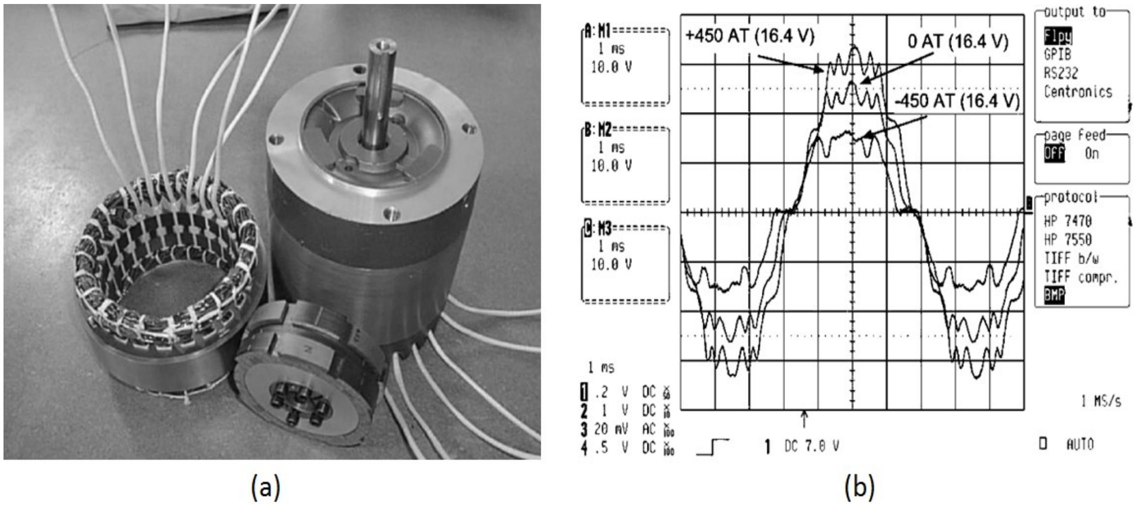

Figure 2-28 (a) A CCPM Prototype and (b) its voltage waveforms with different field excitations [45]

Tang et al has also created a very similar 4-pole electric machine in 2001 based on entirely same operating principle as above shown in Figure 2-29. It is called hybrid excitation permanent magnet synchronous generator (HEPMSG). Experimental results show machine has a rated efficiency of 78% [47].

An improved version of the machine is presented in 2005. Major changes are made to its rotor which now has PM on both sides of a pole as shown in Figure 2-30(a). Figure 2-30(b) illustrates its operating principle. It is claimed that the improved design is effectively better than the former design [48].

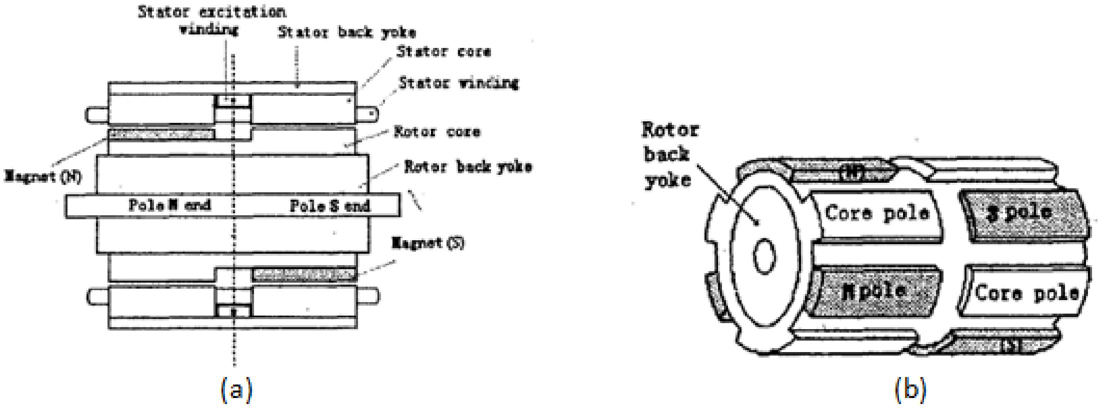

Figure 2-29 (a) Cross-section and (b) rotor structure of HEPMSG [47]

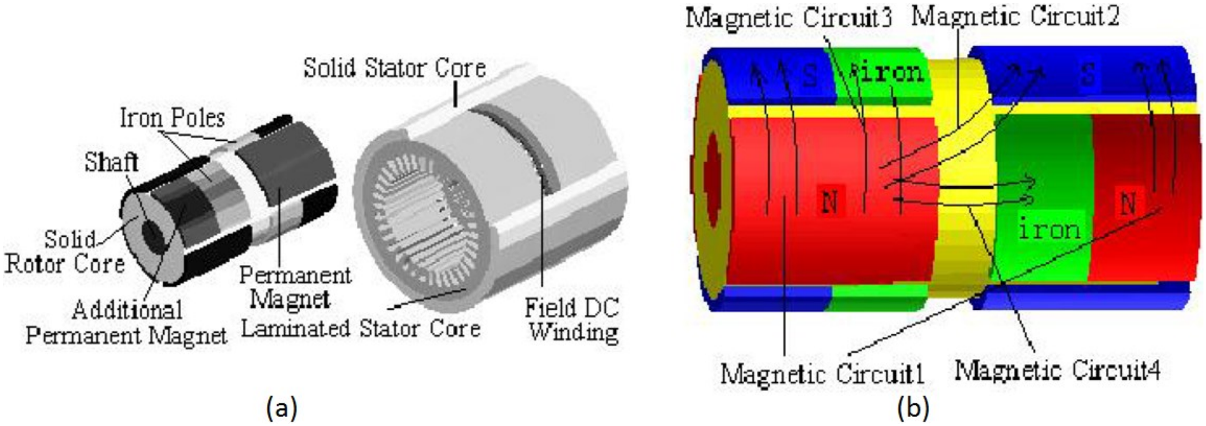

Figure 2-30 (a) An improved HEPMSG and (b) magnetic field diagram of rotor [48]

Table 2-8 Advantages and disadvantages of the consequent-pole permanent-magnet machine

Advantages	Disadvantages
i) Low field MMF requirement for wide air-gap flux control range [44]. ii) Easy improvement of power capability for a wide speed range [44]. iii) Very low demagnetization risk of PMs [44]. iv) Easy to control of air-gap flux by DC current [44].	i) Analytical complexity due to three-dimensional flux distribution*. ii) Additional DC winding in stator reduced power density [45]. iii) Due to radial, axial and tangential flux components, there is extra losses and increased core material [45]. iv) Manufacturing problems [45]. v) High temperature in machine [47]. vi) Significant excitation losses. * vii) Distorted back-EMF waveforms.*

Note: [ ] - Reported in literature, * - Deduction by author

2.4.3.7 Homopolar and bipolar hybrid excitation synchronous machine (HHESM & BHESM)

In 2005, Vido et al discussed two unique HESM designs called homopolar and bipolar hybrid excitation synchronous machine (HHESM and BHESM) shown in Figures 2-31(a) and 2-32(a) respectively. Both machines have the same stator but different rotors and are designed particularly for electric vehicle traction applications. Both rotor designs have 6 pole pairs each made up of a solid core, laminated core and permanent magnets [10].

The flux paths are divided into two categories: homopolar and bipolar flux paths. A homopolar flux path creates only one type of polarity depending on the polarity arrangements of the magnet and direction of current in the field coils. The flux from the magnets passes through the air-gap once [49]. A bipolar flux path creates north and south poles under active area of the rotor with the field windings acting in different polarities. The flux from the magnets passes through the air-gap twice [49]. Figures 2-31(b) and 2-32(b) show the flux paths for both homopolar and bipolar configurations respectively. For HHESM, the total flux passing through armature windings exhibits a DC component while BHESM does not. The bipolar configuration also has a leakage flux path through the magnets.

A prototype shown in Figure 2-33 is constructed and both machines configurations are tested and compared. The prototype is modular and can be assembled into either homopolar or bipolar configuration [10]. It is shown from experiments that air-gap flux control is effective for both configurations, HHESM DC excitation is more efficient due to more solid rotor core material [10]. Maximum flux for HHESM is reached when either north or south-pole saturates since DC field acts on one type of pole. For BHESM, maximum flux is reached when every pole in the machine saturates [10]. Therefore, the BHESM has a wider excitation flux variation and better air-gap flux control. Efficiency is better for HHESM due to the absent of significant leakage flux in the BHESM configuration [10].

Figure 2-34(a) show the EMF waveforms for both HHESM and BHESM at zero field excitation. It can be seen that both machines has quite similar square-ish waveforms. The HHESM EMF waveform seems to be smoother. Figure 2-34(b) shows the HHESM EMF waveforms for under different field winding excitation. The EMF waveform under flux weakening is distorted.

Table 2-9 Advantages and disadvantages of the HHESM and BHESM

Advantages	Disadvantages
i) Good air-gap flux control capability [10]. ii) No demagnetization risk [10]. iii) Slip rings and brushes not required [10].	i) Three-dimensional structures are more difficult to analyze and manufacture. Includes radial, axial and tangential flux flows [49]. ii) Complicated stator and rotor structures [49].

	iii) Significantly more core material requirement than traditional machines [10]. iv) Substantial amount of flux leakage * v) Relatively low maximum efficiency of 87% at rated no-load speed with full field excitation current for HHESM *

Note: [ ] - Reported in literature, * - Deduction by author

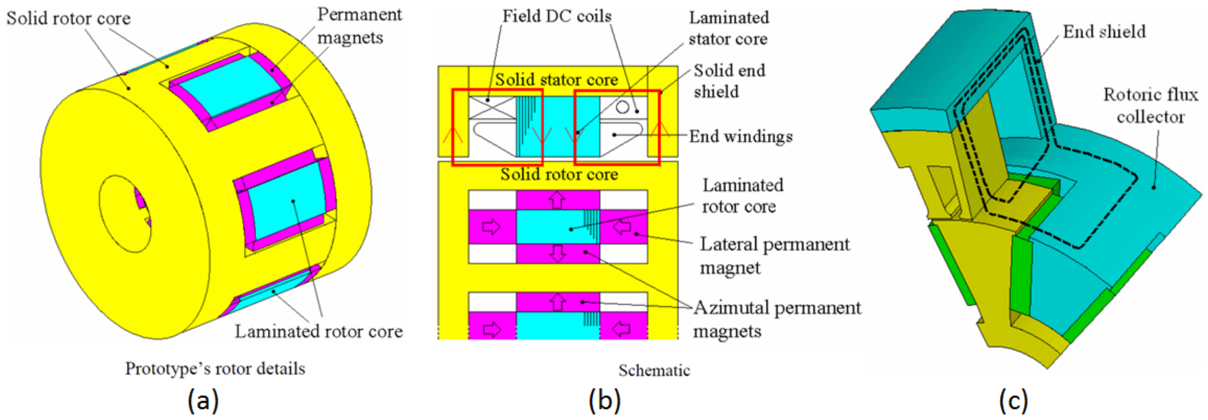

Figure 2-31 (a) HHESM structure and schematic details [10], (b) and (c) homopolar flux paths [49]

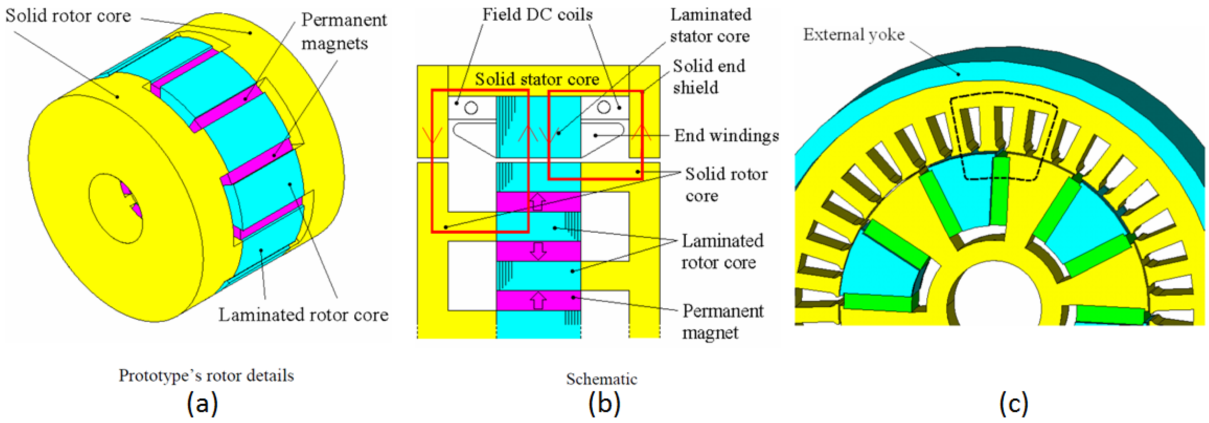

Figure 2-32 (a) BHESM structure and schematic details [10], (b) and (c) bipolar flux paths [49]

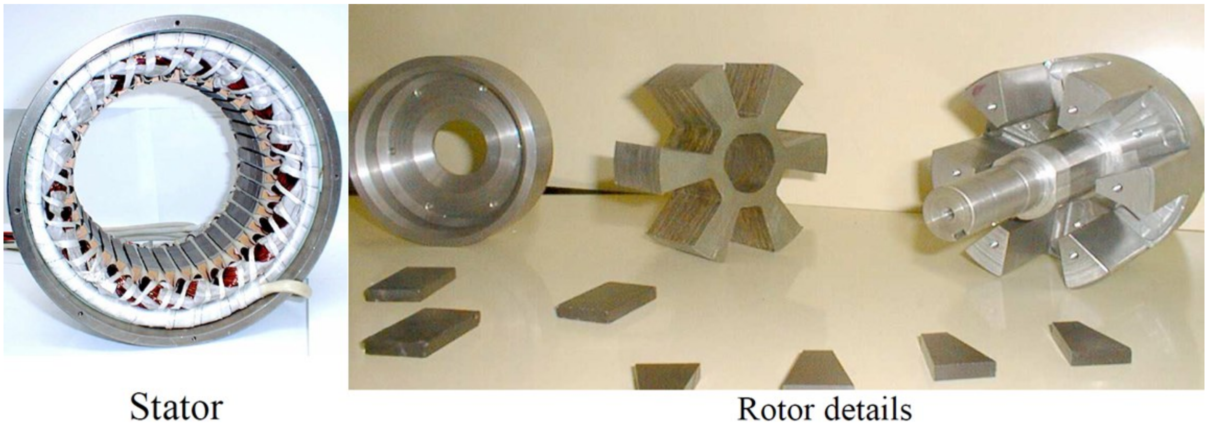

Figure 2-33 Machine prototypes [49]

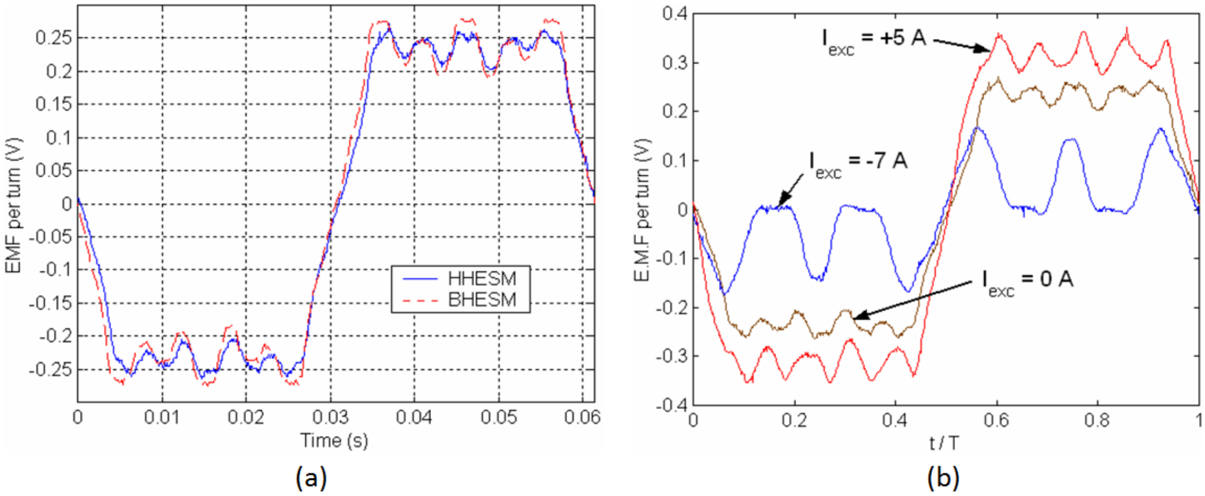

Figure 2-34 (a) The EMF waveforms for both HHESM and BHESM at zero field excitation [10] and (b) HHESM EMF waveforms for under different field winding excitation [49]

Improving on the above concepts, Vido et al proposed two HESM concepts in 2011 and 2012 as shown in Figure 2-35 [32][35]. The former machine uses similar operating principle as HHESM. It has modular claw pole rotor design and is able to cancel out induced current completely using field excitation current in the event of a phase winding fault [32].

The latter design works on both homopolar and bipolar flux principles. It has concentrated windings on the stator and all magnets on its rotor are placed in the same polarity. Using the excitation coils, opposite or similar magnetic poles as the permanent magnets can be created.

This gives a strengthening or weakening effect of the air-gap flux respectively [35]. Both designs experience the leakage flux problem as in the BHESM design.

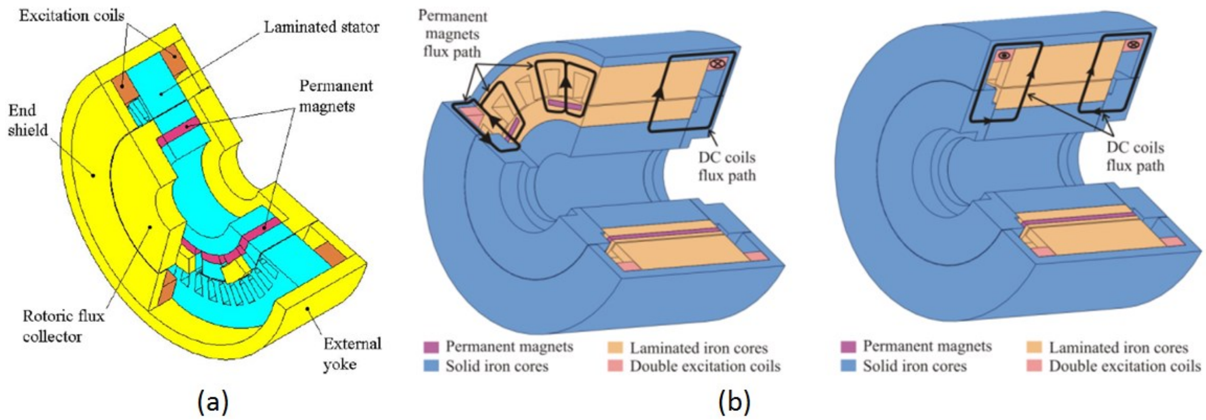

Figure 2-35 (a) New Parallel Double Excitation Synchronous Machine [32] and (b) PM and field winding flux paths of a new HESM [35]

2.4.3.8 Hybrid excitation flux switching permanent magnets synchronous machine (HEFSSM)

In 2007, E. Hoang et al presented the hybrid excitation flux switching permanent magnets synchronous machine illustrated in Figure 2-36(a). It is a switched reluctance machine with additional PM materials and excitation windings. DC current is injected in the excitation windings to strengthen or weakening the PM excitation flux. Iron losses can be reduced by flux weakening. The three phase machine has twelve magnets and coils on its stator. Its rotor has ten teeth [50].

Figure 2-36(b) shows the PM flux lines at zero excitation current. As seen, a portion of the PM flux passes through the air-gap and forms a magnetic circuit with the rotor while the other is a leakage flux. In Figure 2-36(c) and (d), excitation current flows in the excitation coils such that the total excitation flux in the machine increases and decreases respectively [51].

Figure 2-37 shows the prototype of the machine. In order to improve the output voltage waveforms to eliminate the 5n harmonics components, the authors modified the rotor by skewing it with an electrical angle of 7.2°. In Figure 2-38(a), the waveforms show the no-load voltages due to various levels of excitation current in the excitation coils at 3000rpm.

The voltage waveforms are of sinusoidal nature but distorted [50]. Figure 2-38(b) shows the improvement in the voltage waveform. The HEFSSM can be driven by a three phase voltage converter or a diode rectifier [50].

Table 2-10 Advantages and disadvantages of the HEFSSM

Advantages	Disadvantages
i) Fault tolerant structures: Concentrated windings and rugged rotor structure [50].	i) May not be deployed in high temperature environments due to PM materials.*
ii) Simpler cooling system since, most power losses occurs on the stator [51].	ii) Complex stator structure.*
iii) Sinusoidal no-load output voltage reduces harmonics [50].	iii) Expensive lamination core material to reduce high frequency eddy currents.*
iv) High flux and torque densities [51].	iii) High frequency converter and control techniques required.*
v) Capable of high speed or high torque/low speed operation [52].	

Note: [ ] - Reported in literature, * - Deduction by author

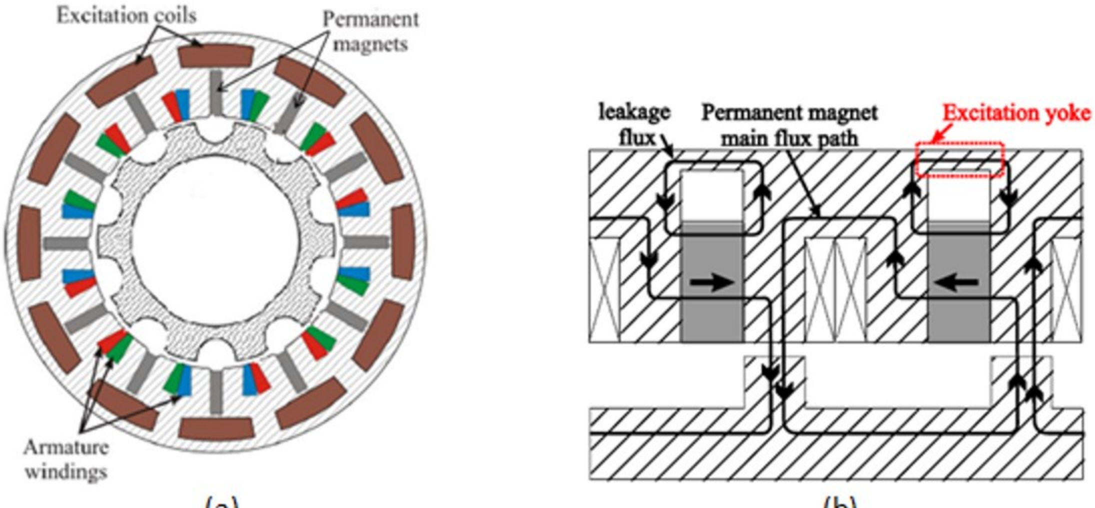

(a) (b)

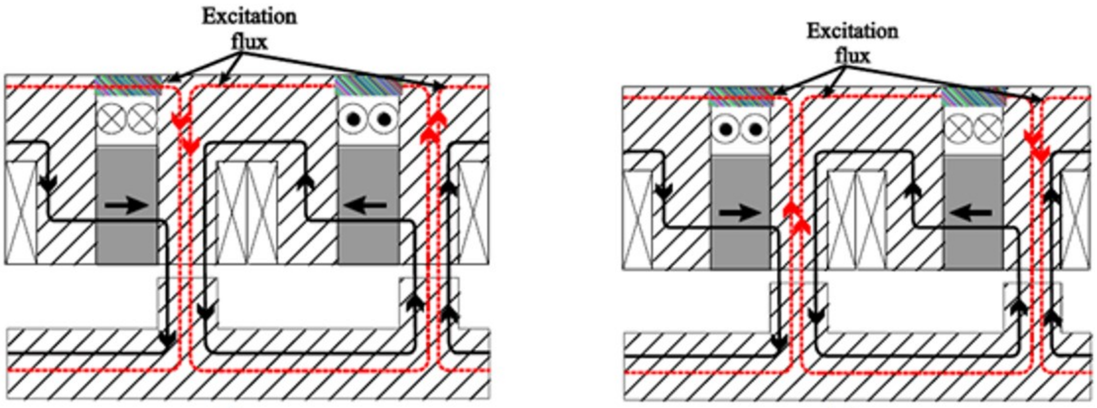

(c) (d)

Figure 2-36 Structure of the HEFSSM; (b) PM flux path at zero excitation current; (c) PM (black) and positive excitation current (red) flux lines; (d) PM (black) and negative excitation current (red) flux lines [51]

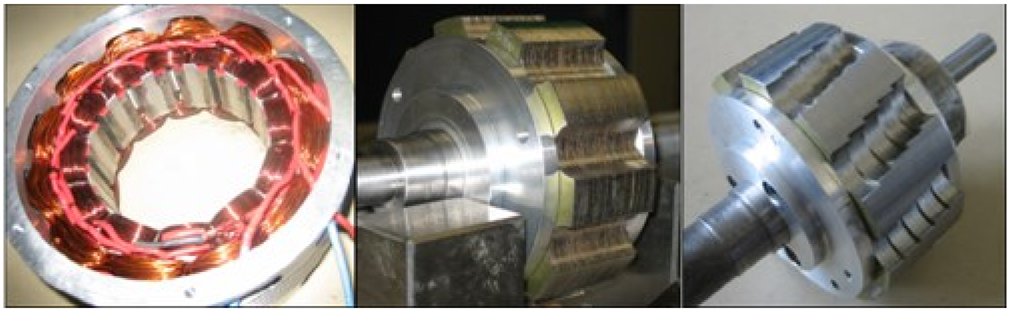

Figure 2-37 Stator iron core and winding, initial rotor and modified rotor [51]

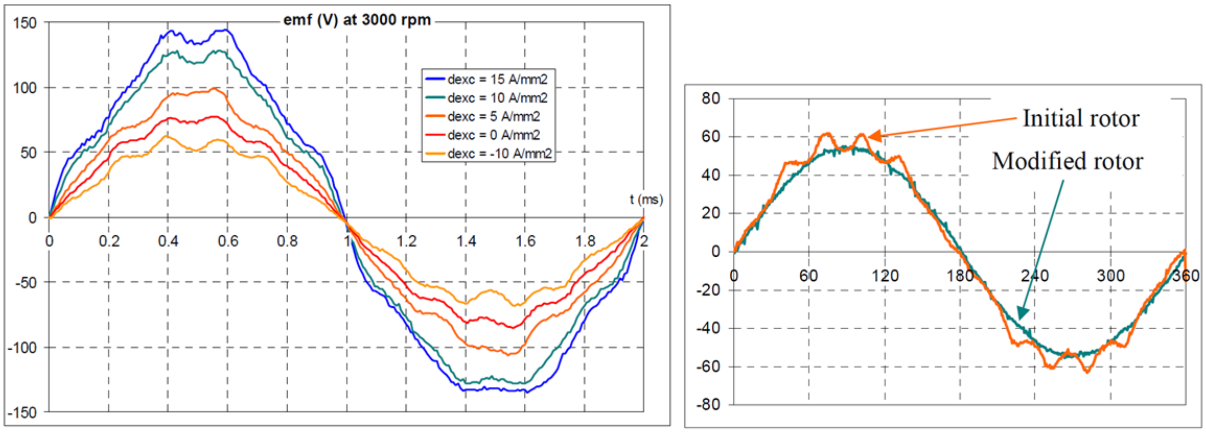

(a) (b)

Figure 2-38 (a) Measured no-load voltage waveforms at 3000 rpm and (b) no-load voltage waveforms of initial rotor and modified rotor [50]

Switch reluctance machines, however, was claimed to be unable to match the levels and power and torque density offered by permanent magnet machines to be used efficiently for electric propulsion [53]

2.4.3.9 Tangential/radial hybrid excitation synchronous generator (T/R- HESG)

In 2010, Shushu Zhu et al presented a novel concept of a tangential/radial hybrid excitation synchronous machine. It is designed mainly for applications in aerospace and off-grid systems. The objectives of the unique structure of the rotor are to provide a fully-adjustable PM magnetic field and to allow self-excitation during start-up without an auxiliary exciter. Therefore, the traditional three-stage brushless synchronous generation excitation as shown in Figure 2-39 can be replaced with a novel two-stage brushless hybrid excitation synchronous generator as shown in Figure 2-40 [54].

Without field excitation, the PM flux will form a magnetic short-circuit in the rotor iron core. However, the rotor core is designed to be saturated so that some magnetic flux passes through the air-gap to the stator. This is to provide sufficient voltage to brushless exciter during start-up. The output voltage is 50V at start-up [55].

When field windings are excited, the magnetic flux produced by the field windings is radial while the flux of the PM is tangential. The problem of uneven air-gap flux is solved by reducing the rotor diameter close to the PMs. The flux from both sources is in parallel as shown in fig. Maximum induced EMF would be at 425V. Figure 2-41 compares output voltage against the field current of the machine and traditional synchronous generator [55].

A prototype of the T/R-HESG is built as shown in Figure 2-42 (a) & (b). Figure 2-42 (c) shows the output voltage waveform at no load [56].

The same university has also presented another T/R- HESG with 16 poles as shown in Figure 2-43. It has similar operating principle as the machine above. However, it has very little PM air-gap flux in the unexcited state. It is specially designed for wind turbine applications [57].

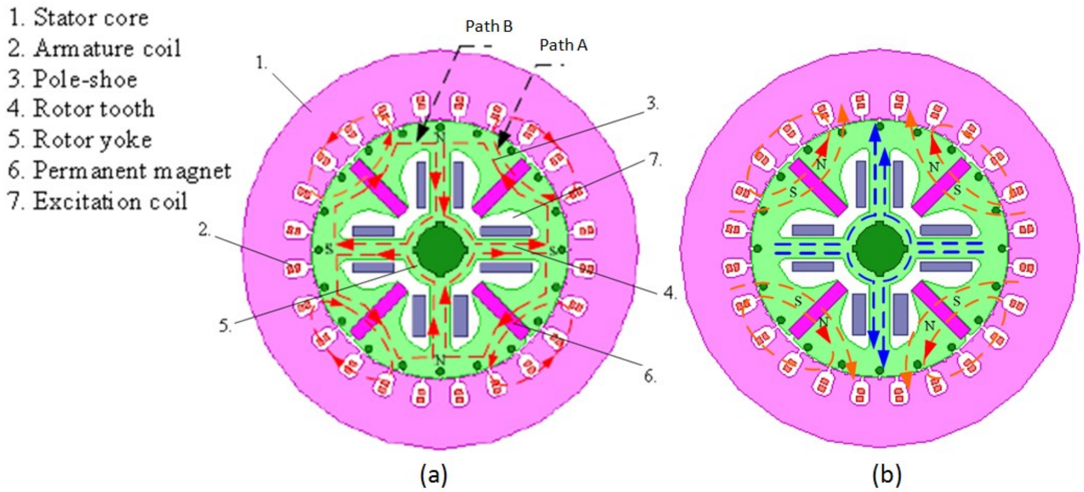

Figure 2-39 (a) Structure and flux distribution of T/R-HESG without excitation current and (b) with excitation current [56]

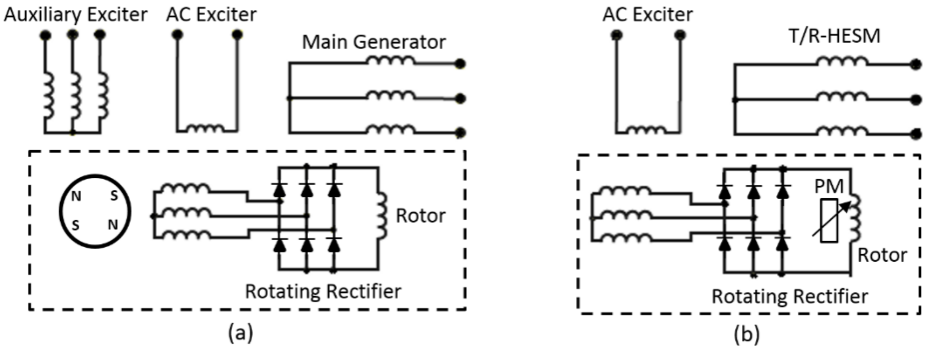

Figure 2-40 (a) Traditional three-stage and (b) two-stage brushless synchronous generator scheme [54]

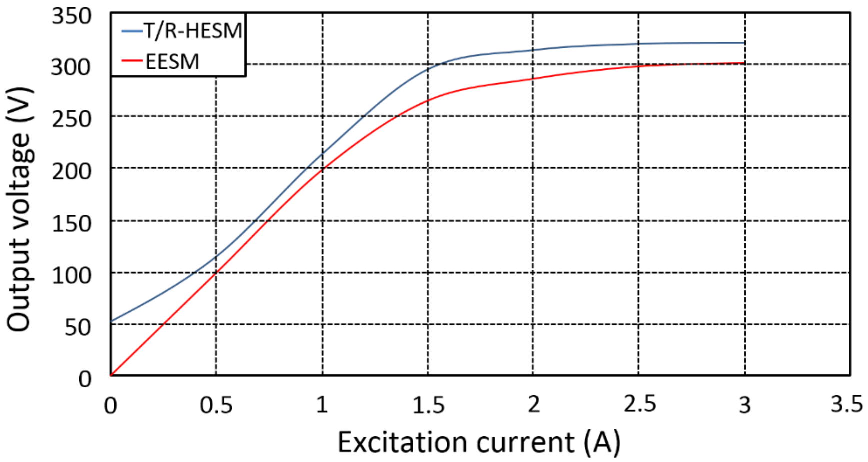

Figure 2-41 Simulation results comparing the T/R-HESM to a tradition synchronous generator [55]

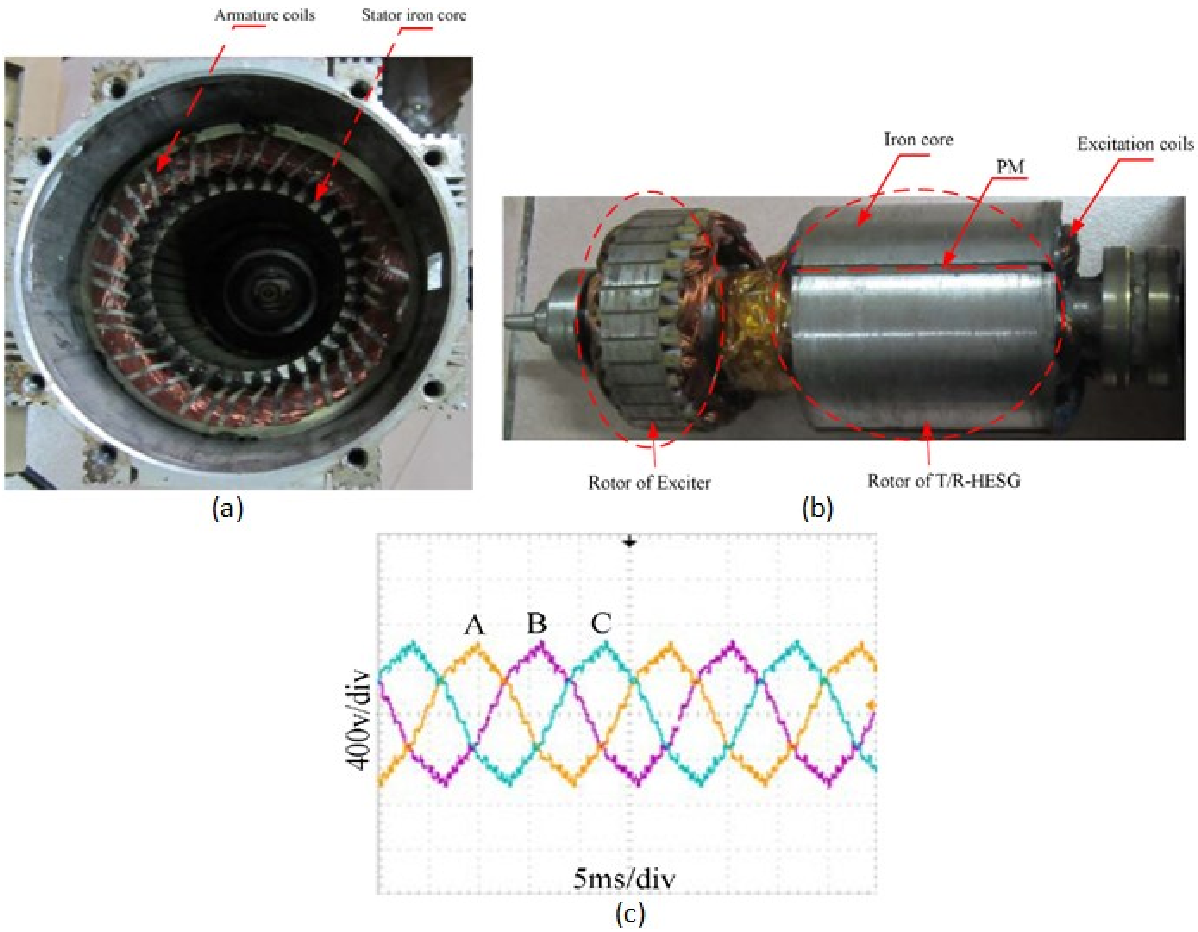

Figure 2-42 (a) Stator of T/R-HESG; (b) its rotor [56] and (c) its no-load voltage waveform [55]

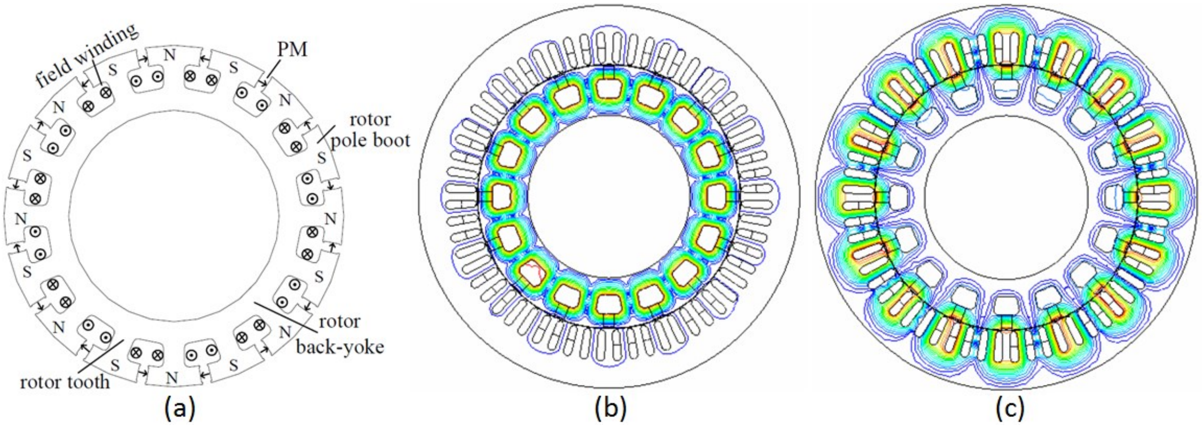

Figure 2-43 (a) Cross section of a 16 pole T/R-HESG; (b) its flux distribution without excitation current and (c) with excitation current [57]

Table 2-11 Advantages and disadvantages of the T/R-HESG

Advantages	Disadvantages
i) Simple and rugged configuration. Easy to manufacture [55]. ii) Total air-gap magnetic flux adjustment [55]. iii) Easy to control induced EMF on stator winding [55]. iv) Wide speed operating range [55]. v) High efficiency [55]. vi) Requires less magnetic materials.* vii) Suitable for fail-safe systems applications.*	i) Naked magnets may be vulnerable to mechanical stress being placed between rotor poles.* ii) High in fifth and seventh harmonics.*

Note: [ ] - Reported in literature, * - Deduction by author

2.4.3.10 Permanent magnet electric generator with variable magnet flux excitation (PMVMFE)

In 2010, Gieras and Rozman patented a PM variable flux machine which works based on the principle of magnetic saturation of a portion of stator core with DC control winding [58]. As shown in the Figure 2-44 (a), a conventional AC stator is fitted with the magnetic flux diverters which also act as slot wedges.

At zero control current, the reluctance of the magnetic shunt is low and almost all the air-gap flux produced by the PMs passes through the shunt, omitting the stator core as shown in Figure 2-44 (b). The induced EMF in the stator winding is close to zero.

At the increase of DC control winding, the magnetic shunt is partially saturated and only a portion of the magnetic flux is allowed through the wedge. On further increase of DC control current until slot wedges becomes fully saturate with permeability close to unity, almost all the air-gap flux from the rotor PMs passes through the stator core. Hence induce a maximum EMF in the stator windings as shown in Figure 2-44 (c).

Figure 2-44(d) shows the amount of excitation current to maintain a constant output voltage value at different speeds.

Table 2-12 Advantages and disadvantages of the permanent magnet electric generator with variable magnet flux excitation

Advantages	Disadvantages
i) Simple in construct.* ii) Possible add on to existing machines design without compromising significant slot space.* iii) Fault tolerant. Electrical generation stops when DC field winding fails.* iv) Easy to control induced EMF on stator winding.*	i) Need high DC current to operate at maximum EMF. Increases temperature in stator core, damages insulation and possible demagnetization. * ii) No strengthening capability.* iii) Due to the nonlinearity of the magnetic circuit, EMF is a nonlinear function of the control current.* iv) Expensive high permeability magnetic shunt material.*

Note: * - Deduction by author

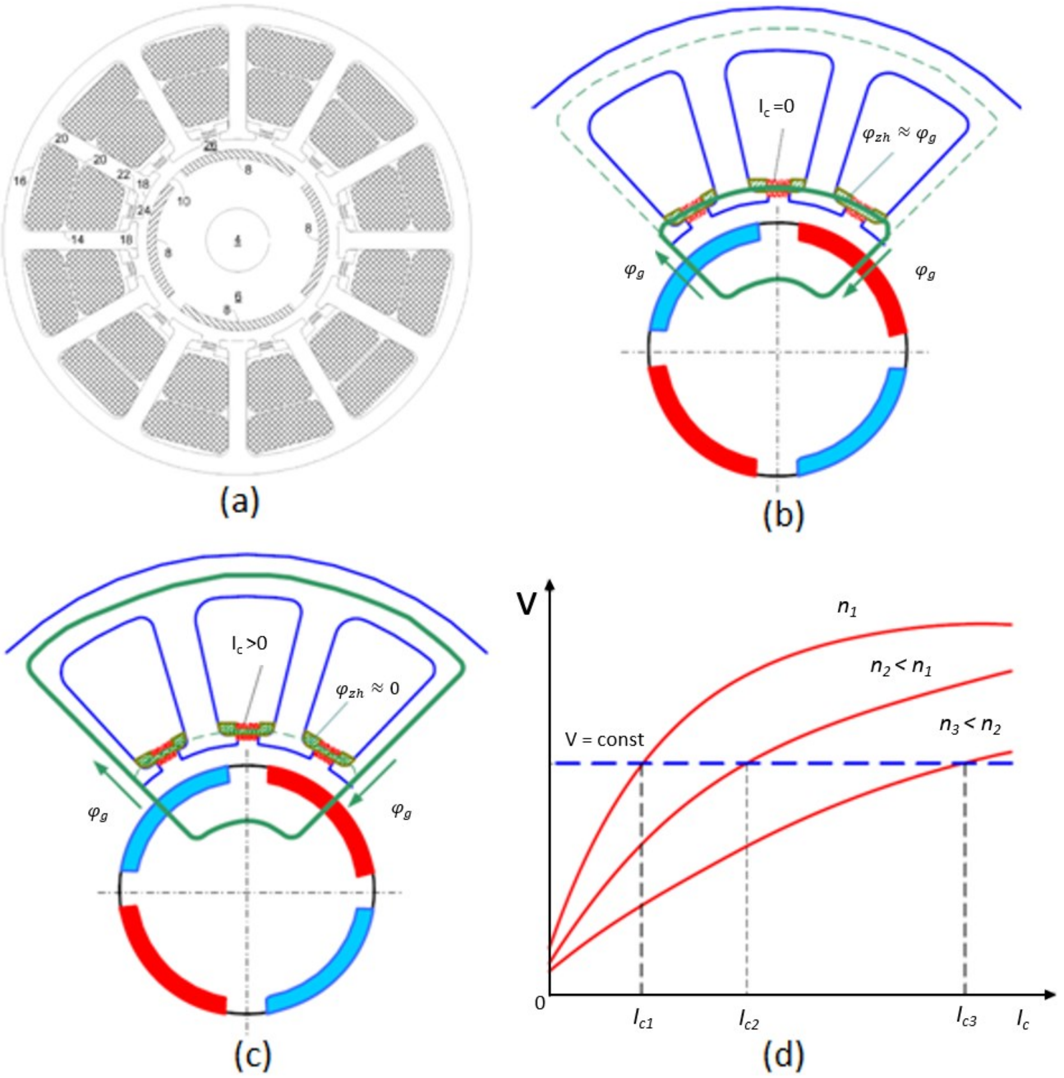

Figure 2-44 (a) Electrical machine with magnetic flux diverter on stator [59]; (b) magnetic flux path at zero control current & (c) when shunt is saturated and (d) Voltage regulation for different speeds [58]

2.4.4 Performance comparisons of published HESM topologies

Technical comparisons and performance ratings of the mentioned HESMs are given in this section.

2.4.4.1 Comparison table

Table 2-13 Comparison table

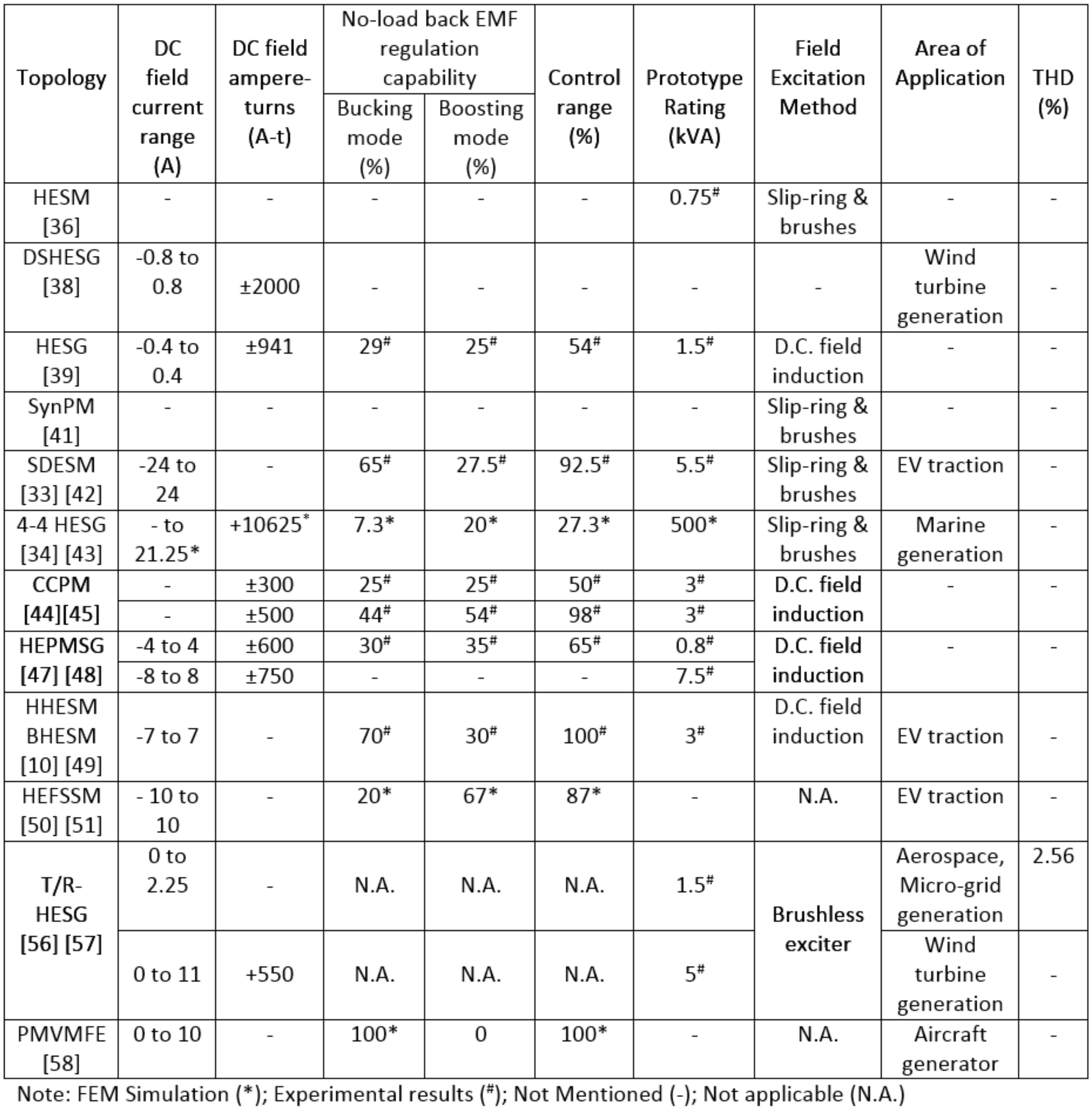

Topology	DC field current range (A)	DC field ampere-turns (A-t)	No-load back EMF regulation capability		Control range (%)	Prototype Rating (kVA)	Field Excitation Method	Area of Application	THD (%)
			Bucking mode (%)	Boosting mode (%)					
HESM [36]	-	-	-	-	-	0.75#	Slip-ring & brushes	-	-
DSHESG [38]	-0.8 to 0.8	±2000	-	-	-	-	-	Wind turbine generation	-
HESG [39]	-0.4 to 0.4	±941	29#	25#	54#	1.5#	D.C. field induction	-	-
SynPM [41]	-	-	-	-	-	-	Slip-ring & brushes	-	-
SDESM [33] [42]	-24 to 24	-	65#	27.5#	92.5#	5.5#	Slip-ring & brushes	EV traction	-
4-4 HESG [34] [43]	- to 21.25*	+10625*	7.3*	20*	27.3*	500*	Slip-ring & brushes	Marine generation	-
CCPM [44][45]	-	±300	25#	25#	50#	3#	**D.C. field induction**	-	-
	-	±500	44#	54#	98#	3#			
HEPMSG [47] [48]	-4 to 4	±600	30#	35#	65#	0.8#	**D.C. field induction**	-	-
	-8 to 8	±750	-	-	-	7.5#			
HHESM BHESM [10] [49]	-7 to 7	-	70#	30#	100#	3#	D.C. field induction	EV traction	-
HEFSSM [50] [51]	- 10 to 10	-	20*	67*	87*	-	N.A.	EV traction	-
T/R-HESG [56] [57]	0 to 2.25	-	N.A.	N.A.	N.A.	1.5#	**Brushless exciter**	Aerospace, Micro-grid generation	2.56
	0 to 11	+550	N.A.	N.A.	N.A.	5#		Wind turbine generation	-
PMVMFE [58]	0 to 10	-	100*	0	100*	-	N.A.	Aircraft generator	-

Note: FEM Simulation (*); Experimental results (#); Not Mentioned (-); Not applicable (N.A.)

2.3.4.2 Overall performance chart

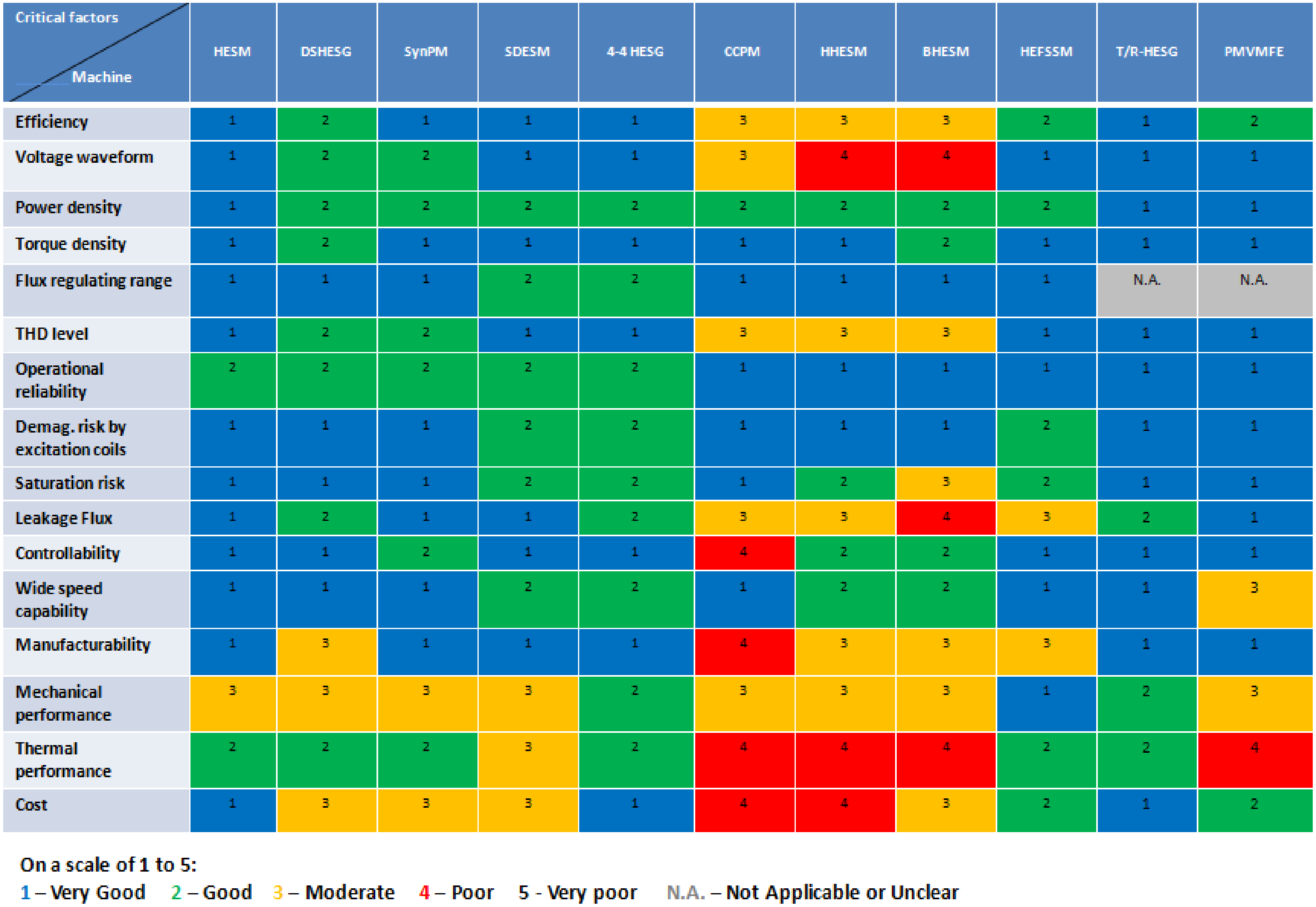

Critical factors / Machine	HESM	DSHESG	SynPM	SDESM	4-4 HESG	CCPM	HHESM	BHESM	HEFSSM	T/R-HESG	PMVMFE
Efficiency	1	2	1	1	1	3	3	3	2	1	2
Voltage waveform	1	2	2	1	1	3	4	4	1	1	1
Power density	1	2	2	2	2	2	2	2	2	1	1
Torque density	1	2	1	1	1	1	1	2	1	1	1
Flux regulating range	1	1	1	2	2	1	1	1	1	N.A.	N.A.
THD level	1	2	2	1	1	3	3	3	1	1	1
Operational reliability	2	2	2	2	2	1	1	1	1	1	1
Demag. risk by excitation coils	1	1	1	2	2	1	1	1	2	1	1
Saturation risk	1	1	1	2	2	1	2	3	2	1	1
Leakage Flux	1	2	1	1	2	3	3	4	3	2	1
Controllability	1	1	2	1	1	4	2	2	1	1	1
Wide speed capability	1	1	1	2	2	1	2	2	1	1	3
Manufacturability	1	3	1	1	1	4	3	3	3	1	1
Mechanical performance	3	3	3	3	2	3	3	3	1	2	3
Thermal performance	2	2	2	3	2	4	4	4	2	2	4
Cost	1	3	3	3	1	4	4	3	2	1	2

On a scale of 1 to 5:

1 – Very Good   2 – Good   3 – Moderate   4 – Poor   5 - Very poor   N.A. – Not Applicable or Unclear

Table 2-14 Overall performance chart

2.5 Summary

In the beginning of this chapter, an overview of marine electrical systems and azimuthing podded propulsors are given. The desired characteristics of the pod motor and its drive are also mentioned. Following that, radial flux machine configuration is concluded to be best suited for azimuthing marine propulsors.

Later in the chapter, the classification, literature review and performance comparisons of HESMs over a range of different applications are covered. As well as, having the combined advantages of PMSM and BLSM, the HESM also has their drawbacks and a higher complexity.

From the overall performance chart, 4-4 HESG and T/R-HESG has the best performances. However, comparing different machines is not straightforward, especially when the some of the machines are not well-optimized. Therefore, many factors such as ratings, designs, constraints, advantages and disadvantages have to be considered to choose a HESM topology.

The most common applications for HESM are i) Electrical generation as they provide high efficiency with flux controllability. ii) Electrical vehicle as it can operate at optimum efficiency at a larger range on the torque-speed curve. For high speed, true flux weakening can be performed by field windings on the rotor. These are the attributes that other machine topologies struggle to do.

Chapter 3 – Design of Benchmark Brushless Synchronous Machine and Hybrid Excitation Synchronous Machine for 5MW Azimuthing Podded Propulsor

3.1 Introduction

In this chapter, the machine design procedures for both BLSM and HESM will be covered. The machine designs must meet the requirements of the 5MW azimuthing podded propulsor while considering the desired characteristics given the previous chapter.

Figure 3-1 shows the design flow of both BLSM and HESM. Compared to the BLSM, the HESM has additional PM excitation. Therefore, the contribution of PM flux to the total field MMF, and PM related problems such as demagnetization and mechanical integrity, have to be considered.

At this preliminary design stage, an analytical method was adopted because it is computationally least expensive. Design factors from experience can also be applied to estimate numerous initial design variables. A machine design program catered for the application is written in Matlab. It can rapidly develop the best fitting designs for a given range of input parameters and limits. From there, the design is enhanced using Ansys-RMxprt software.

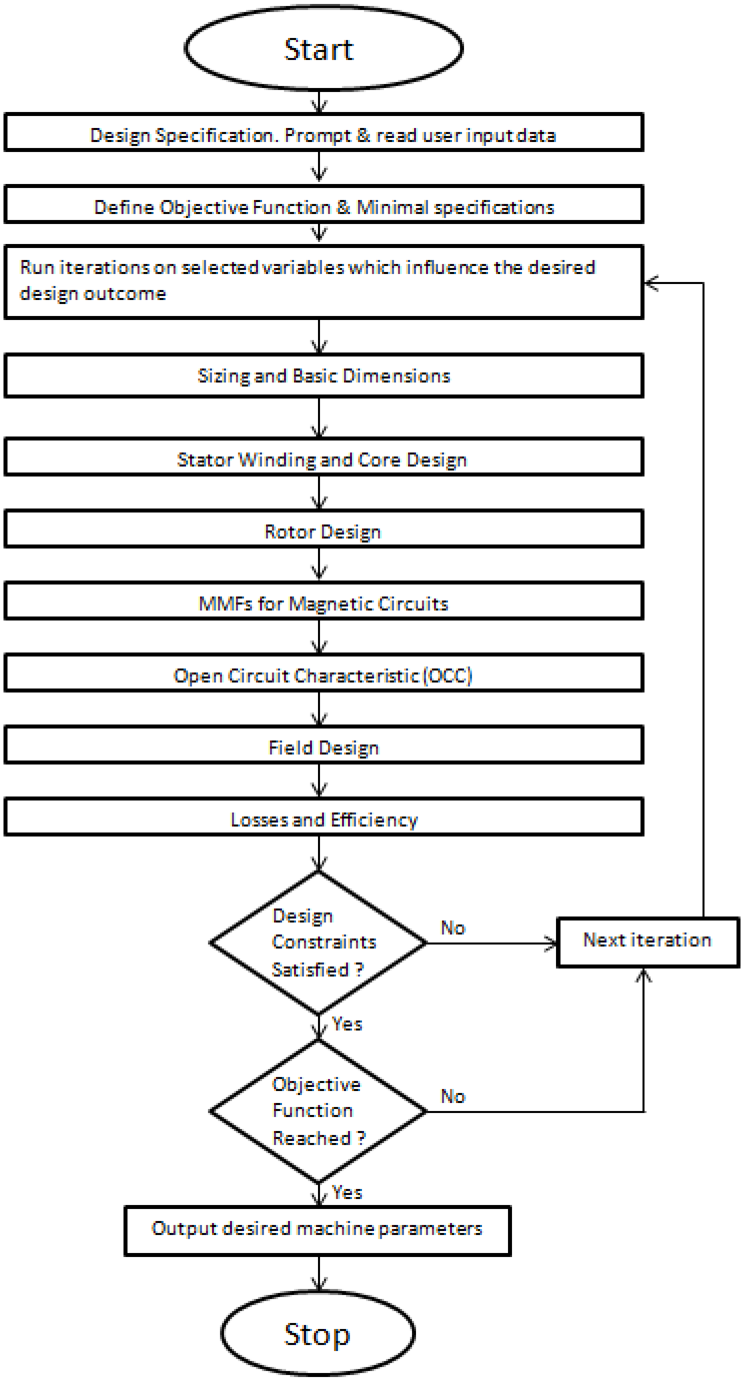

Figure 3-1 Design flowchart for the azimuthing podded propulsor electrical machines

3.2 Design requirements of the propulsion motors

The requirements of propulsion motors are summarized in Table 3-1.

Table 3-1 Design requirements for the azimuthing podded propulsor electrical machines

Parameters	Value	Unit
Rated output power (W)	5	MW
Terminal voltage (V)	3.3	kV
Outer stator diameter	1600	mm
Efficiency	≥95	%
Number of phases	3	–
Stator winding connection	Star	–
Power factor	≥0.95	–
Revolution per minute	110 to 210	rpm
Rotor type	Salient-pole	–

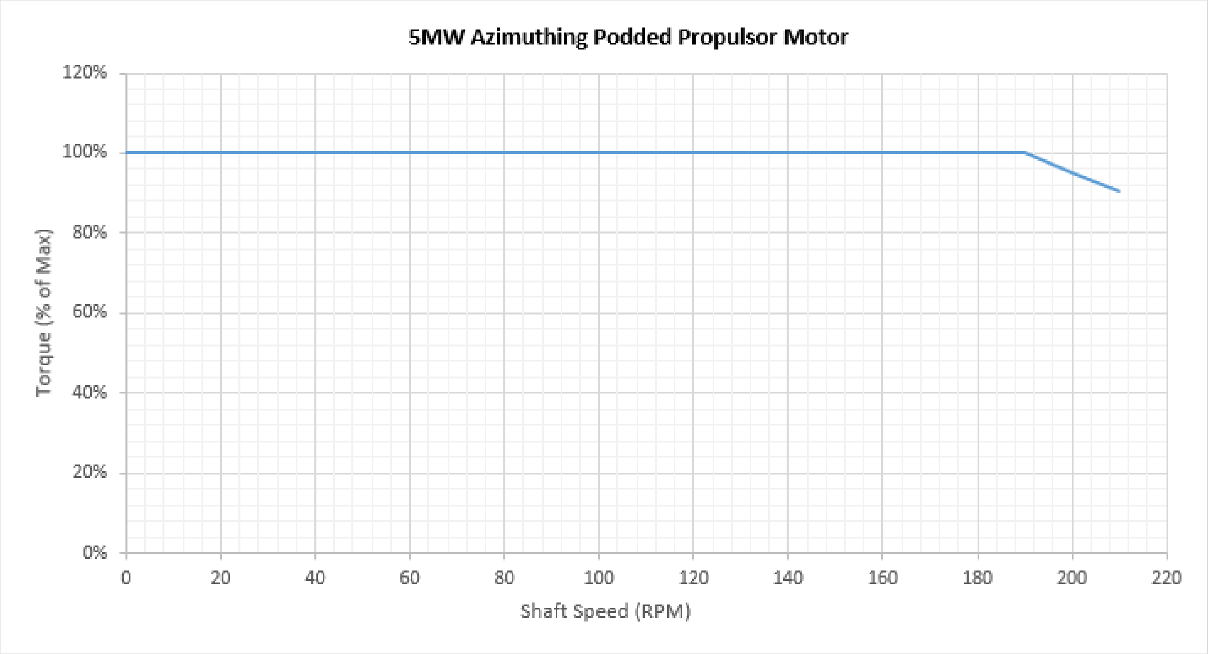

Figure 3-2 Desired torque speed curve of the 5MW BLSM

Figure 3-2 shows the required torque speed characteristic of the propulsor drive. In normal operation, the machine develops rated torque for rotational speeds of 110 to 190 rpm. At higher speeds, the machine moves into the constant power region from 190 to 210 rpm. Since the podded propulsor rotates at a relatively slow maximum speed of 210 rpm, a higher number of poles will favourably increase the torque density. The salient-pole rotor type is the most suitable for this application.

3.3 Design of the common stator

3.3.1 Sizing of machine active parts

3.3.1.1 Output equation

The basic dimensions of the electrical machines can be estimated by using the output equation [60]

$$S = C_o\, D^2\, L\, n_s \tag{3.1}$$

where S is apparent power in kVA, D represents the internal diameter of the stator, L is the core length of the machine, n_s is the synchronous speed in revolution per second (r.p.s) and C_o is the output coefficient given by

$$C_o = 11\, B_{av}\, ac\, K_w \times 10^{-3} \tag{3.2}$$

where B_{av} is the specific magnetic loading defined as the average flux density over the air-gap of a machine and the specific electric loading, ac is the specific electric loading defined as the number of stator ampere conductors per metre of stator periphery at the air-gap, and K_w is the winding factor.

3.3.1.2 Ventilation ducts

For large machines with a long core length, radial ventilation ducts are introduced to dissipate excessive internal temperatures. Cold dry air is forced radially through the ducts providing a suitable and uniform temperature rise of machine in the axial direction as illustrated in Figure 3-3. The number of ventilation ducts n_v with a duct width b_v of 10mm can be obtained from the empirical equation [62]

$$n_v = 0.184(L \times 10^2 - 12.5) \tag{3.3}$$

The overall machine core length is increased due to the accommodation of the radial ventilation ducts.

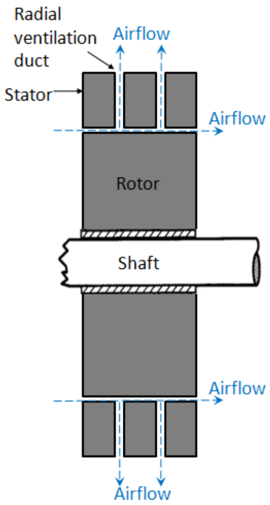

Figure 3-3 Simplified illustration of the airflow through the radial ventilation ducts

3.3.1.3 Electric materials

The choice of electrical materials is important in electrical machine design. They dictate a trade-off between initial and operational costs, machine size, energy efficiency, manufacturing processes and working lifespan. Market availability of the materials must also be taken into account. It is vital to understand these properties to select the best materials for the application. Materials used in electrical machines are classified into three types: conducting, insulating and magnetic. They will be covered in the following sections.

3.3.2 Stator winding and core design

3.3.2.1 Winding configuration

A comparison of the air-gap MMF harmonics of 10, 12 and 14 poles with different number of slots and various coil spans was carried out. Figure 3-4 compares the harmonics analyses of one of the pole and slot combinations of each of the pole number categories. All windings are distributed and short-pitched to reduce higher harmonics. This offers a preliminary insight on the air-gap MMF harmonics generated due to the interaction of poles and slots combination. The actual harmonics of the electric machine, however, depend on many other factors, such as the shape of the rotor poles.

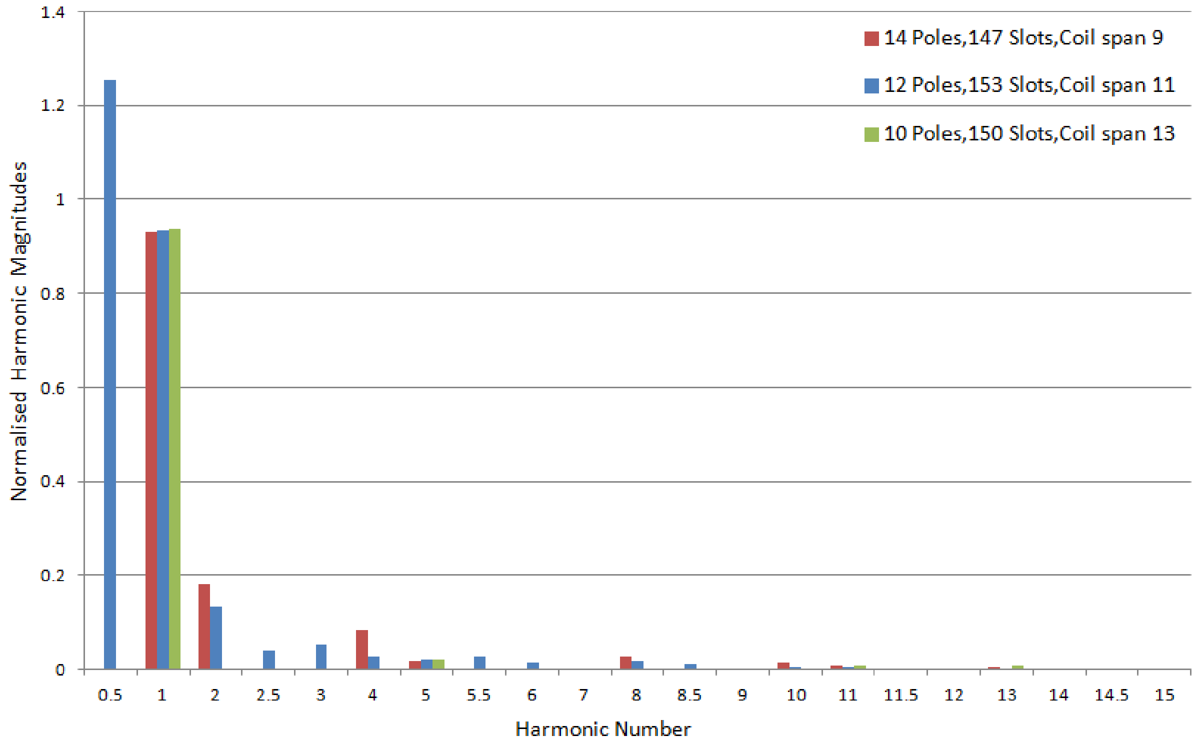

Figure 3-4 Harmonics of the selected slot and pole configurations in each of the pole number category

As seen, the magnitudes of their fundamental, 5th, 7th, 11th and 13th harmonics are very close. The 14-pole configuration performs slightly better in reducing the higher harmonics. The 12-pole configuration is shown to generate sub-harmonics. While they may not affect the electrical performance, they may cause resonance in parts of its mechanical system.

Fractional slot windings provide an effective way of reducing slot harmonic electromotive forces especially when the value of the slot per pole per phase is low. In this case, the 147-slot, 14-pole configuration with a slot per pole per phase of 3.5 (i.e.7/2) has an effective distribution of 7 slot per pole per phase compared to the 150-slot, 10-pole configuration of 5 slot per pole per phase.

The 14-pole configuration has a coil span of 9 compared to the coil span of 13 and 11 for the 10-pole and 12-pole configurations respectively. This reduces copper in the windings and thus the winding resistance. Another benefit of 14-pole configuration is having a smaller stator yoke thickness than 10-pole configuration due to a higher number of poles. The reduction of the stator outer diameter increases the hydrodynamic efficiency of the podded propulsor. This reduces its initial and operational costs.

3.3.2.2 Winding arrangement and construct

A single group of winding arrangement for the 147 slots 14-pole machine with coil span of 9 is shown in Figure 3-5. The entire winding pattern consists of 7 groups. Balanced three-phase star connection has the advantage of eliminating triplen harmonics from line voltage.

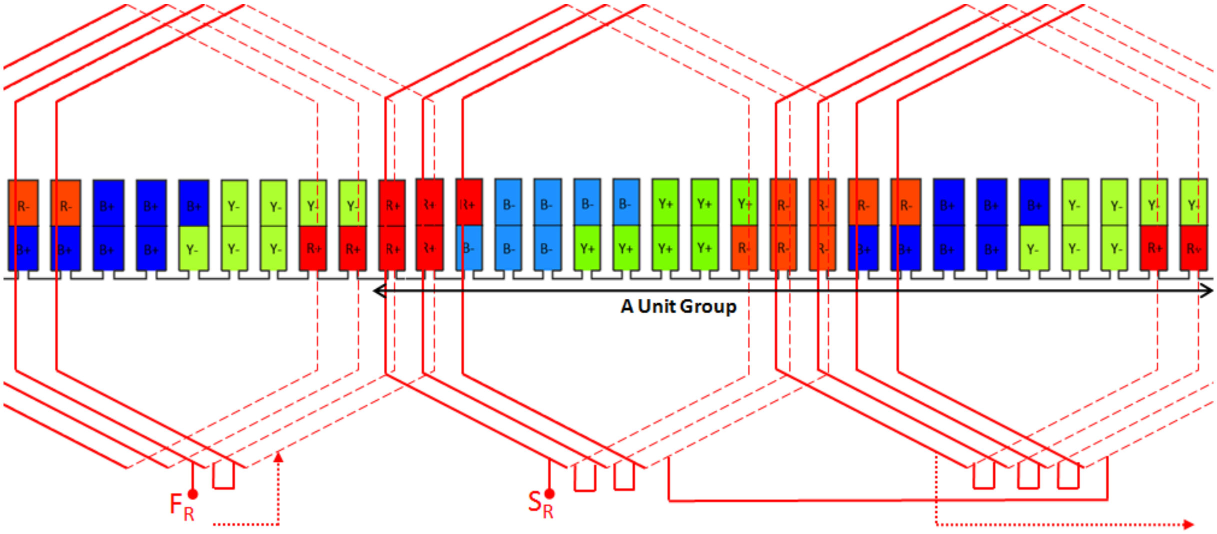

Figure 3-5 Red-phase of the 3-phase, 147 slot 14-pole fractional slot lap winding

3.3.2.3 Winding factor

The stator windings are distributed and short-pitched to eliminate winding harmonics. The winding factor K_w for fractional short-pitched windings can be calculated as follows

$$K_w = K_{dn}\, K_{pn} \tag{3.4}$$

where K_{dn} and K_{pn} are the distribution and pitch factor respectively, given by [61]

$$K_{dn} = \frac{\sin\left(\frac{n\pi}{6}\right)}{M\sin\left(\frac{n\pi}{6M}\right)} \tag{3.5}$$

$$K_{pn} = \sin\left(\frac{y}{\tau_{ps}} \cdot \frac{n\pi}{2}\right) \tag{3.6}$$

where M is the numerator of slot per pole per phase value expressed in improper fraction, n is the harmonic number, y represents stator coil pitch in terms of number of slots and τ_{ps} is pole pitch in terms of number of slots.

3.3.3 Stator core design

Non-uniformly distributed steep-edged voltage pulses from frequency converters cause partial discharges especially in the first turn of the windings. It also contains a substantial amount of harmonics that cause additional losses and temperature rise in the windings. The voltage level directly influences the choice of electrical insulation material and the amount required. Electrical insulation material differs in various parts of the electrical machine. Insulation performance is rated base on thermal grading, dielectric stresses reliability, lifespan and economy. For large machines, IEC60085 insulation Class 180(H) and Class 155(F) are used for Class 130(B) temperatures rises [61][63].

Mica tape is used for slot and inter-turn insulations. Mica has high dielectric strength, low dielectric losses and high surface resistance. It is used in high voltage insulation as it can tolerate high partial discharges and has excellent thermal endurance. The slot separator can be made of Bakelite.

Due to high power rating, prefabricated coils made of performed copper windings are used. Roebel bars maximize the packing factor and reduce eddy current losses in the conductors. Vacuum Pressure Impregnation (VPI) is applied to the machines to eliminate voids. It improves dielectric strength, mechanical strength, thermal conductivity, and protects against the ingression of water and other chemicals. The multi-turn coil winding for open-slot stator is shown in Figure 3-6.

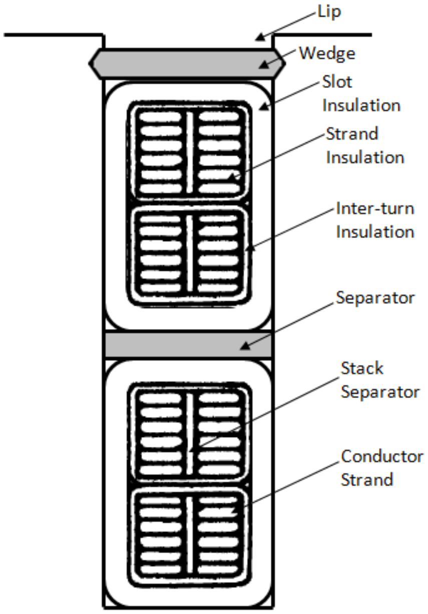

Figure 3-6 Stator conductors in multi-turn coil winding

The number of conductors per slot Z_{slot} is calculated by

$$Z_{slot} = \frac{6T_{ph}}{N_{slot}} \tag{3.7}$$

where N_{slot} is the total number of stator slots and T_{ph} is the number of turns per phase determined by [60]

$$T_{ph} = \frac{V}{\left(\sqrt{3}\ \cdot 4.44\ \varphi\ K_w\ f\right)} \tag{3.8}$$

where f is the electrical machine input frequency and φ is the flux per pole. The flux per pole is

$$\varphi = \frac{(\pi\ B_{av}\ D\ L)}{p} \tag{3.9}$$

where p is the number of poles.

The width of open parallel stator slot w_s is

$$w_s = \frac{\pi D}{N_{slot}} - w_{tooth} \tag{3.10}$$

where the width of stator tooth w_{tooth} is given by

$$w_{tooth} = \frac{\varphi p}{B_{tooth} K_i (L - n_v b_v) \tau_{rot} N_{slot}} \tag{3.11}$$

where B_{tooth} is the flux density in teeth at no load recommended to be between 1.8 to 2.2T [60], K_i is the stacking factor of core laminations normally taken as 0.95, and τ_{rot} is the ratio of pole arc length to pole pitch length normally in the range of 0.6 to 0.72 [61].

The cross-sectional area of conductor A_{cond} is found by

$$A_{cond} = \frac{I_{ph}}{J_s} \tag{3.12}$$

where J_s is the current density of armature windings in the range of 3 to 6 A/mm^2 for forced cooled machine [61] and the phase current I_{ph} is

$$I_{ph} = \frac{Q \times 10^3}{\sqrt{3}\, V} \tag{3.13}$$

The height of stator yoke h_{ys} is calculated by

$$h_{ys} = \frac{\varphi}{2 B_{ys} K_i (L - n_v b_v)} \tag{3.14}$$

where B_{ys} is the flux density in the stator yoke of salient pole machines recommended not to exceed 1.2T [62].

Finally, the stator outer diameter D_o can be determined by

$$D_o = D + 2\left(h_{slot} + h_{ys}\right) \tag{3.15}$$

where slot depth h_{slot} is taken as the sum of the thickness of the bare conductors, insulation, separator, tooth lip, wedge and slack. For a stator core with a large diameter, core sheets of segmental design are required.

3.3.4 Main stator dimensions

Based on the electromagnetic design discussed in the previous sections, a stator design that satisfies the requirements was obtained. The main geometry data of the stator are provided in Table 3-2.

Table 3-2 Main specifications of the BLSM stator

Parameters	Value	Unit
Outer diameter of stator	1600	mm
Inner diameter of stator	1302	mm
Length of stator core	2340	mm
Number of parallel winding branches	1	–
Number of conductors per slot	2	–
Type of steel	M19	–
Number of air ducts	26	–
Width of air ducts	9	mm
Number of sectors per lamination	7	–
Number of stator slots	147	–
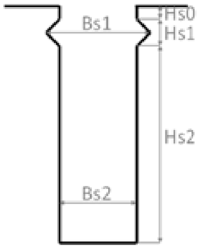 hs0	1	mm
hs1	4	mm
hs2	52.3	mm
bs1	16.9	mm
bs2	15.05	mm

3.4 Design of the BLSM rotor

3.4.1 Rotor design

To find the dimensions of the rotor, the required air-gap length needs to be found. The length of air-gap is a very sensitive parameter which greatly influences the performance of the synchronous machine. A larger air-gap provides better cooling at the gap surface, lower tooth pulsation losses, lower acoustic noise, smaller unbalanced magnetic pull, and gives rise to a low value of synchronous reactance. Figure 3-7 shows a salient rotor pole with typical field winding and insulation arrangements.

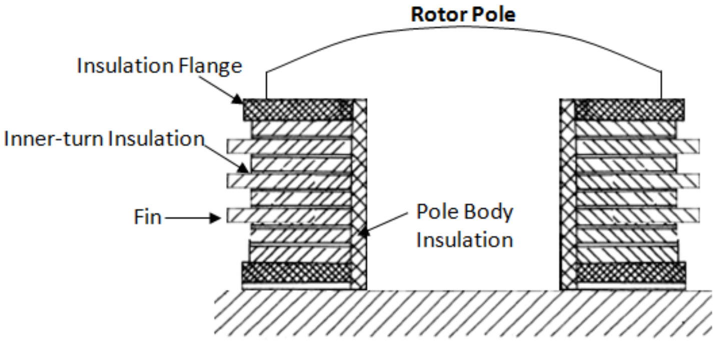

Figure 3-7 A salient rotor pole with typical field winding and insulation arrangements

No-load ampere-turns per pole AT_{fo} is given by [60]

$$AT_{fo} = \frac{2.7\ T_{ph}\, I_{ph}\, K_w}{p} \cdot SCR \tag{3.16}$$

where *SCR* is the Short-Circuit Ratio defined as the ratio of field current required to produce open circuit rated armature voltage to the field current required to produce the rated short circuit armature current and is also the reciprocal of per-unit direct-axis [64].

Air-gap length l_{ag} is calculated by

$$l_{ag} = \frac{0.8\, AT_{fo}\, \mu_0\, \tau_{rot}}{B_{av}\, K_{gap}} \tag{3.17}$$

where K_{gap} is the gap contraction factor [60].

The width of the pole body w_{pole} is

$$w_{pole} = \frac{1.2\,\varphi}{B_{pole}\,K_i\,l_{pole}} \tag{3.18}$$

where l_{pole} is the axial length of pole body, B_{pole} is the flux density in pole body assumed to be 1.6T and leakage flux correction factor of 1.2 is taken [65].

The height of rotor yoke h_{yr} is

$$h_{yr} = \frac{1.2\,\varphi}{2B_{yr}\,K_i\,l_{pole}} \tag{3.19}$$

where B_{yr} is the flux density in rotor yoke recommended not to exceed 1.2T [62].

The outer diameter of rotor D_r can thus be found by

$$D_r = D - 2l_{ag} \tag{3.20}$$

The dimensions of the rotors and field winding design requirements can be calculated following references [60] and [62].

3.4.1.1 Damper winding

The purpose of the damper bars is to provide starting torque during starting as an asynchronous machine. They also function to damp out oscillations and load shocks. Damper windings are usually constructed base on empirical knowledge as its mechanisms are too complicated and diverse to compute accurately [65].

The number of damper bars N_{bar} can be calculated by [61]

$$N_{bar} = \frac{\tau_{rot}\,N_{slot}}{0.8\,p} \tag{3.21}$$

As a guide, about 10% of the cross-sectional area of the armature copper winding is used for copper damper bars. Higher resistivity materials for damper bars (e.g. brass) are also commonly used to increase starting torque. However, this is at the expense of pull-in torque and magnetic shielding effect [65][66]. Damper slot pitch has to diverge by 10 to 15% from the slot pitch of the stator to avoid pulsation of the flux and noise [67]. The diameter of damper bar D_{bar} can be calculated by [61]

$$D_{bar} = \sqrt{\frac{0.32\,\pi\, ac\, D^2}{J_{bar}\,\tau_{rot}\,N_{slot}\,p}} \tag{3.22}$$

where J_{bar} is the current density in the damper bars.

Since the denominator of the slot per pole per phase is 2, it may not be necessary to shift the damper bars to reduce the slot harmonics. For robustness, copper end plates are used instead of a complete damper end ring. The plates are shaped like the poles and rotor yoke. They are situated at the both axial ends of the rotor and extend beneath the first row of pole bolts. They are also more rugged and do not obstruct the axial airflow between the rotor poles [65]. Care must be taken to ensure pole shoe is mechanical strong enough to support the damper windings under runaway speeds.

To avoid overheating of the damper winding during starting, the temperature rise of the damper bars ΔT are calculated by [66]

$$\Delta T = \frac{P_c}{C_p m_{bar}} \Delta t \tag{3.23}$$

where Δt is the elapsed time, C_p is the specific heat capacity of the damper bars, m_{bar} is the mass of the damper bar, P_c is the losses in each damper bar given as

$$P_c = I_{bar}^2 R_{bar} \tag{3.24}$$

where I_{bar} is the damper bar current and R_{bar} is the resistance of the damper bar.

3.4.1.2 Rotor construct

To reduce space harmonics content, sinusoidal flux distribution is obtained by proper shaping and proportioning of the pole shoe. The pole face is shaped such that the radial air-gap length increases from the pole centre to pole tips, obtained by [61]

$$g(x) = \frac{g}{\cos\frac{\pi}{\tau}x}\ , for\ \frac{-\tau_p}{2} < x < \frac{\tau_p}{2} \tag{3.25}$$

where τ_p is pole arc, τ is pole pitch, g is air-gap length at the centre of pole face. In common practice, the ratio of $g(\tau_p/2)$ to g is normally taken between 1.5 to 2.25.

The height of pole shoe depends on the space required to accommodate the damper winding while retaining sufficient structural strength. As the rotor is subjected only to low peripheral speeds, the poles are attached to the rotor yoke by bolts and screws. The height of the pole is dependent on the on field winding design.

Unlike most conventional electrical machines, the rotor shaft of this machine does not extend through the middle of the rotor. Instead, stub shafts are bolted onto both axial ends of the rotor yoke. The side of the stub shafts bolted onto the rotor yoke must have a minimum diameter similar to that of the outer diameter of the rotor yoke. In this way, the inertia of the rotor can be significantly reduced. Shaft bearings, brushless exciter and propeller will be mounted onto the rotor shafts depending on pod design.

The diameter of rotor shaft D_{shaft} can be determined by [68]

$$D_{shaft} = 0.112\sqrt{\frac{\mathrm{P_o}}{n_{rotor}}} \tag{3.26}$$

where $\mathrm{P_o}$ is power output in kilowatts and n_{rotor} is the rotational speed of rotor shaft.

3.4.2 Magnetomotive forces for the electrical machine magnetic circuit

From B-H curve of the magnetic material, the magnetic field strength can be determined from the flux densities at each part of the machine. The magnetomotive forces (MMF) are then determined by multiplying the magnetic field strength by the related magnetic path length.

Figure 3-8 Open-slot Carter coefficient

3.4.2.1 Air-gap MMF

The air-gap coefficient K_{ag} is [62]

$$K_{ag} = \frac{\pi\, D\, L}{[\pi D - w_s K_{cc-slot}\, N_{slot}][L - n_v b_v K_{cc-duct}]} \tag{3.27}$$

where $K_{cc\text{-}slot}$ and $K_{cc\text{-}duct}$ are the Carter's coefficient for open slots and ventilation ducts respectively obtained from Figure 3-8.

Air-gap MMF AT_{ag} is found by

$$AT_{ag} = \frac{K_{ag}\, B_{av}\, l_{ag}}{\mu_0 \tau_{rot}} \tag{3.28}$$

where μ_0 is the permeability of free space.

3.4.2.2 Stator teeth and core MMF

M-19 silicon steel laminations make up the stator and rotor core. M-19 silicon steel has properties such as low core loss, and good permeability at low and intermediate inductions. It is suitable for high efficiency large rotating equipment [69]. The B-H curve of M-19 silicon steel is shown in Figure 3-9.

The flux density in the narrow end of tooth B_{tnar} can be found by

$$B_{tnar} = \frac{\varphi\, p}{K_i(L - n_v b_v)\left[\pi\left(D + {}^{2}\!/_{3}\, h_{slot}\right) - w_s N_{slot}\right] \tau_{rot}} \tag{3.29}$$

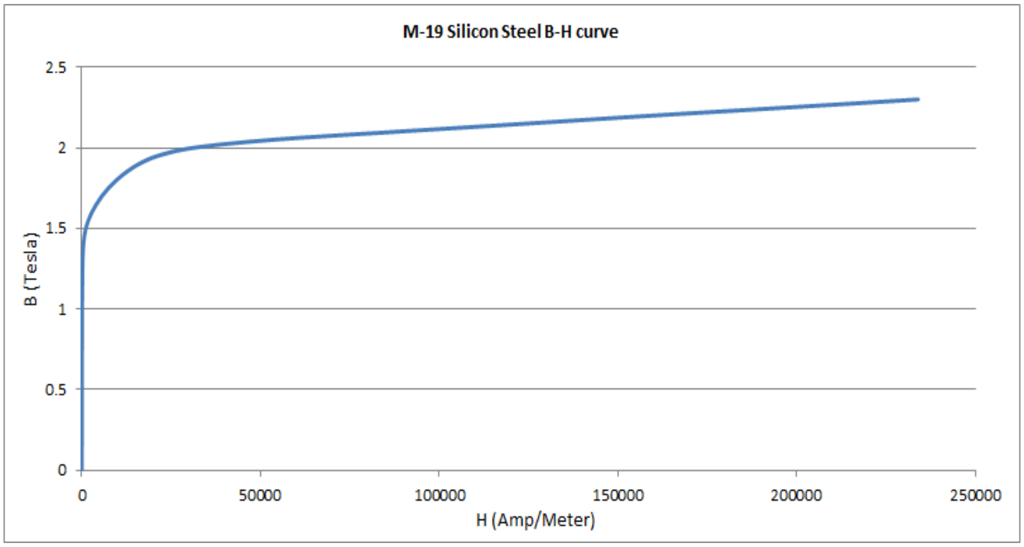

Figure 3-9 B-H curve of M-19 silicon steel [70]

From the B-H curve of M-19 silicon steel, the magnetic field strength at the tooth H_{tooth} corresponding to B_{tnar} is found. The MMF required for stator tooth AT_{tooth} is thus

$$AT_{tooth} = H_{tooth} h_{slot} \tag{3.30}$$

The flux density in the stator yoke B_{ys} can be found by

$$B_{ys} = \frac{\varphi}{K_i(L - n_v b_v)(D_o - D - 2h_{slot})} \tag{3.31}$$

The length of magnetic path in the stator yoke l_{ys} is

$$l_{ys} = \frac{\pi(D + 2h_{slot} + h_{ys})}{2p} \tag{3.32}$$

The MMF required for the stator yoke AT_{ys} is

$$AT_{ys} = l_{ys}H_{ys} \tag{3.33}$$

where H_{ys} is magnetic field strength at stator yoke.

The MMF required for the stator yoke can be found by finding the corresponding value of ampere per metre (A/m) on the M-19 B-H curve and multiplying it with l_{ys}.

3.4.2.3 Rotor core and pole MMF

The flux density in the rotor yoke B_{yr} can be found by

$$B_{yr} = \frac{\varphi + \varphi_{ls} + \varphi_{lp}}{2\,L\,h_{yr}} \tag{3.34}$$

The leakage flux from poles shoes φ_{ls} and from pole bodies φ_{lp} can be found following reference [60][71].

The length of magnetic path of the rotor yoke l_{yr} is

$$l_{yr} = \frac{\pi(D_r - 2h_{pole} - h_{yr})}{2p} \tag{3.35}$$

where h_{pole} is the height of rotor pole.

The MMF required for the rotor yoke AT_{yr} can be found by finding the corresponding value of A/m on the M-19 B-H curve and multiplying it with l_{yr}.

$$AT_{yr} = l_{yr}H_{yr} \tag{3.36}$$

where H_{yr} is magnetic field strength at rotor yoke.

In a similar manner, the MMF required for the rotor pole AT_p is [60]

$$AT_p = \frac{1}{3}h_{pole}\left(2H_{bottom} + H_{top}\right) \tag{3.37}$$

where H_{bottom} and H_{top} are the magnetic field strengths at the bottom and top of the rotor pole respectively.

3.4.2.4 Total MMF of magnetic circuit

Total no-load MMF AT_{nl} at rated voltage is the sum of the air-gap, stator teeth, stator core, rotor core and pole MMFs given by

$$AT_{nl} = AT_{ag} + AT_{tooth} + AT_{ys} + AT_{yr} + AT_p \tag{3.38}$$

3.4.3 Field current and winding calculations

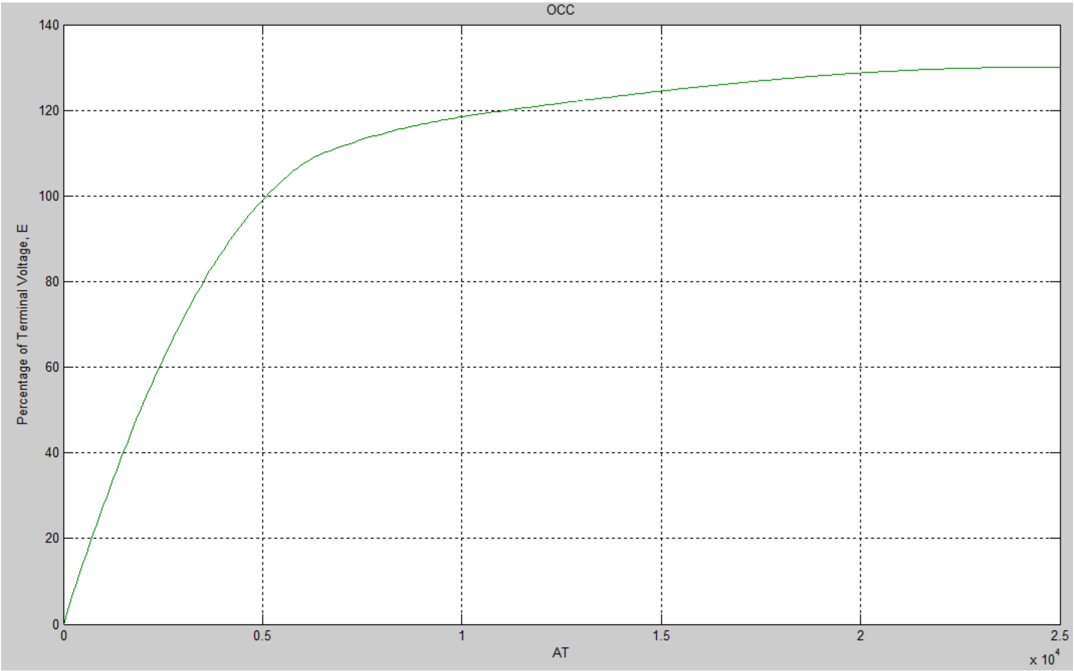

Figure 3-10 OCC curve

The Open Circuit Characteristic (OCC) gives the relation between terminal voltage and the corresponding field MMF. Terminal voltages of up to 130% of rated voltage are considered. The required ampere turns (AT) corresponding to the voltages can be found. The OCC curve of the BLSM is shown in Figure 3-10.

The field excitation corresponding to the internal generated voltage can be obtained using the OCC curve.

$$\bar{E}_g = \bar{V}_{ph} + \bar{I}_{ph}(R_{ac} + jX_l) \tag{3.39}$$

where $\bar{E}_g$ is the per unit internal generated voltage phasor, $\bar{V}_{ph}$ is the per unit phase voltage phasor, R_{ac} is the per unit phase resistance of armature winding, X_l is the per unit stator leakage reactance.

The direct-axis armature MMF AT_{ad} is calculated by [60]

$$AT_{ad} = \frac{2.7\ T_{ph}\, I_{ph}\, K_w\, \rho_d}{p} \tag{3.40}$$

where is ρ_d the direct-axis reduction factor given by [72]

$$\rho_d = \frac{\tau_{rot}\pi + \sin(\tau_{rot}\pi)}{4\sin\left(\tau_{rot}\pi/2\right)} \tag{3.41}$$

The required field current I_f can be found by [60]

$$I_f = \frac{\rho_{cu}\, l_f\, AT_{fl}\, J_f}{V_f} \tag{3.42}$$

where ρ_{cu} is the electrical resistivity of the copper, l_f is the length of the field winding, AT_{fl} is the ampere-turns at full-load, V_f is the voltage per field coil and J_f is the current density in the range of 3 to 5 A/mm^2 [61].

Number of field winding turns T_f is

$$T_f = \frac{AT_{fl}}{I_f} \tag{3.43}$$

Height of the field coil h_f is [60]

$$h_f = T_f\left(h_c + h_{fi}\right) + h_{buck} \tag{3.44}$$

where h_c is the height of a field conductor, h_{fi} is the height of the insulation per conductor, and h_{buck} is the height of the field winding buckling space.

For this design, strip-on-edge field winding conductor is used and Vee blocks are used to support the field coils as shown in Figure 3-11.

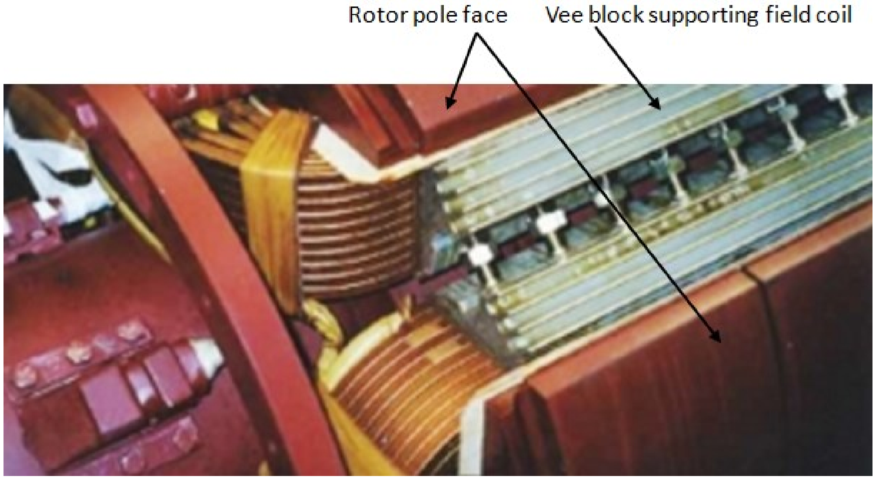

Figure 3-11 Vee blocks supporting field coils of a salient pole rotor [73]

3.4.4 Main rotor and field winding dimensions

Table 3-3 Main specifications of the BLSM rotor and field winding

Parameters	Value	Unit
Minimum air-gap	7.9	mm
Outer diameter	1286.2	mm
Length of rotor	2340	mm
Type of steel	M19	–
Pole-shoe width	209.2	mm
Pole-shoe height	36	mm
Pole-body width	136	mm
Pole-body height	96	mm
Ratio of max. to min. air-gap	1.5	–
Mechanical pole embrace	0.73	–
Number of turns per pole	44	–
Width of wire	40	mm
Thickness of wire	1.5	mm

Based on the electromagnetic design discussed in the previous sections, a rotor design that satisfies the requirements was obtained. The main data of the rotor and its field winding are provided in Table 3-3.

3.5 Machine parameters and performance assessment

3.5.1 Resistance of stator winding

The resistance per phase R_{ph} of the stator winding is [62]

$$R_{ph} = \rho_{cu}\left(\frac{MLT_a\, T_{ph}}{A_s}\right) \tag{3.45}$$

where A_s is the cross-sectional area of stator conductor, and the mean length of turn of a armature winding $\mathrm{MLT_a}$ is given by

$$MLT_a = 2L + 4(E + F) + \left[\frac{4\pi(D + 2h_{slot})}{P} \cdot \tau_c\right] \sec\frac{\gamma}{2} \tag{3.46}$$

where τ_c is coil pitch (in fractions) and for E, F and γ refer to Figure 3-12(a).

3.5.2 Resistance of rotor winding

The resistance of each field coil R_f is [62]

$$R_f = \rho_{cu}\left(\frac{MLT_f\, T_f}{A_f}\right) \tag{3.47}$$

where A_f is the cross-sectional area of field winding strip.

In large synchronous machines, a radius $\mathrm{r_l}$ at the edge of the pole end plate is included to ensure no damage occurs when the insulation is bent around the pole. An illustration of the mean length of turn of the field coil MLT_f is shown in Figure 3-12 (b). MLT_f can be calculated by

$$MLT_f = 2\left[l_{pole} + w_c - 4(r_1 + t_1) + \pi r_2\right] \tag{3.48}$$

where t_1 is the radial thickness of coil insulation and w_c is width of rotor coil strip across the pole body and r_2 is the radius of mean path of field winding copper strip at edge of the pole end plate.

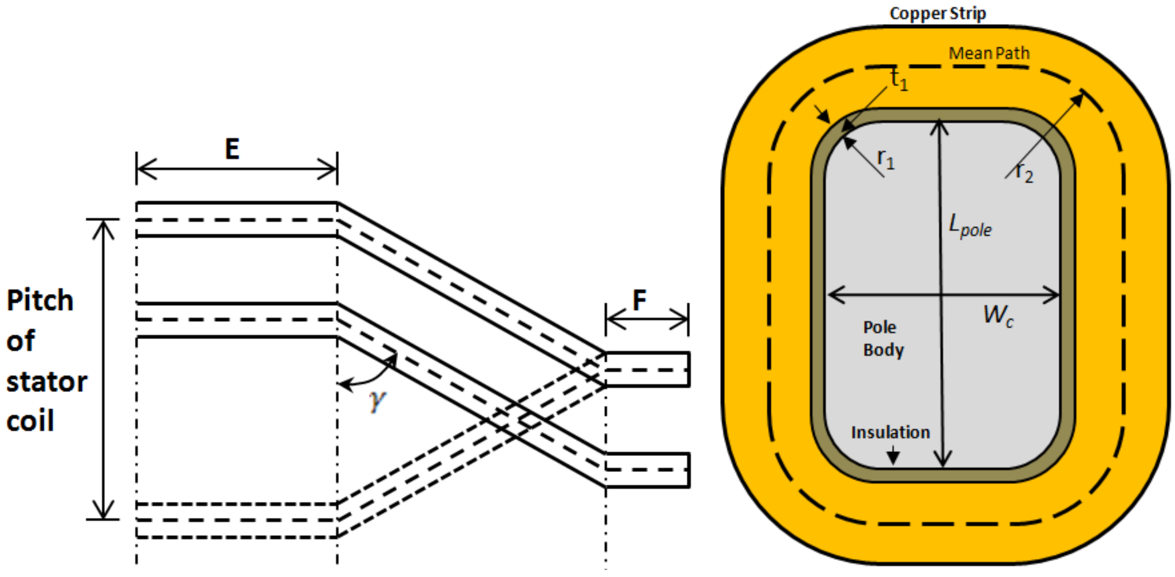

(a) (b)

Figure 3-12 Mean length of turn of (a) armature winding and (b) field coil

3.5.3 Leakage reactance

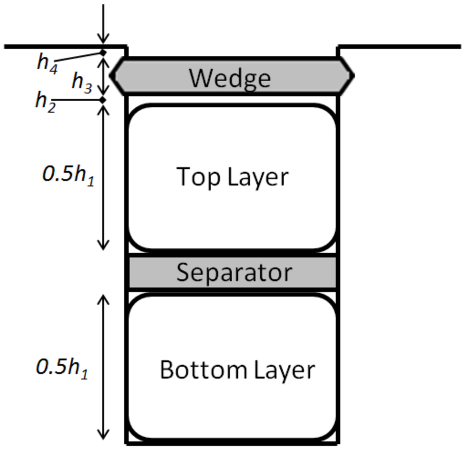

Figure 3-13 Stator slot permeance leakage factor for open slot design

The permeance of the open slots λ_s are calculated by [61]

$$\lambda_s = \left(\frac{h_1}{3w_s} + \frac{h_2}{w_s} + \frac{2h_3}{w_s + w_{so}} + \frac{h_4}{w_{so}}\right) \qquad (3.49)$$

where h_1 is the height occupied by the insulated conductor in the slot, h_2 is the space above conductor and below the wedge, h_3 & h_4 are the height of the wedge and lip respectively as shown in Figure 3-13. w_s & w_{so} is the width of the slot and its opening respectively.

The overhang leakage factor $L_o\lambda_o$ [60]

$$L_o\lambda_o = \frac{K_s\tau^2}{\pi\tau_s} \tag{3.50}$$

where τ_s is the slot pitch, and K_s is the leakage factor from the curve in Figure 3-14.

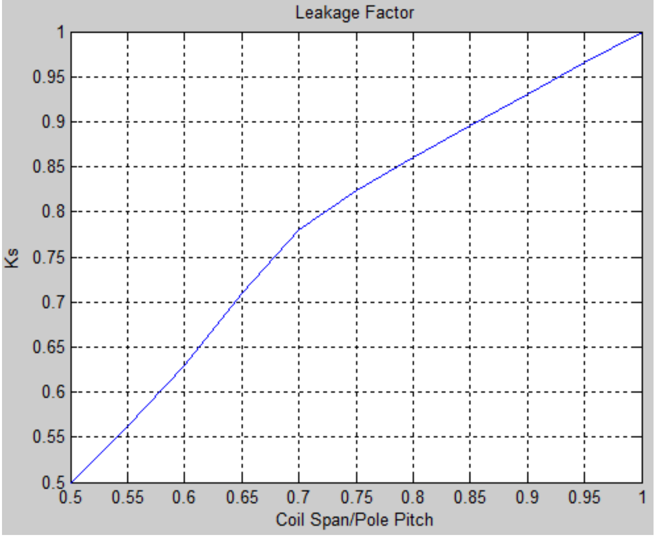

Figure 3-14 Leakage factor curve [60]

Per unit stator leakage reactance X_l is given by [62]

$$X_l = \frac{I_{ph}x_l}{\sqrt{3}\,V} \tag{3.51}$$

where stator leakage reactance x_l is

$$x_l = \frac{8\pi f\mu_0 T_{ph}^2}{p\,q}(L\lambda_s + L_o\lambda_o) \tag{3.52}$$

where q is slot per pole per phase.

3.5.4 Magnetizing reactance

The per unit magnetizing reactance per phase of a machine with a uniform air-gap X_m is [1][61]

$$X_m = \frac{\sqrt{3} I_{ph} x_m}{V} \tag{3.53}$$

where magnetizing reactance x_m is given by

$$x_m = \frac{2mf\mu_0 T_{ph}^2 K_w^2 DL}{l_{ag} K_{ag} p^2} \tag{3.54}$$

where m is the number of phases.

3.5.4.1 Direct-axis synchronous reactance

The per unit unsaturated direct-axis synchronous reactance X_D is given by [62]

$$X_D = X_l + X_{ad} \tag{3.55}$$

where per unit direct axis armature reaction reactance X_{ad} is

$$X_{ad} = \frac{\rho_d \tau_{rot} B_{m1}}{B_{av}} X_m \tag{3.56}$$

where B_{m1} is the maximum fundamental flux density component in machine core.

3.5.4.2 Quadrature-axis synchronous reactance

The per unit unsaturated quadrature-axis synchronous reactance X_Q is given by [1][62]

$$X_Q = X_l + X_{aq} \tag{3.57}$$

where per unit quadrature axis armature reaction reactance X_{aq} is

$$X_{aq} = \left[\frac{4\,\tau_{rot} + 1}{5} - \frac{\sin(\tau_{rot}\pi)}{\pi}\right] X_m \tag{3.58}$$

3.5.5 Magnetizing current

For three-phase balanced armature windings sinusoidally distributed in space, the value of the magnetizing current per phase I_m is given by [1][62]

$$I_m = \frac{0.37\, AT_{m1} p}{K_{w1} T_{ph}} \tag{3.59}$$

where AT_{m1} is the fundamental magnetizing MMF and K_{w1} is the fundamental winding factor.

3.5.6 Power losses and efficiency

3.5.6.1 Copper losses

Electrical copper conductors of good quality have low resistance. The electrical resistivity of copper is taken at the maximum allowable temperature of 120°C.

Total stator copper loss P_{cus} is given by [60]

$$P_{cus} = 3 I_{ph}^2 \left(R_{pho} + K_{dav}\, R_{phs} \right) \tag{3.60}$$

where R_{pho} is the resistance per phase of conductors in the overhang, R_{phs} is the resistance per phase of conductors in slots, and K_{dav} is the average eddy current loss factor given by [60]

$$K_{dav} = 1 + \frac{(\alpha h')^4\, N^2}{9} \tag{3.61}$$

where h' is the height per stand, N is the number of conductor layers and $\propto$ is given by

$$\propto = \sqrt{\frac{\pi \mu_0 f w_{cs}}{\rho_{cu} w_s}} \tag{3.62}$$

where w_{cs} is width of conductor and w_s is width of slot.

Field winding copper loss P_{cuf} can be calculated by

$$P_{cuf} = p\, I_f^2\, R_f \tag{3.63}$$

3.5.6.2 Iron losses

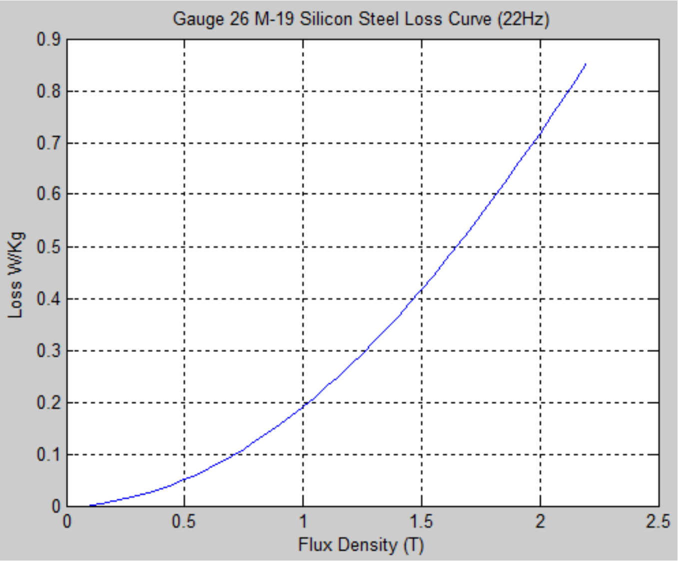

Figure 3-15 M-19 silicon steel loss curve at 22 Hz [70]

Using the core loss curve shown above in Figure 3-15, the iron loss per kg in the stator teeth and core can be found. The iron losses are function of flux density and frequency. Iron loss in the teeth P_i can be found by

$$P_i = P_{mt} m_t \tag{3.64}$$

where P_{mt} is the iron loss per kg in the tooth and m_t is the total mass of the teeth on the stator. The density of silicon steel is approximately 7850 kg/m^3.

Similarly, the stator core iron loss P_s is found by

$$P_s = P_{ms} m_s \tag{3.65}$$

where P_{ms} is the iron loss per kg in stator core and m_s is the mass of the stator core.

Total iron losses P_{ti} is given by

$$P_{ti} = CF_i(P_i + P_s) \tag{3.66}$$

where CF_i is the iron loss correction factor [65].

3.5.6.3 Total losses

The total losses of the machine at rated load P_t is

$$P_t = P_{cus} + P_{cuf} + P_{ti} + P_{fw} + P_{stray} \tag{3.67}$$

where P_{fw} and P_{stray} are the friction and windage losses, and stray losses respectively.

3.5.7 Efficiency and rotating torque

3.5.7.1 Efficiency

The percentage efficiency of the machine η can be calculated by

$$\eta = \frac{P_{out}}{P_{out} + P_t} \times 100 \tag{3.68}$$

where P_{out} is the rated output power.

3.5.7.2 Rotating torque

$$T_{Shaft} = \frac{P_{out}}{2\pi n_s} \tag{3.69}$$

where T_{Shaft} is the shaft output torque.

3.6 Rotor design for HESM

3.6.1 Permanent magnet calculation for HESM

The series hybrid excitation configuration is chosen due to its simpler design structure thus better manufacturability. Permanent magnets will be installed on the surface of the HESM rotor poles. It has a salient-pole construction, similar to that of the BLSM. The minimum required magnet thickness (along the direction of magnetization) for the HESM design has to be calculated. High values of permeance coefficient in the magnetic circuit can minimize the risk of demagnetization. This can be achieved by using magnets with sufficient thickness.

In modern days, life expectancy of a marine vessel is about 25 to 30 years. It is imperative that the magnets survive the entire lifespan of the vessel without any physical and magnetic degradation. For this reason, measures must be included in the pod to protect the magnets from physical and magnetic damage. The permeance coefficient *pc* can be calculated by [74]

$$pc = \frac{l_m A_g}{\varphi_{ml} A_m k_{cc-slot} l_{ag}} \tag{3.70}$$

where l_m is the magnet thickness, A_m is the magnet pole-face area, A_g is the air-gap area per pole and φ_{ml} is the magnet flux leakage factor in the range of 0.85 to 0.95.

The magnetic flux density due to the influence of field excitation B_{mt} can be calculated by

$$B_{mt} = B_m + \frac{NI\mu_0\mu_r A_g}{\mu_r k_{cc-slot} l_{ag} A_m + l_m A_g} \tag{3.71}$$

where B_m is the flux density of the magnet, μ_r is the relative permeability of recoil line and *NI* is the ampere-turns of the field winding.

Demagnetization is a serious threat that can occur due to overheating and large opposing magnetic fields. It is necessary that the magnets are protected from being partially or entirely demagnetized. Maximum current limiting protection in the power converter is configurable and short-circuit currents can be limited to non-critical values. Current limiters, circuit breakers and IGBT power semiconductors are able to cut off the power supply very rapidly. High Temperature Superconducting current (HTS) limiters can do that in milliseconds [75]. The magnetic flux density B_d in the magnet after demagnetization can be found by [74]

$$B_d = B_m - \frac{6k_{w1} T_{ph} k_{ad} I_{s-c} p_m}{\sqrt{2}\pi\, p\, A_m \left(1 + p_m R_g\right)} \tag{3.72}$$

where I_{s-c} is the phase short-circuit current, k_{ad} is the armature-reaction flux coefficient, p_m is the magnet permeance and R_g is the air-gap reluctance.

Rotor temperature of 120°C is assumed as a safety measure. It is greater than the allowable temperature in the motor. Temperature sensors should be situated in the machine to provide over-temperature warning.

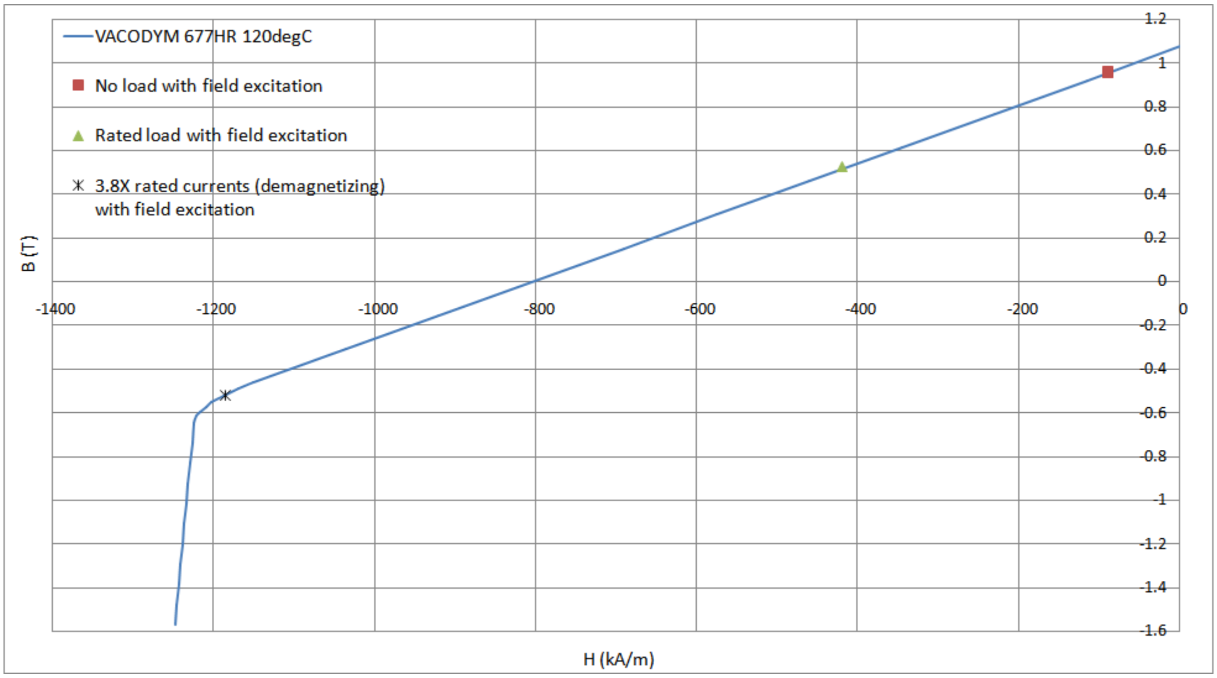

Figure 3-16 Demagnetization curve with magnet operating points at no load, rated load and in a demagnetization event [76]

Vacodym 677HR magnetic aging resistant and anti-corrosion coated cuboid shaped magnets by Vacuumschmelze GmbH & Co. KG is a reliable choice. Figure 3-16 shows the estimated magnet operating points on the Vacodym 677HR demagnetizing curve at no-load, rated load and at a demagnetizing current 3.8 times the rated currents. Magnets of 4mm in thickness were used. Field excitations are applied in each case. In every case, the magnetic force stays within the reversible part of the characteristic profile, though it is reduced almost to the level at knee of the demagnetizing curve in the demagnetization case.

3.6.2 Main rotor and field winding dimensions of the HESM

With the contribution of the PM excitation, the required field winding turns for the HESM is less than that of the BLSM. Therefore, base on the requirements, the rotor of the HESM can be designed in a similar manner as that of the BLSM. The main data of the rotor and its field winding are provided in Table 3-4.

Table 3-4 Main specifications of the HESM rotor and field winding

Parameters	Value	Unit
Minimum air-gap	4	mm
Outer diameter	1294	mm
Length of rotor	2340	mm
Type of steel	M19	–
Type of NdFeB magnets	Vacodym 677HR	–
Pole-shoe width	209.2	mm
Pole-shoe height	36	mm
Pole-body width	136	mm
Pole-body height	71	mm
Ratio of max. to min. air-gap	1.5	–
Mechanical pole embrace	0.72	–
Number of turns per pole	44	–
Width of wire	40	mm
Thickness of wire	1	mm

3.7 Mechanical considerations

In large machines, the rotor diameter is limited by the maximum allowable peripheral speed. To ensure secure mechanical mounting even at runaway speed (at twice of rated speed), stresses acting upon the magnets and pole mounting bolts due to centrifugal force σ_c are calculated by

$$\sigma_c = \frac{m_c r_c \omega_c^2}{A_c} \tag{3.73}$$

where m_c is the mass of a PM or pole, ω_c is the mechanical angular speed, r_c is the radius of curvature and A_c is the cross-sectional area of the magnet or bolts.

It is found that the tensile strength of NdFeB magnets and bolts yield strength far exceeds the calculated stress acting upon them due to the centrifugal forces at runaway speed. An overall magnetic attraction force also remains between the magnets and its contact surface. However, it is still possible for the magnet to migrate on the rotor of the motor due to large circumferential accelerations. Therefore, a magnet protection system such as the one shown in Appendix A is required. It must be noted that the above calculation is simplified and a thorough mechanical analysis requires a separate study.

3.8 Machine design program, V-curves program, and Ansys-RMxprt optimization

3.8.1 Machine design program

The design of an electrical machine is a Pareto optimality problem that requires both expertise and experience. The design program given in Appendix B is a first-order design tool for rapid sizing of the machine which helps speed up the design process. It can find optimum solutions for the machine design problem and output the basic design specifications.

To minimise computation, it is necessary to limit the large number of variables. Therefore, the most influential variables are identified so that minimum and maximum constraints can be applied in the program. Selected design variables pertaining specifically to this machine are:

1) Inner diameter of stator –longer the rotor pole body, higher the torque.
2) Short Circuit Ratio (SCR) –affects a range of other parameters including length of air-gap, short-circuit current, etc.
3) Magnetic flux densities in stator yoke, teeth and rotor pole body–maximize magnetic material usage while avoiding saturation.
4) Current densities in the stator and rotor windings–temperature rise limit.

The design constraints are:

1) Efficiency
2) Power density

3.8.2 V-curves program

The V-curves is an important part of synchronous motor design. It shows the relation between armature current and field current with constant shaft load and terminal voltage. The V-curves program in Appendix C outputs the V-curves of the designed synchronous motor. It also displays the power factor compound curves.

3.8.3 Design optimisation using Ansys-RMxprt

Using Ansys-RMxprt, the machine design is enhanced before proceeding to finite element modelling. Generic Algorithm (GA) optimization and parametric analysis are performed to search for the optimum values automatically. The Ansys-RMxprt design specification for the 5MW azimuthing podded propulsor synchronous machine is given in Appendix D.

3.9 Summary

This chapter addresses the design procedures, concepts and calculations of both BLSM and HESM. The analytical design is arrived first by using a machine design program written by the author and later Ansys-RMxprt with optimisation techniques.

It is known that analytical calculations which are based heavily on assumptions, are not as accurate compared to numerical methods. However, it offers speed in the preliminary machine design process. Therefore, the machine design has to be optimised using FEM.

Chapter 4 – Modelling and Optimization of BLSM and HESMs

4.1 Introduction

In the previous chapter, the electrical machines are designed using analytical methods. To ensure the machines meet their requisite performances, machine design factors and assumptions taken have been largely pessimistic. In this chapter, FEM modelling is used to provide accurate and optimal designs. A BLSM and two variants of HESMs, namely Model1 and Model2, are created. The difference between Model1 and Model2 machines is that the latter has more PM materials on one edge of each pole. This design reduces the effect of armature reaction. Major design improvements are covered. The electromagnetic simulations of the electrical machines are analyzed using finite element method software, Ansys-Maxwell.

4.2 FEM modelling of electrical machines

4.2.1 External circuit winding connection

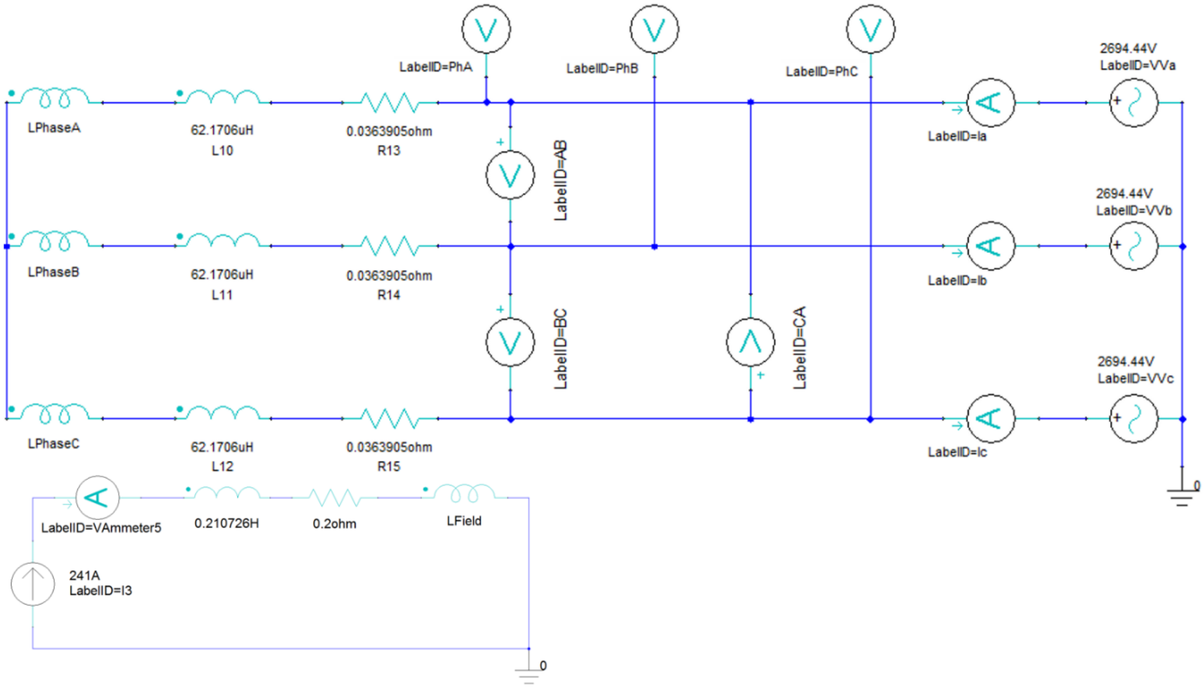

Figure 4-1 Winding connections of the BLSM in Ansys-Maxwell circuit editor software

Figure 4-1 shows the BLSM winding connections for time-stepping simulations. Three-phase stator windings and field winding circuits are built using Ansys-Maxwell circuit editor software. Damper circuit is set as ‘end-connection’. The HESMs have similar winding connections.

4.2.2 Mesh implementation

The process of arriving at the ‘sufficient’ mesh density in a finite element model is a compromise between accuracy and cost. The accuracy of the obtained solution is usually a function of the mesh resolution. If a mesh is too dense, it will require a large amount of computer resource and run times. Mesh quality is refined until the solution does not change significantly with each refinement. Critical areas of the model, particularly the air-gap, have much a finer mesh. Figure 4-2 shows the generated meshes for the BLSM, Model1 and Model2 machines.

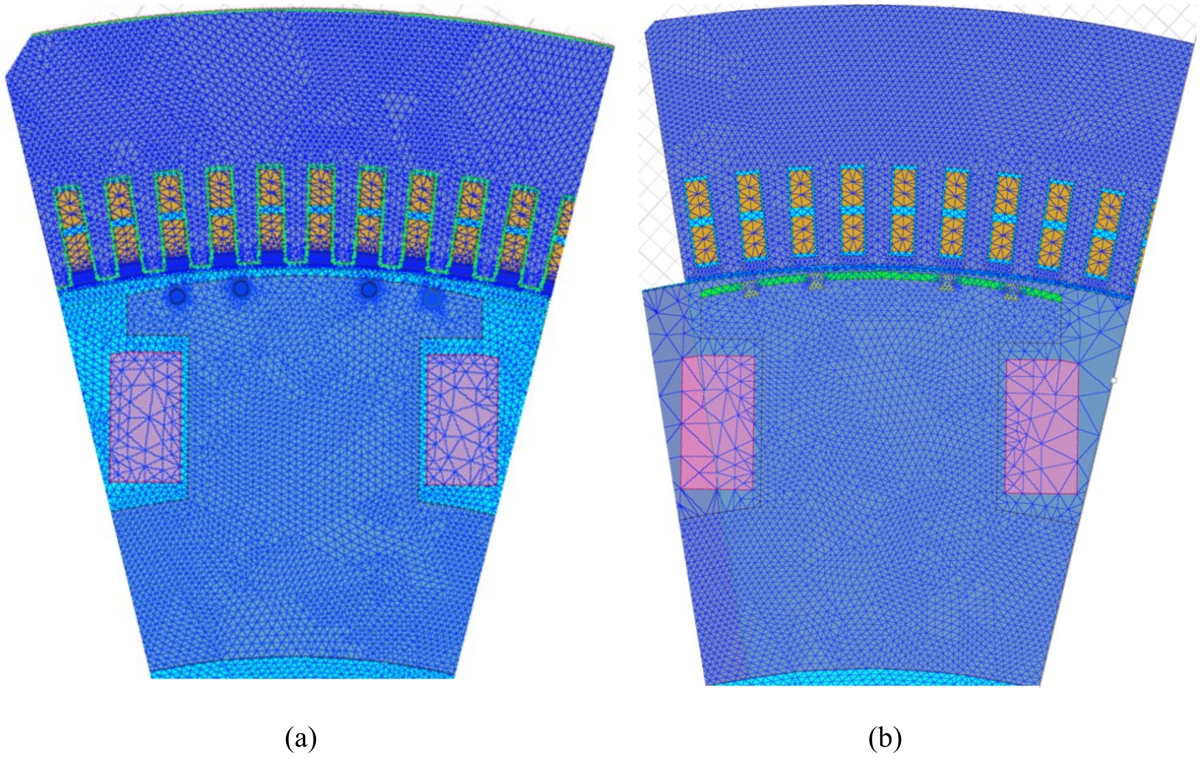

(a) (b)

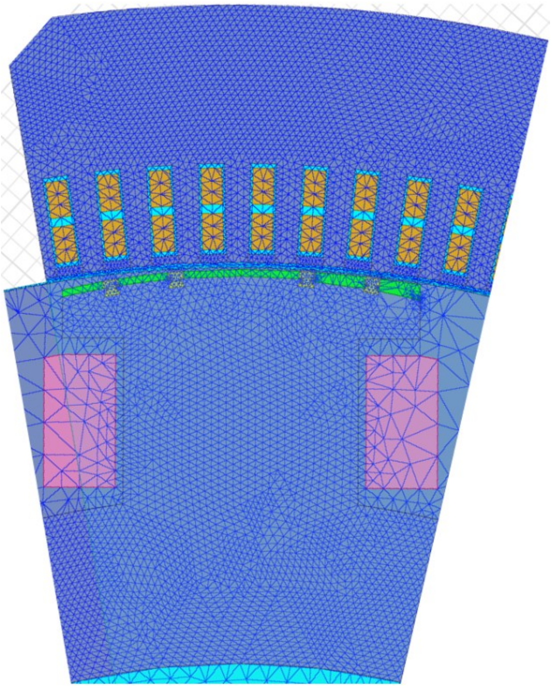

(c)

Figure 4-2 Mesh generation in FEM model for (a) BLSM (b) Model1 (c) Model2 machines

4.2.3 Flux density distributions in BLSM and HESMs

Base on flux density distribution, each part of the electrical machines are optimised so that the core materials are well utilized at full-load operation. The volume of the machines are kept minimum without compromising electrical efficiencies significantly.

By limiting the range of parameters in the multi-objective optimization, the computations are significantly reduced. Noteworthy problems in the design processes are stated in this section. Figures 4-3 to 4-5 show the full-load operation results of BLSM, Model1, and Model2 machines respectively.

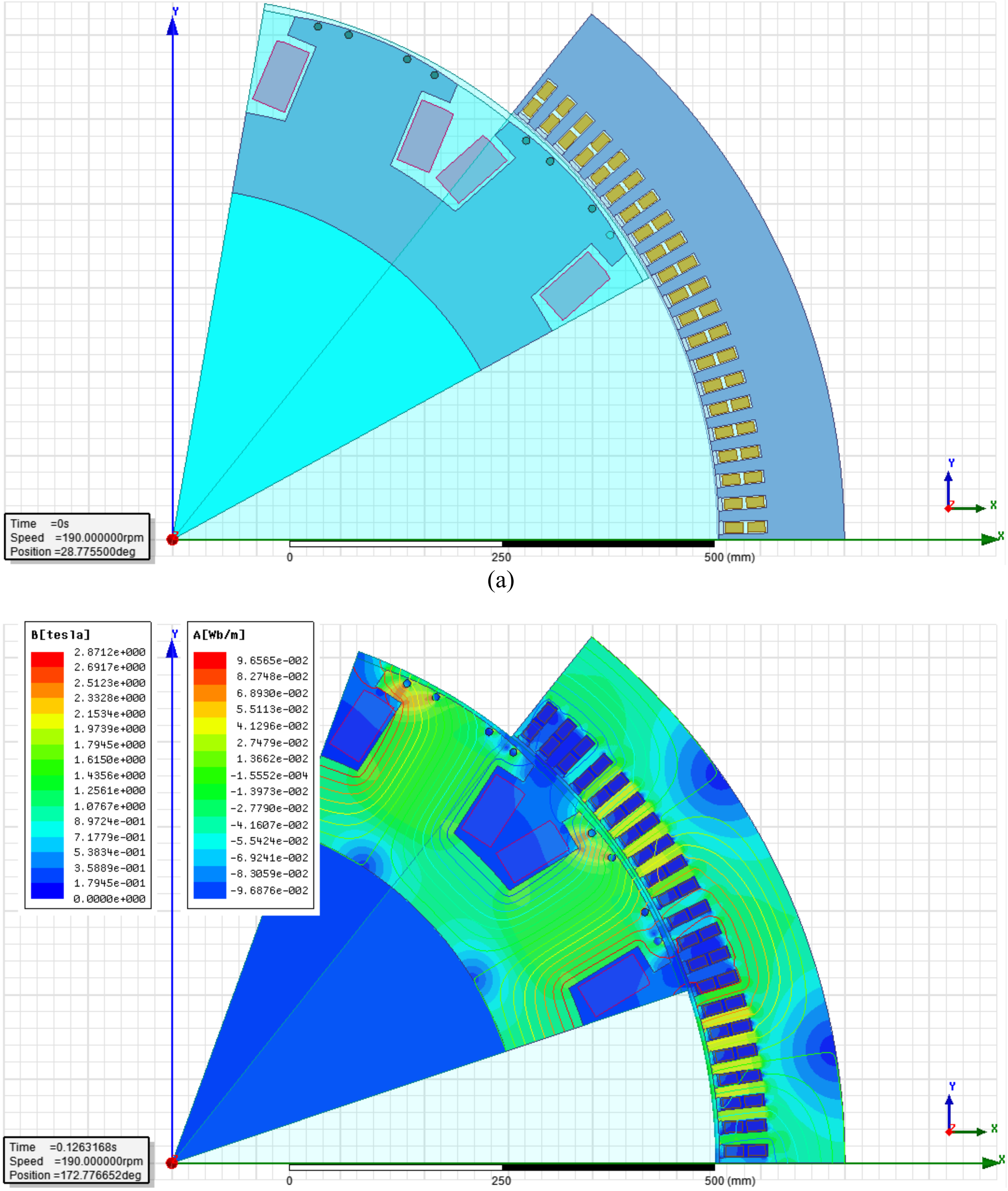

(a)

(b)

Figure 4-3 (a) FEM model of BLSM, (b) its magnetic flux density and field lines at full-load operation

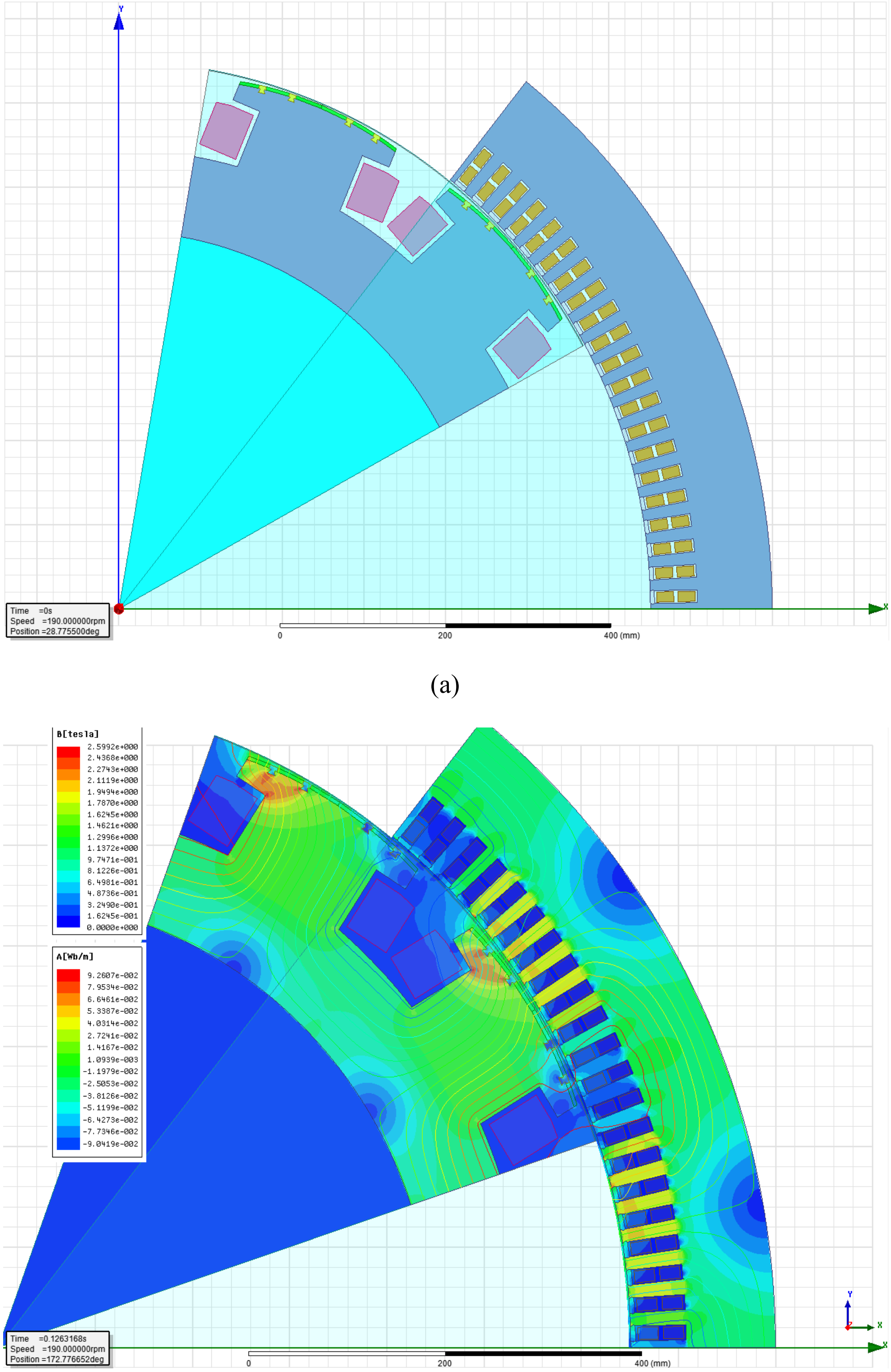

(a)

(b)

Figure 4-4 (a) FEM model of Model1 machine, (b) its magnetic flux density and field lines at full-load operation

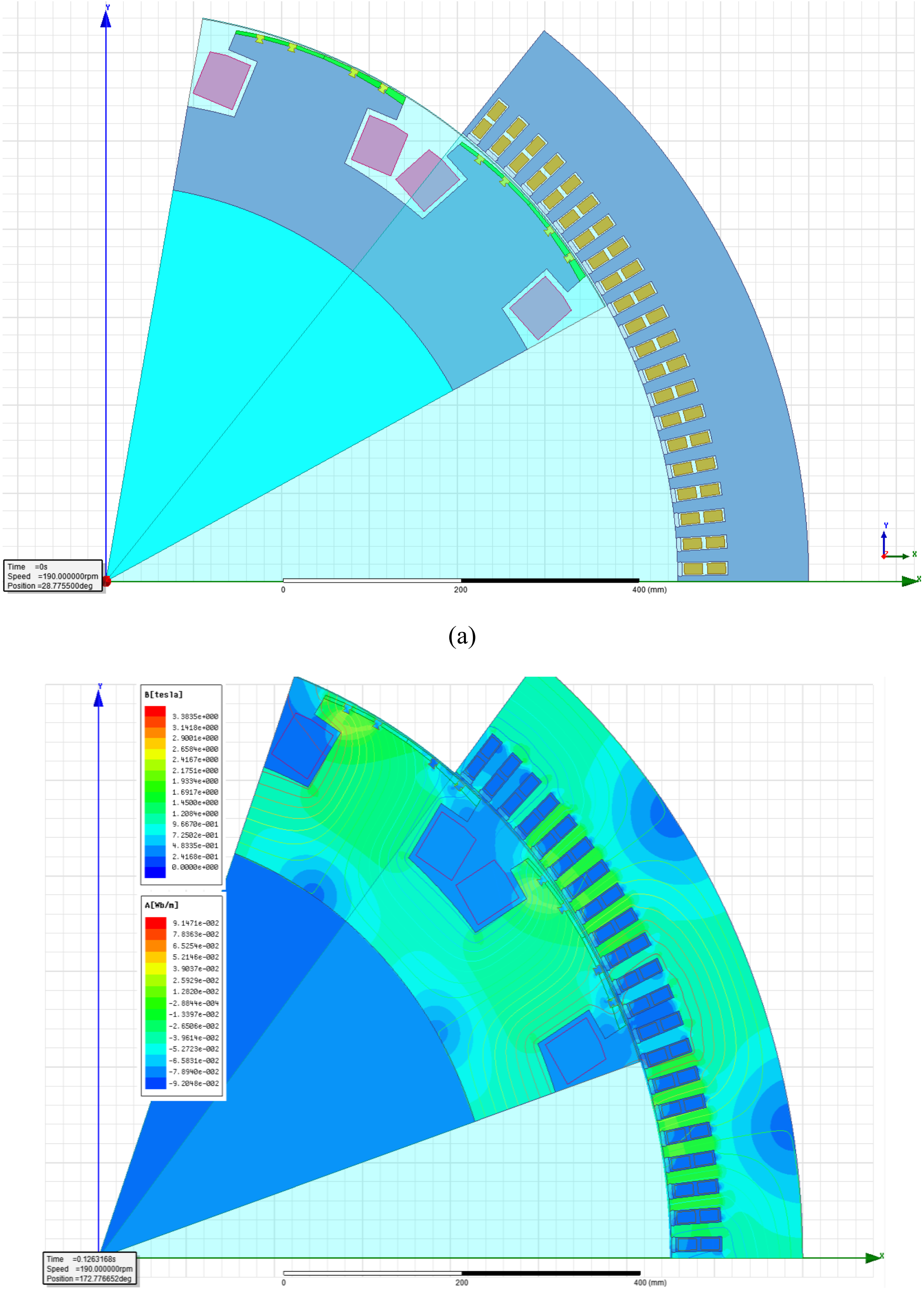

(a)

(b)

Figure 4-5 (a) FEM model of Model2 machine, (b) its magnetic flux density and field lines at full-load operation

4.2.3.1 Stator and rotor dimensions

The armature windings and stator teeth occupy the limited amount of space on the stator. Considerable effort has been focused on optimizing their dimensions. The size of the conductors is limited by the allowable current density. Stator teeth must not be completely saturated at rated load. A long tooth will have lower mechanical rigidity and has high leakage reactance. Stator and rotor yoke flux densities are kept well below saturation values.

Due to armature reaction, pole shoes have to contain enough core material as the leading edges of the poles are more saturated than the trailing edge of the poles.

4.2.3.2 Air-gap length and shape of pole face

The length of air-gap is a very sensitive parameter that greatly influences the performance of the machine. A large air-gap presents a large reluctance to the path of the armature flux. This reduces the effect of the armature reaction. It also allows better cooling at the gap surface, lower slot pulsation losses, reduced noise level, and smaller unbalanced magnetic pull. However, a larger field MMF is required, increasing the losses and cost of the machine.

As mentioned earlier, the length of the air-gap over the salient pole arc is not uniform. Instead, it increases from centre to the edges of the poles to produce the require magnetic field distribution. A larger increment gives a lower the line EMF THD. However, this is at the expense of torque production.

If the ratio of pole arc to pole pitch is too large, the inter-pole flux leakage becomes excessive. This will cause high flux densities in the pole bodies and uneven flux distributions over the stator side. A ratio of pole arc to pole pitch too small may leave insufficient pole shoe overhang to support the field windings. It is a compromise between leakage flux and torque production.

4.3 Implementation of magnetic wedges on stator slots

The implementation of magnetic slot wedges on slow-moving motors with high number of poles has significant improvements on the motor’s full-load temperature rise, power factor and efficiency [77][78][79]. Open parallel stator slots are used due preformed coils. Open slots create slot harmonics because of the non-uniform permeance of the stator teeth along the air-gap. Installing magnetic wedges reduces the slot harmonics and the equivalent air-gap, rendering the open slots equivalent to semi-open slots [80][81].

4.3.1 Characteristics and properties of magnetic slot wedges

The composition of materials that makes up the magnetic slot wedges are usually iron powder, glass material and epoxy resin. The content of iron powder can range from 1% to 75%, depending on the extent of corona suppression or performance requirement [82]. Magnetic slot wedges gives a smoother air-gap flux distribution reducing the surface core losses [79]. Main impacts of the smaller effective air-gap length (lower Cartier coefficient) are reduction of magnetizing current, starting current, and temperature rise. These features are especially useful in totally enclosed motors [83]. In inverter-fed motors, magnetic noises due to tangential forces acting on the stator teeth and high frequency bearing currents can be mitigated [84][85]. Short-circuit fault current will also be lower due to the increased leakage flux through the wedges [86].

However, when permeability of the magnetic slot wedges becomes higher, the core losses tend to increase [87]. The increased iron content also structurally weakens the wedge. An excessively high permeability may lead to even more losses than without using magnetic wedges. In this case, starting and pull-out torque will also suffer.

Considerable electromagnetic force is induced on the wedge and the windings especially during starting. Hence, its mechanical breakdown capability will weaken [78]. Vacuum pressure impregnation for the machine can provide greater mechanical strength for the wedges. It is a compromise between reliability and permeability of the magnetic wedge. Therefore, they should be customized for each machine [87]. Cost of the magnetic slot wedges is also several times higher than that of the non-magnetic wedges [88].

4.3.2 Choice of magnetic wedges

The choice of the magnetic wedges must be taken after considering the influential factors mentioned. The design of the wedge influences its structural strength. Doubling the thickness of the wedge material quadruples the strength of the wedge [82]. While introducing magnetic wedges, changes to the reactance and the losses of the machine should be kept minimal.

Magnoval® 2232 magnetic wedges from Isovolta AG, is suitable selection for this application [89]. Its B-H curve is shown in Figure 4-6. Compared to the standard wedge, pedestal wedge as shown in Figure 4-7 helps to further reduce lateral buckling and slot harmonics.

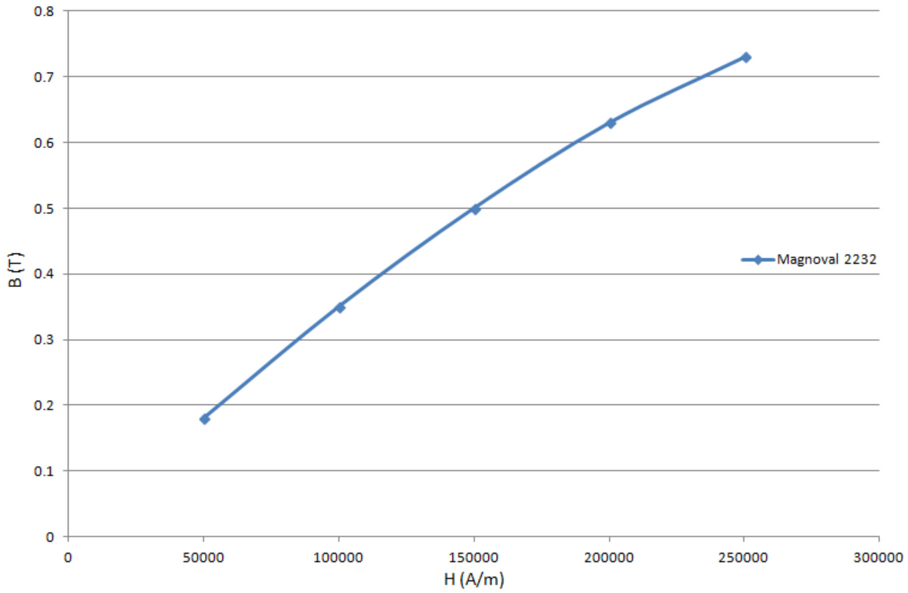

Figure 4-6 B-H curve of Magnoval® 2232 [89]

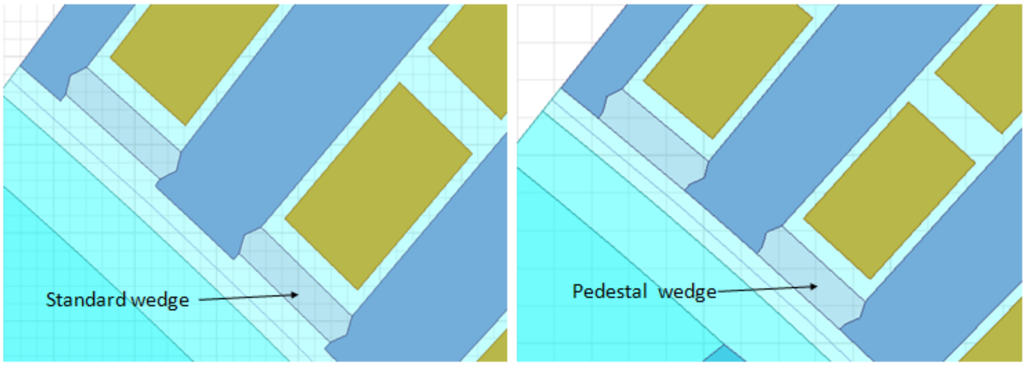

Figure 4-7 Standard wedge (left) and pedestal wedge (right)

4.3.3 Simulation results

Magnetostatic simulations of the BLSM were carried out using wedges of various permeabilities and sizes. Full-load field currents are applied and armature windings are open-circuited. The non-magnetic wedges are assumed to have a relative permeability similar to that of air. Wedges with relative permeability of 10 are used as a reference. Figures 4-8 and 4-9 show the air-gap flux density waveforms and their harmonic spectrums respectively.

As seen, magnetic wedges with a higher permeability can alleviate slot ripples on the air-gap flux. Pedestal magnetic wedges perform better than the standard ones of similar permeability. The fundamental harmonic magnitude can be substantially increased and the slot harmonics (20th and 22th) can be significantly reduced by the use of magnetic wedges. The higher fundamental harmonic amplitude indicates that the motor requires a lower magnetizing current.

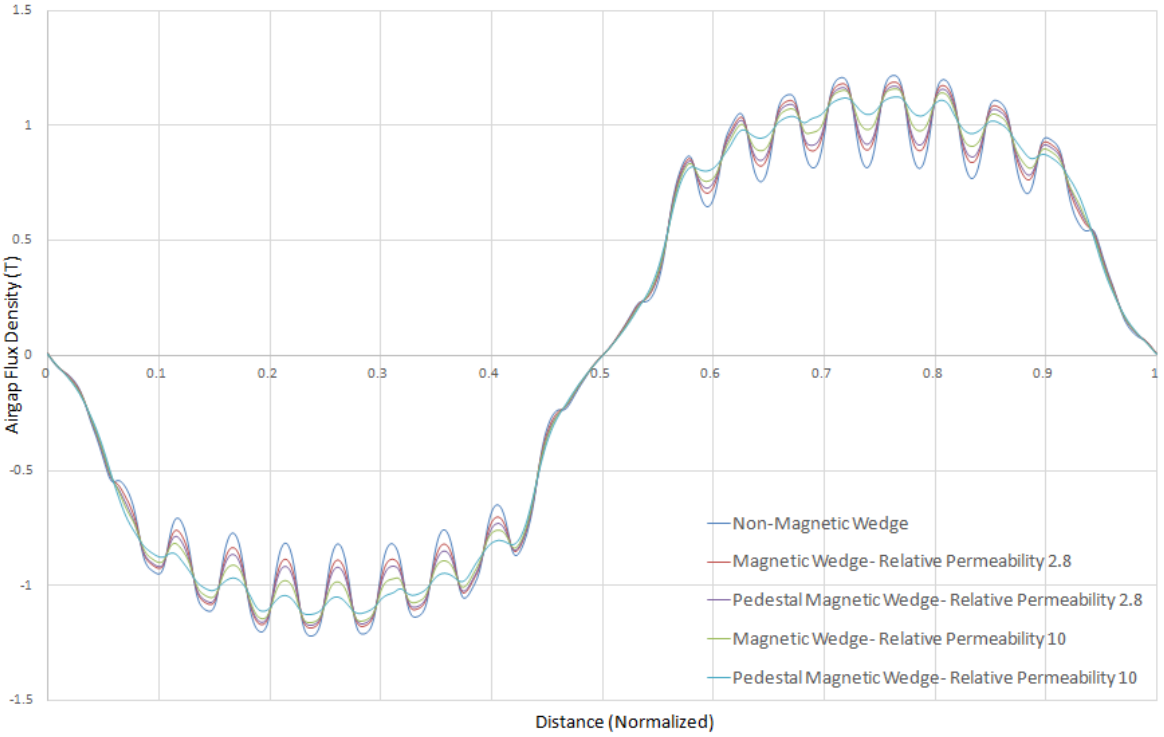

Figure 4-8 Air-gap flux density waveforms of BLSM using magnetic slot wedges of different permeabilities

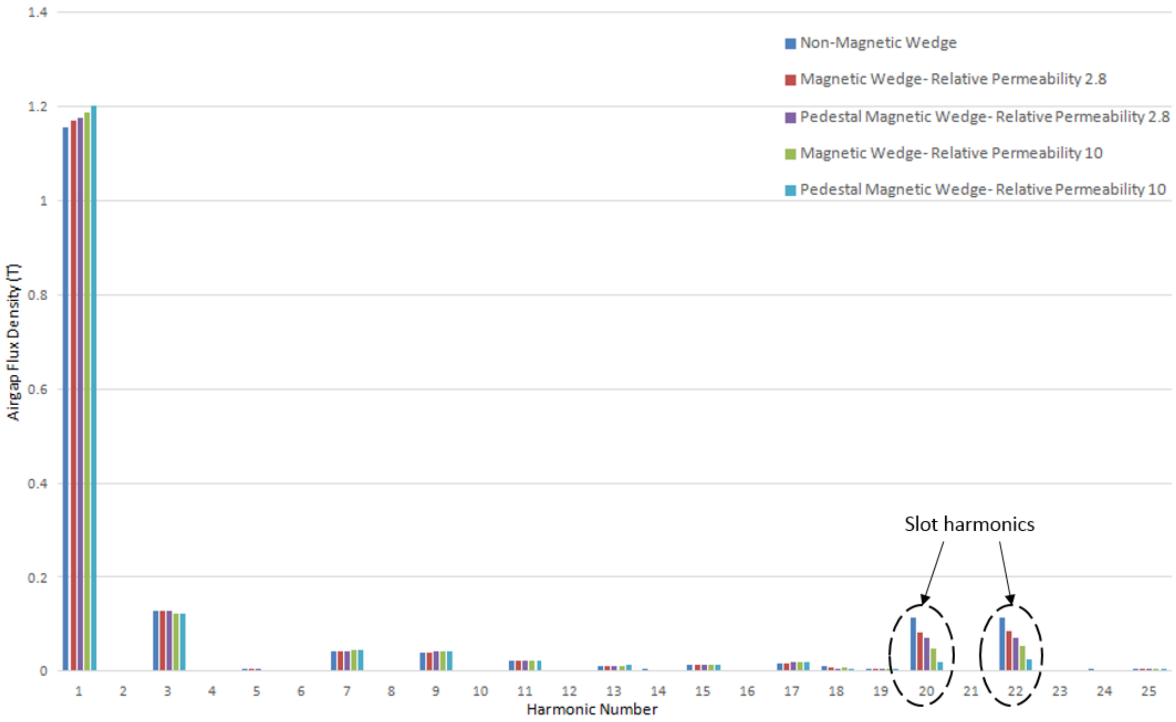

Figure 4-9 Harmonic analyses of the air-gap flux density waveforms of BLSM

Figures 4-10 and 4-11 show the flux densities of the machine using standard and pedestal magnetic wedges respectively. It can be seen that wedges with higher permeabilities give the effect of a smaller effective air-gap in the machines. Hence, less magnetization current is required.

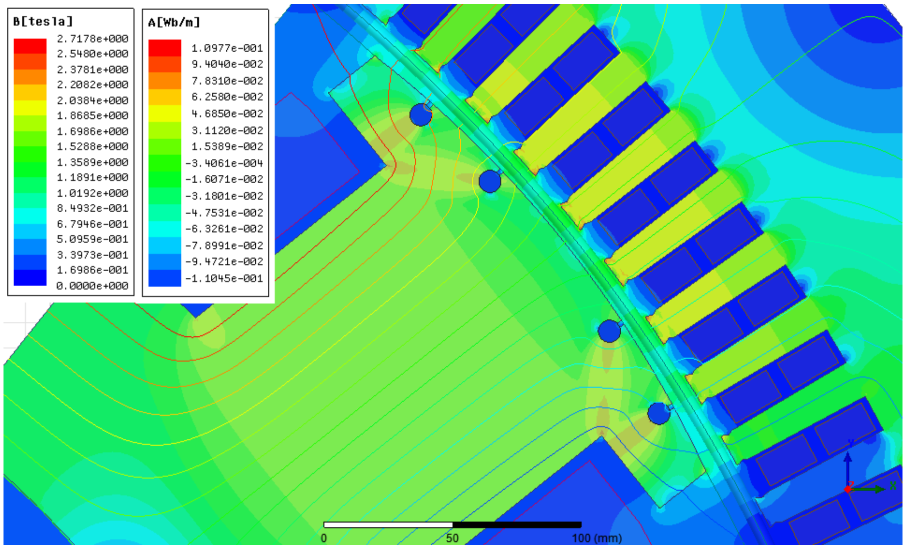

(a)

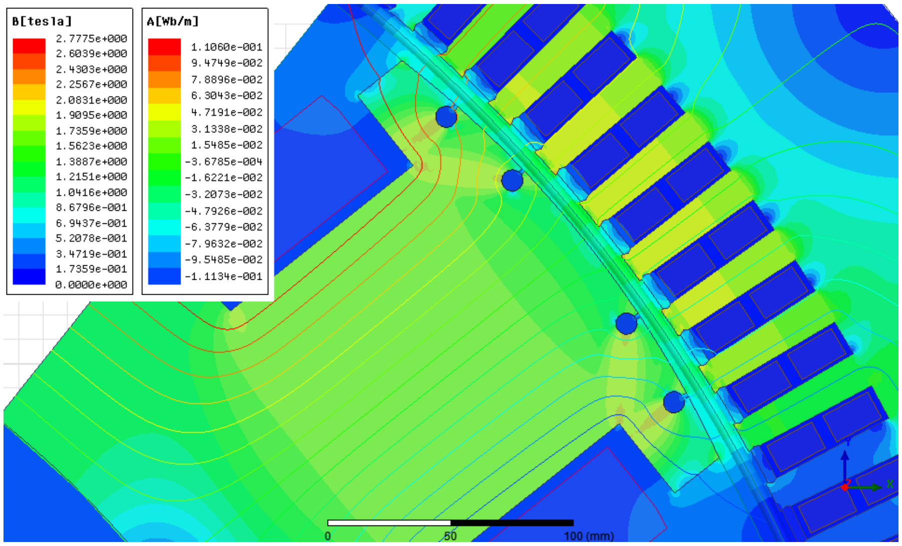

(b)

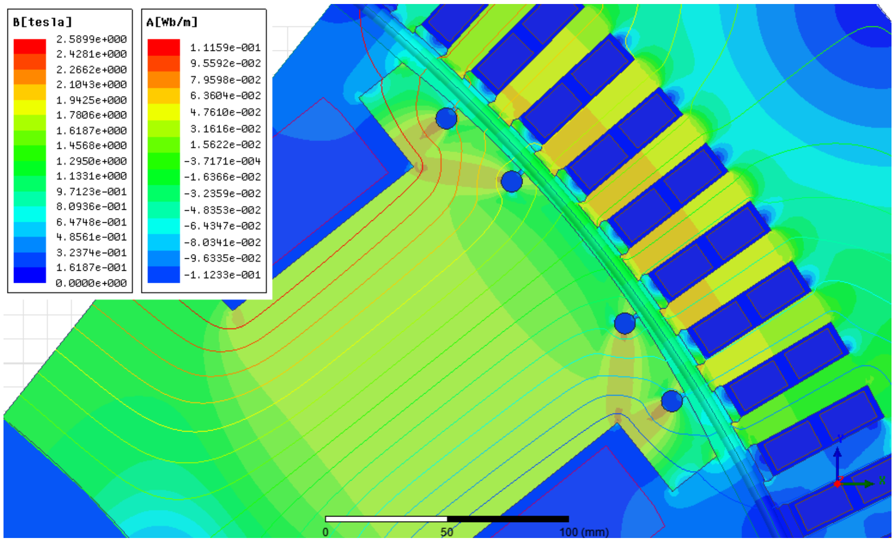

(c)

Figure 4-10 Magnetic flux densities in the magnetic wedges with different magnetic permeabilities (a) no wedges ($\mu_r = 1$), (b) $\mu_r = 2.8$, (c) $\mu_r = 10$; and its effects on the flux densities of different parts of the machine at no-load

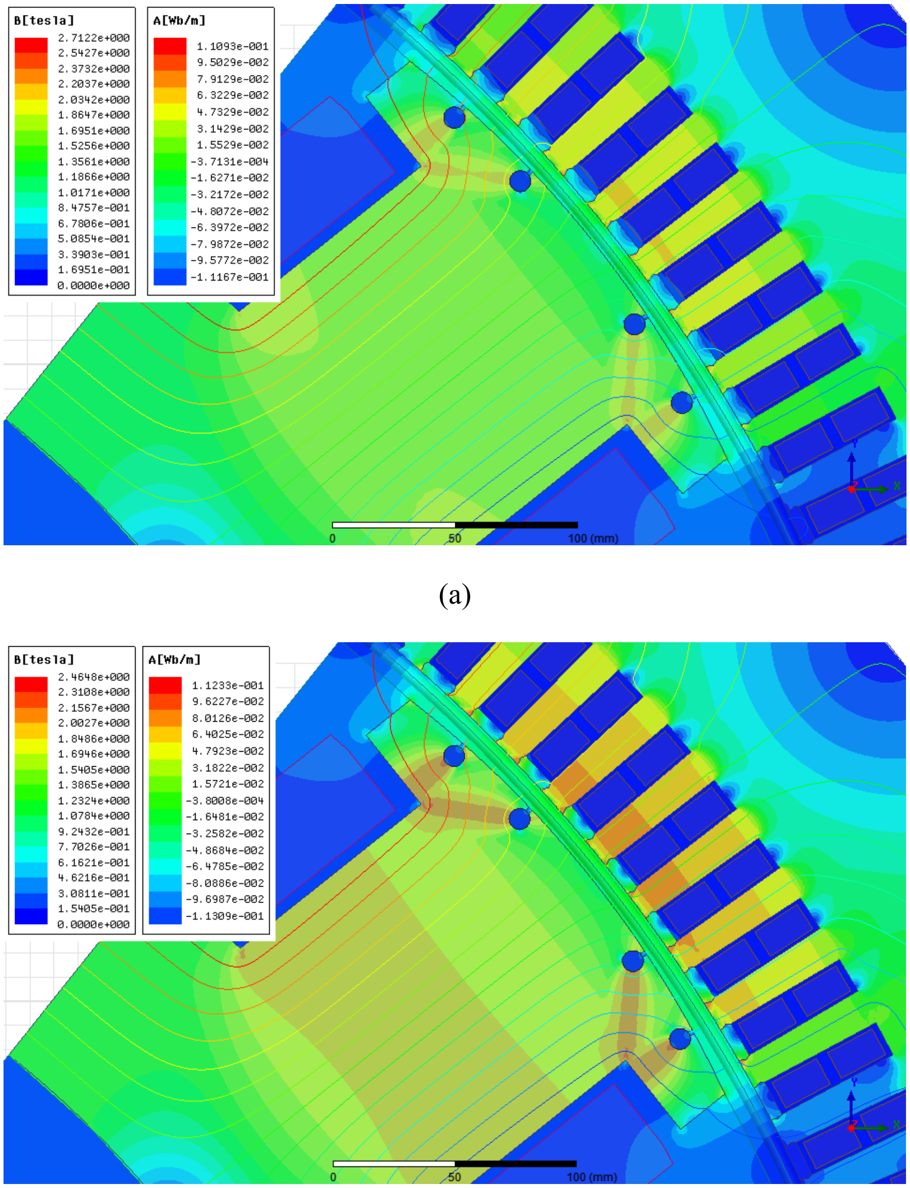

(a)

(b)

Figure 4-11 Magnetic flux densities in the pedestal magnetic wedges with different magnetic permeabilities (a) $\mu_r = 2.8$, (b) $\mu_r = 10$; and its effects on the flux densities of different parts of the machine at no-load

The moving torque response of the BLSM at full-load using different magnetic slot wedges is shown in Figure 4-12. Due to increase of leakage reactance, magnetic slot wedges lower the steady state output torque below that when using non-magnetic wedges. There is little difference in output torque when using either pedestal magnetic wedge or the standard magnetic wedge.

Time response analysis for phase current of BLSMs at rated load using different magnetic slot wedges is shown in Figure 4-13. Machines with magnetic wedges have a lower phase current than the one without. There is little difference in the phase current between using pedestal magnetic wedges and standard magnetic wedges. Therefore, in the process of selecting magnetic slot wedges, sufficient starting and pull-out torque of the motor must be ensured.

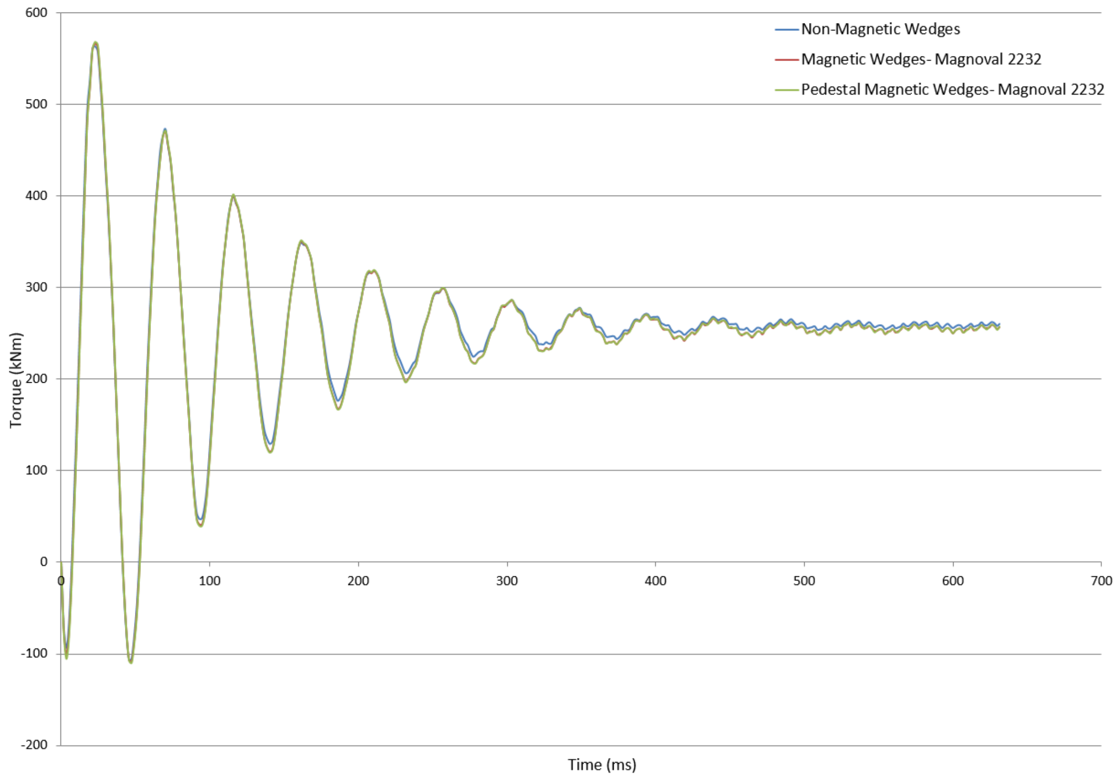

Figure 4-12 Moving torque analyses of the BLSM at full-load using different magnetic slot wedges

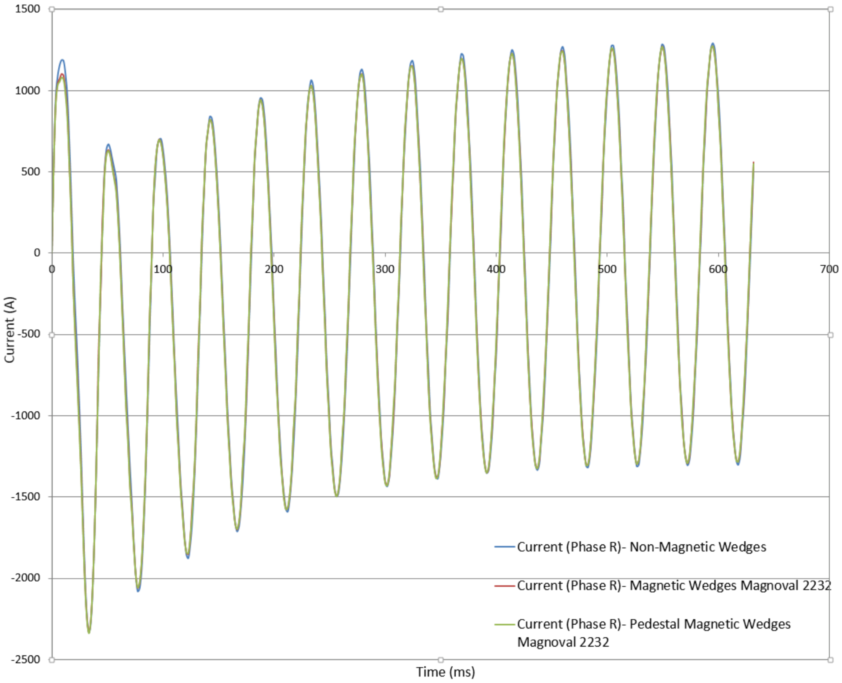

Figure 4-13 Time response analyses of phase current of the BLSM at rated load using different magnetic slot wedges

4.3.4 Cogging torque

Cogging torque describes the attraction or interaction of the rotor magnets to the stator teeth within an un-energized motor. It arises from the variation of the magnetic reluctance of the stator teeth seen by the magnets as the rotor rotates. It is given by [90]

$$T_{cog} = \sum_{1}^{p} \left(-\frac{1}{2} \varphi_g^2 \frac{dR}{d\theta} \right) \tag{4.1}$$

where φ_g is the magnet flux crossing the air-gap, R is the total reluctance through which the flux φ_g passes, and θ is the mechanical angular position of the rotor.

Figure 4-14 and 4-15 shows the cogging torque waveforms of Model1 and Model2 machines with and without using magnetic wedges respectively. The cogging torques are low in both of the HESMs. They are further reduced by the magnetic wedges to 0.024% and 0.14% of rated torques of Model1 and Model2 machines respectively.

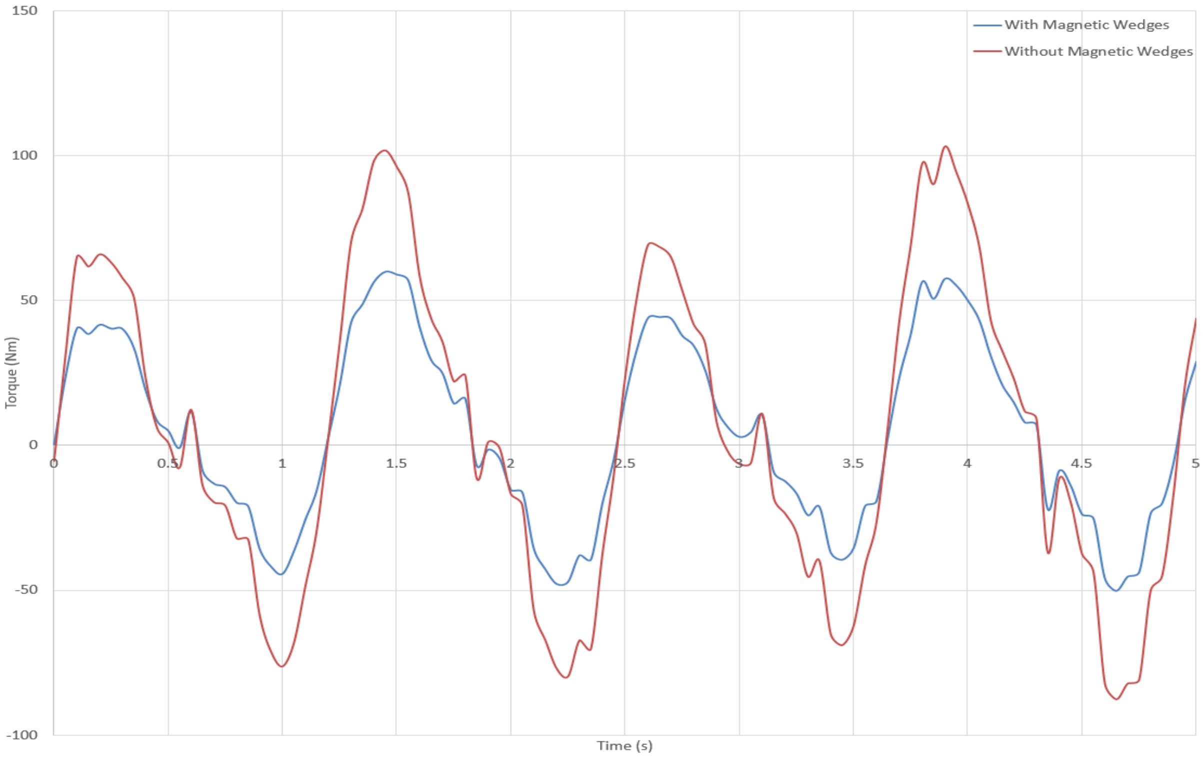

Figure 4-14 Cogging torque waveforms of Model1 machine with and without magnetic wedges

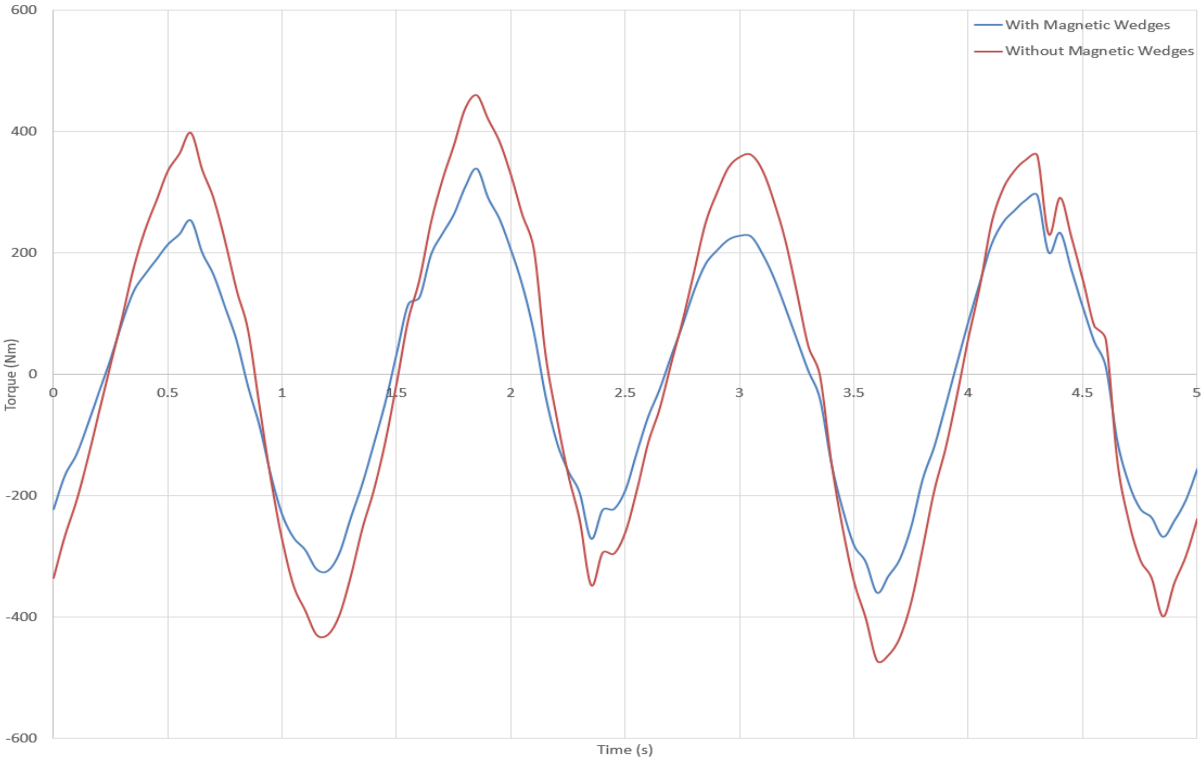

Figure 4-15 Cogging torque waveforms of Model2 machine with and without magnetic wedges

4.4 Damper winding design

After determining the size, material and number of damper bars per pole for the starting conditions, positions of damper bars on the poles have to be found.

Slot openings on the stator cause air-gap permeance harmonics, which induces voltages and produce currents in the rotor damper winding. The induced currents produce their own air-gap MMF, which produce reaction fluxes that lead to stator EMF time harmonics. The level of THD produced maybe significant [61][91]. Proper selection of the rotor damper bar pitch prevents rotor bar currents to be induced by the flux density pulsations. It can even be used to attenuate the THD harmonics [61][92].

Transient FEM simulations in this study take into account of the effects of eddy currents and dynamic field current. This method provides the most accurate results. However, it required significant amount of simulation time. For high quality results, extremely fine meshes and step size must be used. The slot permeance variation causes an alternating current perturbation in the field winding. Therefore, an external field circuit must be used in the simulation [93].

It is recommended to have sampling points of at least double that of the Nyquist-Shannon sampling theorem [93][94]. As a result, time step for this operation would be extremely small (35th harmonics require a time step of $3.22\text{x}10^{-4}$ seconds). Simulation has to be run long enough to avoid the transients of field circuit and damper starting current. For the two-dimensional (2D) FEM model, the end effects are included using lumped parameters. Figure 4-16 illustrates the position of damper bars on a rotor pole.

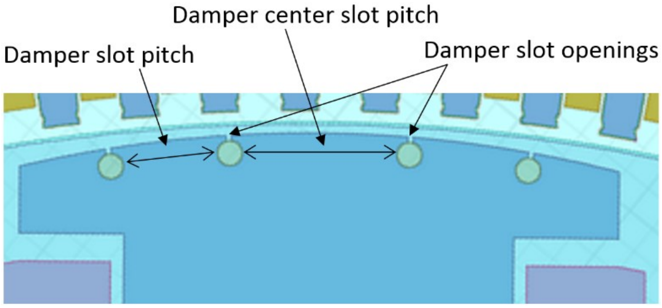

Figure 4-16 Position of damper bars on a rotor pole

4.4.1 Damper slot pitch

The damper slot pitch is varied in the range of 10 - 15% of the stator slot pitch beginning from the lowest span as shown in Figure 4-17 from (a) to (b) respectively. Position of damper winding at (c) is progressed into (d), which has a wide centre slot pitch and yields lowest line EMF THD. Figure 4-18 and 4-19 show the line and phase back-EMF waveforms of damper bar configuration (d) and its line back-EMF harmonic spectrum respectively. It can be seen that the line voltage waveform is very sinusoidal.

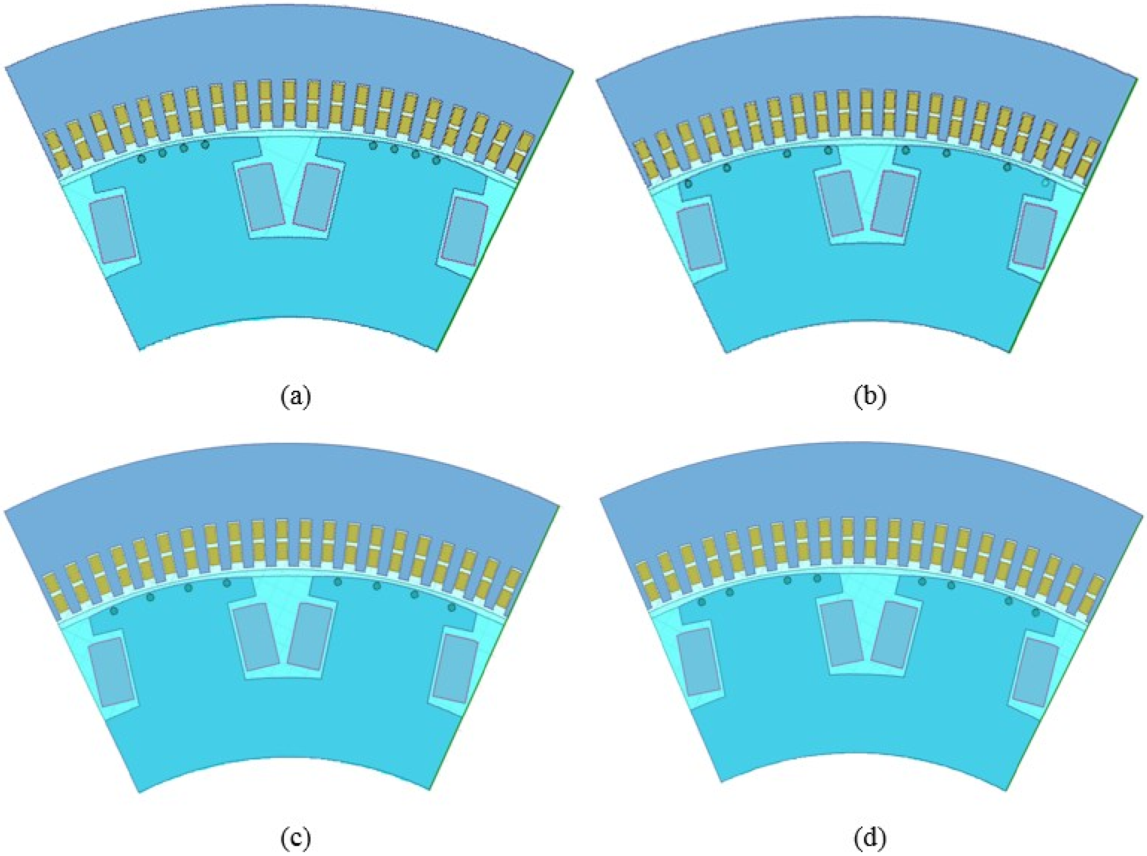
(a) (b) (c) (d)

Figure 4-17 Positions of damper winding on the rotor pole from least span (a) to widest span (b). Position of damper winding at (c) is progressed into (d), which has a wide centre slot pitch and yields lowest line EMF THD

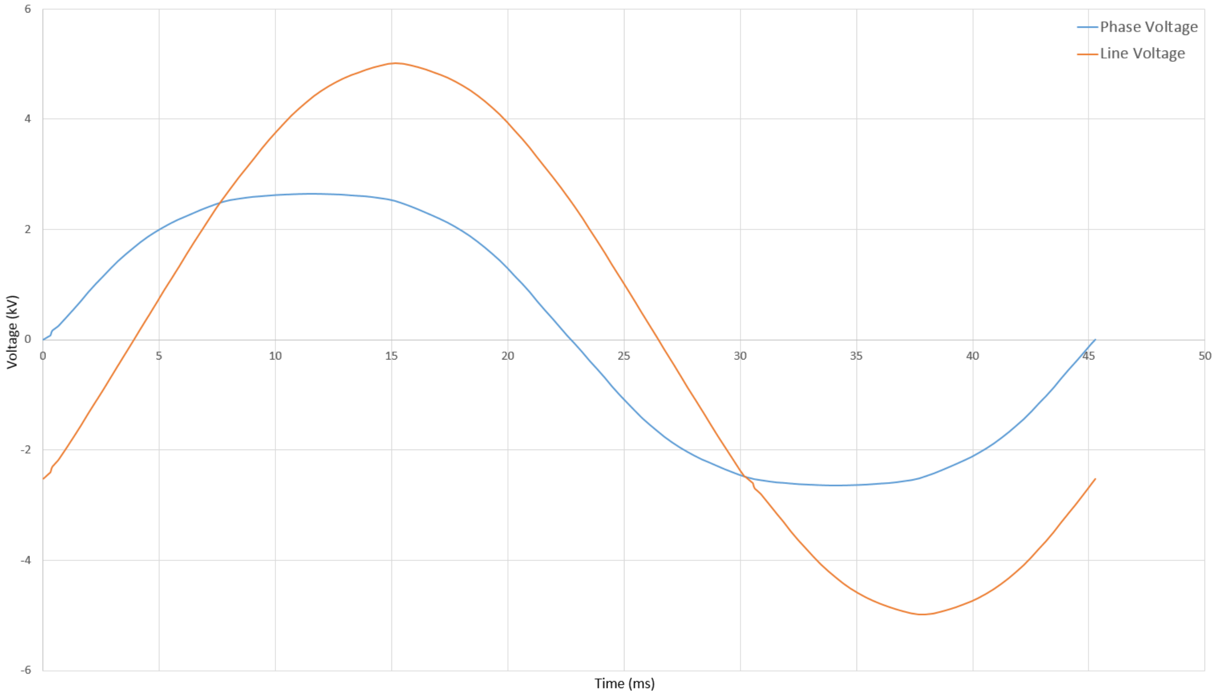

Figure 4-18 Line and phase back-EMF waveforms of the BLSM with damper winding configuration (d)

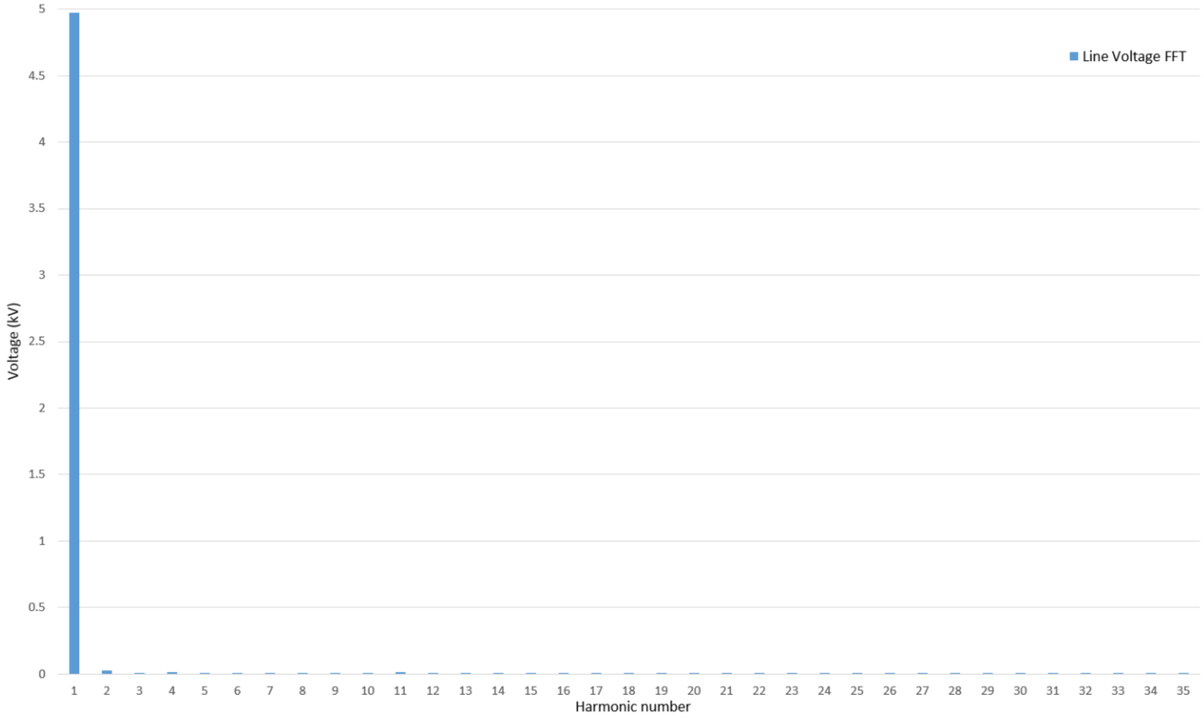

Figure 4-19 Harmonic spectrum of line back-EMF waveform of BLSM with damper winding configuration (d)

Figure 4-20 compares only the higher harmonics as they are very small in comparison with the fundamental. THD results in Table 4-1 shows that the fractional slot winding configuration is very effective in eliminating slot ripple influence on the air-gap MMF. The influence of the position of damper bars on the open-circuit line voltage THD is negligible.

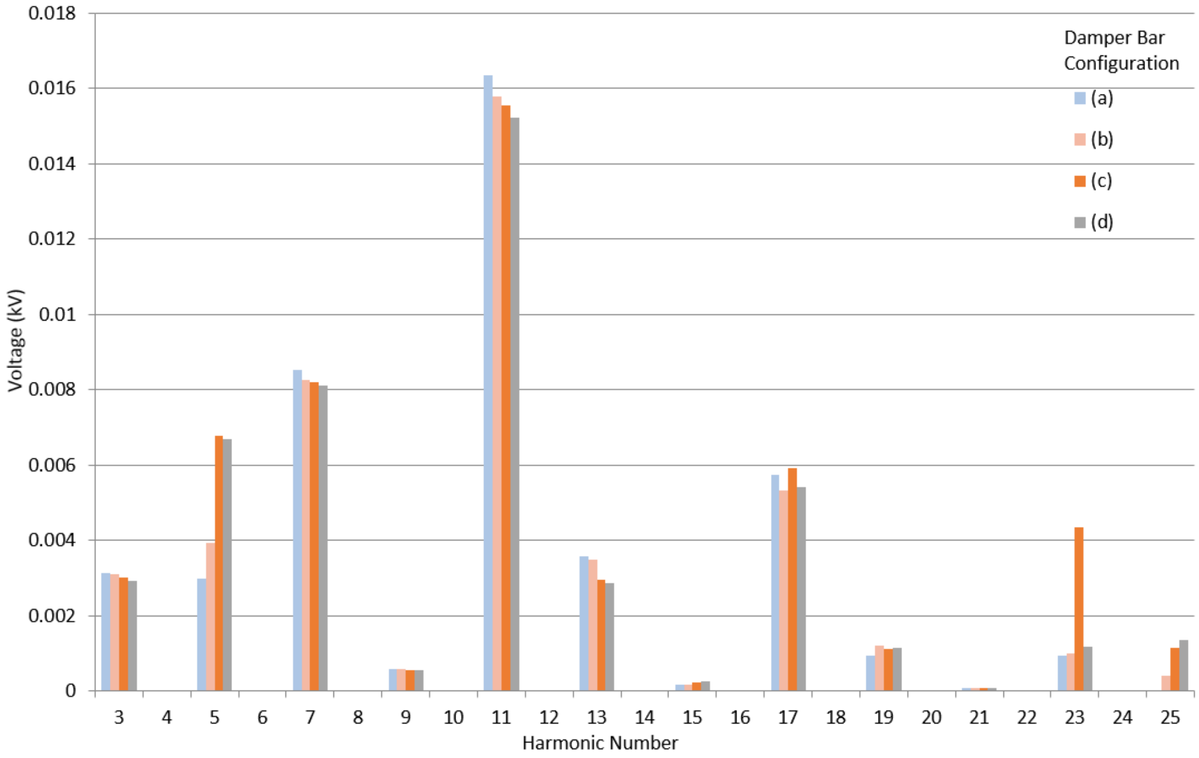

Figure 4-20 Higher harmonics of line back-EMF of BLSM with different damper bar configurations

Table 4-1 Line back-EMF THDs of BLSM with different damper bar configurations, considered up to the 35th harmonic

Damper Bar Configuration	(a)	(b)	(c)	(d)
Line-line Back EMF THD (%)	0.747548	0.739128	0.747137	0.738964

4.4.2 Damper winding configuration for torque performance

A mirror asymmetry in the air-gap permeability of two adjacent poles can be used to reduce slot harmonics and disturbances in motor start-ups. This is due to anti-phase effect [65][92]. Its underlying principle is given by [65]

$$c = \frac{\sin(2pn_{ss}\pi)}{2p\sin(n_{ss}\pi)} \cdot \sin\left(n_{ss}\frac{\pi}{2} + n_{ss}\frac{\Delta_{dr}}{\tau_{pr}}\pi\right) \tag{4.2}$$

where c is a constant which ideally be zero, Δ_{dr} is the shift of a single pole pair, τ_{pr} is the rotor pole pitch and n_{ss} is the stator slot harmonics given by

$$n_{ss} = 1 + 2kmq \qquad\qquad k = \pm1, \pm2, \ldots \tag{4.3}$$

Figure 4-21 illustrates the shifting of the damper bars. The damper bars in configuration (a) are not shifted. Those in configuration (b), (c) and (d) are shifted by an equivalent of 25, 50 and 75 % of stator slot pitch respectively. In configuration (e), the damper bars are totally buried in iron, without damper slot opening on its rotor pole.

The torque performances for each of the configurations are shown in Figure 4-22. As seen, damper windings with a wider shift develop more torque at synchronization and have a settling time almost identical to the damper winding without shift. Configuration (e) develops less torque during synchronization. It also produces a considerable amount of torque ripple at steady-state operation. The oscillations may be caused by lagging damper winding currents due to appreciable damper inductance.

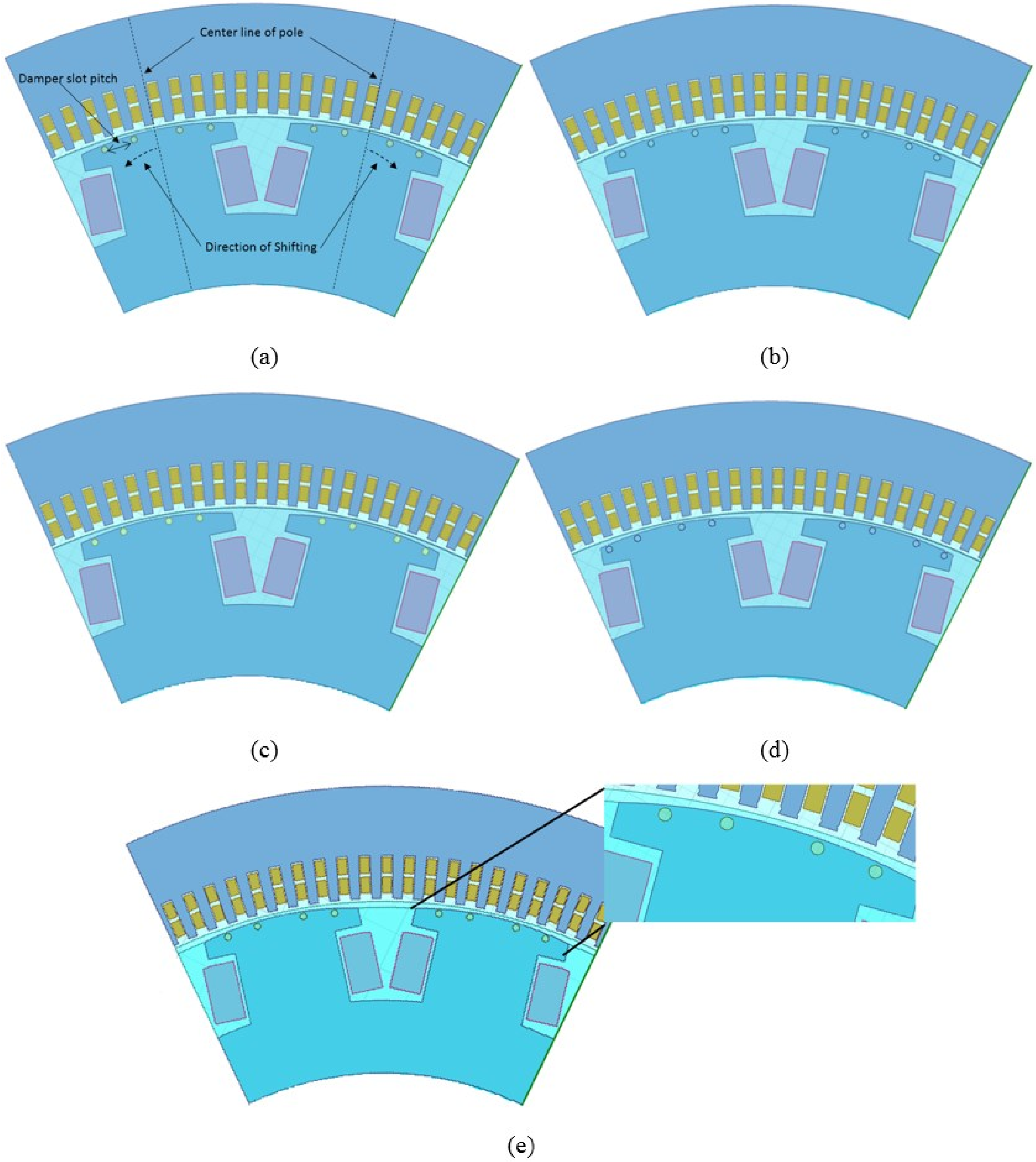

(a) (b) (c) (d) (e)

Figure 4-21 Damper winding configurations

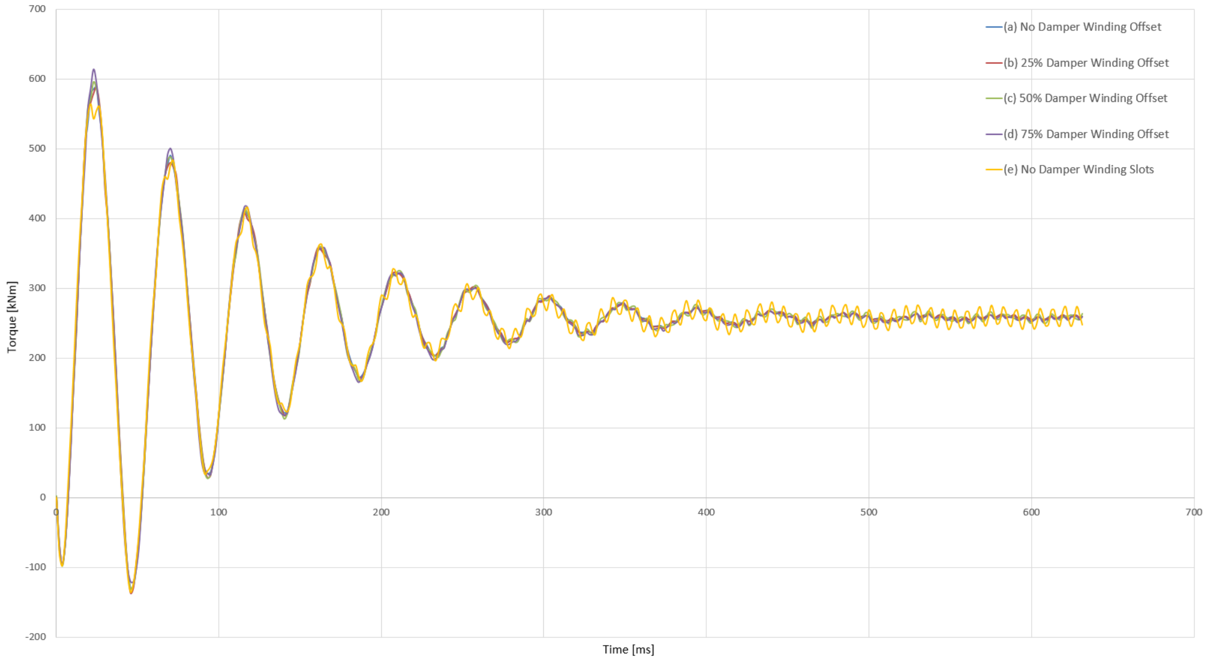

Figure 4-22 Transient torque response of the BLSM at synchronization and its steady-state torque at rated load with different damper winding configurations

4.5 Demagnetization of magnets

Demagnetization of the PMs is an irreversible process which should be avoided in all situations. One of the main reasons that cause the demagnetization of the magnets is the short-circuit current. A short-circuit event can produce significant current-induced magnetic flux that opposes the PM flux. Insufficient pole MMF to withstand the opposing flux will result in demagnetization of the PMs. The amount of magnet material on the rotor is a crucial factor as it directly influences the cost and performance of the machines.

The level of demagnetizing flux the magnets could withstand without being permanently demagnetized can be found by FEA simulation. Different levels of demagnetizing fluxes are applied at various positions of the poles. Positions of magnets on the poles most vulnerable to demagnetization are found.

Demagnetizing currents at 4 times the rated currents are found to be sufficient to reduce the flux densities of some magnets in both machines to -0.5T, close to the knee of their demagnetization curve at 120°C (Appendix E). Rated field currents are applied to the field windings of each machine. Figures 4-23 and 4-24 show flux density vector plots of the demagnetization at 4 times rated current and the flux density distributions on the poles in Model1 and Model2 machines respectively. In Figures 4-23(a) and 4-24(a), areas circled by the red dash lines show where the fluxes are opposite to that driven by the magnets. In Figures 4-23(b) and 4-24(b), the blue curves show the flux density distributions on the poles at normal operation while the red curves show the effect of the demagnetizing fluxes on the flux density distributions. The points which experience the most severe demagnetization are circled by the red dashed lines.

As a short-circuit current can be several times the peak value of the rated current, the inverter drive must provide adequate protection. The stator currents rise rapidly at the beginning of a short-circuit. High frequency currents will induce currents on the damper bars. A flux-screen is formed which shields the stator magnetic field from penetrating the magnets, forcing it to the leakage paths in the vicinity of the air-gap [60][65][74][95].

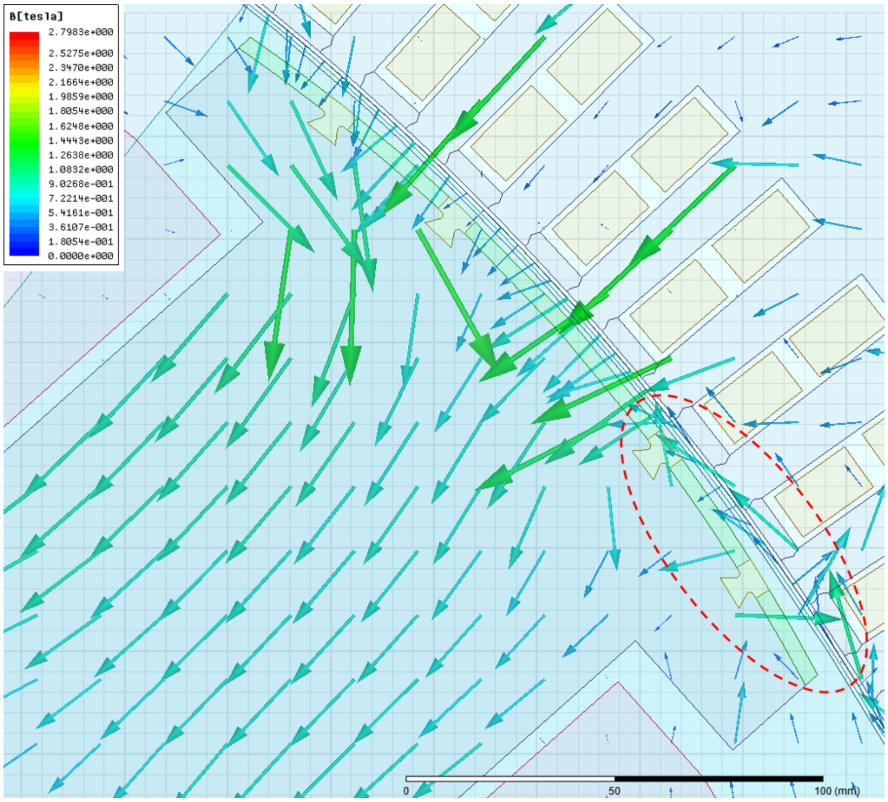

(a)

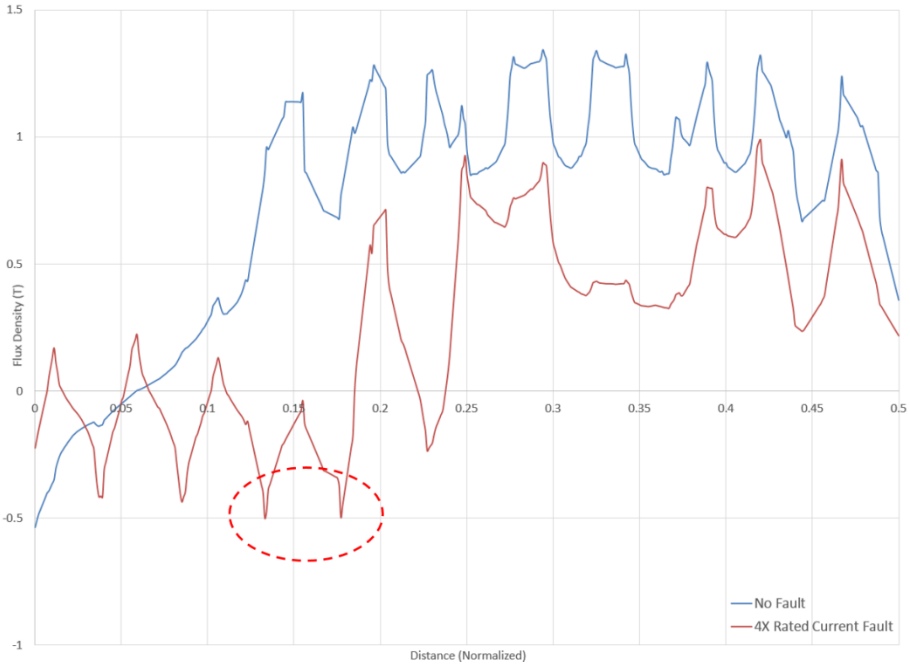

(b)

Figure 4-23 (a) Flux density vector distribution in the cross-sectional area for a pole of Model1 machine demagnetized under 4 times rated current, and (b) its flux density plot of the magnets.

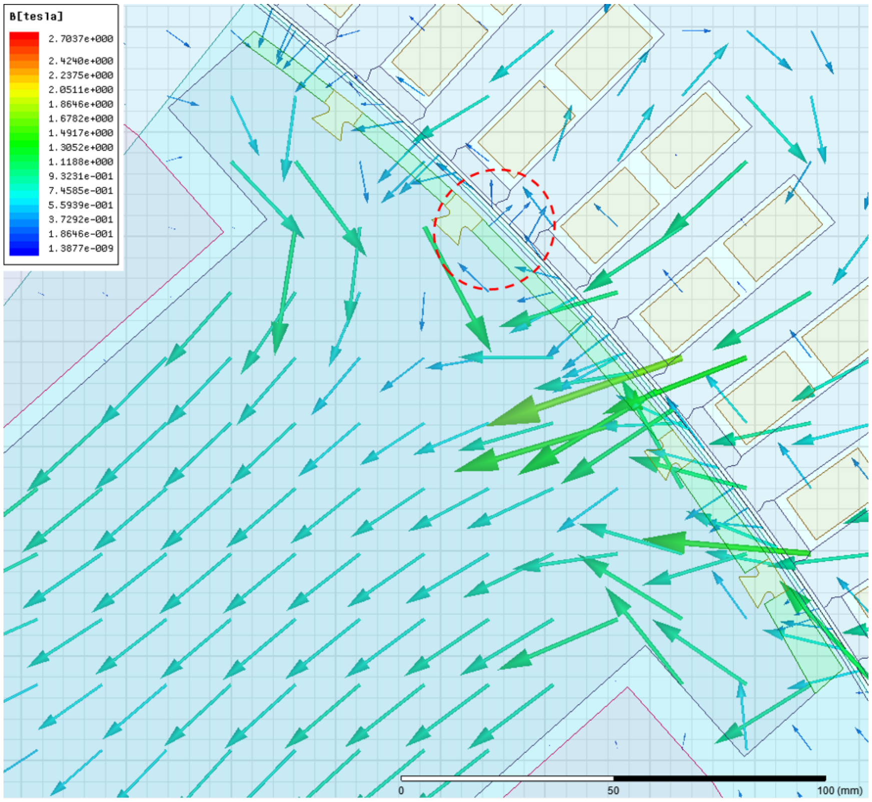

(a)

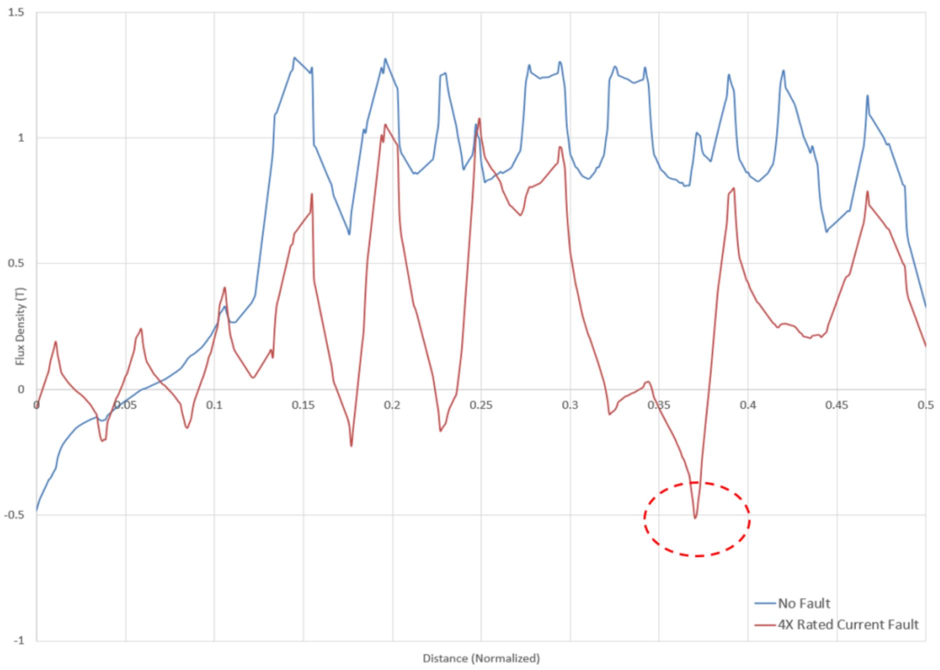

(b)

Figure 4-24 (a) Flux density vector distribution in the cross-sectional area for a pole of Model2 machine demagnetized under 4 times rated current, and (b) its flux density plot of the magnets.

4.6 Summary

In this chapter, FEM modelling is used to provide accurate and optimal designs of the machines. The pre-processing stage is a crucial part of the modelling as it determines the accuracy of the solution and its computing time. This includes the setup of boundary conditions, meshes, time steps and surface approximations of the models. Employing an external circuit also improves accuracy.

The amounts of active core materials in the machines are kept to a minimum by optimising the flux distributions, ensuring efficient use of the materials in every part. This reduces the cost and volume of the machines.

The main purpose of installing magnetic wedges in the machine stator is to reduce slot harmonics in the air-gap flux. In our case, pedestal shaped wedges are found to be more effective than the normal shaped wedges. Cogging torques of the HESMs are also reduced.

The positions of damper windings on the rotor pole shoe can be used to improve the voltage THD of the machines. Damper winding offset can also improve its torque performance. In this case, it was shown that the fractional slot winding eliminates a large amount of slot harmonics and the position of the dampers bars does not seem to pose a significant effect on both voltage THD and torque performances.

At rated operation, the permanent magnets on the rotor of the HESMs are shown to be able to withstand demagnetization currents 4 times the magnitude of rated peak current. The choice of the ratio of PM flux to field excitation flux is crucial as it may determine if the PMs will survive the demagnetization event.

Chapter 5 – Performances Comparisons of BLSM and HESMs

5.1 Introduction

In this chapter, finite element method is applied to model the transient and steady-state characteristics of the presented BLSM and HESMs. Post-process analyses of their simulations are performed and their results are compared. Thermal performances of the machines and economic feasibility of the HESMs are also investigated.

5.2 Torque, voltage, current and losses

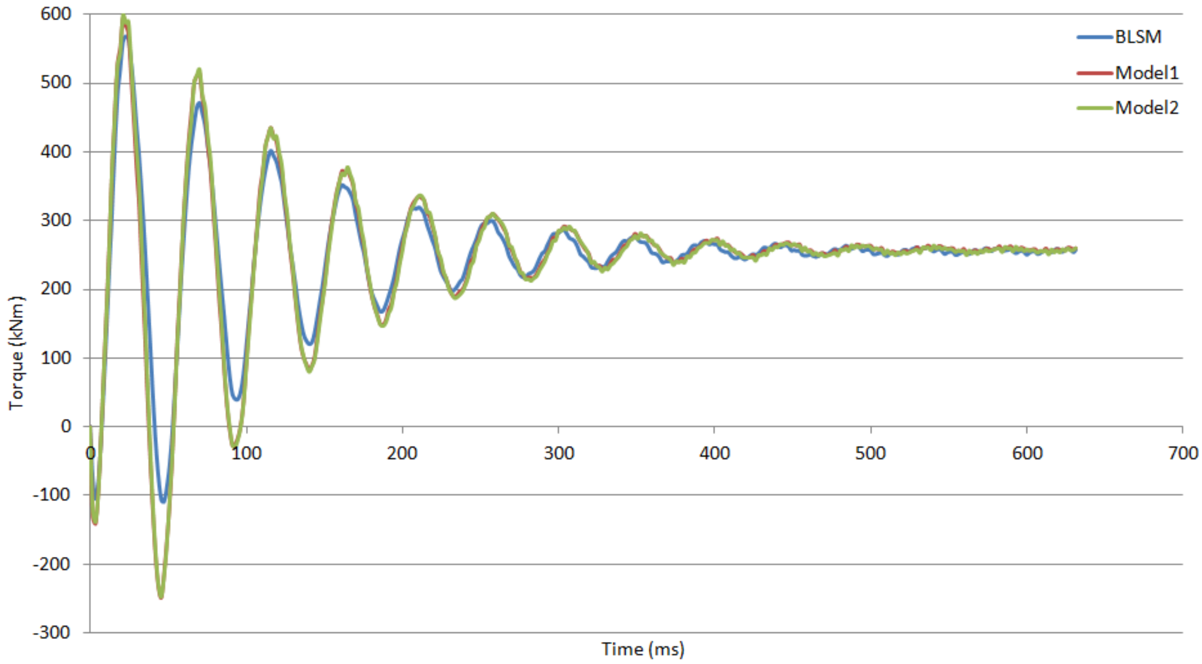

Figure 5-1 Output torque response of the BLSM, Model1 and Model2 machines at rated load

The time stepping FEM analyses for all three machines are performed at rated-operation. The time response plots are illustrated until steady-state. Figure 5-1 shows the waveform of torque response immediately after synchronization (pull-in). It can be seen that the HESMs has higher torque fluctuations and settles to steady-state at a slightly longer time than the BLSM. All of the machines are able to deliver rated steady-state output torque of 252kNm.

Torque ripple is quite similar amongst the machines, being favorably low at a maximum of 3.56% of its rated torque.

Figure 5-2 and 5-3 shows the three-phase terminal voltage and current waveforms for the BLSM and HESMs at rotor synchronization. The HESMs have higher transient voltage and current fluctuations than the BLSM. The time for the machines to reach steady-state rated operation is comparable. Their phase voltages and current waveforms are very sinusoidal. Rated line-voltage and current of the machines are 3300V and 920A respectively.

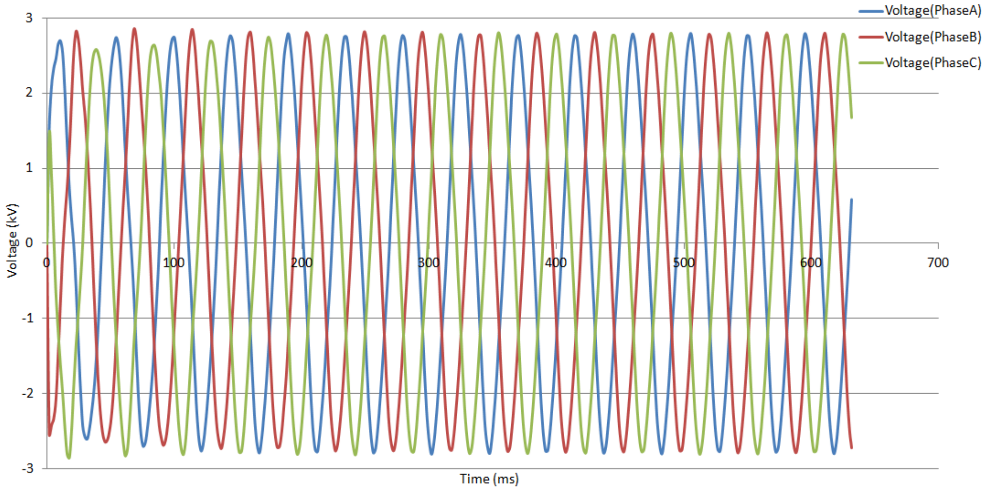

(a)

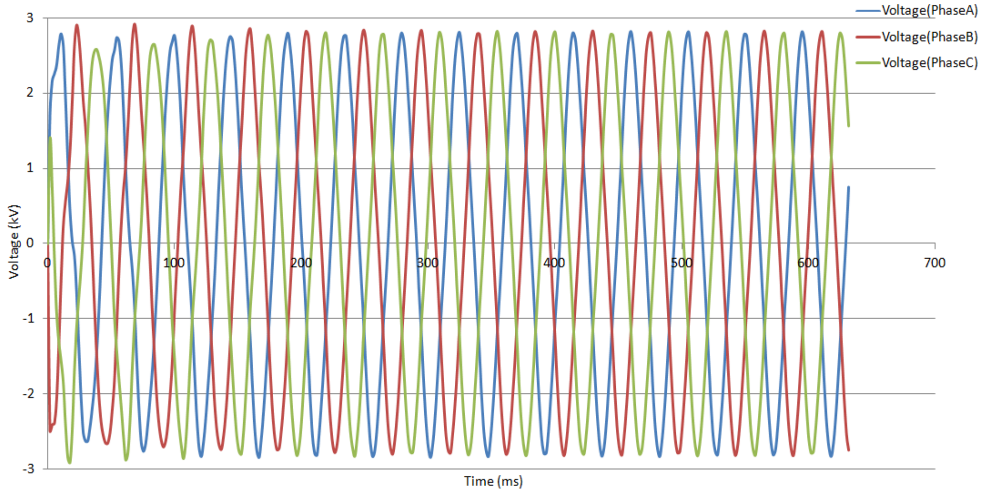

(b)

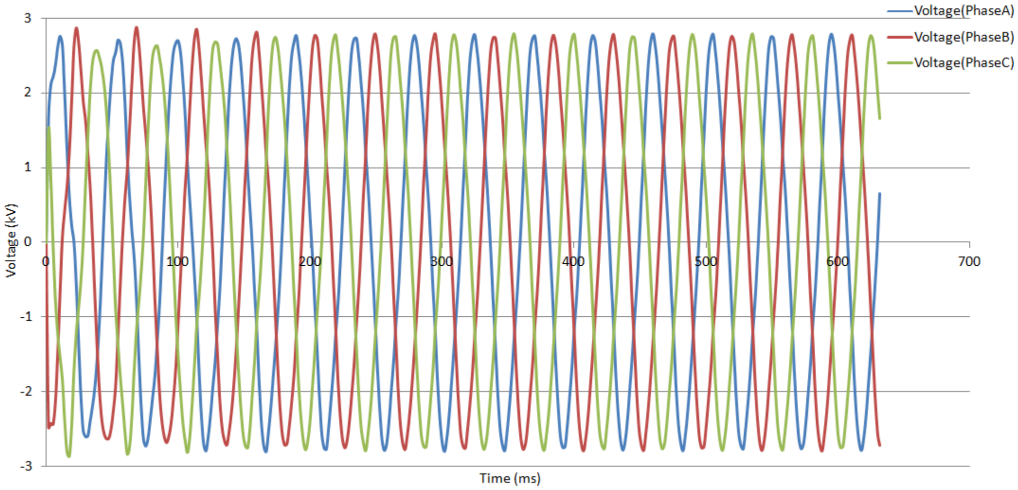

(c)

Figure 5-2 Phase voltages time responses of (a) BLSM, (b) Model1, (c) Model2 machines at rated load

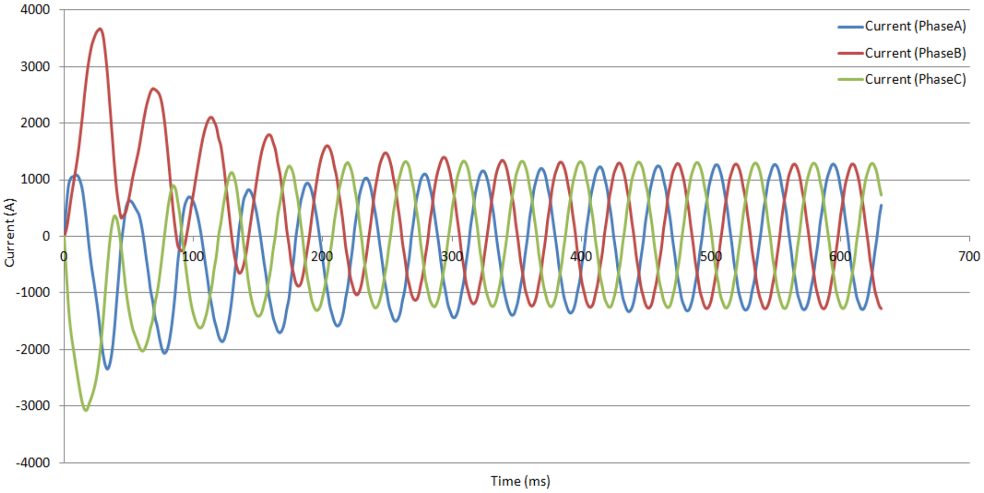

(a)

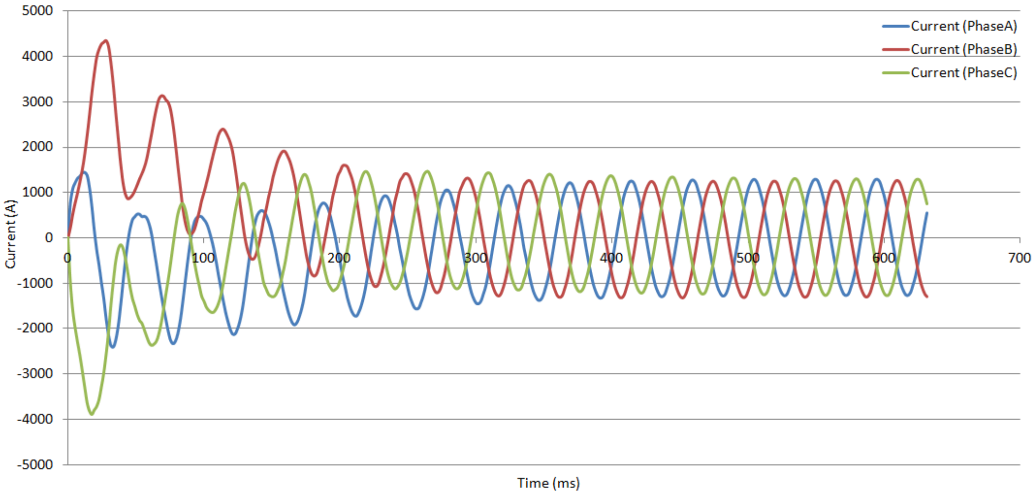

(b)

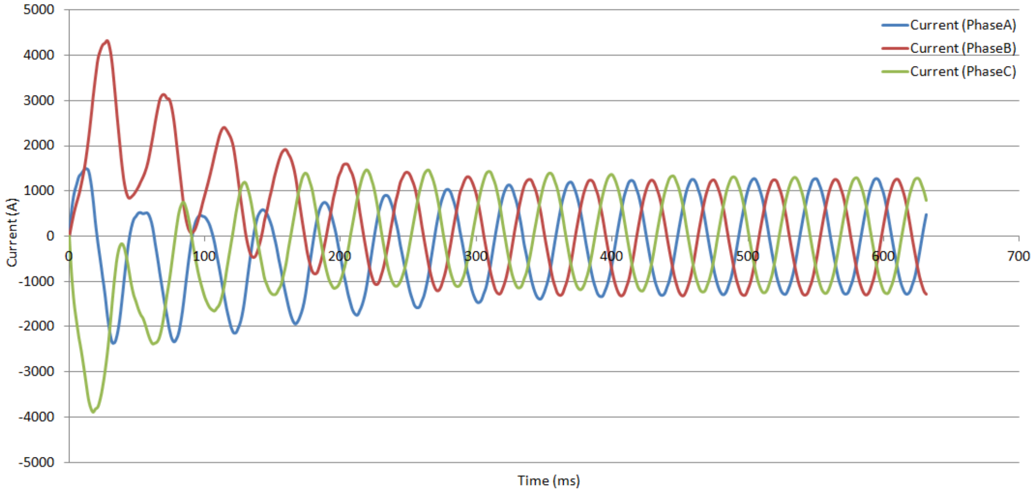

(c)

Figure 5-3 Phase currents time responses of (a) BLSM, (b) Model1, (c) Model2 machines at rated load

The transient field excitation voltage is shown in Figure 5-4. The transient field voltages of the HESMs are higher than those of the BLSM, peaking at approximately 17kV. Although, the high voltages drop rapidly in a short duration of time to an average of almost 0V, field insulation must be rated to withstand the voltage transients.

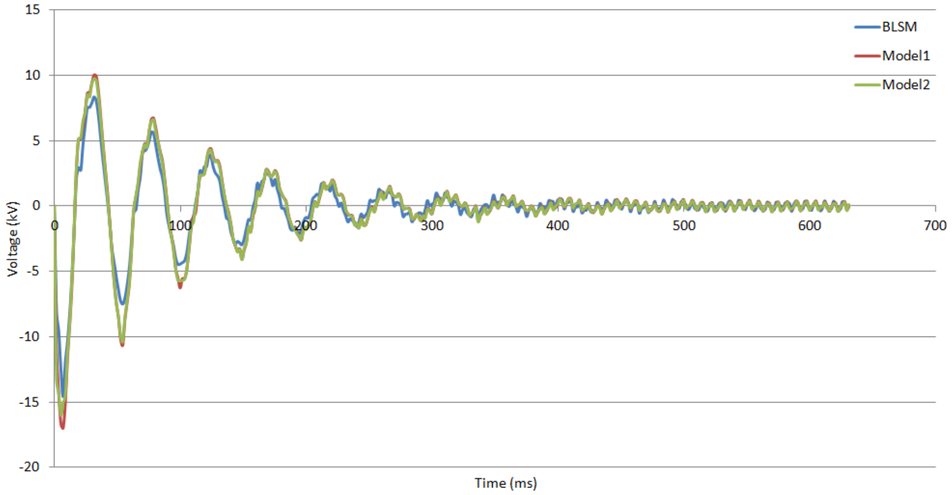

Figure 5-4 Transient field excitation voltages of the machines at rated load

The transient and steady-state electromagnetic losses waveforms of the machines are shown in Figure 5-5. Core loss comprises of hysteresis and eddy current losses. Copper losses are the copper resistivity losses in the stranded conductors of the machines.

At steady-state, the average core losses and copper losses for the BLSM are 15kW and 128.1kW respectively. Its electromagnetic efficiency is 97.1% at rated operation. For Model1, average steady-state core losses and copper losses are 16.5kW and 109.2kW respectively with electromagnetic efficiency of 97.56% at rated operation. Average steady-state core losses and copper losses for Model2 are 16.7kW and 104.9kW respectively with electromagnetic efficiency of 97.63% at rated operation. All machines are operating at the temperature of 120°C. With lower copper losses, the HESMs are more efficient that the BLSM.

Only a three-dimensional (3D) FEA can yield accurate results for eddy currents losses on the PMs. However, this is computationally expensive. To limit eddy currents losses on the surface of the rotor of the HESMs, segmented permanent magnets should be employed.

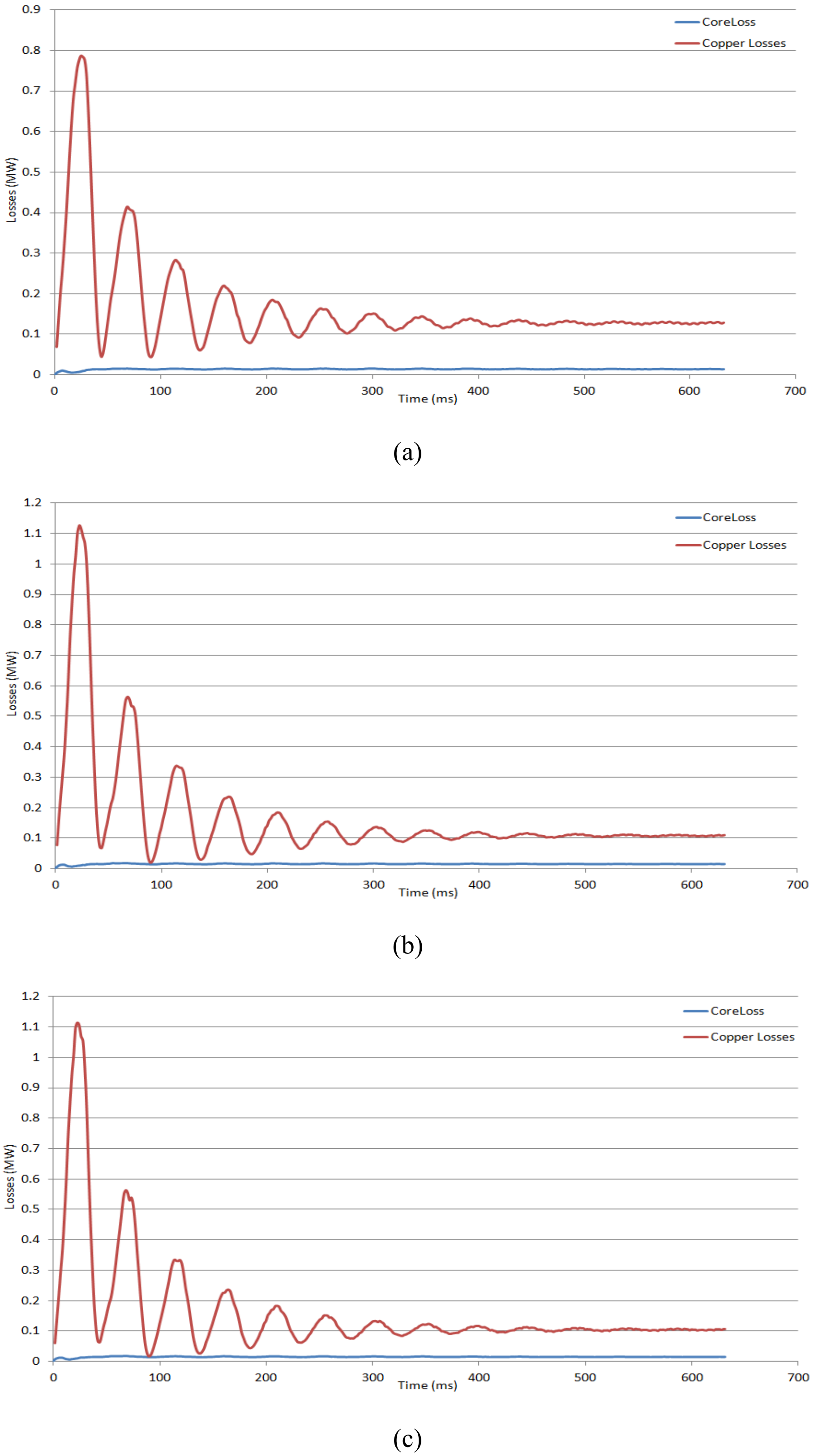

Figure 5-5 Losses of (a) BLSM, (b) Model1, (c) Model2 machines at rated load

5.3 Armature reaction

Most synchronous motors are designed to operate at unity power factor [96]. At unity power factor, the cross-magnetizing effect on the air-gap flux is at its strongest. The leading edge of the pole will be partly-magnetized and its trailing edge partly-demagnetized. Due to this effect, the machine will incur a net loss of flux.

Since throughout most of its lifespan, the azimuthing podded propulsor rotates in a preferred direction, armature reaction mitigation designs can be employed. The effectiveness of the armature compensation can be optimized for an operating range. For this study, the mesh sizes of the FEM models are kept identical. They are operated at rated unity power factor.

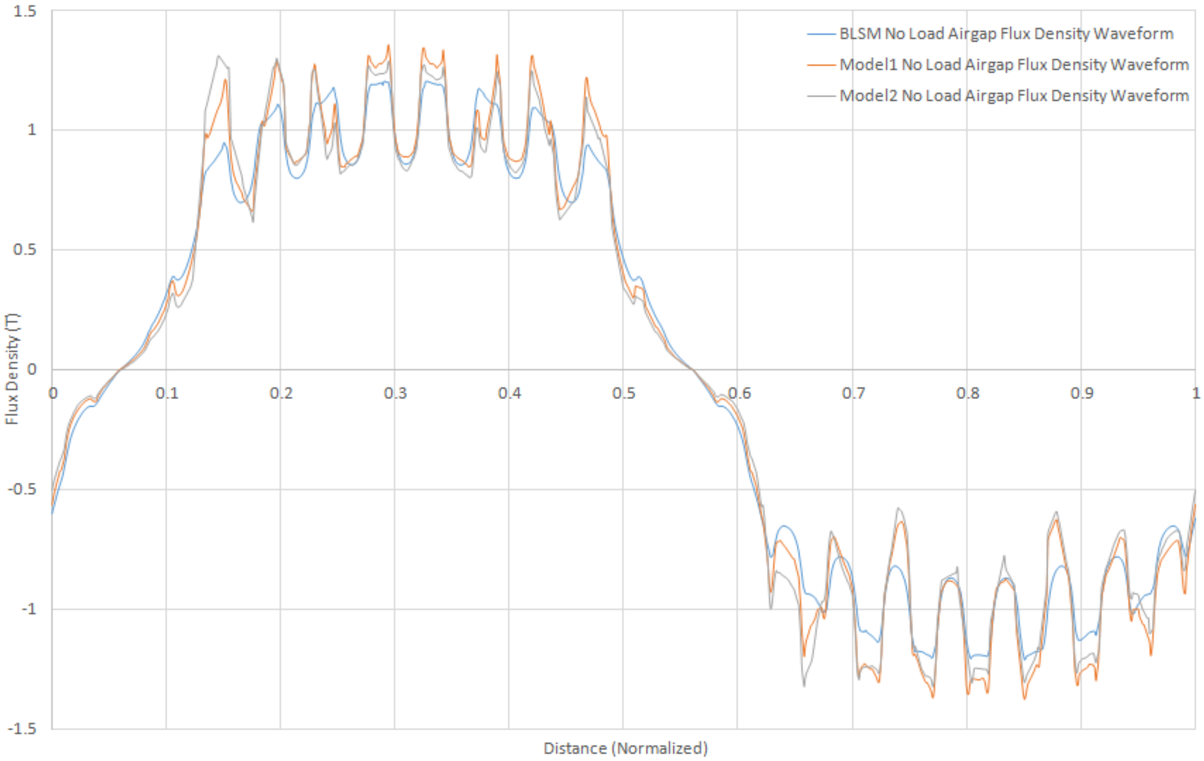

Figure 5-6 Air-gap flux densities of BLSM and HESMs at no-load operation

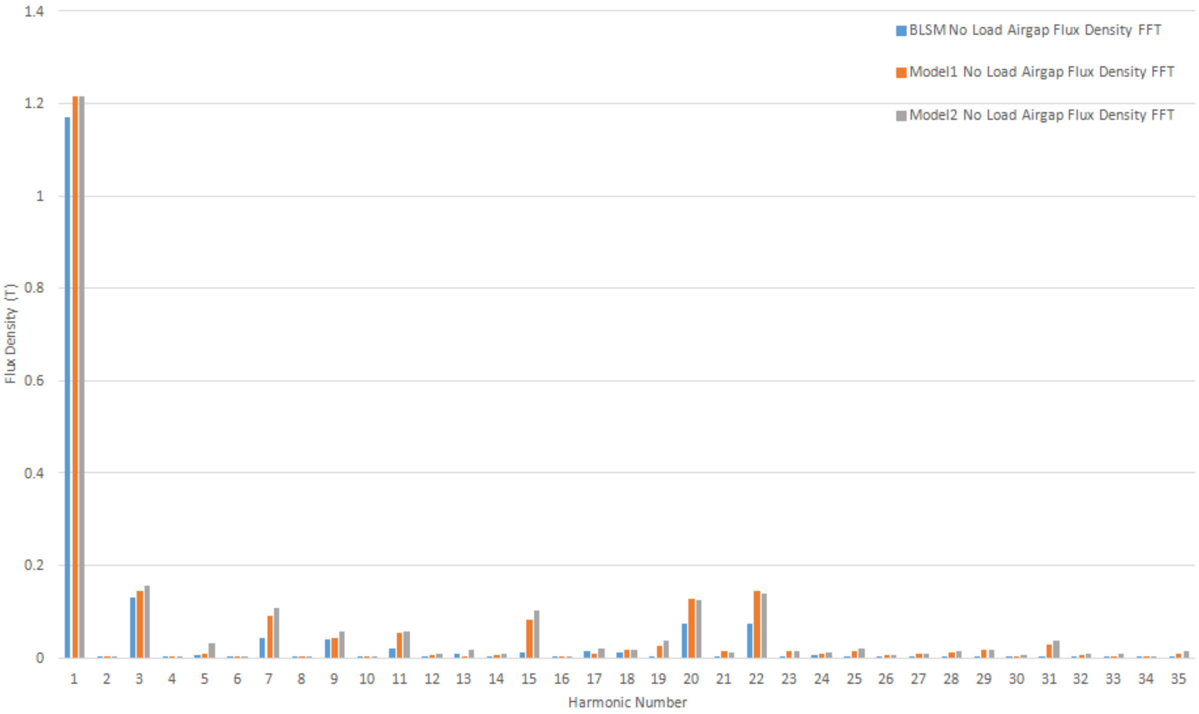

Figure 5-7 Air-gap flux harmonics of BLSM and HESMs at no-load operation

Figures 5-6 and 5-7 show the comparison of air-gap flux densities of the machines and their harmonics at no-load operation respectively. It can be observed that the BLSM produces the most sinusoidal air-gap flux waveform. Model2 machine has the least sinusoidal air-gap flux waveform due to uneven asymmetrical PM distribution on its rotor. Odd air-gap flux harmonics are more pronounced in the HESMs. The 20th and 22th harmonics are slot harmonics. Both Model1 and Model2 have higher air-gap flux densities than BLSM.

Figures 5-8 and 5-9 show the comparison of air-gap flux densities and their harmonic analyses of the machines at rated operation respectively. It can be observed that the air-gap flux waveforms of the machines are distorted due to the effect of armature reaction. The trailing edge of the Model2 machine has a higher flux density compared to the others due to increased PMs situated on the rotor pole of the trailing edge.

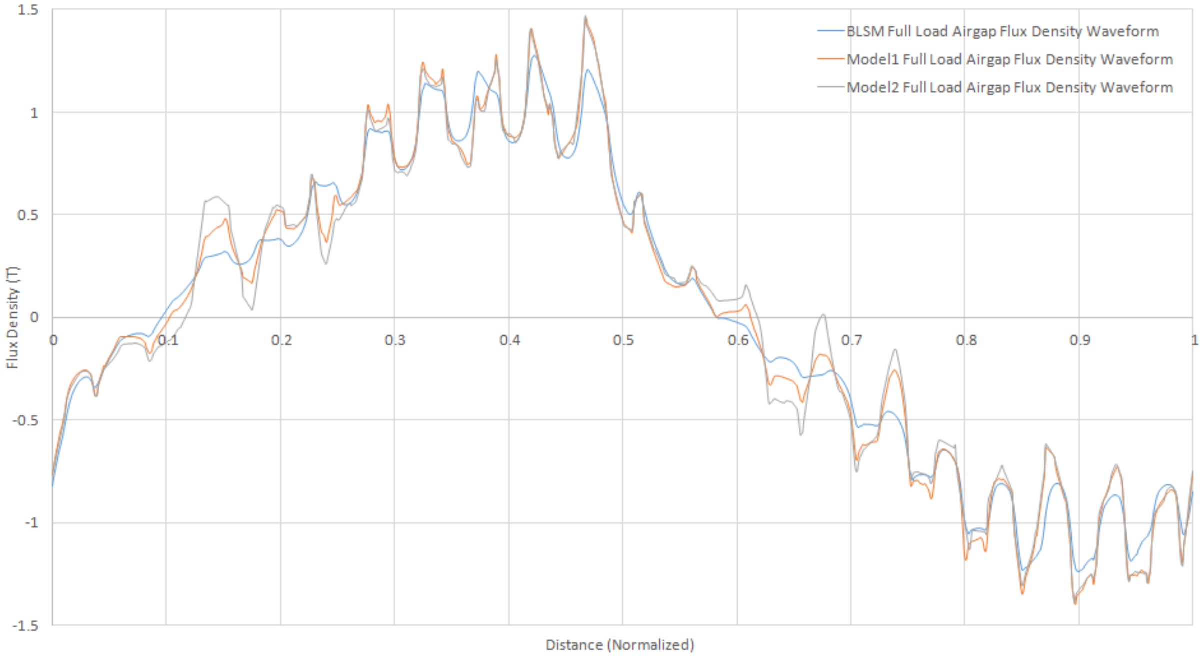

Figure 5-8 Air-gap flux densities of BLSM and HESMs at rated operation

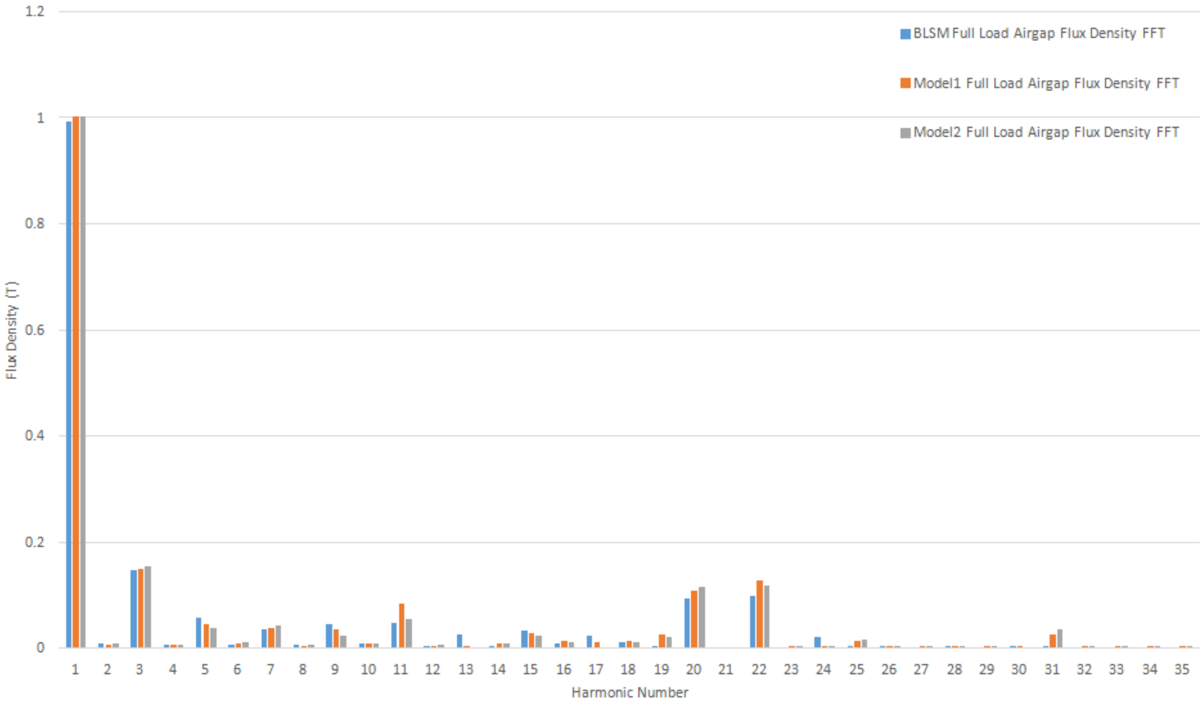

Figure 5-9 Air-gap flux harmonics of BLSM and HESMs at rated operation

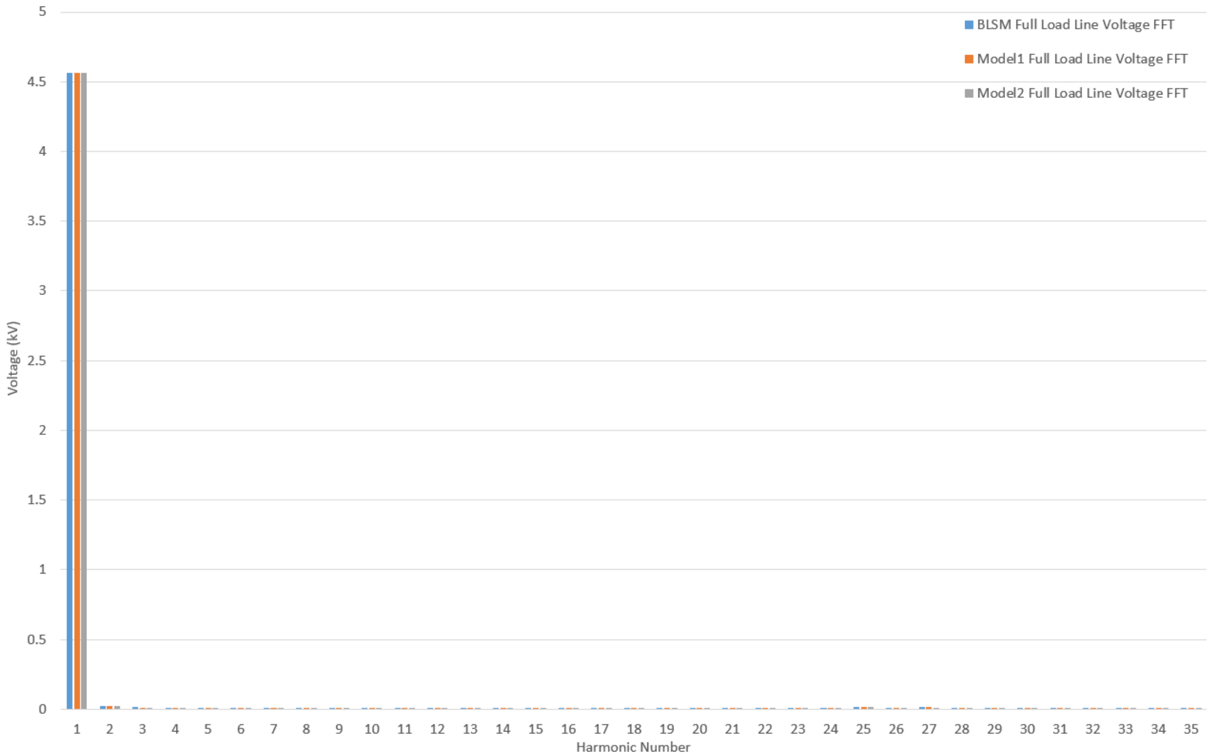

Figure 5-10 Line back-EMF harmonics of BLSM and HESMs at rated operation

Table 5-1 Line back-EMF THDs of BLSM and HESMs for no-load and full-load operations

Electrical Machine	BLSM	Model1	Model2
No-Load Line-line Back EMF THD (%)	0.73912	0.95599	1.01244
Full-Load Line-line Back EMF THD (%)	0.91306	0.82570	0.81209

Figure 5-10 shows the full-load line back-EMF harmonics of the machines. Table 5-1 shows their line back-EMF THDs for both no-load and full-load operations. At no-load operation, the HESMs line back-EMFs have a higher percentage of THDs compared to BLSM. However, they perform better than the BLSM at full-load operation. Model2 produce a slightly more sinusoidal back-EMF voltage waveform than Model1. Bi-directional rotation operation is possible for Model2 machine. However, in the ‘reverse’ rotation it develops less torque for a similar excitation. This is because the now leading edge of the pole has more permanent magnet excitation. This entails magnetic saturation and enlarges the effects of armature reaction.

5.4 Determination of direct and quadrature synchronous reactance

In a synchronous motor, a large value of synchronous reactance entails excessive change of power factor with load and a limited pull-out torque [60]. A lower synchronous reactance implies a larger effective air-gap and thus the increase of number of ampere-turns required to be produced by the field windings.

The d-axis and q-axis synchronous reactances, X_d and X_q, can be found from a slip test. The machine is driven by a motor with the field winding open-circuited, and a normal positive sequence voltage is applied to the stator. In the simulation, the slip is very small such that damper currents will not produce an appreciable error.

Figure 5-11 shows the armature line voltage and line current waveforms, while Figure 5-12 shows the induced field winding EMF waveform of the BLSM. When armature MMF is aligned with the d-axis, the voltage across the open field is zero which identifies the X_d of the machine. Similarly, X_q is identified with the voltage maximum in the field. They can be found by the following equations [64]

$$X_d = \frac{V_{(at\ I_{ph(\mathrm{min})})}}{\sqrt{3}I_{ph(\mathrm{min})}} \tag{5.1}$$

$$X_q = \frac{V_{(at\ I_{ph(\mathrm{max})})}}{\sqrt{3}I_{ph(\mathrm{max})}} \tag{5.2}$$

The reactances of HESMs are found in a similar manner. Table 5-2 below shows the per unit values of the d and q-axis synchronous reactances. The synchronous reactances of the machines are a basis for performance comparison. As seen, their values are comparable.

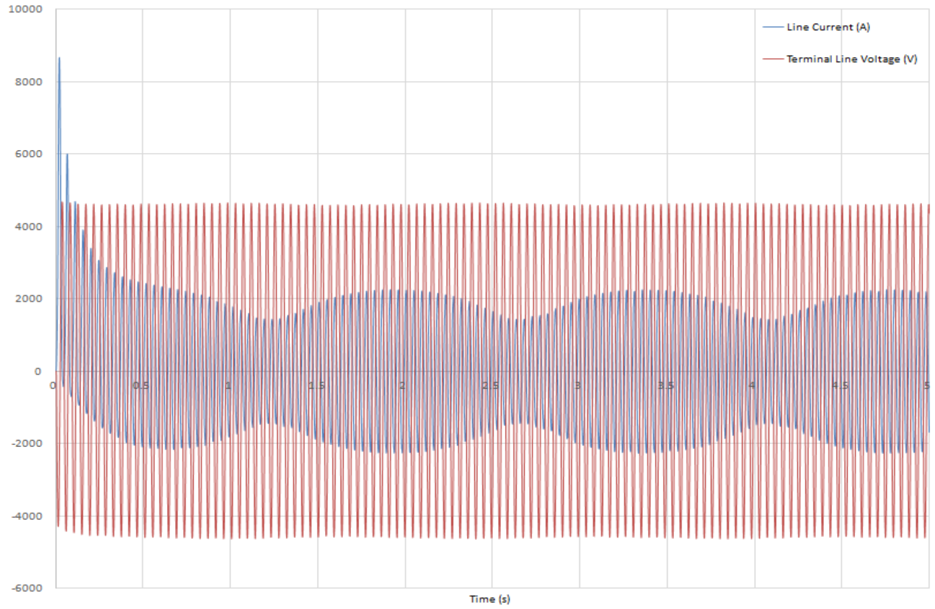

Figure 5-11 Terminal line voltage (red) and current (blue) of BLSM

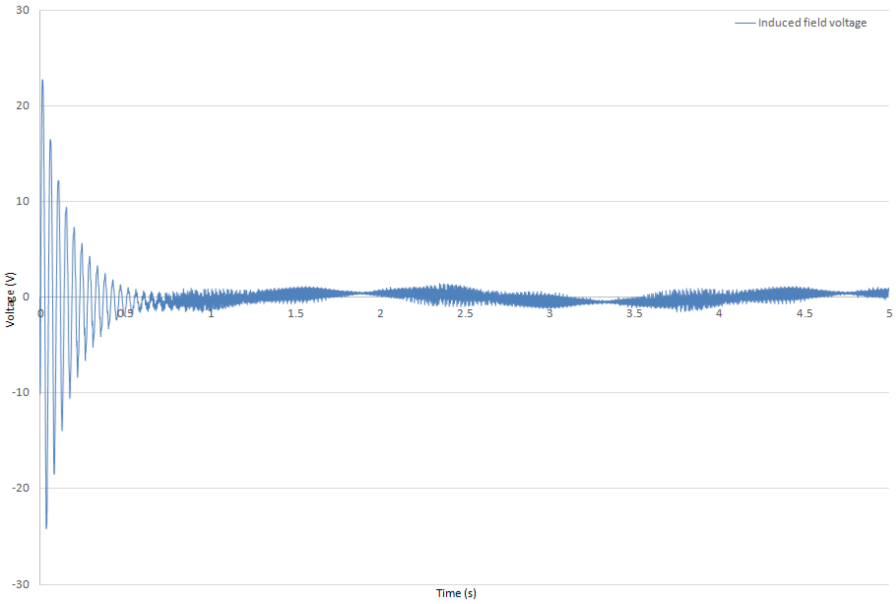

Figure 5-12 EMF induced in the field winding of BLSM

Table 5-2 Direct and quadrature synchronous reactance of the electrical machines

Reactance / Machine	X_d (p.u.)	X_q (p.u.)
BLSM	0.985	0.619
Model1	1	0.628
Model2	0.994	0.618

5.5 V-curves

Figure 5-13 shows the V-curves of the three machines at 10%, 50% and 100% of rated loadings. Each curve has a range of 0.8 lagging to 0.8 leading power factor. The points on the curves with lowest armature current correspond to unity power factor operation point. Due to the PMs, the HESMs require a lower field excitation to deliver the same amount of load torque. At rated load operation with unity power factor, the PM excitation contributes to 33.33% of the rotor flux for Model1 machine and 39.6% for Model2 machine.

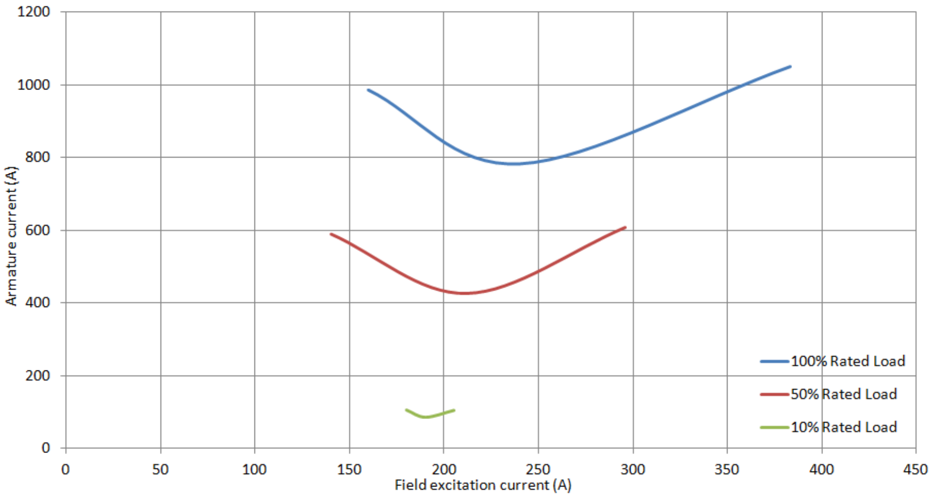

(a)

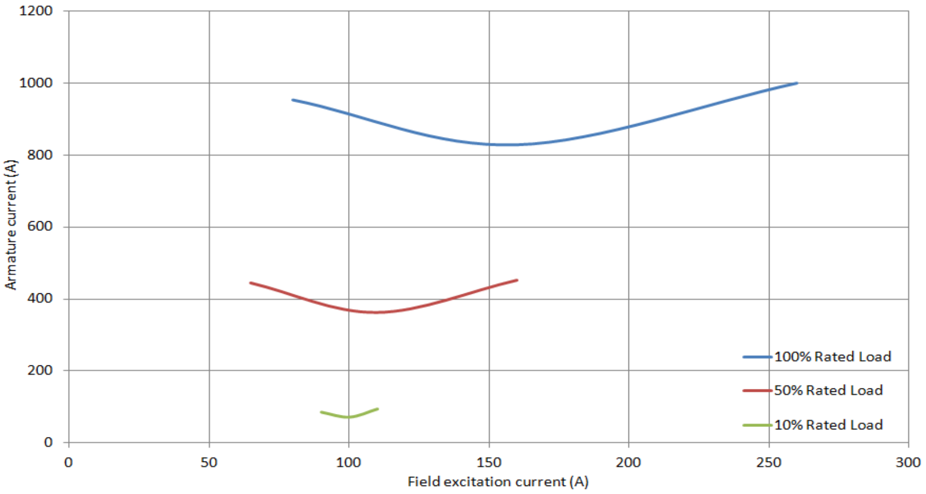

(b)

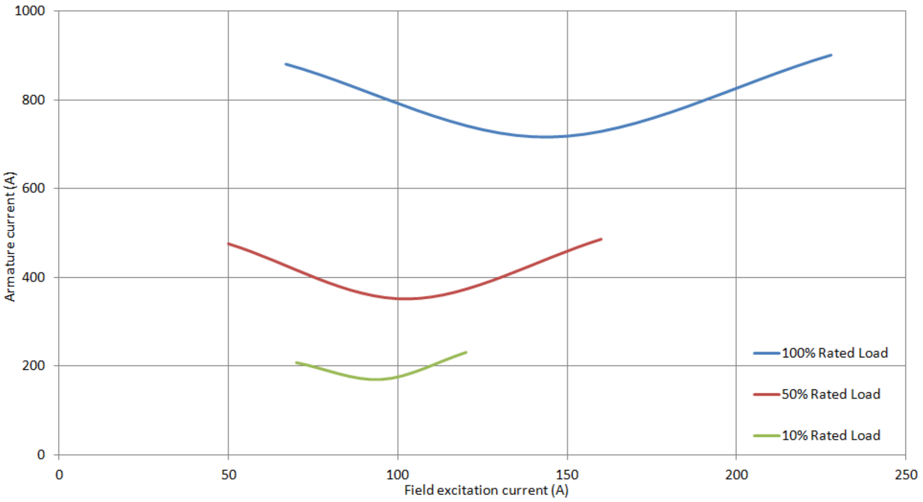

(c)

Figure 5-13 V-curves of (a) BLSM, (b) Model1, and (c) Model2 machines

5.6 Torque performances

The torque speed capability curves in Figure 5-14 show that the machines have the capability to deliver the required load torque up to the rated speed of 190 rpm and operate to the maximum speed of 210 rpm at the constant power region.

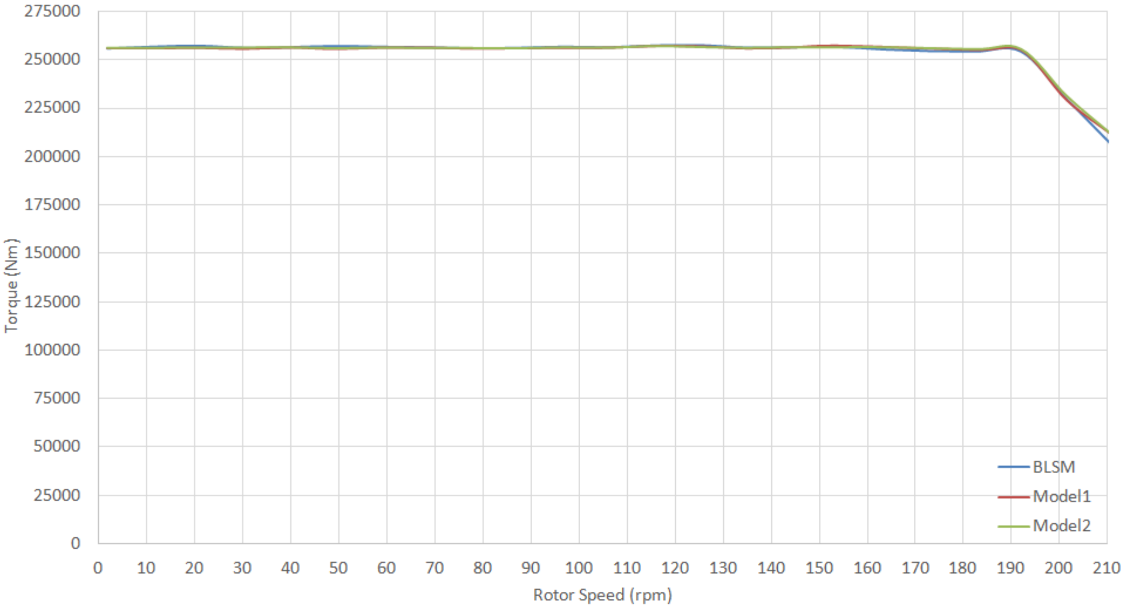

Figure 5-14 Torque speed characteristics of the motors

Figure 5-15 shows the acceleration of the machines from stationary to rated speed. Rated armature voltages and frequency are applied at starting. Starting torque is achieved using damper windings. The machines are run up to 95 % rated speed before field windings are excited. The actual machines are started using power electronics which may offer more control and gradual speed increment. As seen, the HESMs have a higher accelerating speed than the BLSM.

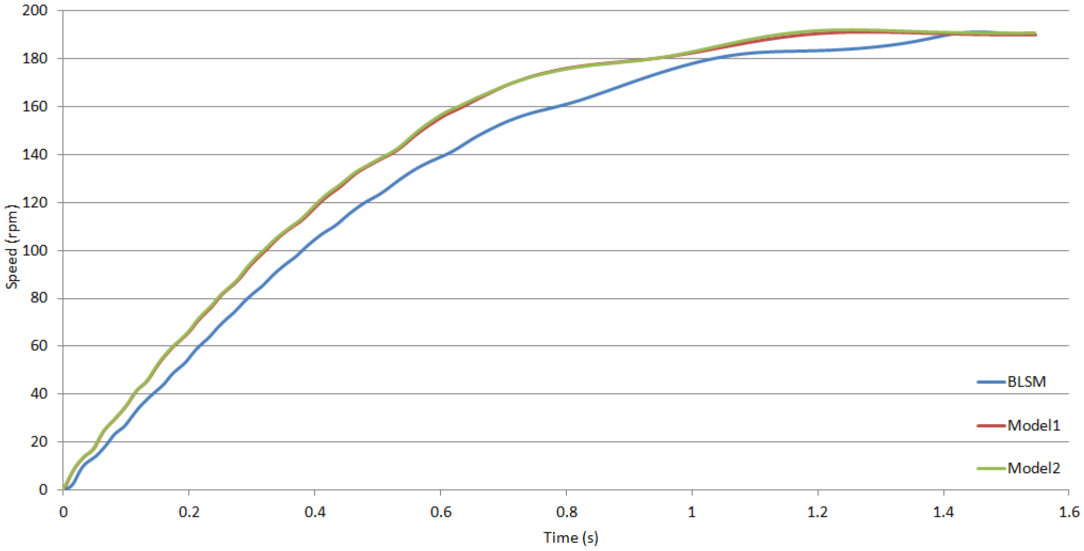

Figure 5-15 Acceleration of the machines from stationary to rated speed

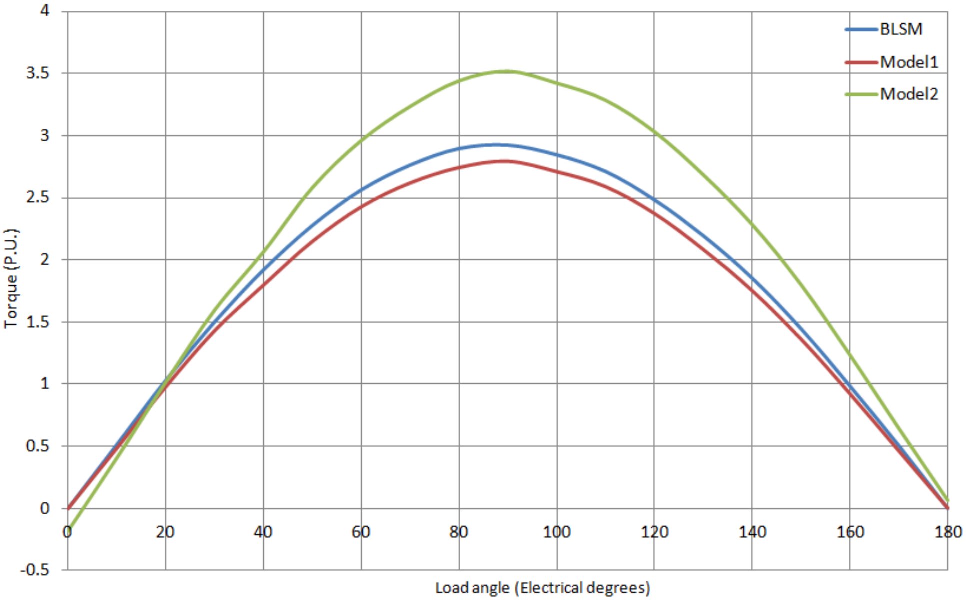

Figure 5-16 Output torque vs. load angle

Output torque is plotted against load angle for each of the three machines as shown in Figure 5-16. Rated operation is achieved at unity per unit output torque. As seen from the results, Model2 machine has a significantly higher peak torque. Thus, it has a higher pull-out torque than the other machines. However, the direction of its resultant field slights a little away from the direct-axis of the pole construction compared to the other machines.

5.7 Thermal analysis

Heat removal is a very important aspect in electrical machine design. Temperature rise in the machine determines its ability to operate constantly under various conditions. Electrical machines comprise of different classes of insulations catering to different temperatures. If overheating occurs, insulations will breakdown leading to short-circuit faults and damages to the machine. Dissipation of heat occurs in three modes: Conduction, convection and radiation. The cooling system must be designed to keep the temperature in the machine below the maximum allowable temperature at the operating conditions.

5.7.1 BLSM thermal modelling

Motor-CAD software is used to solve for the steady-state temperature of the BLSM at rated load operation. The losses in different parts of the machine are calculated using the Ansys-Maxwell 2D and imported into Motor-CAD. Copper losses are calculated at 120°C. According to ISO 3046-1, maximum ambient air temperature in pod and sea-water temperature are taken as 45°C and 32°C respectively [97]. Outer stator temperature can be assumed to maintain at a stable temperature due to the infinite volume of sea water.

The cooling effect reacts as a function of power. They increase with the ship's speed. Air in the pod is pressurized to keep water from entering the pod in the event of a sealing problem. For constant rated operation, the minimum required volume of air through air-gap and its velocity in the machine are found to be $14m^3/s$ and113m/s respectively. Figure 5-17 shows steady-state temperatures in the BLSM at rated operation in the radial direction and axial direction.

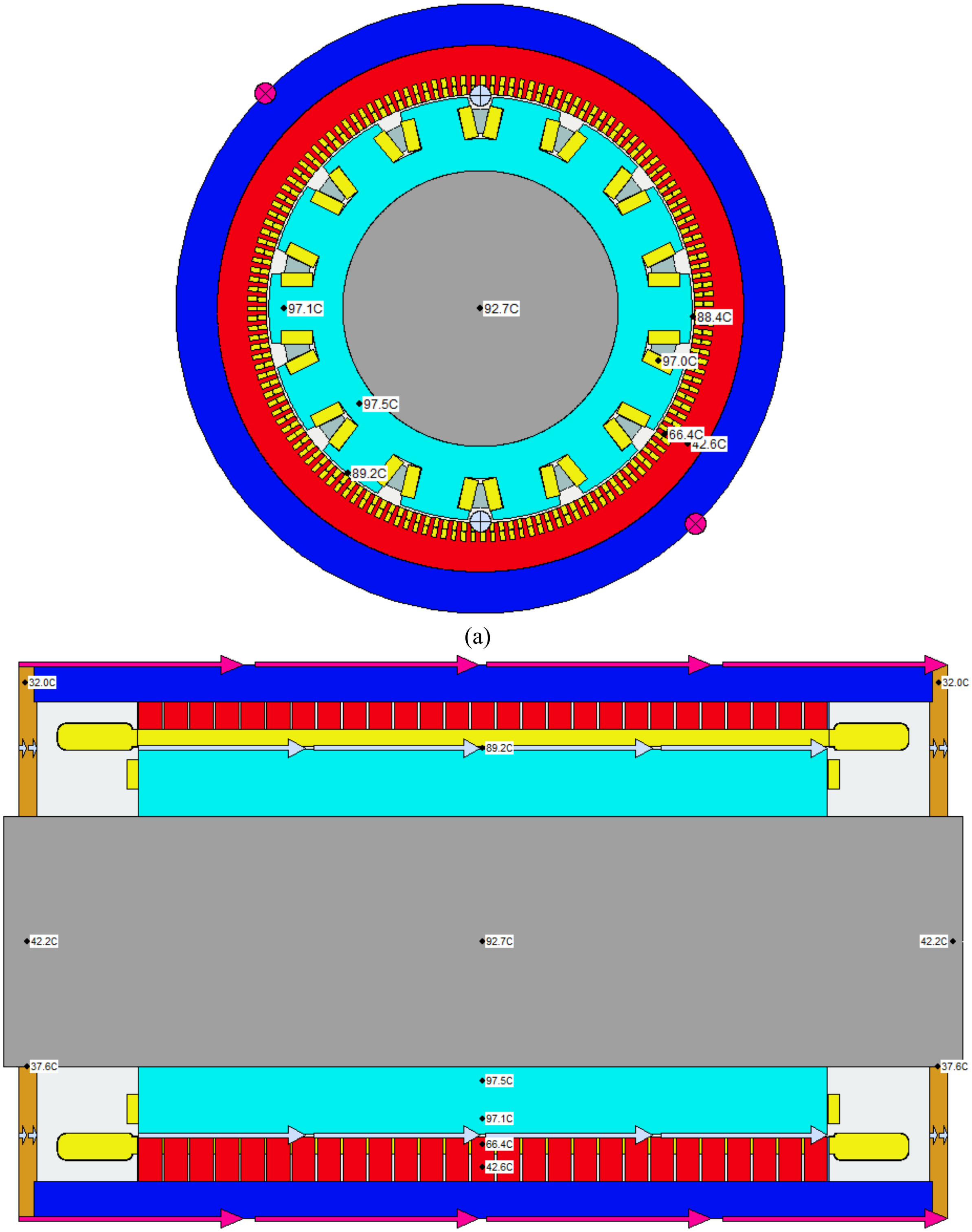

(a)

(b)

Figure 5-17 Steady-state temperatures in the BLSM at rated operation in the (a) radial direction and (b) axial direction

5.7.2 HESM thermal modelling

NdFeB magnets are sensitive to temperature change. When the temperature of the magnet increases, its magnetic properties decline. Therefore, care must be taken to ensure that the rotor temperature be maintained within allowable temperature.

Due to MotorCAD software being limited to only standard machine topologies, it is not possible to create models of the HESMs. Although more accurate results can be obtained from FEA and computational fluid dynamics (CFD), they are too computationally expensive. Therefore, simplified 2D lumped-parameter based thermal models are used to compare temperature rise of BLSM and HESMs.

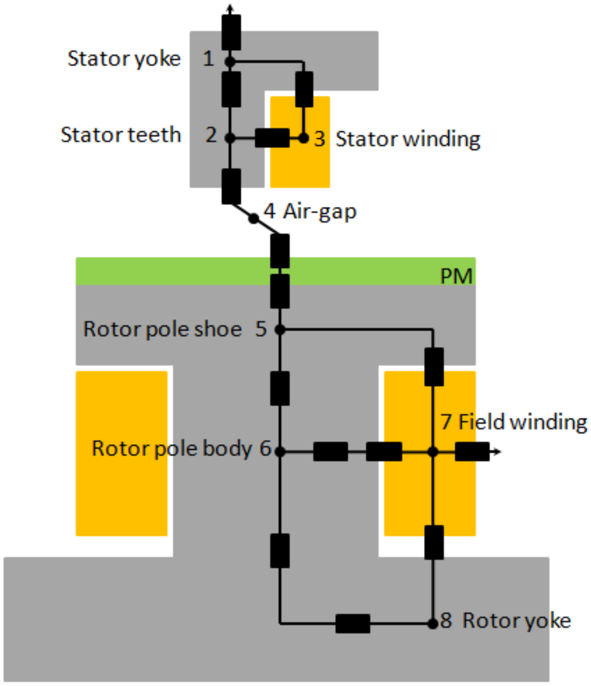

Figure 5-18 Simplified thermal resistance network of the HESM in its radial direction

A simplified thermal resistance network of HESM is shown in Figure 5-18. Major machine components are represented with thermal resistances and are connected with nodes. Geometric symmetry is employed. Windings losses are considered to be uniformly distributed. Iron losses are placed mainly in the stator teeth, yokes and pole. Due to the lamination on the electric steel sheets, heat conductivity is significantly higher in the radial direction than in the axial direction [98]. Therefore, heat flow is only considered in the radial direction.

The conduction and convection thermal resistances, R_{cd} and R_{cv} respectively, are given as [65]

$$R_{cd} = \frac{l_h}{\lambda_h A_h} \tag{5.3}$$

$$R_{cv} = \frac{1}{\alpha_h A_h} \tag{5.4}$$

where l_h is the length of body in the heat flow direction, λ_h is the thermal conductivity, α_h is the convection coefficient, and A_h is the cross-sectional area of body.

For steady-state analysis, the temperature rise for each node relative to the reference temperature is calculated with the matrix equation [98]

$$\mathbf{\Delta T} = \mathbf{G}^{-1}\mathbf{P} \tag{5.5}$$

where **P** is the vector containing the power losses in each node, $\mathbf{\Delta T}$ is the temperature rise vector, and **G** is a thermal conductance square matrix given as

$$\mathbf{G} = \begin{bmatrix} \sum_{i=1}^{n} \frac{1}{R_{1,i}} & -\frac{1}{R_{1,2}} & \cdots & -\frac{1}{R_{1,n}} \\ -\frac{1}{R_{2,1}} & \sum_{i=1}^{n} \frac{1}{R_{2,i}} & \cdots & -\frac{1}{R_{2,n}} \\ \vdots & \vdots & \ddots & \vdots \\ -\frac{1}{R_{n,1}} & -\frac{1}{R_{n,2}} & \cdots & \sum_{i=1}^{n} \frac{1}{R_{n,i}} \end{bmatrix} \tag{5.6}$$

where $R_{n,n}$ is the thermal resistance of different parts of the machine. The nth diagonal element is the sum of the network conductances connected to node n, and the non-diagonal elements are conductances between nodes.

Determining convection coefficients at different locations of the machine are very demanding due to the fluid velocity, surface properties and complex geometry. Thus, the accurate calculation of convection heat transfer is a complicated task. This would require 3D computational fluid dynamics and expertise in the field of fluid dynamics. Empirical coefficients for large slow rotating synchronous machines in References [62] & [65] are used. The temperature rise of the BLSM in its stator and rotor are 15.78°C and 69.34°C respectively. In comparison, those of the Model1 HESM are 15.67°C and 68.61°C respectively. For the Model2 HESM, temperature rise in the stator and rotor are 15.62°C and 67.73°C respectively.

This section shows that regardless of the lower thermal conductivity of the NdFeB magnets, the temperature rise in HESMs are within acceptable limits and are generally lower than the BLSM. Higher airflow rate can be administered to further improve the cooling of the machine. Due to the complexity of the thermal problem, detailed analysis should be done in a separate study.

5.8 Radial pressure and mode frequency

5.8.1 Radial pressure

The radial electromagnetic force of an electrical machine causes objectionable radial vibration and unbalanced pull on the stator structure. The stress caused by the force is known as radial pressure. Radial pressure causes deformations on the stator core known as mode shapes, which are functions of machine geometry, configuration, and material properties [100]. Each mode shape has its own natural mode frequency. High noise and vibrations will result when these natural mode frequencies coincide with any of the harmonics of the magnetic radial force.

The radial pressure distribution and its frequency contents are dependent on stator excitation. In theory, balanced stator windings should not exert any radial force on the stator structure [99]. According to the Maxwell stress tensor, the radial and the tangential components of the magnetic forces per unit area, F_{rad} and F_{tan} respectively, at any point of the air-gap is [100]

$$F_{rad} = \frac{B_{rad}^2 - B_{tan}^2}{2\mu_0} \tag{5.7}$$

$$F_{tan} = \frac{B_{rad}B_{tan}}{\mu_0} \tag{5.8}$$

where B_{rad} is the radial flux density and B_{tan} is the tangential flux density.

Figures 5-19(a), 5-20(b), and 5-21(a) show the radial pressure distributions on the stator structure and their fast Fourier transform (FFT) analyses which identifies the mode orders of the BLSM, Model1 and Model2 machines respectively. The prominent orders are 7, 14, 21, 28 and so on. It also show the change of their magnitudes from no-load to full-load operation. Figure 5-19(b) shows the change of lower order mode from fourteenth to seventh as the condition is changed from no-load to full-load in the BLSM. Figures 5-20(b) and 5-21(b) show that for the Model1 and Model2 machines, their dominant seventh-order modes are reduced under full-load.

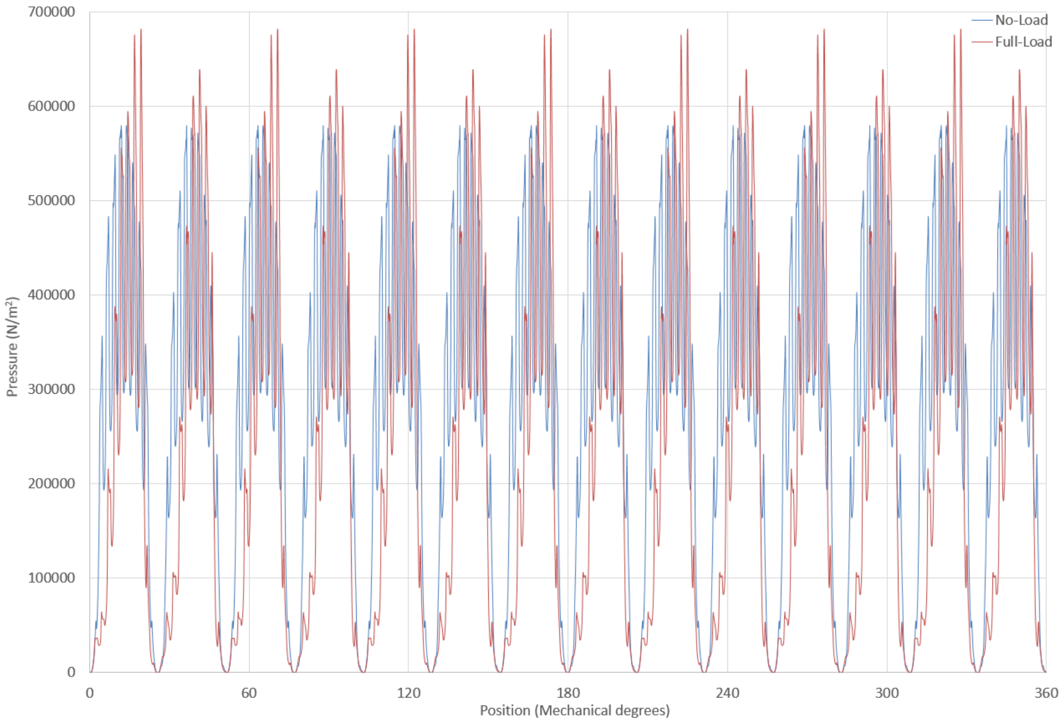

(a)

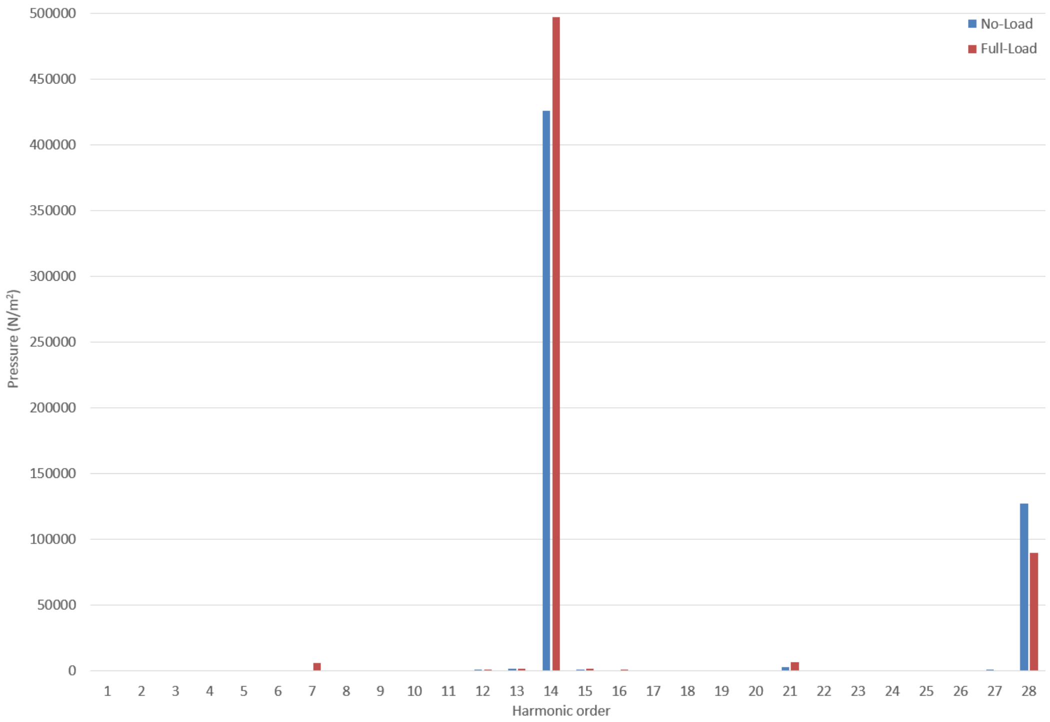

(b)

Figure 5-19 Radial pressure distributions of BLSM and their FFT analyses

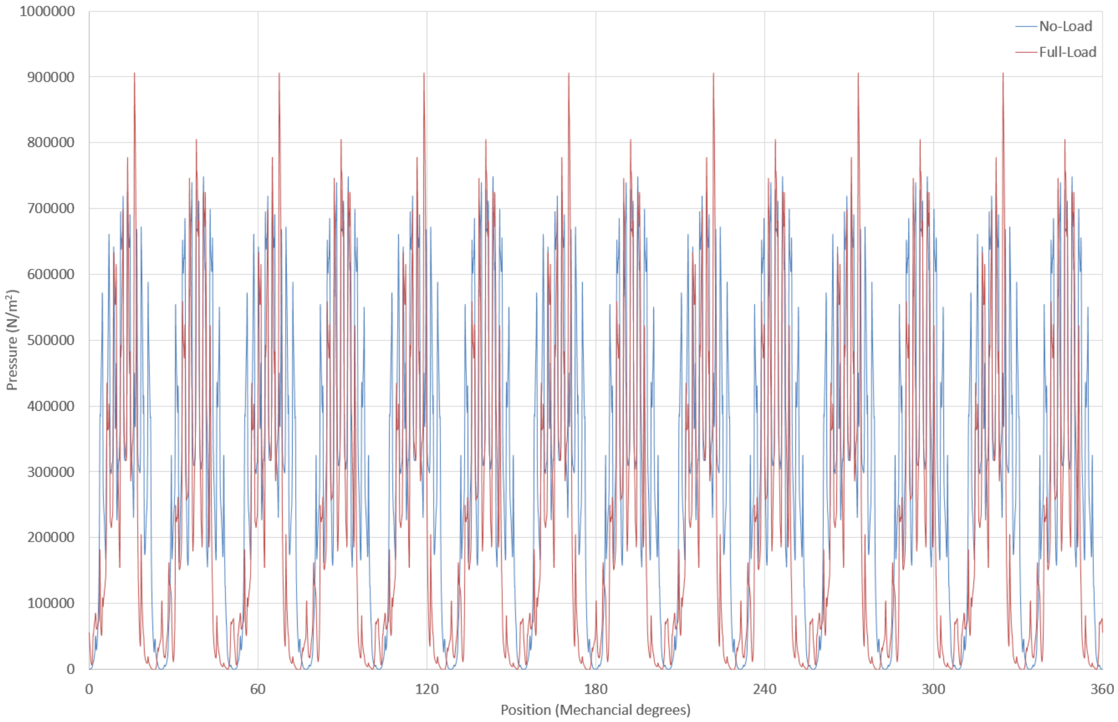

(a)

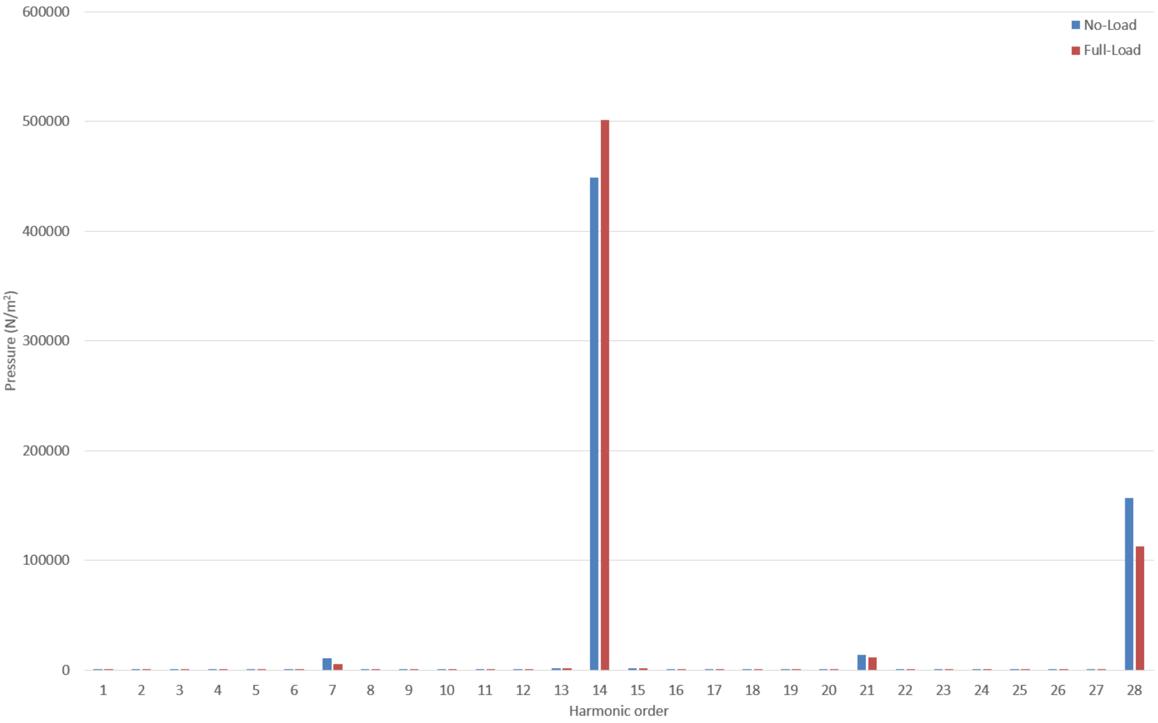

(b)

Figure 5-20 Radial pressure distributions of Model1 machine and their FFT analyses

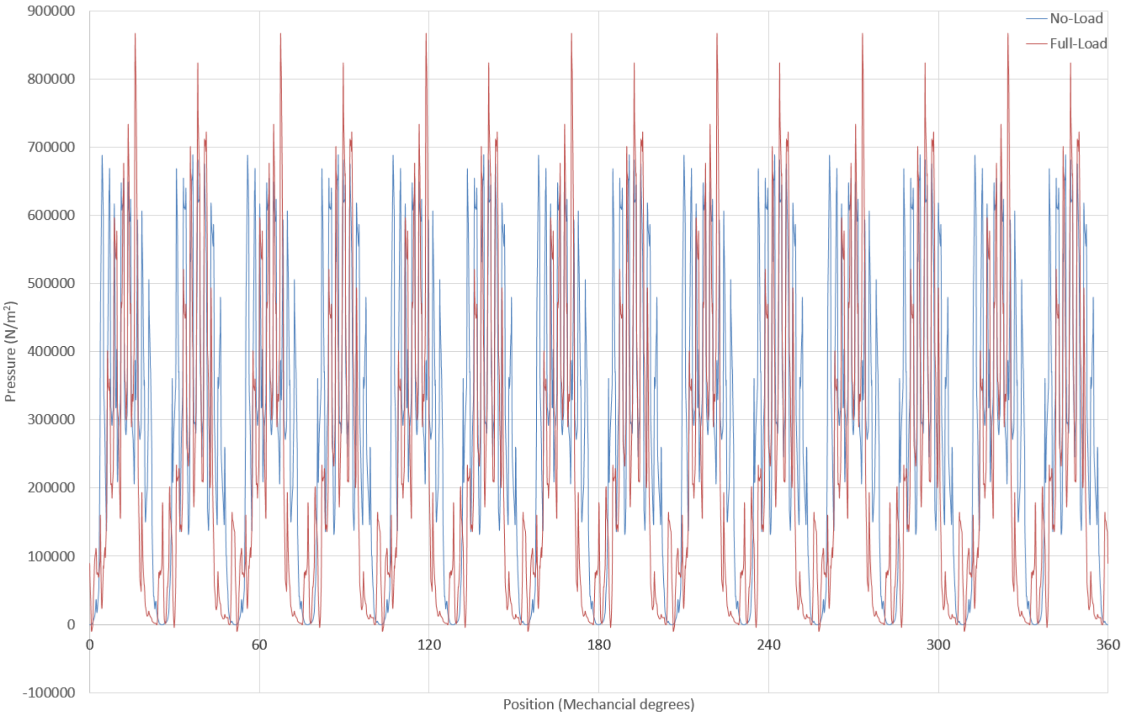

(a)

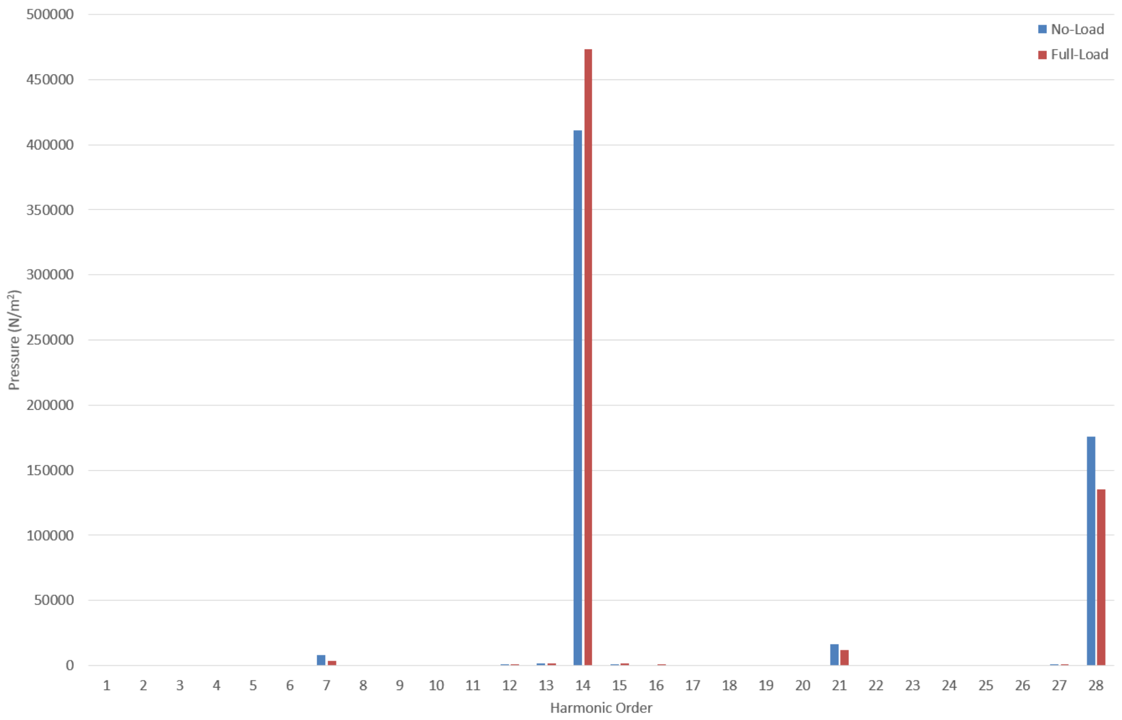

(b)

Figure 5-21 Radial pressure distributions of Model2 machine and their FFT analyses

5.8.2 Natural mode frequency

The calculation of zero mode frequencies is given by [100]

$$f_{(z=0)} = \frac{1}{2\pi r_y}\sqrt{\frac{\in}{\rho_s \Delta}} \tag{5.9}$$

where z is the mode number, r_y is the mean radius of stator yoke, $\in$ is the Young's modulus of elasticity of stator material, $\rho_s$is the density of the material, and

$$\Delta = 1 + \frac{W_t}{W_y} \tag{5.10}$$

where W_y is the weight of stator yoke and W_t is the total weight of the stator comprised of teeth, windings and insulation weights.

The calculation of mode frequencies for mode 2 and higher are given by [99]

$$f_{(z\geq 2)} = \frac{f_{(z=0)} z(z^2-1)i}{\sqrt{\left\{(z^2+1)+i^2\,(z^2-1)(4z^2+{}^{z^2\Delta_z}/_{\Delta}+3)\right\}}} \tag{5.11}$$

where

$$\Delta_z = 1 + \frac{1.91 A_{sp} h_{slot}^3\, W_t\, S}{r_y\, L\, h_{ys}^3 W_p}\left[\frac{1}{3}+\frac{h_{ys}}{2h_{slot}}+\left(\frac{h_{ys}}{2h_{slot}}\right)^2\right] \tag{5.12}$$

and

$$i = \frac{h_{ys}}{2\sqrt{3}r_y} \tag{5.13}$$

where A_{sp} is the stator pole area, and W_p is the weight of stator teeth.

The three of the machine have similar stator and pole numbers and thus have similar mode frequencies. Table 5-3 shows that the low mode frequency is very high compared to the excitation frequency (22.167Hz) and its harmonics at the machines' rated speed. Therefore, the inverter-driven machines are not susceptible to resonance under normal operation.

Table 5-3 Low mode number and frequency

Mode Number	Mode Frequency (Hz)
7	1672.1

5.9 Economic feasibility of HESMs

Although the HESMs are more energy efficient than the BLSM, in order to be competitive in the market, they have to be economically attractive. A simplified economic analysis is carried out to find out the economic viability of the HESMs.

Figure 5-22 shows the calculated weight of the machines and the contribution of their respective active parts. The HESMs have slightly lower overall masses (~2.5% and ~3% mass reduction for Model1 & Model2 machines respectively) than the BLSM with almost 36% reduction in the field copper usage. Torque density of the HESMs are increased by using PMs.

The price of the materials per kg (in USD) in Year 2015 is $180/kg (average cost) for NdFeB magnets, $9/kg for copper wires, $2.5/kg silicon steel laminations, and $ 7/kg for copper bars [101][102]. Figure 5-23 shows the cost of the machines and the contribution of their respective active parts. The costs of the HESMs are significantly higher (~31% & ~40% for Model1 & Model 2 machines respectively) than the BLSM due to the high cost of PM materials. Miscellaneous machine parts are assumed 15% of the total cost of the other parts of BLSM.

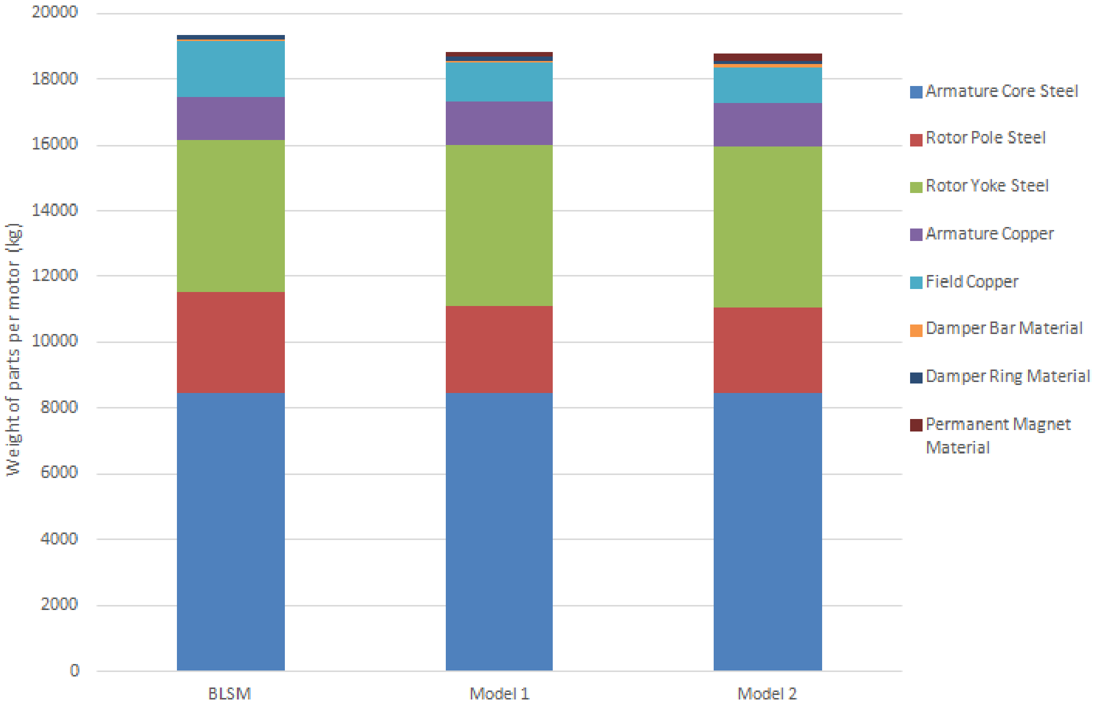

Figure 5-22 Weights of the active parts of the machines

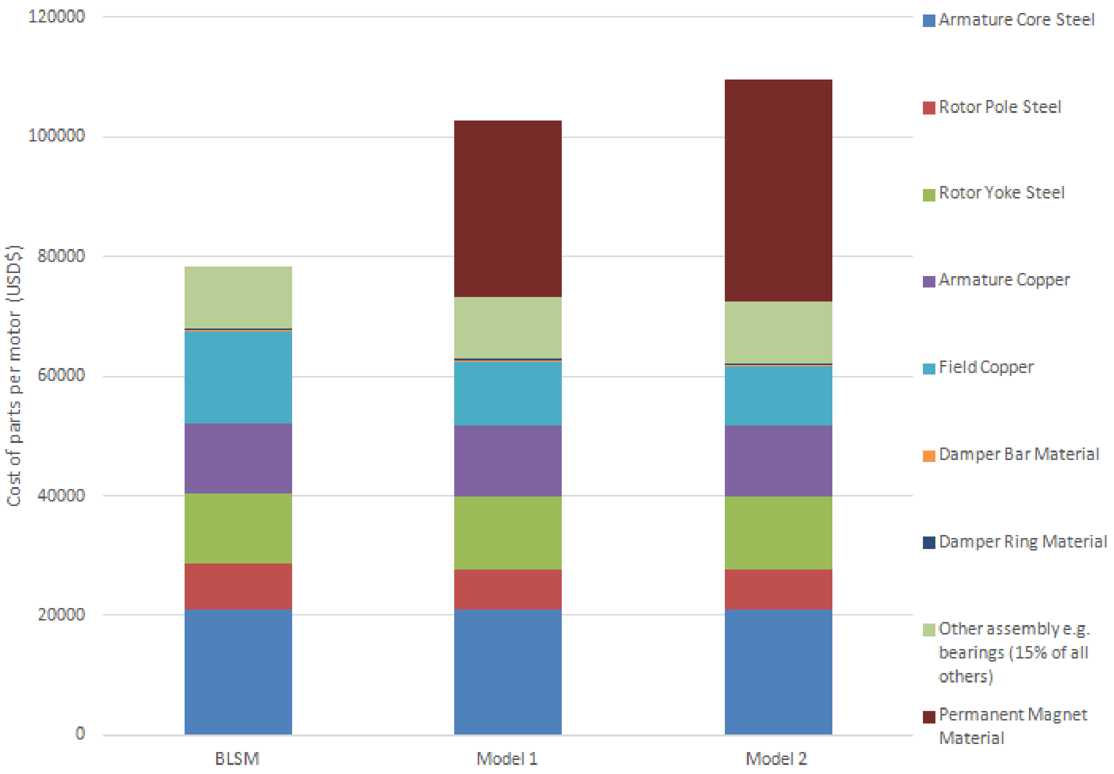

Figure 5-23 Costs of the active parts of the machines

Assuming labor cost is 40% of total hardware cost, labor overhead is 40% of labor cost, and a manufacturer overhead and profit factor of 1.29. Manufacturer component cost is calculated by

$$Manufacturer\ Component\ Cost\ (USD\$) = Overhead\ \&\ profit\ factor$$

$$\times\ (Total\ hardware\ cost + Labour\ Cost + Labour\ Overhead) \qquad (5.14)$$

The manufacturer component costs and their cost difference with respect to BLSM are shown Table 5-4 below.

Table 5-4 Manufacturer component cost and the cost difference comparison of the machines

Cost (USD$) / **Machines**	**BLSM**	**Model 1**	**Model 2**
Manufacturer Component Cost	157405.2	206768	220529.7
Cost difference w.r.t BLSM	0	49362.76	63124.51

Annual operating cost (including maintenance cost of 10% of electricity cost) on marine vessels can be estimated by

$$Annual\ Operating\ Cost\ (USD\$) =$$

$$Electricity\ Cost\ on\ Vessel\ \times\ Energy\ Consumption\ per\ year \tag{5.15}$$

where

$$Energy\ Consumption\ per\ year\ (kWh) =$$

$$Motor\ Power\ Consumption\ \times Hours\ of\ Operation\ per\ year \tag{5.16}$$

where

$$Motor\ Power\ Consumption\ (kW) = \frac{Rated\ machine\ output\ power}{\eta} \tag{5.17}$$

Assuming marine vessel electricity cost USD\$(0.11 to 0.385)/kWh depending on the type of fuel and efficiency of the electrical generation system. Given a marine vessel operates an average of 300 days a year, 24 hours a day, the additional payback period in years for using HESMs can be calculated by

$$Addition\ Payback\ Period\ (Years) \tag{5.18}$$

$$= \frac{Manufacturer\ Component\ Cost\ of\ HESM - Manufacturer\ Component\ Cost\ of\ BLSM}{Annual\ Operating\ Cost\ of\ BLSM - Annual\ Operating\ Cost\ of\ HESM}$$

Figure 5-24 shows the additional economic payback period analysis for HESMs compared to BLSM. It is apparent that the payback period can be greatly affected by the cost of electricity, ranging from 0.6 to 2.3 years, corresponding to highest and lowest electricity prices respectively. In comparison to the machine lifespan of at least 20 years, the extended break-even point (BEP) is a relatively short.

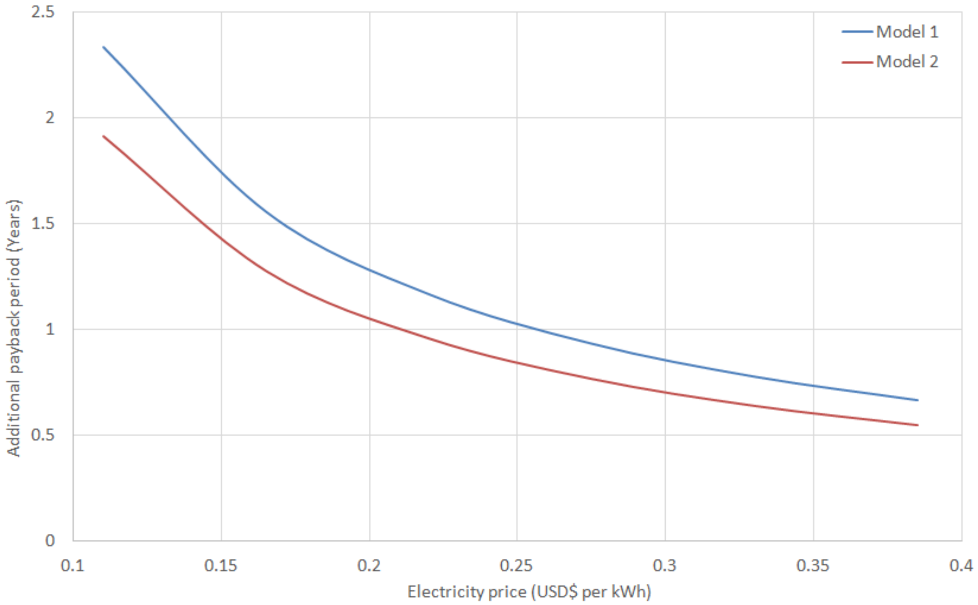

Figure 5-24 Additional economic payback period for HESMs compared to BLSM

5.10 Summary

The object of this chapter is to compare the performances between the BLSM and the HESMs. It is shown that machine characteristics of the HESMs such as torque, voltage, current, and synchronous reactance, are comparable to those of BLSM. The HESMs are able to operate at higher efficiencies.

The effect of armature reaction compensation has been demonstrated using FEA simulation in HESM Model2 machine. Its progressive air-gap on the salient poles is formed by using permanent magnets. They reduce the effect of cross-magnetization during loaded operation therefore creating a more sinusoidal air-gap flux. It is shown that the design improves the terminal voltage THD and operational efficiency. The progressive air-gap geometry can be catered to specific requirements.

V-curves show the required armature currents and field excitation currents to achieve the necessary power factor at a particular load. It can be seen that the HESMs require less field excitation than the BLSM at similar loadings.

Based on torque speed characteristics, all of the machines are able to deliver rated torque and speed. Above base speed, the machines operate at the constant power region. The machines achieve rated speed rapidly when starting with rated line voltage and frequency. As damper windings of the HESMs are closer to the stator, they accelerate faster than the BLSM. At rated operation, their load angles are comparable. Model2 machine is shown to have a higher pull-out torque than the other machines making it more stable under load shocks.

Thermal analysis using Motor-CAD software is performed only for BLSM as it has model templates only for established machine topologies. This serves as a guide for the results of thermal resistance networks of BLSM and HESMs. The thermal resistance networks were simplified and did not yield very accurate results. It was carried out mainly to compare the temperatures between BLSM and HESMs. Results show that the overall temperatures in the HESMs are lower than that of the BLSM. The temperature of the PMs lies in a safe region.

FFT analyses are performed on the radial pressure of the air-gap for no-load and full-load operations. The low mode frequency is significantly larger than the excitation frequency of the machines. Therefore, the risk of resonance during operation is low.

Economic feasibility of HESMs is performed with the BLSM taken as the benchmark machine. The HESMs is found to cost significantly higher (up to 40%) than the BLSM mainly due to the higher cost incurred due to NdFeB magnets. However, depending on the price of electricity, the additional payback period with respect to the BLSM can be up to 2.3 years. This is relatively short considering the HESMs are expected to have a lifespan of at least 20 years.

The HESMs have shown that they are able to deliver similar, if not better performances than the BLSM of a similar machine frame.

Chapter 6 – Test Machines and Experiment Results

6.1 Introduction

In this chapter, the effectiveness of the armature reaction compensation technique by situating permanent magnets on the demagnetizing edge of the rotor poles is investigated. This technique relates more prominently to the HESM Model2 machine design, although armature reaction compensation is also noticeable in the HESM Model1 machine.

As it would be unfeasible to test the concept in the actual sizes of the podded electrical machines, low-power proof-of-concept (POC) experimental tests were carried out. Since designing and fabricating a prototype machine would be both time-consuming and expensive, off-the-shelf wound field synchronous machines readily available in the market are selected. However, by using an off-the-shelf machine, the progressive magnet air-gap design of HESM Model2 machine was not possible to be implemented. This is due to the low permeability of the PM material (close to that of air). Reducing the height of the rotor pole shoes in order to install a layer of PM material will increase the effective air-gap length. Even a small increment to the effective airgap length alters the machine parameters, especially its inductances. As a result, the rotor field windings together with the permanent magnets may not be able to generate the sufficient flux per pole as per its rated design. Therefore, the experiment has been simplified to test the concept by positioning permanent magnets installed on the rotor poles of the commercial machine.

The experimental tests have encountered some limitations due unavailable equipment and are carried out at a maximum of slightly above half full-load; nevertheless, the tests are sufficient to verify the main concepts.

In the following sections, the experimental performances of the original machine (unmodified) are compared with the modified machine together with their respective FEA simulation results. Experimental measurements of driving-torque, speed, induced voltages, currents, power and harmonics are taken and characteristic curves are plotted.

6.2 Test machine

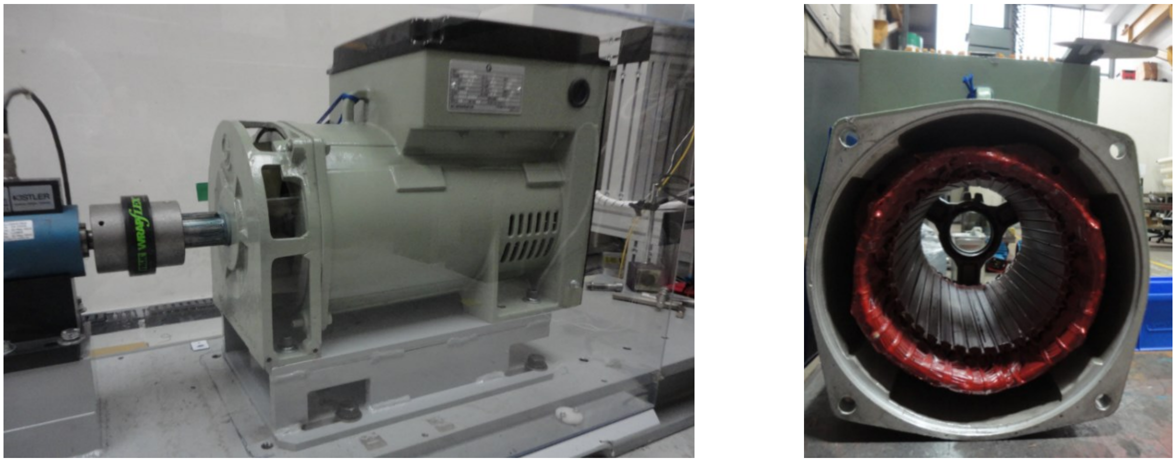

(a) Synchronous machine mounted on test rig (b) Stator

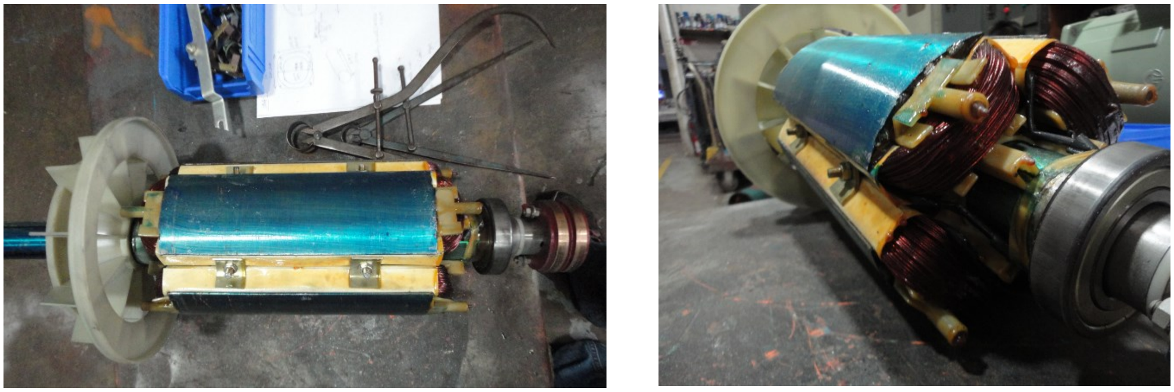

(c) Radial view of the rotor (d) Axial view of the rotor

Figure 6-1 (a) The synchronous machine used for the experiment. (b) to (d) machine dismantled for dimensional measurements

The test machine is a commercially available 12.5kVA, 1500rpm, 4-pole, slip-ring wound-field synchronous generator as shown in Figure 6-1. Test results from original machine are used as benchmark for the experiment.

6.3 Machine modification

6.3.1 Rotor modification using finite element modelling

A second machine identical to that of the first is modified to have armature reaction compensation. FEA simulations are used to select the most suitable grade of NdFeB magnets, their sizes, and locate the optimum position on the rotor pole shoe. The modified pole shoes must be able to support the inclusion of the magnets while retaining their structural integrity.

Demagnetization of the magnets must be avoided at all operating conditions. Magnets with excessively high flux densities may distort the air-gap flux such that it worsens the performance of the machine instead of improving it. Operating temperature of the machine is also a crucial factor for the selection of magnet grade.

Figure 6-2 shows the FEA models of both the original and modified machines. Figure 6-3 shows the simulated air-gap flux density of both machines at half-load operation. At this unity power factor operating point, the cross magnetising effect is at its maximum strength (for experiment). Positions of the permanent magnets on the rotor are determined for this particular operating point.

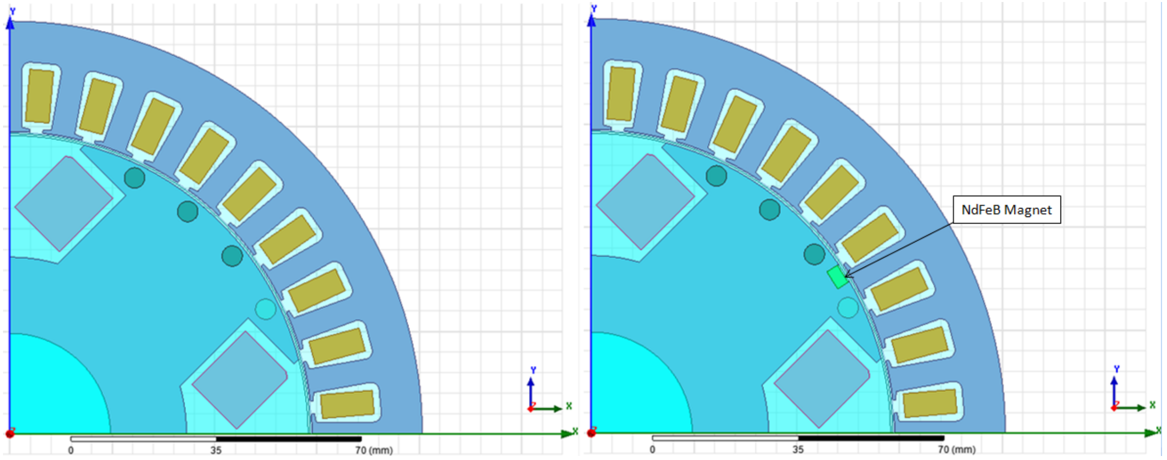

Figure 6-2 FEM models of original machine (left) and modified machine (right) in Ansys-Maxwell

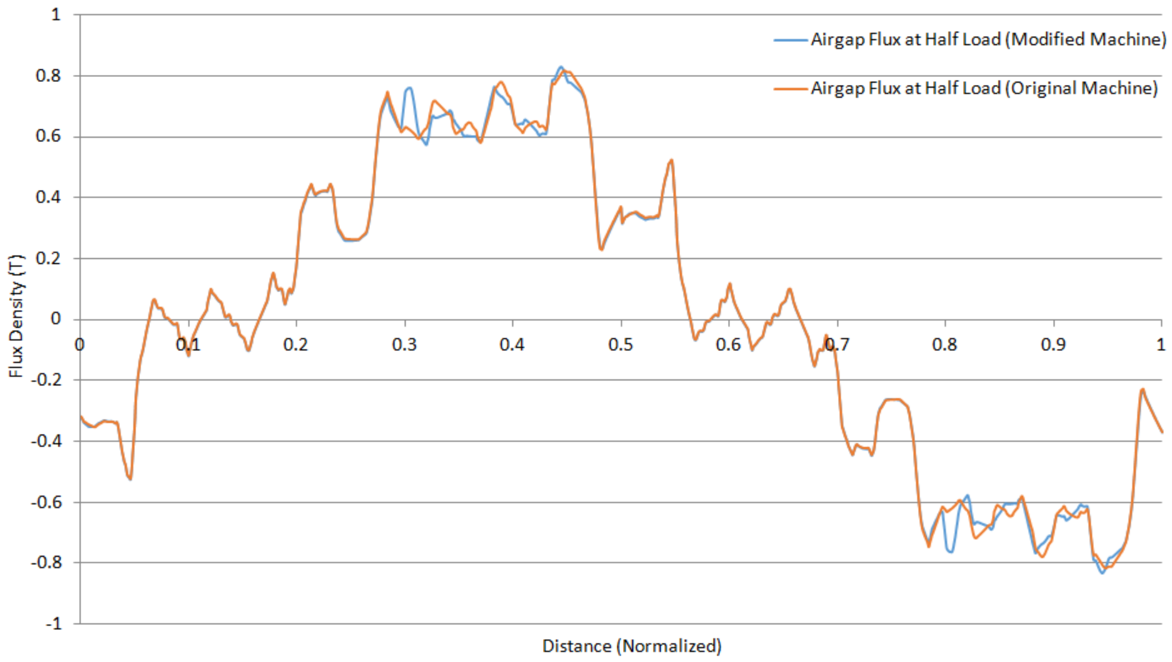

Figure 6-3 Air-gap flux densities of test machines

As seen in the FEM model, the surface of the magnet facing the stator side is not flushed with the rotor pole face. Various groove depths are simulated to find the allowable tolerance in the event of imperfections in the milling and magnet bonding process. It is found that a second air-gap of 0.25mm is the maximum acceptable tolerance for effective armature reaction compensation. Modification work must be precise and should not be allowed to exceed this limit. The modified rotor design shows similarities with the one published by Li Li et al. [103]. However, their machine has significantly different design features and did not have experimental results to verify their concept.

6.3.2 Modification work

The groove is precisely milled out on the rotor surface using a high performance milling machine. Ni-Cu-Ni coated N38-SH magnets are placed and bonded with specialized adhesive into the groove. Magnets are installed according to the polarity of the rotor pole. Segmented magnets are used to reduce eddy current losses. Figure 6-4 shows the modifications on the machine rotor.

(a) Top view of groove milled into side of pole face

(b) Axial view of groove

(c) Magnets installed on rotor poles in accordance to their respective polarities

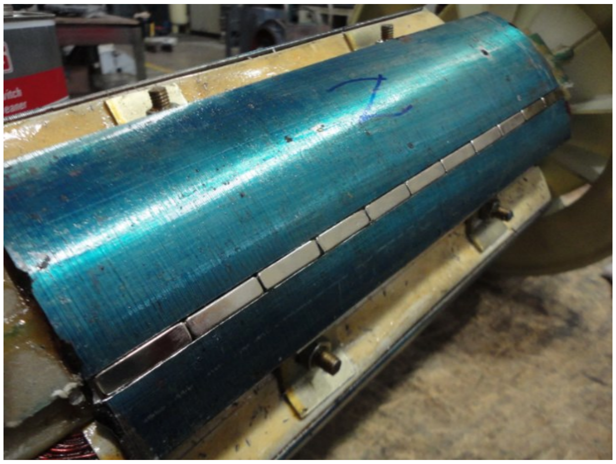

(d) Close up view of the segmented magnets placed and glued into the groove

Figure 6-4 Modification work on the machine rotor

6.4 Experiment setup and results

The phasor diagrams of a salient-pole three-phase synchronous machine in generating and motoring modes are depicted in Figure 6-5. The circuit diagrams for the experimental tests are shown in Figures 6-6 and 6-7 respectively.

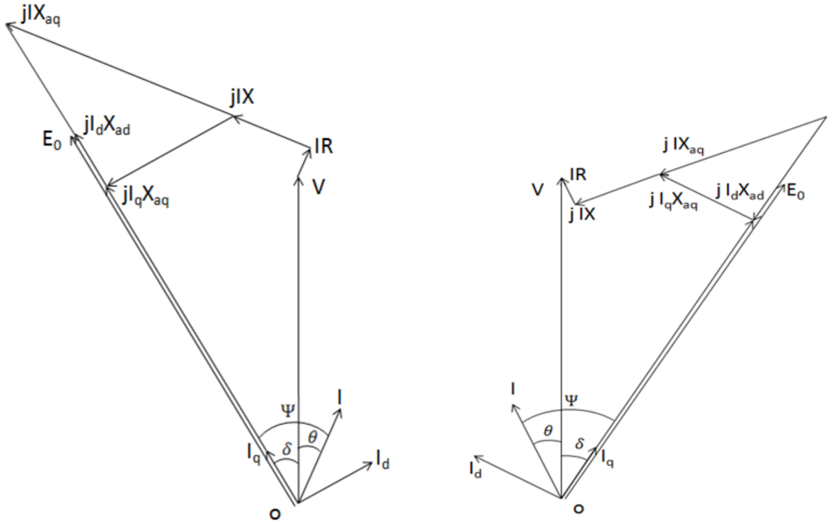

(a) Generator (b) Motor

Figure 6-5 Phasor diagrams of salient-pole three-phase synchronous machine in (a) generating mode (b) motoring mode

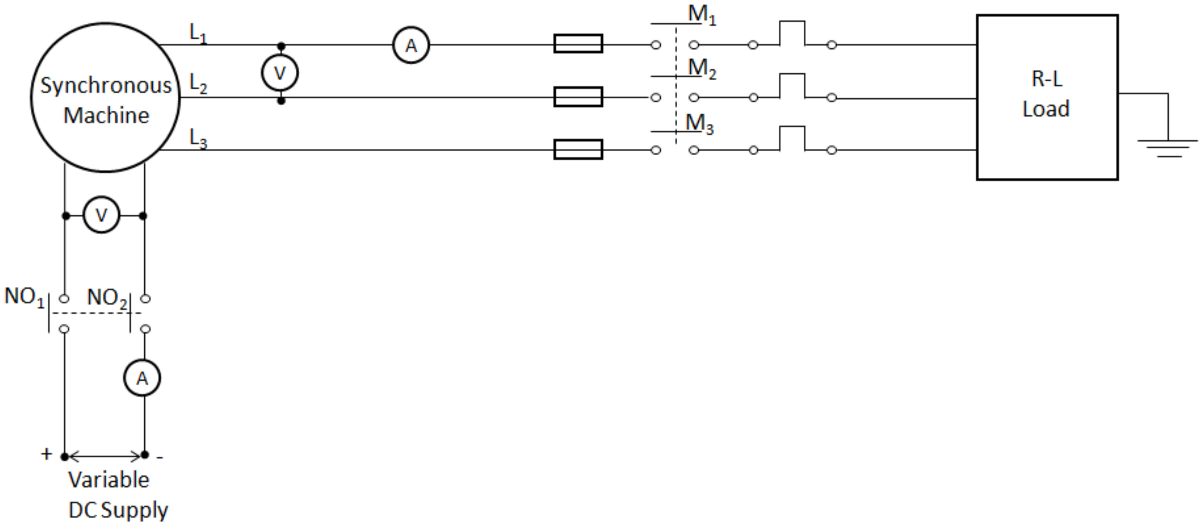

Figure 6-6 Schematic for the synchronous machine in generating mode

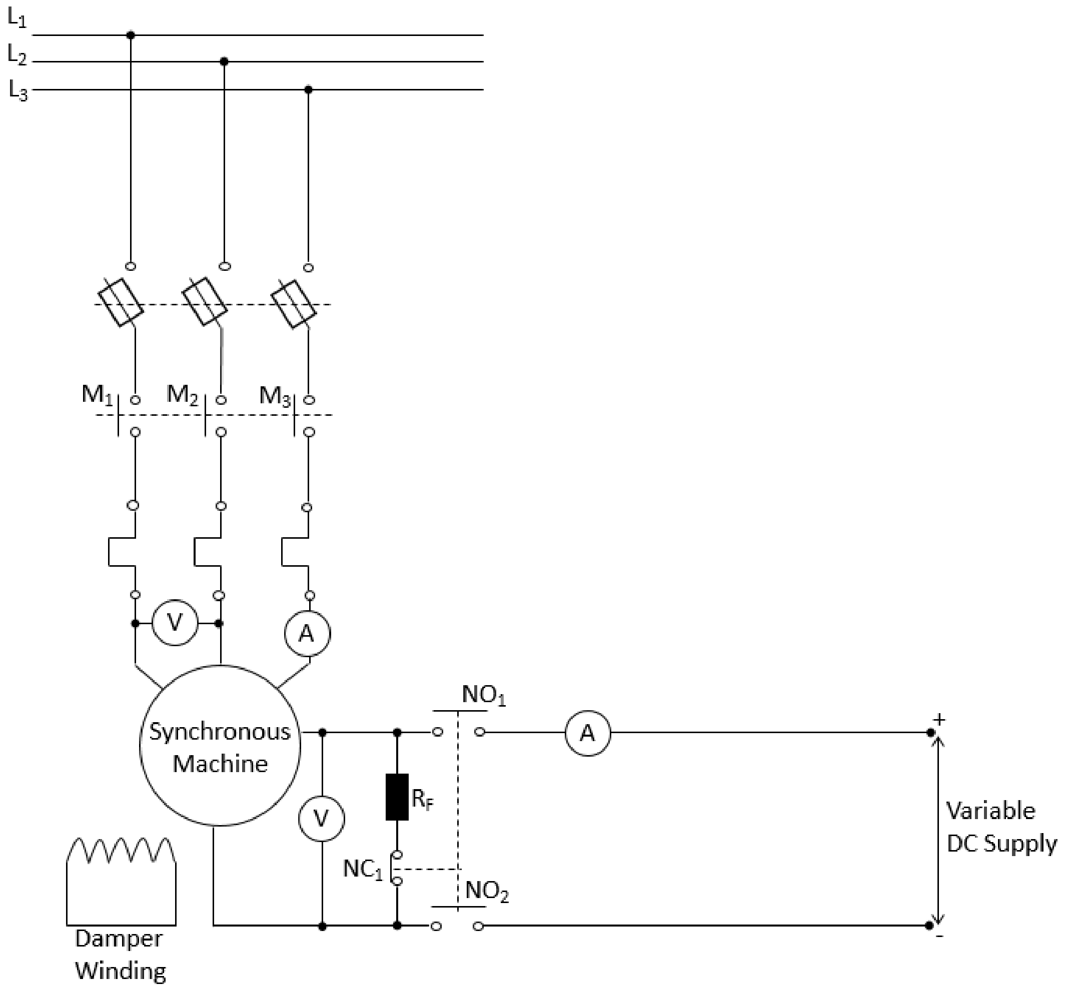

Figure 6-7 Schematic for the synchronous machine in motoring mode

The stators and rotors are energized by AC and DC power sources respectively. Contactors, fuses, overload relay and circuit breaker are used in the experiments for circuit protection. Even though the podded electrical machine is used only as a motor, the experimental machine is also operated as a generator to obtain its back-EMF waveform.

By varying the field excitation or connecting to various inductive loads, the power factor angle can be altered to obtain different levels of armature reaction. Figure 6-8 shows the laboratory and some of its equipment.

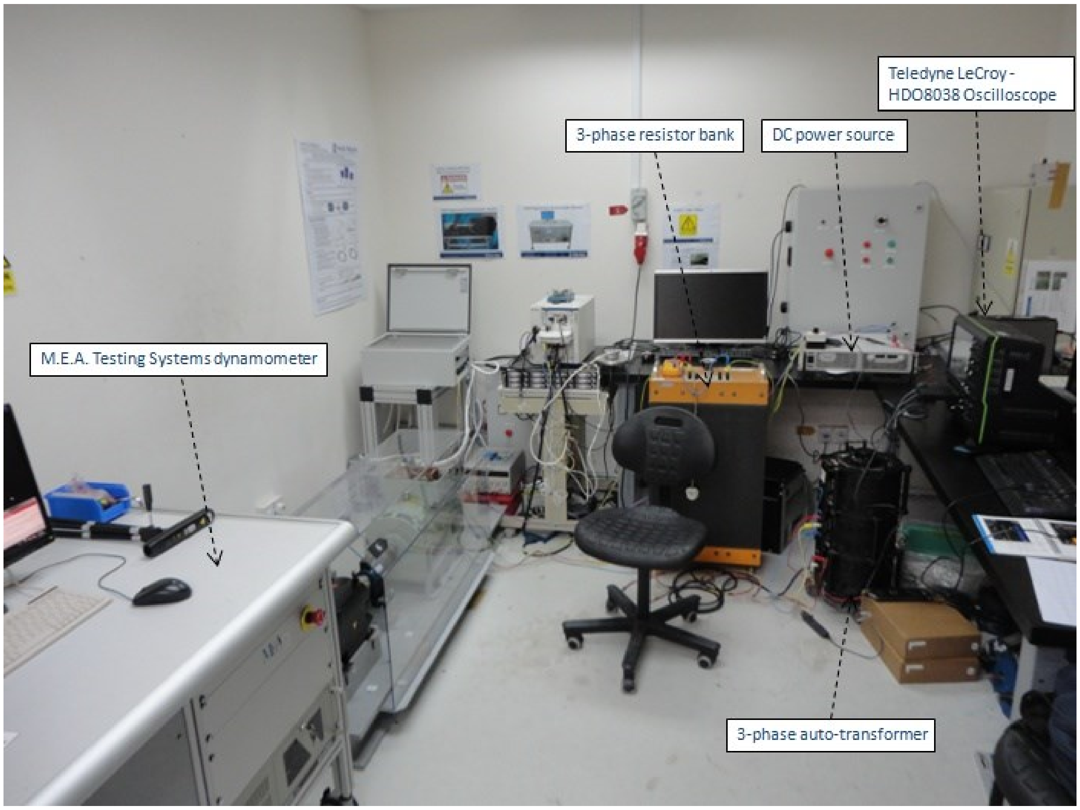

Figure 6-8 Laboratory and some of its equipment

6.4.1 Generator operation

To understand the effects of the armature reaction compensation on the air-gap flux, the back-EMF waveforms of both machines are analyzed. The machines are operated based on rated values under different loads. These values are referenced in the datasheet in Appendix F. Line voltage output and rated operating speed are kept constant at 415V and 1500rpm, respectively. Waveforms of stator and rotor windings, power factor, and harmonic distortion can be captured using the oscilloscope. Values are given in terms of root mean square.

6.4.1.1 No-load operation

Figure 6-9 shows the armature and field voltage, and current waveforms of the modified machine.

Figure 6-10 compares the line voltage harmonic analyses of both machines from experimental and simulated results under no-load operation. From the experiment, the original machine has slightly lower 3rd and 6th harmonics compared to that of the modified machine. From simulation, however, the original machine has lower 5th harmonics. The 13th harmonics are prominent in both machines. There is also a lower amount of higher harmonics in the simulated line voltage than that of the experiment. In simulation, triplen harmonics are almost completely eliminated due to the use of wye armature winding connection. This is due to the ideal conditions in simulations as compared to the experiment.

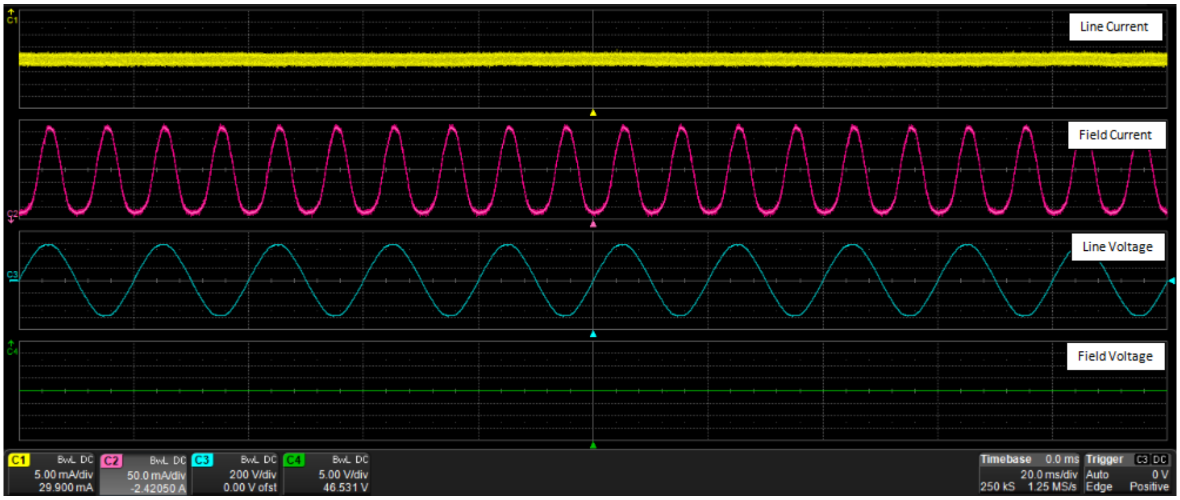

Figure 6-9 Oscilloscope display of voltage and current waveforms of the modified machine at no-load.

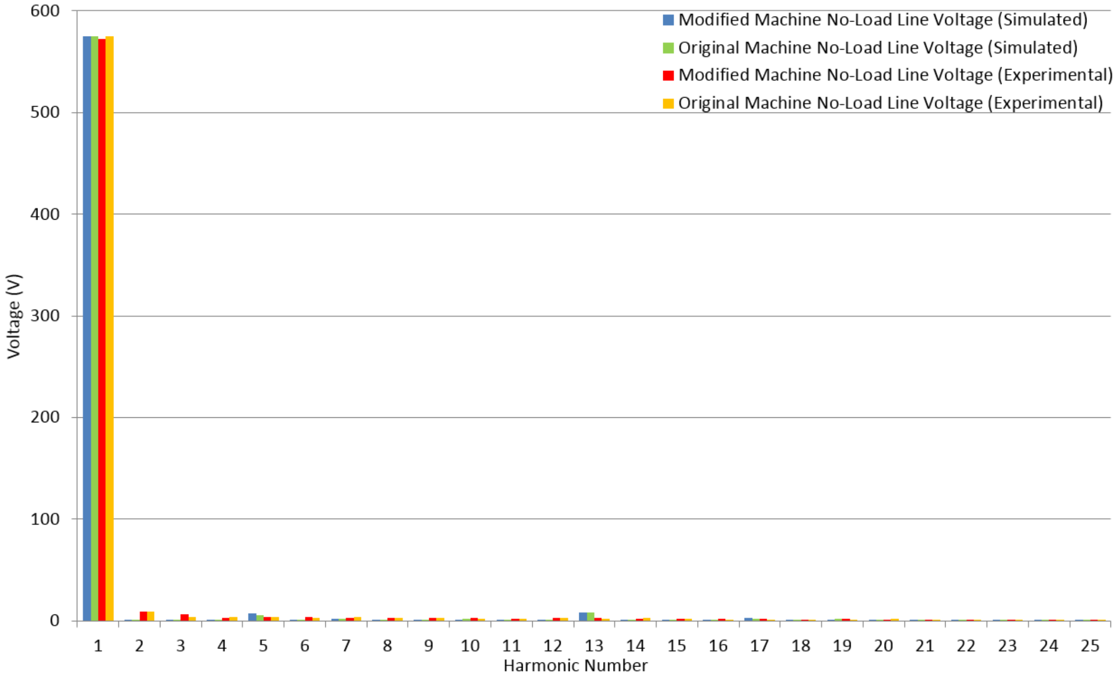

Figure 6-10 No-load line voltage harmonics of the machines

The no-load results are shown in Table 6-1. The experimental line voltage THDs of the modified machine are higher than those of the original machine, consistent with the FEA results.

Table 6-1 Experimental results at no-load operation

Machine	V_L [V]	I_L [A]	*f* [Hz]	V_f [V]	I_f [A]	*Drive-torque* [Nm]	*THD* V_L (%)
Original (Simulation)	415.3	0	50	39.6	2.2	0.037	1.98
Modified (Simulation)	415.2	0	50	39.6	2.2	0.037	2.07
Original (Experiment)	415	0	50	50.3	2.57	2.1	2.21
Modified (Experiment)	415	0	50	46.5	2.42	2.4	2.43

6.4.1.2 Loaded operations

For loaded operations, the machines are operated at close to unity power factor in both experiments and simulations. At unity power factor, the cross-magnetizing effect on the rotor air-gap flux would be at its most severe interaction. The magnets of the modified machine will be facing the demagnetizing flux from the armature side. These tests will demonstrate the effectiveness of the armature reaction compensation.

Figure 6-11 shows the line voltage harmonic analyses of both machines under quarter-load operation. The harmonic analysis shows that the 3rd harmonics in the modified machine are lower than that of the original machine. The reduction in the 3rd harmonic is indicative to lower airgap flux distortion in the air-gap [96]. From simulations, the line voltage harmonics of the modified machine are lower in magnitude for the 7th, 13th, 17th, and 19th harmonics than those in the original machine. In both experiment and simulation, the 5th harmonic is slightly higher for the modified machine than the original one.

The line voltage harmonic analyses of the machines under half-load operation are shown in Figure 6-12. From experiment, as in quarter-load operation, the 3rd harmonics in the modified machine are lower than those of the original machine. From simulations, the line voltage of the modified machine has lower harmonic magnitude for 13th, 17th, and 19th harmonics compared to those of the original machine. The 5th harmonic from experiment is slightly higher for the modified machine than the original machine whereas in simulation it is lower for the modified machine.

Table 6-2 and 6-3 show the respective experimental results for half-load and quarter-load operations of both machines. The line voltage THDs of the modified machine from experiment are lower, consistent with the FEA results.

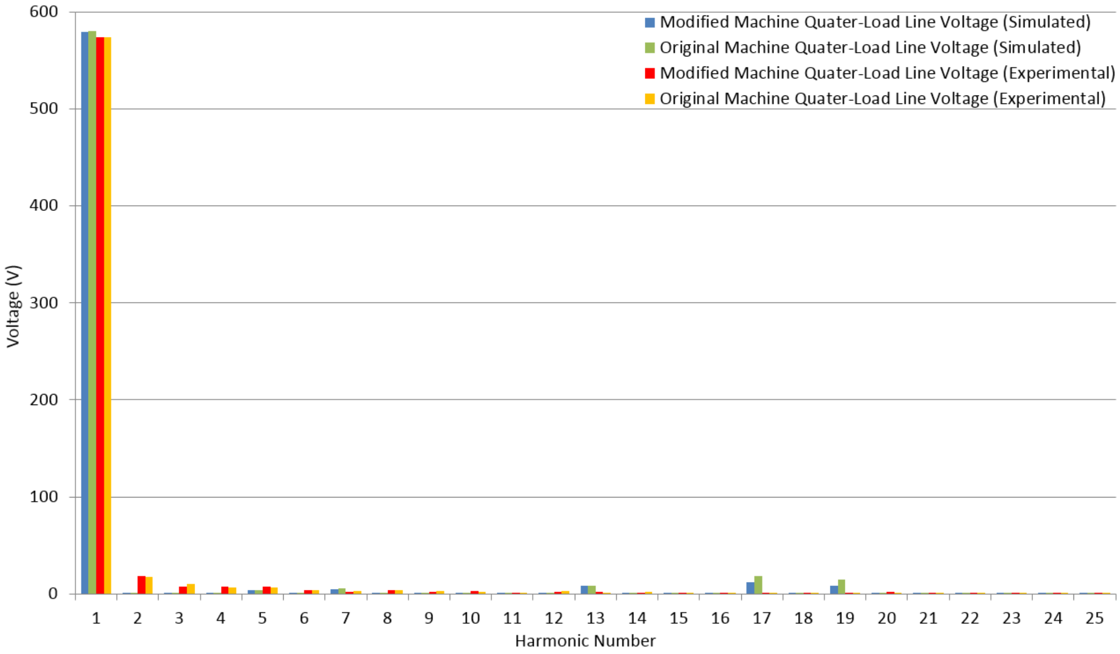

Figure 6-11 Quarter-load line voltage harmonics of the machines

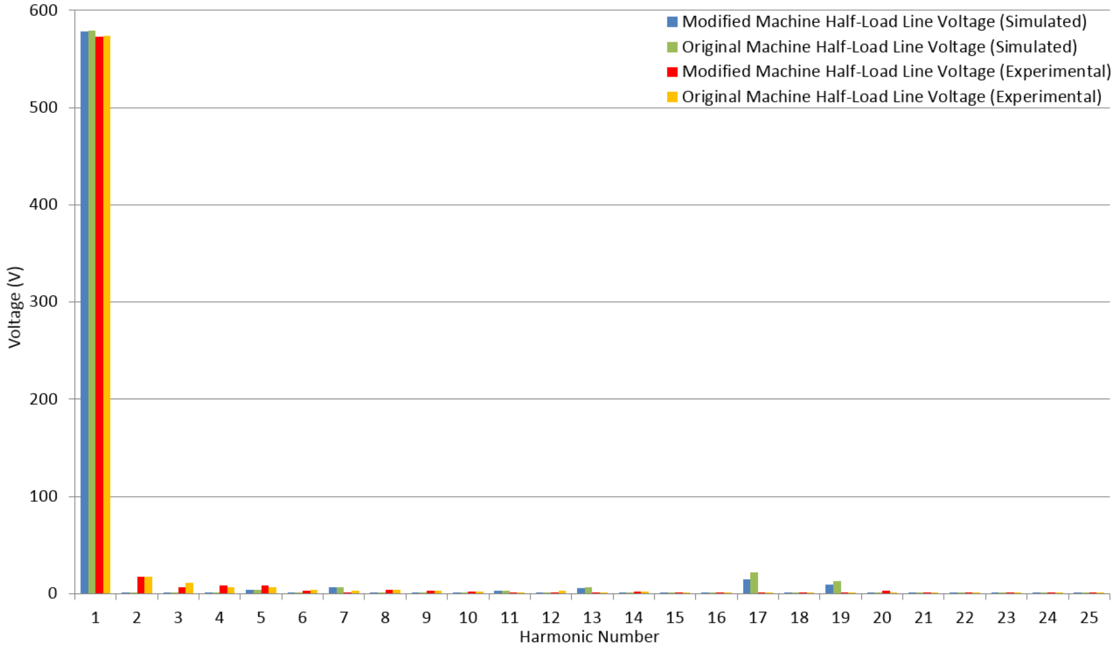

Figure 6-12 Half-load line voltage harmonics of both machines

Table 6-2 Experimental results at quarter-load operations

Machine	V_L [V]	I_L [A]	f [Hz]	V_f [V]	I_f [A]	*Output Power* [kVA]	*Power factor (lag)*	*Drive-torque* [Nm]	*THD* V_L (%)
Original (Simulation)	415.1	4.7	50	51.3	2.85	3.38	1	-	4.58
Modified (Simulation)	415	4.7	50	51.12	2.84	3.38	1	-	3.16
Original (Experiment)	415.3	4.97	50	50	2.75	3.57	0.95	26.3	4.23
Modified (Experiment)	415.1	4.82	50	48.2	2.68	3.46	0.95	25.6	3.92

Table 6-3 Experimental results at half-load operations

Machine	V_L [V]	I_L [A]	f [Hz]	V_f [V]	I_f [A]	*Output Power* [kVA]	*Power factor (lag)*	*Drive-torque* [Nm]	*THD* V_L (%)
Original (Simulation)	415	8.9	50	59.4	3.3	6.4	1	-	4.7
Modified (Simulation)	415	8.92	50	59.4	3.3	6.41	1	-	3.39
Original (Experiment)	415.2	8.8	50	56.7	3	6.33	0.95	46	4.47
Modified (Experiment)	414.7	8.83	50	55.8	2.95	6.35	0.95	46.2	4.22

FEA modelling consistently shows a lower line voltage THD compared to that of the experiment. Again, this may be due to the ideal conditions of the simulations. In reality, the performances of the machines may be affected by numerous factors such as manufacturing tolerances, temperature, non-uniform air-gap, etc. A 3D FEA model may also yield better simulation results.

6.4.2 Motor operation

Power flow is reversed into the synchronous generator to operate it in motoring mode. As the machines are not designed for motoring purposes, the machine manufacturer recommended that they should be derated. Rated line voltage is supplied to the armature windings. The field current is varied for under-excited and over-excited motor operations.

The V-curves of both machines are plotted as shown in Figure 6-13. The points with the lowest armature current values correspond to unity power factor operation. The purpose of the curves is to compare the variations in the magnitudes of the armature currents as the excitation voltages of both machines are varied.

As the machines are not primarily designed for motoring, magnetic saturation occurs even under low-load conditions. This causes the machines to vibrate violently prompting the experiment to stop. As a result, V-curves of higher loadings are unobtainable. V-curves of low loading values are not stable enough to yield conclusive results.

Due to the experimental limitations, FEA simulations were used to obtain the V-curves of the machines instead. Figure 6-14 (a) shows the V-curves of the original machine. The curves show a power factor range from 0.8 lagging to 0.8 leading. The lowest y-axis point on each curve corresponds to unity power factor operation. The non-linear characteristics of the magnetic core material can be observed as the load increases. The V-curves show that the machine requires a significant increase of current excitation even for small increment of loading. This is indicative of magnetic saturation of the core material.

Figure 6-14(b) shows the V-curves of the modified machine. Compared to the original machine for the similar power factor and loadings, the modified machine requires lower field excitation, however, it draws a higher armature current. At 0.8 leading power factor, excitation required by both machines are comparable. This is due to the severe saturation in the stator core material. Figure 6-15 shows the high saturation levels in the machines, especially in the stator cores, even at delivering a low output torque of 18Nm. Due to the inclusion of magnets, rotor of the modified machine are more magnetically saturated than that of the original machine. At above 18Nm, core material becomes severely saturated and does not yield proper results.

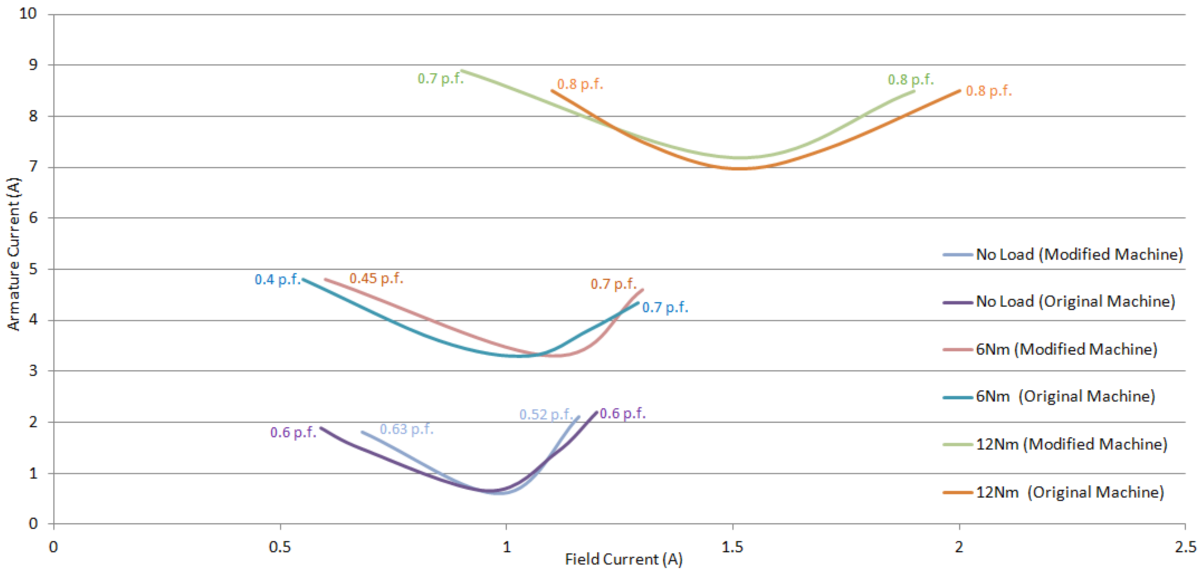

Figure 6-13 V-curves of synchronous machines in motor operation from experiment

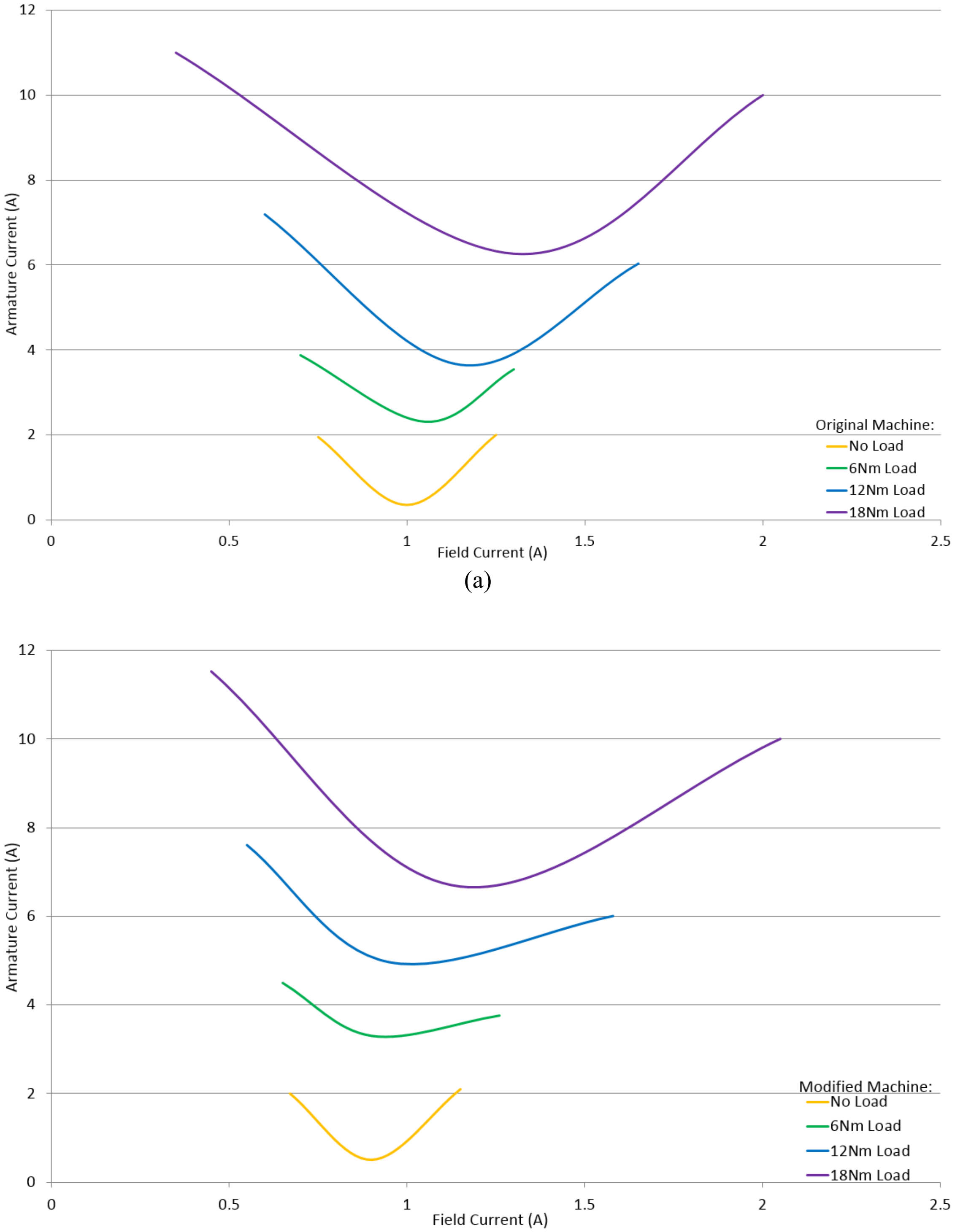

Figure 6-14 V-curves of the (a) original machine and (b) modified machine in motor operation from simulation

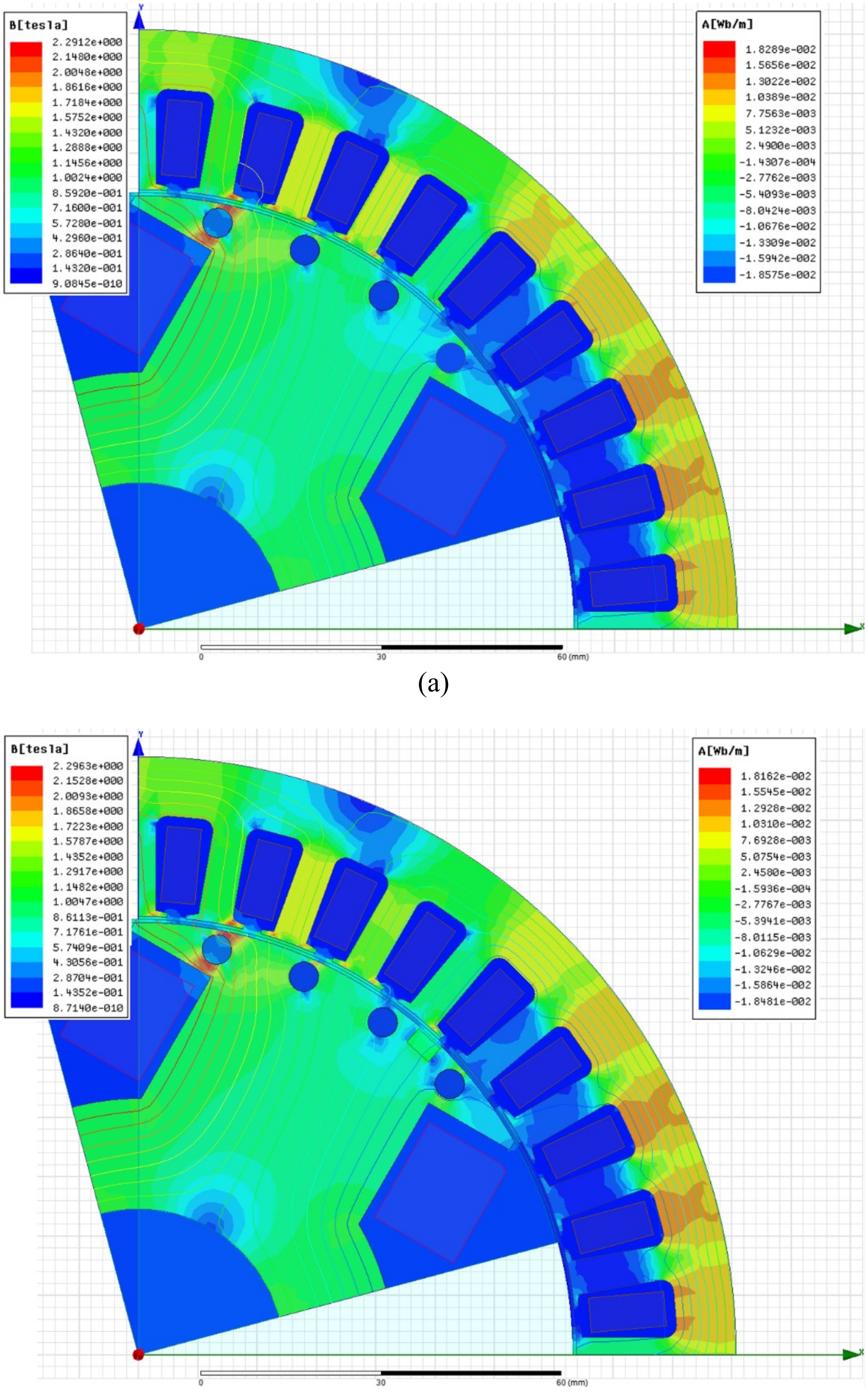

(a)

(b)

Figure 6-15 FEM models showing saturation levels in the (a) original machine and the (b) modified machine when delivering an output torque of 18Nm at 0.8 leading power factor

6.5 Summary

The intention of the experiment is to verify the concept of armature reaction compensation. FEA simulations are used to find the optimal size and position of the magnets installed on the rotor. Choice of the grade of NdFeB magnets plays a crucial role. Magnet flux that is excessively strong will inadvertently worsen the air-gap harmonics. Based on the results from the FEA simulations, the actual machine was modified. Before the modification work, both machines were tested to ensure that their output voltages and THDs are essentially identical. In motoring mode, the magnets will be situated on the trailing edge of the each pole.

In the experiment, both generating and motoring modes were performed. The purpose of generator operation is to obtain the back-EMF waveforms so as to understand the effectiveness of the armature reaction compensation technique. Due to limitations of some equipment, only up to half full-load test is achieved. Simulation and practical results both agree that the technique is able to improve line voltage THDs. Thus, the concept is sufficiently verified. V-curves from motoring operation are used to show the relation of armature current to field current. Unfortunately, in the motoring mode, the machines are unable to deliver conclusive results due to saturation even at a very low load. As a result, the V-curves of respective machines were obtained using FEM simulations. Similar to the experiments, the core material of the machines becomes magnetically saturated under low loadings. Due to the severe saturation of the core material, a conclusive comparison between the machines under motor operation mode cannot be drawn. This should be left for future work where a motor built for this purpose should be used.

The test results along with FEA simulations confirm that that such an armature reaction compensation technique can be implemented and might be of practical interest.

Chapter 7 - Conclusions

In this research work, a benchmark BLSM and two variants of HESMs (Model1 and Model2) are presented. BLSM is one type of electrical machines currently used in the azimuthing podded propulsion. An alternative to the BLSM is the PMSM which has a better efficiency due to the absence of field winding losses. However, due to the high cost of the PM material, it is not attractive for higher power ratings applications.

The HESMs have the advantages of WFSG and PMSM combined such as high efficiency, high power factor, and variable field excitation. The operation principle of the presented Model1 and Model2 HESMs are based on employing two different excitation sources on the same rotor. Field excitation provides the main excitation flux while PM is a secondary source of excitation. Utilizing PM excitation improves efficiency and can provide armature reaction compensation. Unfortunately, it also inherits their disadvantages especially those related to PM usage.

The objective of this research work is to evaluate the performances of the HESMs by comparing them with those of the BLSM, and thus determine if such technology is viable for the azimuthing podded propulsor application and the marine market.

The research work includes:

- A background overview of the problems in relating to permanent magnet materials and more efficient propulsion drives.

- Comprehensive literature review on IFEP, podded propulsion market, electrical machine topologies and characteristics for marine propulsion, different configurations of the HESMs, and their principle of operation, advantages and disadvantages.

- Development of the electromagnetic design of the BLSM and HESMs with analytical and numerical methods.

- Optimization work and design enhancements for BLSM and HESMs using FEM.

- Performance analyses of BLSM and HESMs to investigate if they meet the requirements for the azimuthing podded propulsor application. Thermal analyses of BLSM and HESMs under rated steady-state operating conditions. Economic analysis for cost comparisons between BLSM and HESMs.

- Experimental testing of a modified synchronous machine to verify the applied armature reaction compensation technique.

From FEA simulations, Model1 and Model2 HESMs have demonstrated that they are able match the performances of the benchmark BLSM. At the same time, they can deliver better efficiencies, have lower voltage waveform harmonic contents, and overall lower operating temperatures. Model2 machine has also demonstrated armature reaction compensation capability due to the progressive air-gap formed by PMs on its poles. Economic analysis of HESMs shows that while their capital costs are higher compared to the BLSM, they have a relatively short additional payback time due to savings from higher operating efficiency.

Thermal analyses based on simplified thermal resistance network are carried out mainly to compare temperatures between BLSM and HESMs. Although the results from the thermal resistance network differ from those of Motor-CAD, they are able to provide consistent results for comparisons between BLSM and HESMs. It is shown that the temperatures in the machines, especially for the PMs, lies in a safe region.

For the experiment, as building actual sized prototypes are not feasible, off-the-shelf synchronous machines were used. To compensate for armature reaction, a machine has magnets installed on a single edge of each of its poles. Another identical unmodified machine is used as a control for the experiment. The effectiveness of the compensation technique was tested, in both generating and motoring mode. Line-voltage THDs were shown to be reduced by armature reaction compensation in generating mode. Numerical results also show a relatively good correspondence with the experimental results. Due to magnetic saturation, the machines are unable to function as a motor.

To sum up, it could be concluded that the proposed HESMs seems to be a possible alternative for the BLSM for azimuthing podded propulsor application.

7.1 Suggestions for future work

Future research work for the HESM topology is suggested as follows:

- The experimental study of the HESMs should be performed in a full-scaled test. A prototype machine, in the MW range, should be fabricated. FEM results should be verified with the experimental results. Data for the full operational speed range should be obtained.
- Investigate the mechanical structure of the HESMs in detail. Expose and solve any potential problems in the retaining brackets (see Appendix A) for the permanent magnets on the surface of the rotor poles.
- Explore specific applications of the armature reaction compensation technique. Unidirectional rotating electric machines such as generators in power plants are preferred.
- The HESM topology demonstrated very attractive properties for applications such as micro-grid generators. It can easily supply power to a variable inductive load compared to a permanent magnet synchronous generator and has higher efficiency than conventional synchronous generators. Future research work for the HESM topology should proceed in this direction.

References

[1] J. F. Gieras, *Permanent Magnet Motor Technology: Design and Applications.* 3th ed. CRC Press, 2009.

[2] U.S. Department of Energy (DOE) (2011) *Critical Materials Strategy*

[3] U.S. Environmental Protection Agency (2012) *Rare Earth Elements: A Review of Production, Processing, Recycling, and Associated Environmental Issues.*

[4] E. P. Furlani (2001). *Permanent Magnet And Electromechanical Devices: Materials, Analysis, And Applications*. Academic Press.

[5] ARPA-E. (2013). *Research Funding for Rare Earth Free Permanent Magnets.* [Online] Available: http://arpa-e.energy.gov/?q=arpa-e-programs/react.

[6] M. Humphries (2013) *Rare Earth Elements: The Global Supply Chain. Congressional Research Service.*

[7] Adam Currie (2013). *Rare Earth Prices Unlikely to Replicate 2003 Decline.* [Online] Available: http://investingnews.com/daily/resource-investing/critical-metals-investing/rare-earth-investing/rare-earth-prices-unlikely-to-replicate-2003-decline/

[8] Patrice Christmann (2015). The Rare Earth Elements in the European Context. Bureau de Recherches Géologiques et Minières

[9] International Maritime Organization (2014) Nitrogen Oxides (NOx) – Regulation 13. [Online] Available: http://www.imo.org/en/OurWork/Environment/PollutionPrevention/AirPollution/Pages/Nitrogen-oxides-(NOx)-%E2%80%93-Regulation-13.aspx

[10] L. Vido, Y. Amara, M. Gabsi, M. Lecrivain, and F. Chabot,"Compared performances of homopolar and bipolar hybrid excitation synchronous machines," *Industry*

Applications Conference, 2005. Fourtieth IAS Annual Meeting. Conference Record of the 2005, vol.3, pp.1555, 1560 Vol. 3, 2-6 Oct. 2005

[11] T. J. McCoy, "Trends in ship electric propulsion," *Power Engineering Society Summer Meeting, 2002 IEEE* , vol.1, pp.343, 346 vol.1, 25-25 July 2002

[12] V. Landwehr (2006). *AX104 Bourbon Orca* [Online] Available: http://www.tugboats.de/bourbon_orca_article.html

[13] J King & I Ritchey. (2002). Marine propulsion: The transport technology of the 21st century?. *Ingenia*, Issue 12

[14] Munir Asif, *"Electric Propulsion"*, Helsinki University of Technology, Helsinki/Finland, 2006

[15] World Ship Society Port of New York Branch. (2004) *Queen Mary 2 ~ Construction of the Largest Liner in the World Part Three* [Online] Available: http://www.worldshipny.com/qm2pt3.shtml

[16] M. Oliver. (2011). *Norwegian Epic Exclusive – Big Ship, No Pods!* [Online] Available: https://malcolmoliver.wordpress.com/category/norwegian-cruise-line-ncl/page/3/

[17] S. Balashov, *"Design of marine generators for alternative diesel-electric power systems",* M.Sc Thesis, Faculty of Technology Department of Electrical Engineering, Lappeenranta University Of Technology, Finland, 2011

[18] ASEA Brown Boveri (ABB). (2015). [Online] Available: http://new.abb.com/marine/systems-and-solutions/electric-propulsion/azipod

[19] Rolls-Royce Holdings plc. (2015). [Online] Available: http://www.rolls-royce.com/~/media/Files/R/Rolls-Royce/documents/customers/marine/podded-propulsors.pdf

[20] ABB. (2004). *Compact Azipod® Propulsion.* [Online] Available: http://imistorage.blob.core.windows.net/imidocs/90580p006%20compact%20azipod.pdf.

[21] Siemens-Schottel-Propulsor (SSP). (2010). *Siemens-Schottel-Propulsor (SSP).* [Online] Available: http://www.siemens.com/press/pool/de/events/industry/is/2010-09-smm/IIS201009679e.pdf

[22] L. Bergh & U.Helldén, "Electrical systems in pod propulsion", M.Sc Thesis, Dept. Energy and Environment, Division of Electric Power Engineering, Chalmers University Of Technology, Göteborg, Sweden, 2007

[23] Marine Accident Investigation Branch (MAIB). (2011). *Report on the investigation of the catastrophic failure of a capacitor in the aft harmonic filter room on board RMS Queen Mary 2 while approaching Barcelona.* [Online] Available: http://www.maib.gov.uk/cms_resources.cfm?file=/QM2Report.pdf.

[24] C. N. Doerry. (2006). *Designing All Electric Ships.* [Online] Available: http://www.doerry.org/norbert/papers/060325imdcdesigningallelectricwarships1-presentation-final.pdf.

[25] R. D. Klug, and N. Klaassen, "High power medium voltage drives - innovations, portfolio, trends,"*, 2005 European Conference on Power Electronics and Applications*, pp.10 pp.,P.10

[26] General Electric (GE). (2013). *MV7000* [Online] Available: http://www.gepowerconversion.com/sites/gepc/files/product/MV7000%20brochure_en.pdf.

[27] K. Kamiev, J. Nerg, J. Pyrhonen, V. Zaboin, and J. Tapia, "Feasibility of an Armature-Reaction-Compensated Permanent-Magnet Synchronous Generator in

Island Operation," *, IEEE Transactions on Industrial Electronics*, vol.61, no.9, pp.5075,5085, Sept. 2014

[28] J. F. Gieras, R. J. Wang, and M. J. Kamper. *Axial Flux Permanent Magnet Brushless Machines*. 2nd ed. Springer, 2008.

[29] A. M. El-Refaie, "Fault-tolerant PM machines: A review," *Electric Machines and Drives Conference, 2009. IEMDC '09. IEEE International*, pp.1700, 1709, 3-6 May 2009

[30] S. M. Husband, and C. G. Hodge, "The Rolls-Royce transverse flux motor development," *Electric Machines and Drives Conference, 2003. IEMDC'03. IEEE International* , vol.3, pp.1435,1440 vol.3, 1-4 June 2003

[31] A. Mitcham, "Transverse flux motors for electric propulsion of ships," *IEE Colloquium on New Topologies for Permanent Magnet Machines (Digest No: 1997/090)*, pp.3/1,3/6, 18 Jun 1997

[32] B. Nedjar, S. Hlioui, Y. Amara, L. Vido, M. Gabsi, and M. Lecrivain, "A New Parallel Double Excitation Synchronous Machine,"*, IEEE Transactions on Magnetics*, vol.47, no.9, pp.2252, 2260, Sept. 2011

[33] D. Fodorean, A. Djerdir, A. Viorel, and A. Miraoui, "A Double Excited Synchronous Machine for Direct Drive Application—Design and Prototype Tests,"*, IEEE Transactions on Energy Conversion*, vol.22, no.3, pp.656, 665, Sept. 2007

[34] K. Kamiev, J. Nerg, J. Pyrhonen, V. Zaboin, V. Hrabovcová, and P. Rafajdus, "Hybrid excitation synchronous generators for island operation," *Electric Power Applications, IET* , vol.6, no.1, pp.1,11, January 2012

[35] B. Nedjar, S. Hlioui, M. Lecrivain, Y. Amara, L. Vido, and M. Gabsi, "Study of a new hybrid excitation synchronous machine," *International Conference on Electrical Machines (ICEM), 2012 XXth*, pp.2927, 2932, 2-5 Sept. 2012

[36] N. Naoe, and T. Fukami, "Trial production of a hybrid excitation type synchronous machine," *Electric Machines and Drives Conference, IEMDC. IEEE International*, pp.545, 547, 2001

[37] X. Liu, H. Lin, C. Yang, S. Fang, and J. Guo, "Static characteristic of a novel dual-stator hybrid excited synchronous generator based on 3D finite element method", *International Conference on Electrical Machines and Systems, ICEMS*, pp.1539,1543, 8-11 Oct. 2007

[38] X. Liu, H. Lin, Z. Q. Zhu, C. Yang, S. Fang, and J. Guo, "A Novel Dual-Stator Hybrid Excited Synchronous Wind Generator,"*, IEEE Transactions on Industry Applications*, vol.45, no.3, pp.947, 953, May-june 2009

[39] X. Fu, and J. Zou, "Numerical Analysis on the Magnetic Field of Hybrid Exciting Synchronous Generator"*, IEEE Transactions on Magnetics*, vol.45, no.10, pp.4590, 4593, Oct. 2009

[40] X. Fu, and J. Zou, "Design and analysis of a novel Hybrid Excitation Synchronous Generator," *3rd IEEE Conference on Industrial Electronics and Applications, ICIEA*, pp.2074, 2077, 3-5 June 2008

[41] X. Luo, and T. A. Lipo, "A synchronous/permanent magnet hybrid AC machine,"*, IEEE Transactions on Energy Conversion*, vol.15, no.2, pp.203, 210, Jun 2000

[42] D. Fodorean, I. A. Viorel, A. Djerdir, and A. Miraoui, “Double-Excited Synchronous Motor with Wide Speed Range: Numerical and Experimental Results,” Iranian Journal of Electrical and Computer Engineering, vol. 5, no. 1, 2006

[43] K. Kamiev, J. Nerg, J. Pyrhonen, V. Zaboin, and J. Tapia, "Feasibility of different excitation methods of synchronous generators in island operation,"*, International Conference on Electrical Machines (ICEM)*, pp.2902, 2908, 2-5 Sept. 2012

[44] J. A. Tapia, F. Leonardi, and T. A. Lipo,T.A., "Consequent pole permanent magnet machine with field weakening capability," *Electric Machines and Drives Conference, IEMDC. IEEE International* , pp.126, 131, 2001

[45] J. A. Tapia, F. Leonardi, and T. A. Lipo, "Consequent-pole permanent-magnet machine with extended field-weakening capability," *IEEE Transactions on Industry Applications*, vol.39, no.6, pp.1704, 1709, Nov.-Dec. 2003

[46] J. A. Tapia, F. Leonardi, and T. A. Lipo, "A design procedure for a PM machine with extended field weakening capability," *37th IAS Annual Meeting. Conference Record of the Industry Applications Conference*, vol.3, pp.1928, 1935 vol.3, 13-18 Oct. 2002

[47] H. Zhang, Q. Li, Z. An, and R. Tang, "Theory and design of hybrid excitation permanent magnet synchronous generators," *Proceedings of the Fifth International Conference on Electrical Machines and Systems, ICEMS*, vol.2, pp.898, 900 vol.2, Aug 2001

[48] H. Wang, Z. An, R. Tang, and Y. Niu, "Design of a hybrid excitation permanent magnet synchronous with low voltage regulation," *Proceedings of the Eighth International Conference on Electrical Machines and Systems ICEMS,* vol.1, pp.480, 483 Vol. 1, 27-29 Sept. 2005

[49] L. Vido, M. Gabsi, M. Lecrivain, Y. Amara, and F. Chabot, "Homopolar and bipolar hybrid excitation synchronous machines,"*, IEEE International Conference on Electric Machines and Drives*, pp.1212, 1218, 15-15 May 2005

[50] E. Hoang, M. Lecrivain, S. Hlioui, and M. Gabsi, "A new structure of a switching flux synchronous polyphased machine with hybrid excitation,", *European Conference on Power Electronics and Applications,* pp.1,8, 2-5 Sept. 2007

[51] E. Hoang, M. Lecrivain, S. Hlioui, and M. Gabsi, "Hybrid excitation synchronous permanent magnets synchronous machines optimally designed for hybrid and full

electrical vehicle,", *IEEE 8th International Conference on Power Electronics and ECCE Asia (ICPE & ECCE),* pp.153, 160, May 30 2011-June 3 2011

[52] E. Hoang, M. Lecrivain, and M. Gabsi, “Flux-Switching Dual Excitation Electrical Machine,” US Patent 7868506, Jan 11, 2011

[53] C. G. Hodge, and D. J. Mattick. The electric warship. *Trans IMarE*. 108 (2), pp 109–125, 1995.

[54] S. Zhu, C. Liu, Y. Xu, and Y. Ma, “Design and Experimental Study of a Novel Two-stage Brushless,” *International Conference on Renewable Energies and Power Quality*. (ICREPQ’11), pp. 321, 1-4. April 2010

[55] S. Zhu; C. Liu; Y. Xu; and X. Zhou, "Characteristics and experimental study on a novel Tangential/Radial Hybrid Excitation Synchronous Machine,"*, 2nd IEEE International Symposium on Power Electronics for Distributed Generation Systems (PEDG)*, pp.883, 886, 16-18 June 2010

[56] Y. Ning, C. Liu, R. Jiang, J. Xu, and S. Zhu, "A novel tangential radial hybrid excitation synchronous variable frequency aircraft generator,"*, 15th International Conference on Electrical Machines and Systems (ICEMS)*, pp.1,5, 21-24 Oct. 2012

[57] K. Xiao, C. Liu, and Q. Zhou, "The structural and characteristic study on the novel parallel magnetic path hybrid excitation synchronous generator," *International Conference on Electrical Machines and Systems, ICEMS*, pp.3608, 3611, 17-20 Oct. 2008

[58] J. F. Gieras, "PM synchronous generators with hybrid excitation systems and voltage control Capabilities: A review,"*, International Conference on Electrical Machines (ICEM)*, pp.2573, 2579, 2-5 Sept. 2012

[59] J. F. Gieras, “Permanent magnet dynamoelectric machine with variable magnetic flux excitation,” US patent 7777384, Aug 17, 2010

[60] M. G. Say, *Alternating Current Machines*. 5th ed. London: Pitman, 1984.

[61] Ion Boldea, *Synchronous Generators (The Electric Generators Handbook)*. CRC Press, 2005.

[62] J. H. Walker, *Large Synchronous Machines: Design, Manufacture and Operation* . London: Oxford University Press, 1981.

[63] International Electrotechnical Commission Standard 60085 Electrical Insulation-Thermal Evaluation and Designation, *3rd edition, 2004.*

[64] D. P. Kothari, and I. J. Nagrath, *Electric Machines*, 4th ed. India: Tata McGraw-Hill Education Pvt. Ltd., 2010.

[65] J. Pyrhönen, T. Jokinen, and V. Hrabovcova, *Design of Rotating Electrical Machines*. Wiley, 2009.

[66] H. Karmaker and Chunting Mi, "Improving the starting performance of large salient-pole synchronous machines," in *IEEE Transactions on Magnetics*, vol. 40, no. 4, pp. 1920-1928, July 2004.

[67] K. Vogt, *Design of Electrical Machines (Berechnung elektrischer Maschinen)*. Weinheim: Wiley-VCH Verlag GmbH, 1996.

[68] E. Oberg, F. D. Jones, and H. H. Ryffel, *Machinery's Handbook.* 29th ed. Industrial Press, Incorporated, 2012

[69] H. A. Toliyat, and G. B. Kliman, *Handbook of Electric Motors*, 2nd ed. CRC Press, 2004.

[70] Proto Laminations Inc. [Online] Available: http://www.protolam.com/page5.html.

[71] A. Shanmugasundaram, and R. Palani, *Electrical Machine Design Data Book*. India: New Age International, 1979.

[72] V. A. Balagurov, F. F. Galtieev, and A. N. Larionov, Permanent Magnet Electrical Machines. Moscow, Russia: Energia, 1964.

[73] General Electric (GE). (2015). *Laminated Salient Pole Rotors* [Online] Available: http://www.gepowerconversion.com/product-solutions/synchronous-motors/laminated-salient-pole-rotors

[74] J. R. Hendershot and T. J. E. Miller, *Design of Brushless Permanent-Magnet Machines*, 2nd ed. Motor Design Books LLC, 2010.

[75] Siemens AG. (2014). *Siemens: Superconducting technology Superconducting fault current limiters* [Online] Available: http://www.siemens.com/press/pool/de/pressemitteilungen/2014/corporate/factsheet-supraleiter_e.pdf

[76] Obtained from manufacturer: Vacuumschmelze GmbH & Co. KG. (2015). *Vacodym 677HR Demagnetizing Curves.*

[77] H. de Swardt. (2007). *Marthinsen &Coutts: Changing the wedge material in an electric motor (Rev. 07)* [Online] Available: http://www.rmwg.co.za/Presentations/Magnetic_Wedges/Magnetic_Wedges_Rev_03.pdf

[78] M. Dems, K. Komeza, and J.K. Sykulski, “Analysis of Effects of Magnetic Slot Wedges on Characteristics of Large Induction Motors,” *ISEF 2011 - XV International Symposium on Electromagnetic Fields in Mechatronics, Electrical and Electronic Engineering,* ps.3.5, 2011.

[79] K. W. Lee, J. Hong, D. Hyun, S. B. Lee, E. J. Wiedenbrug, M. Teska, C. Lim "Detection of Stator-Slot Magnetic Wedge Failures for Induction Motors Without Disassembly," *IEEE Transactions on Industry Applications*, vol. 50, no. 4, pp. 2410-2419, July-Aug. 2014.

[80] D. Toma, D. Marius, M. Gheorghe, M. Martian, and L. Gheorghe. *Performances analysis of an induction motor prototype for direct drive traction system of tramcar.* [Online] Available: http://www.jee.ro/covers/art.php?issue=WE1226321819W49182f9b35239

[81] B. J. Chalmers, and J. Richardson, "Performance of some magnetic slot wedges in an open-slot induction motor," in *Proceedings of the Institution of Electrical Engineers*, vol.114, no.2, pp.258-260, Feb. 1967.

[82] S. Cary, J. Hanson, C. Evans, and I. Blokhintsev, "Electric rotating machine standards part II: Magnetic wedge design & monitoring methods," *Petroleum and Chemical Industry Conference (PCIC)*, pp.1-8, 19-21 Sept. 2011

[83] T. R. Gaerke, and D.C. Hernandez, "The Temperature Impact of Magnetic Wedges on TEFC Induction Motors," *IEEE Transactions on Industry Applications*, vol.49, no.3, pp.1228-1233, May-June 2013

[84] F. J. T. E. Ferreira, M. V. Cistelecan and A. T. de Almeida, "Evaluation of Slot-Embedded Partial Electrostatic Shield for High-Frequency Bearing Current Mitigation in Inverter-Fed Induction Motors," *IEEE Transactions on Energy Conversion*, vol. 27, no. 2, pp. 382-390, June 2012.

[85] R. Curiac, and H. Li, "Improvements in energy efficiency of induction motors by the use of magnetic wedges," *Petroleum and Chemical Industry Conference (PCIC)*, pp.1-6, 19-21 Sept. 2011.

[86] Z Milojković, "Application of magnetic wedges for stator slots of hydrogenerators," *Proc. International Council on Large Electric Systems (CIGRE) Session*, pp1-8, 2010.

[87] Y. Takeda, T. Yagisawa, A. Suyama and M. Yamamoto, "Application of magnetic wedges to large motors,"*IEEE Transactions on Magnetics*, vol. 20, no. 5, pp. 1780-1782, Sep 1984.

[88] H. de Swardt. (2007). *Marthinsen & Coutts: Electric motor failure prevention: wedge failures (rev. 08)* [Online] Available: http://www.mandc.co.za/pdfs/Electric-Motor-Failure-Wedges.pdf.

[89] Obtained from manufacturer: Isovolta AG. (2014). *Magnoval® 2232*.

[90] D.C. Hanselman, *Brushless Permanent Magnet Motor Design*, 2nd ed. Magna Physics Publishing, 2006

[91] I. Panayotov and D. Sotirov, "Study of the influence of damper winding on the harmonics contents of line voltage on synchronous machine with integer number of slot for pole and phase," *Efficacité énergétique –sources d'énergies renouvelables – protection de l'environnement COFRET'*, pp 1-4, 2012.

[92] J. H. Walker, "Slot ripples in alternator e.m.f. waves," *Proceedings of the IEE - Part II: Power Engineering*, vol. 96, no. 49, pp. 81-92, February 1949.

[93] P. A. Hargreaves, B. C. Mecrow and R. Hall, "Open circuit voltage distortion in salient pole synchronous generators with damper windings," *IET International Conference on Power Electronics, Machines and Drives (PEMD),* pp. 1-6, 2010.

[94] C. E. Shannon, "Communication in the Presence of Noise," *Proceedings of the IRE*, vol. 37, no. 1, pp. 10-21, Jan. 1949.

[95] K. Kamiev, J. Nerg and J. Pyrhonen, "Design of damper windings for direct-on-line permanent magnet synchronous generators," *EUROCON 2009, EUROCON '09. IEEE*, St.-Petersburg, pp. 783-790, 2009.

[96] T. Wildi, *Electrical Machines, Drives and Power Systems*, 5th ed. Prentice Hall, 2002.

[97] ISO 3046-1:2002(en), Reciprocating internal combustion engines — Performance — Part 1: Declarations of power, fuel and lubricating oil consumptions, and test methods — Additional requirements for engines for general use.

[98] J. Nerg, M. Rilla and J. Pyrhonen, "Thermal Analysis of Radial-Flux Electrical Machines With a High Power Density," in *IEEE Transactions on Industrial Electronics*, vol. 55, no. 10, pp. 3543-3554, Oct. 2008.

[99] R. Islam and I. Husain, "Analytical Model for Predicting Noise and Vibration in Permanent-Magnet Synchronous Motors," in *IEEE Transactions on Industry Applications*, vol. 46, no. 6, pp. 2346-2354, Nov.-Dec. 2010.

[100] J. F. Gieras, C. Wang, and J. C. Lao, *Noise of Polyphase Electric Motor*, Boca Raton, FL: Taylor & Francis, 2006.

[101] Contact with NingBo Jin Ke Magnetics Co. Ltd. (2015)

[102] P. Christmann.(2015). *The Rare Earth Elements in the European context.* [Online] Available:http://www.mineralinfo.fr/sites/default/files/upload/documents/Aster_REE/anr_aster_23_04_15_01_rare_earth_elements_in_eu_context_christmann.pdf

[103] L. Li, A. Foggia, A. Kedous-Lebouc, J. C. Mipo and L. Kobylansky, "Some armature reaction compensation methods numerical design of experiments and optimization for a hybrid excitation machine," *Electric Machines and Drives Conference (IEMDC)*, Miami, FL, pp. 832-838, 2009.

Appendix A

A.1 Proposed PM protection for HESMs

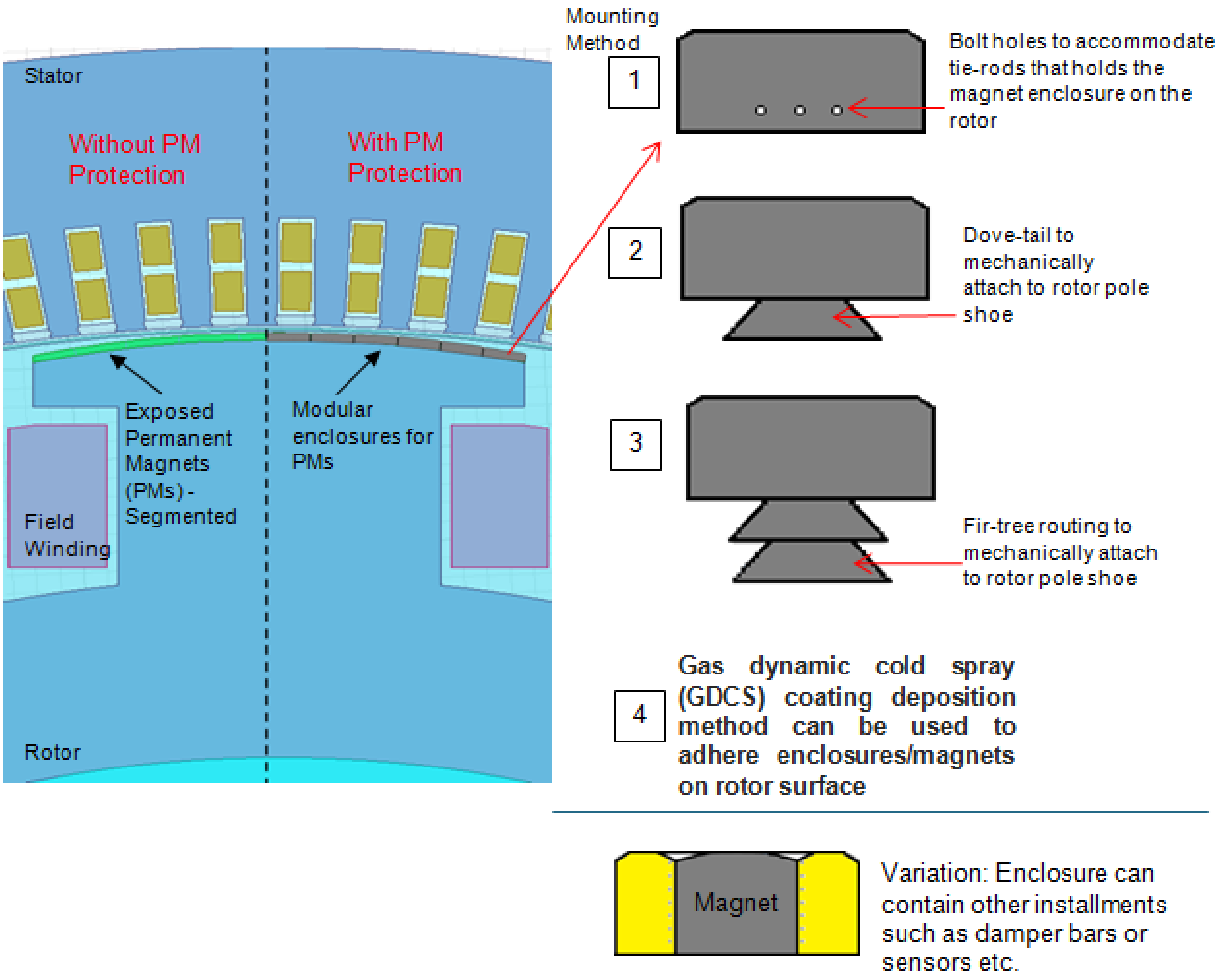

Bolt holes to accommodate tie-rods that holds the magnet enclosure on the rotor

Dove-tail to mechanically attach to rotor pole shoe

Fir-tree routing to mechanically attach to rotor pole shoe

Gas dynamic cold spray (GDCS) coating deposition method can be used to adhere enclosures/magnets on rotor surface

Variation: Enclosure can contain other installments such as damper bars or sensors etc.

Appendix B

B.1 Machine design program

```
clear all
clc

% disp('
');
% disp('
');
%
disp('******************************************************************');
% disp('**************** Salient-Pole Synchronous Machine
****************');
%
disp('******************************************************************');

list= fopen ('Optimal_Parameters.m', 'w');
Num= 0; P1= 0; P2= 0; P3= 0; P4= 0;
Efficiencymax= 92;
% PowerDensitymin= 23;
% TempriseSmin= 53;
% TempriseFmin= 61;

for D= 1.2:0.05:1.35
for Ji= 5: 0.5 :6;
for Bt= 1.8: 0.05: 1.9;
for Bc= 1.15: 0.05 :1.2;
for SCR= 1;
for Brcore= 1.1: 0.05 :1.2;
for Jfield= 4000000:500000:5000000;

%Basic Dimensions
V= 3300;
RPM= 190;
PF= 1;
pole= 14;
Kw= 0.932;
f= (pole*RPM)/120;
spp= 3.5;
Temp= 120;
uo= 4*pi*1e-7;
KW= 5235;
KVA= KW/PF;
KVAD= [1000 5000 10000 20000];
BavD= [0.58 0.61 0.63 0.65];
acD= [40e3 58e3 76e3 95e3];
Bav= interp1 (KVAD, BavD, KVA, 'pchip');
ac= interp1 (KVAD, acD, KVA, 'pchip');
```

```
% Main Dimensions
Co= 11*Bav*ac*Kw*1e-3;
ns= 2*f/pole;
L= (ceil((KVA/(D^2*Co*ns))*100))/100;
polepitch= (pi*D)/pole;
Lbypolepitch = L/polepitch;
nv= ceil(L/0.09);
bv= 0.01;
Ls= L-nv*bv;
Kiron = 0.95;
Liron= Ls*Kiron;
Vr= pi*D*ns;
polefluxi= (Bav*pi*D*L)/pole;
Tphi= V/(sqrt(3)*4.44*polefluxi*Kw*f);
Zph= Tphi*2;
S= spp*pole*3;
slotpitch= (pi*D)/S;
Zsi= (Zph*3)/S;
Zs= ceil(Zsi*2)/2;
Tph= (Zs*S)/6;
Iph= (KVA*1000)/(sqrt(3)*V);
slotloading= Iph*Zs;
poleflux= V/(sqrt(3)*4.44*f*Kw*Tph);
polearc= 0.72*polepitch;

% Stator Dimensions
Asi= (Iph/Ji)*1e-6;
Teethperpole= ceil(polearc/slotpitch);
bt= poleflux/(Bt*Liron*Teethperpole);
Wsi= slotpitch - bt;
Winsmm= 5.3;
Wins= Winsmm * 1e-3;
Wc= ceil((Wsi- Wins)* 1e3)/1e3;
Ws= 1*Wc + Wins;
btWsratio= bt/Ws;
Hc= ceil((Asi/Wc)*2*1e3)/(2*1e3);
As= Wc*Hc*0.98;
J= Iph/As;
Hinsi = 20.3;
Hins= (Hinsi)*1e-3;
Hs= Zs*Hc + Hins;
LmtS= (2*L + 2.5*polepitch + 0.05 * V/1000 + 0.15);
ResP= (1.734*1e-8)*(1+ 0.00393* (Temp - 20));
Rph= ResP*LmtS*(Tph/As);
DCloss= 3*Iph^2*Rph;
alpha= sqrt((pi*uo*f)/ResP) * sqrt(Wc/Ws);
Layer= 4;
ah= alpha* Hc/(Layer/2);
Keav= 1 + (ah)^4 * ((Layer)^2)/9;
Eddyloss= (Keav)*DCloss;
PtS= 1.15*(DCloss + Eddyloss);
Reffpu= (Iph* Rph) /(V/sqrt(3));
KgCu= 3* LmtS* As* Tph* 8940;
HsWsratio= Hs/Ws;

% Leakage Reactance
```

```
h1= Zs * Hc + (8*0.2 + 4*2 + 1.5)* 1e-3;
h2= (4*2 + 1.5)* 1e-3 ;
Hwedge= 4 * 1e-3;
Hlip= 1 * 1e-3;
WsO= Ws;
PermS= h1/(3*Ws) + h2/Ws + (2*Hwedge)/(Ws + WsO) + Hlip/WsO;
Xss= 8*pi*f*(Tph^2)*L*(PermS*uo)/(pole*spp);
coilspan= 9;
coilspanA= coilspan/S * 360;
polepitchA= 360/pole;
CsPp=  coilspanA/polepitchA;
CSbPPD = [0.5 0.6 0.7 0.8 0.9 1];
ksD= [0.5 0.63 0.78 0.86 0.93 1];
Ks= interp1 (CSbPPD, ksD, CsPp,'pchip');
L0Lm0= (Ks*polepitch^2)/(pi*slotpitch);
Xo= 8*pi*f*(Tph^2)*(L0Lm0*uo)/(pole*spp);
xl= Xss + Xo;
Xl= (Iph*xl)/(V/sqrt(3));
coreflux= poleflux/2;
coredepthi= coreflux/(Bc*Liron);
Douti= D+ 2*(Hs + coredepthi);
Dout= ceil ((Douti* 1e3)/10)*10 /1e3;
if Dout >= 1.60
    continue;
end;
coredepth= (Dout - D)/2 - Hs;

% Rotor Dimensions
ATa = (2.7*Tph*Iph*Kw)/pole;
ATfo = SCR*ATa;
ATgap = 0.8*ATfo;
Bgap = Bav/(polearc/polepitch);
Kgap= 1.18;
Lgapi = (ATgap*uo)/(Bgap*Kgap);
Lgap = floor(Lgapi*10*1e3)/(10*1e3);
Drotor = D - 2 * Lgap;
Lpb = L - 0.015;
Lpbiron = Lpb*Kiron;
fluxpb = 1.2* poleflux;
Bpb= 1.6;
Apb = fluxpb/Bpb;
bpb = Apb/Lpbiron;

% Field Winding Dimensions
PPD = [0.1 0.2 0.3 0.4 0.5];
DFD = [0.03 0.036 0.04 0.045 0.05];
DepthF = interp1 (PPD, DFD, polepitch, 'pchip');
IfTf = 1.12 * ATa;
pfField = 0.85;
AreaCuF= IfTf/Jfield;
AreaF= AreaCuF/pfField;
Hfield= AreaF/DepthF;
Hshoe= 0.028;
Hpole = Hfield + Hshoe + 0.017;
FluxRC = fluxpb/2;
DepthRC = FluxRC/(Brcore * Lpbiron);
```

```
bshoe= bpb + 2*DepthF + 0.016;
KgPoles = (bpb*Hpole + bshoe*Hshoe) *Lpbiron*pole*7850;
KgYoke = ( ((Drotor - 2 * Hpole)^2) /4 - ((Drotor - 2*Hpole - 2*DepthRC)^2)
/4 ) *pi * Lpbiron *7850;
LgapPolepitchratio = Lgap/polepitch;

% Damper Windings Dimensions
Jdamper= 4;
Adamper= (0.2 * ac * polepitch)/Jdamper *1e-6;
Ndamper= round(polearc/(0.8* slotpitch));
Abar= (Adamper/Ndamper);
Dbar= 2*sqrt(Abar/pi);

% Magnetic Circuits
WsLgapratio= Ws/Lgap;
WsLgapratioD= [0 1 2 3 4 5 6 7 8 9 10 11 12];
CCD= [0 0.15 0.28 0.38 0.46 0.51 0.55 0.59 0.62 0.64 0.66 0.68 0.7];
CCgap = interp1 (WsLgapratioD, CCD, WsLgapratio, 'pchip');
slotcoe = slotpitch/(slotpitch - Ws * CCgap);
bvLgapratio= bv/Lgap;
CCv = interp1 (WsLgapratioD, CCD, bvLgapratio, 'pchip');
ductcoe= L/(L-nv*bv*CCv);
airgapcoe= slotcoe * ductcoe;
ATagap= (airgapcoe * Bgap * Lgap)/uo ;
btnar= pi*(D+(2/3)*Hs)/S- Ws;
Bnar= poleflux/(Liron * btnar * Teethperpole);
M19AppHD= [5591.10689 7448.318413 9708.81567 12486.93162 16041.48364
21249.42062 31313.49588 53589.44688 88477.4846 124329.4105 159968.5693
197751.6043 234024.7513];
M19AppBD= [1.7 1.75 1.8 1.85 1.9 1.95 2 2.05 2.1 2.15 2.2 2.25 2.3];
AppH= interp1 (M19AppBD,M19AppHD,Bnar,'spline');
ATtooth= AppH * Hs;
AcoreS= coredepth * Liron;
BcoreS= poleflux /(2 * AcoreS);
M19HD= [0 15.120714 22.718292 27.842733 31.871434 35.365044 38.600588
41.736202 44.873979 48.087807 51.437236 54.975221 58.752993 62.823644
67.245285 72.084406 77.4201 83.350021 89.999612 97.537353 106.201406
116.348464 128.547329 143.765431 163.754169 191.868158 234.833507
306.509769 435.255202 674.911968 1108.325569 1813.085468 2801.217421
4053.653117 5591.10689 7448.318413 9708.81567 12486.93162 16041.48364
21249.42062 31313.49588 53589.44688 88477.4846 124329.4105 159968.5693
197751.6043 234024.7513];
M19BD= [0 0.05 0.1 0.15 0.2 0.25 0.3 0.35 0.4 0.45 0.5 0.55 0.6 0.65 0.7
0.75 0.8 0.85 0.9 0.95 1 1.05 1.1 1.15 1.2 1.25 1.3 1.35 1.4 1.45 1.5 1.55
1.6 1.65 1.7 1.75 1.8 1.85 1.9 1.95 2 2.05 2.1 2.15 2.2 2.25 2.3];
M19H= interp1 (M19BD,M19HD,BcoreS,'spline');
LcoreS= pi*(D + 2*Hs + coredepth)/(2*pole);
ATcoreS= LcoreS * M19H;
ATL= ATagap + ATtooth + ATcoreS;
Cshoes= (pi*(Drotor - Hshoe))/pole - bshoe;
Cpoles= (pi*(Drotor - Hshoe - Hpole))/pole - bshoe;
FluxLshoe= 4*uo*ATL*((L*Hshoe)/Cshoes +
1.47*Hshoe*log10(1+(pi/2)*bshoe/Cshoes));
FluxLpole= 2*uo*ATL*((Lpb*Hpole)/Cpoles +
1.47*Hpole*log10(1+(pi/2)*bpb/Cpoles));
Fluxpmin= poleflux + FluxLshoe;
```

```
Fluxpmax= Fluxpmin + FluxLpole;
Bpmin= Fluxpmin / Apb;
Bpmax= Fluxpmax / Apb;
M19H1= interp1 (M19BD,M19HD,Bpmin,'spline');
M19H2= interp1 (M19BD,M19HD,Bpmax,'spline');
ATpole= (2/3 * M19H1 + 1/3 * M19H2) * Hpole;
Fluxyoke= (poleflux + FluxLshoe + FluxLpole) /2;
Ayoke= L * DepthRC ;
Byoke= Fluxyoke/Ayoke;
M19H3= interp1 (M19BD,M19HD,Byoke,'spline');
Lyoke = (Drotor - 2*Hpole - DepthRC)*pi/ (2*pole);
ATyoke= M19H3 * Lyoke;
ATfo= ATagap + ATtooth + ATcoreS + ATpole + ATyoke;

% OCC
E = [100 110 120 130];
ATT= zeros(1,5);
EE= zeros(1,5);
EE (1) = 0;
ATT (1) = 0;
Bgapx = zeros(1,4);
ATagapx= zeros(1,4);
Bstx= zeros(1,4);
M19Hst= zeros(1,4);
ATstx= zeros(1,4);
Bscx= zeros(1,4);
M19Hsc= zeros(1,4);
ATscx= zeros(1,4);
Bpminx= zeros(1,4);
M19Hpmin= zeros(1,4);
Bpmaxx= zeros(1,4);
M19Hpmax= zeros(1,4);
ATpolex= zeros(1,4);
Brcx= zeros(1,4);
M19Hrc= zeros(1,4);
ATrcx= zeros(1,4);
ATTx= zeros(1,4);
for i = 1:4;
Bgapx(i) = Bgap* E(i)/100;
ATagapx(i)= (airgapcoe * Bgapx(i) * Lgap)/uo ;
Bstx(i) = Bnar* E(i)/100;
M19Hst(i) = interp1 (M19AppBD, M19AppHD, Bstx(i), 'spline');
ATstx(i) = M19Hst(i)* Hs;
Bscx(i) = BcoreS* E(i)/100;
M19Hsc(i) = interp1 (M19BD,M19HD,Bscx(i), 'spline');
ATscx(i) = M19Hsc(i)* LcoreS;
Bpminx(i) = Bpmin* E(i)/100;
M19Hpmin(i) = interp1 (M19BD, M19HD, Bpminx(i), 'spline');
Bpmaxx(i) = Bpmax* E(i)/100;
M19Hpmax(i) = interp1 (M19BD, M19HD, Bpmaxx(i), 'spline');
ATpolex(i) = (2/3 * M19Hpmin(i) + 1/3 * M19Hpmax(i)) * Hpole;
Brcx(i) = Byoke* E(i)/100;
M19Hrc(i)= interp1 (M19BD, M19HD, Brcx(i), 'spline');
ATrcx(i) = M19Hrc(i)* Lyoke;
ATTx(i) = ATagapx(i) + ATstx(i) + ATscx(i) + ATpolex(i) + ATrcx(i);
ATT(i + 1) = ATTx(i);
```

```
EE(i + 1) = E(i);
end;

% Field Winding Parameters
PFangle= acos(PF);
PFangled= PFangle*(180/pi);
Vph= V/sqrt(3);
Zpu= Vph/Iph;
X= Zpu*Xl;
Eg= sqrt((Vph*PF+Iph*Rph)^2+(Vph*sin(PFangle)+Iph*X)^2);
Eg2= 1 + (0.95-1i*0.3122)*(Reffpu + 1i*Xl);
EgAbspu= abs(1 + (0.95 - 1i*0.3122)*(Reffpu + 1i*Xl));
EgAbs= EgAbspu * (3300/sqrt(3));
EgAng= angle(1 + (0.95 - 1i*0.3122)*(Reffpu + 1i*Xl));
EgAngd= EgAng*(180/pi);
Egpu= Eg/Vph;
ATocc= interp1(EE,ATT, Egpu*100, 'pchip');
PAPPratioD = [0.5 0.6 0.7 0.8 0.9 1.0];
KrD = [0.2 0.26 0.35 0.5 0.68 0.98];
PAPPratio= polearc/polepitch;
Kr = interp1(PAPPratioD, KrD, PAPPratio, 'pchip');
EgEoAngle = 24 * (pi/180);
PAAng= PAPPratio * pi;
ARf= (PAAng+sin(PAAng))/(4*sin(PAAng/2));
ATad = ATa * ARf;
AT1 = ATocc * cos(EgEoAngle);
Phi = PFangle + EgAng + EgEoAngle;
AT2 = ATad * sin(Phi);
ATFL = AT1 + AT2;
E0 = interp1(ATT,EE,ATFL, 'pchip');
reg=(E0- E(1) )/E(1)*100;

% Field Winding Design
ExciterV = 440;
VFcoil= (0.9*ExciterV)/pole;
Inspole= 0.01;
Lmtf= 2*Lpb + pi*(bpb + DepthF + 2*Inspole);
Afconi= (ResP * Lmtf * ATFL)/VFcoil;
bfcon= ceil(DepthF*1e3)/1e3;
Tfconi= Afconi/bfcon;
Tfcon= ceil(Tfconi*2e3)/2e3;
Afcon= bfcon * Tfcon * 0.98;
Ifield= Afcon * Jfield;
Tfield= ceil(ATFL/Ifield);
If0= ATTx(1)/Tfield;
ResF= (ResP * Lmtf * Tfield)/Afcon;
HFcon= Tfield*(Tfcon + 0.0002);
FBuckling= Hfield - HFcon;
AKIfield= VFcoil/ResF;
AKATFL= AKIfield*Tfield;
Vfn= Ifield * ResF * (235 + 120)/255;
Vex2= 1.1 * Vfn;
Vex= ceil(Vex2/5)*5;
Iex1= 1.1*Ifield;
Iex= ceil(Iex1/10)*10;
KWex= Vex*Iex/1e3;
```

```
% Losses & Efficiency
Fculoss= Ifield^2 * ResF * pole;
BLloss= 0.7 * 2 * Ifield;
Totfculoss= Fculoss + BLloss;
KgFcu= Lmtf * Afcon * Tfield * pole * 8940;
ExciterEff= 0.98;
Pex= Fculoss/ExciterEff;
ExLoss= Pex - Fculoss;
Friwindloss= 0.01 * KVA * PF * 1e3;
Dstcen= D + 2* (Hs/2);
spcen= (pi*Dstcen)/S;
btcen= spcen - Ws;
KgTeeth= 7850 * S * btcen * Liron * Hs;
B20D= [0.1 0.2 0.3 0.4 0.5 0.6 0.7 0.8 0.9 1 1.1 1.2 1.3 1.4 1.5 1.55 1.6
1.65 1.7 1.75 1.8 1.85 1.9 1.95 2 2.05 2.1 2.15 2.2];
WKgratioD= [0.002254983 0.008577666 0.018740427 0.032628338 0.050163281
0.071286169 0.095949584 0.12411399 0.155745536 0.190814653 0.229295121
0.271163399 0.316398146 0.36497985 0.416890553 0.4441 0.472 0.5007 0.53
0.56 0.5906 0.6218 0.6534 0.6855 0.7181 0.7512 0.7848 0.8188 0.8533];
tipkg= interp1(B20D, WKgratioD, Bnar, 'pchip');
teethloss= tipkg * KgTeeth;
Dmcore= D + 2 * Hs + coredepth;
KgCore= 7850 * (coredepth*Liron) * (pi*Dmcore);
cipkg= interp1(B20D, WKgratioD, BcoreS, 'pchip');
coreloss= cipkg * KgCore;
Totironloss= 1.7* (teethloss + coreloss);
Totallosses= PtS + Totironloss + Totfculoss + ExLoss + Friwindloss;
Rout= KVA*PF*1e3;
InputW= Rout + Totallosses;
Efficiency= Rout/InputW * 100;
if Efficiency <= 92.5
    continue;
end;

% Temperature Rise
slotculoss= Ls/(LmtS/2) * DCloss;
Totscloss= slotculoss + Totironloss + Eddyloss;
Asout= (pi*Dout*L) + 2*(pi/4)*(Dout^2 - D^2);
cool1= 0.03;
Disscoe1= Asout/cool1;
Asin= pi * D * L;
cool2= 0.03/(1 + (0.1 * Vr));
Disscoe2= Asin/cool2;
Aduct= (pi/4) * (Dout^2 - D^2) * nv;
cool3= 0.1/(0.1 * Vr);
Disscoe3= Aduct/cool3;
DisscoeT= Disscoe1 + Disscoe2 + Disscoe3;
TempriseS= Totscloss/DisscoeT;
% if TempriseS >= 120
%     continue;
% end;
coolF= 0.1/(1 + (0.1 * Vr));
Fsurface= 2*Lmtf*Hfield + 2*Lmtf*DepthF;
DisscoeF= Fsurface/coolF;
TempriseF= (Fculoss/pole)/DisscoeF;
```

```
% if TempriseF >= 120
%     continue;
% end;

% Power & Torque Density
KgCuT= KgCu + KgFcu;
KgIronT= KgCore + KgTeeth + KgPoles + KgYoke;
KgTotal= (KgCuT + KgIronT) * 1.01;
PowerDensity= KW/KgTotal;
TorqueDensity= (KW/(2*pi*RPM/60))/KgTotal;
% if PowerDensity >= 25
%     continue;
% end;

% Optimal Design Selection
Num = Num + 1;
if Efficiency >= Efficiencymax
    Efficiencymax = Efficiency;
end;
if abs (Efficiency - Efficiencymax) <= 0.0001
    P2 = Num;
end;
% if PowerDensity <= PowerDensitymin
%     PowerDensitymin = PowerDensity;
% end;
% if abs (PowerDensity - PowerDensitymin) <= 0.001
%     P1 = Num;
% end;
% if TempriseS <= TempriseSmin
%     TempriseSmin = TempriseS;
% end;
% if abs (TempriseS - TempriseSmin) <= 0.0001
%     P3 = Num;
% end;
% if TempriseF <= TempriseFmin
%     TempriseFmin = TempriseF;
% end;
% if abs (TempriseF - TempriseFmin) <= 0.0001
%     P4 = Num;
% end;
fprintf (list,' -----------------------------------------------------------
---------------------------------------------------------------------------
---------------------------------------------------------------------------
---------------------------------------------------------------------------
---------------------------------------------------------------------------
---------------------------------------------------------------------------
--------------------------------------------------------\n');
fprintf (list,' Num=%3d | D=%6.3f | Dout=%6.3f | L=%6.3f |
L/polepitch=%6.3f | Vr=%6.3f | Slots=%6.3f | J=%6.3f | Jfield=%6.3f |
Zs=%6.3f | ac/Slot=%6.3f | ConductorS=%6.3fX %6.3f | Slot=%6.3fX %6.3f |
Bc(For Continue)=%6.3f | Bcore=%6.3f | Brcore(For Continue)=%6.3f |
Byoke=%6.3f | Bpb=%6.3f | Bt=%6.3f | SCR=%6.3f | Lgap=%6.5f |
Efficicency=%6.3f | Power Density=%6.3f | Packing Factor=%6.3f |
TempriseS=%7.5f | TempriseF=%6.3f | ATFL=%6.3f | AKATFL=%6.3f |
Ifield=%6.3f | AKIfield=%6.3f\n', Num, D, Dout, L, Lbypolepitch, Vr, S, Ji,
Jfield, Zs, slotloading, Wc, Hc, Ws, Hs, Bc, BcoreS, Brcore, Byoke, Bpb, Bt,
```

```
SCR, Lgap, Efficiency, PowerDensity, ((As*Zs)/(Ws*Hs)), TempriseS,
TempriseF, ATFL, AKATFL, Ifield, AKIfield);
end;
end;
end;
end;
end;
end;
end;
fprintf (list, '\n\n%6.2f KVA, %6.2f V, %6.2f RPM, %6.2f Hz, %6.2f PF:-\n',
KVA, V, RPM, f, PF);
fprintf (list,' -- ----- ----- ---- ---- --- ---- -- ---- --- ----- ----
\n');
fprintf (list, '               Best in the category
');
fprintf (list, '\nFor maximum efficiency, choose no. = %3d(% 5.2f)', P2,
Efficiencymax);
% fprintf (f2, '\nFor most power dense, choose no. = % 3d (%5.2f)', P1,
PowerDensitymin);
% fprintf (f2,' \nFor minimum stator winding temperature rise, choose no.
= %3d (%4.2f)', P3, TempriseSmin);
% fprintf (f2,' \nFor minimum rotor winding temperature rise, choose no. = %
3d (%4.2f)', P4, TempriseFmin);
fclose (list);
```

Appendix C

C.1 V-curves program

```
%%%%%%%%%%%%%%%%%%%%%%%%%%%%%%%%%%%%%%%%%%%%%%%%%%%%%%%%%%%%
%  V-Curves for Salient-Pole Synchronous Motor
%%%%%%%%%%%%%%%%%%%%%%%%%%%%%%%%%%%%%%%%%%%%%%%%%%%%%%%%%%%%

clear;
% Rated values
VL= 3300; KVA= 5000; PF= 1; PR= KVA*PF;
% Assume Xus= 1pu
Xus= VL^2/(KVA*1000); Xl= 6.21706e-005; Ra= 0.0363905;
Xd= Xus*0.996222; Xq= Xus*0.63517;
%------------------------OCC curve(L-L Voltage)---------------------------
Voc= [0 1123 2232.09 3165.3 3630.43 3892.73 4055.54]';
Ifoc=[0 50 100 150 200 250 300]';
%-----------------------------Rated Ia & If-------------------------------
Iam= 1000*KVA/VL/sqrt(3)*(PF+1i*sin(acos(PF)));
Vt= 1+1i*0.00;
SetI= (PF+1i*sin(acos(PF)));
SetEf= Vt- 1i*SetI*0.63517 - SetI*0.0363905;
SetLoadAng= abs(angle(SetEf));
SetInternalAng= acos(PF)+ SetLoadAng;
SetIq= Iam* cos(SetInternalAng)* (cos(SetInternalAng)-
1i*sin(SetInternalAng));
SetId= Iam* sin(SetInternalAng)* (cos((pi()/2)-
SetInternalAng)+1i*sin((pi()/2)-SetInternalAng));
Ear= abs(VL/sqrt(3)-1i*Iam*Xl-Iam*Ra);
Ife= interp1(Voc/sqrt(3),Ifoc,Ear,'pchip');
Ifb= Ifoc(2)/(Voc(2)/sqrt(3))*Ear;
SetXssd=(Xd-Xl)*Ifb/Ife+Xl;
SetXssq= Xq;
Ef=abs(VL/sqrt(3)-1i*SetId*SetXssd-1i*SetIq*SetXssq-Iam*Ra);
IfR=interp1(Voc/sqrt(3),Ifoc,Ear,'pchip')*Ef/Ear;
axis([0, IfR, 0, abs(Iam)]);
% --------------------------Output Power Values---------------------------
Ncurves=11; Pout=linspace(0, PR, Ncurves)*1000;
% --------------------------Set PF angle range----------------------------
PFang=linspace(-60, 60, 50)*pi/180; n=length(PFang);
for v=1:Ncurves
   for k=1:n
          %---------------------Leading Condition-------------------------
           if(PFang(k)>0)
           LeadI= (cos(PFang(k))+1i*sin(PFang(k)));
           LeadEf= Vt- 1i*LeadI*0.63517 - LeadI*0.0363905;
           LeadLoadAng= abs(angle(LeadEf));
           LeadInternalAng= abs(PFang(k) + LeadLoadAng);
           Ia(k)=Pout(v)/sqrt(3)/VL/cos(PFang(k));
           I=Ia(k)*cos(PFang(k))+1i*Ia(k)*sin(PFang(k));
```

```
            LeadIq= I* cos(LeadInternalAng)* (cos(LeadInternalAng)-
1i*sin(LeadInternalAng));
            LeadId= I* sin(LeadInternalAng)* (cos((pi()/2)-
LeadInternalAng)+1i*sin((pi()/2)-LeadInternalAng));
            Ear=abs(VL/sqrt(3)-1i*I*Xl-I*Ra);
            Ife=interp1(Voc/sqrt(3),Ifoc,Ear,'pchip');
            Ifb=Ifoc(2)/Voc(2)/sqrt(3)*Ear;
            Xssd=(Xd-Xl)*Ifb/Ife+Xl;
            Xssq=Xq;
            Ef=abs(VL/sqrt(3)-1i*LeadId*Xssd-1i*LeadIq*Xssq-Iam*Ra);
            If(k)=interp1(Voc/sqrt(3),Ifoc,Ear,'pchip')*Ef/Ear;
            end
       %-----------------------Lagging Condition------------------------
            if(PFang(k)<0)
            LagI= (cos(PFang(k))+ 1i*sin(PFang(k)));
            LagEf= Vt- 1i*LagI*0.63517 - LagI*0.0363905;
            LagLoadAng= abs(angle(LagEf));
            LagInternalAng= abs(PFang(k) + LagLoadAng);
            Ia(k)=Pout(v)/sqrt(3)/VL/cos(PFang(k));
            I=Ia(k)*cos(PFang(k))+ 1i*Ia(k)*sin(PFang(k));
            if(abs(PFang(k))> LagLoadAng)
                LagIq= I* cos(LagInternalAng)*
(cos(LagInternalAng)+1i*sin(LagInternalAng));
                LagId= I* sin(LagInternalAng)* (cos((pi()/2)-
LagInternalAng)-1i*sin((pi()/2)-LagInternalAng));
            end
            if(abs(PFang(k))< LagLoadAng)
                LagIq= I* cos(LagInternalAng)* (cos(LagInternalAng)-
1i*sin(LagInternalAng));
                LagId= I* sin(LagInternalAng)* (cos((pi()/2)-
LagInternalAng)+1i*sin((pi()/2)-LagInternalAng));
            end
            Ear=abs(VL/sqrt(3)-1i*I*Xl-I*Ra);
            Ife=interp1(Voc/sqrt(3),Ifoc,Ear,'pchip');
            Ifb=Ifoc(2)/Voc(2)/sqrt(3)*Ear;
            Xssd=(Xd-Xl)*Ifb/Ife+Xl;
            Xssq=Xq;
            Ef=abs(VL/sqrt(3)-1i*LagId*Xssd-1i*LagIq*Xssq-Iam*Ra);
            If(k)=interp1(Voc/sqrt(3),Ifoc,Ear,'pchip')*Ef/Ear;
            end
      end
   %-------------------------Unity PF Point----------------------------
   UI=  1+1i*0.00;
   UEf= Vt- 1i*UI*0.63517 - UI*0.0363905;
   ULoadAng= angle(UEf);
   UInternalAng= abs(ULoadAng - acos(1));
   Iau=Pout(v)/sqrt(3)/VL;
   UId= Iau* sin(UInternalAng)* (cos((pi()/2)-
UInternalAng)+1i*sin((pi()/2)-UInternalAng));
   UIq= Iau* cos(UInternalAng)* (cos(UInternalAng)-1i*sin(UInternalAng));
   Ear=abs(VL/sqrt(3)-1i*Iau*Xl-Iau*Ra);
   Ife=interp1(Voc/sqrt(3),Ifoc,Ear,'pchip');
   Ifb=Ifoc(2)/Voc(2)/sqrt(3)*Ear;
   Xssd=(Xd-Xl)*Ifb/Ife+Xl;
   Xssq=Xq;
   Ef=abs(VL/sqrt(3)-1i*UId*Xssd-1i*UIq*Xssq-Iau*Ra);
```

```
   Ifu=interp1(Voc/sqrt(3),Ifoc,Ear,'pchip')*Ef/Ear;
   %----------------------0.8 lead PF point------------------------------
   PbI= (0.8+1i*0.6);
   PbEf= Vt- 1i*PbI*0.63517 - PbI*0.0363905;
   PbLoadAng= abs(angle(PbEf));
   PbInternalAng= abs(acos(0.8)+ PbLoadAng);
   Ial=Pout(v)/sqrt(3)/VL/0.8;
   Ile=Ial*(0.8+1i*0.6);
   PbId= Ile* sin(PbInternalAng)* (cos((pi()/2)-PbInternalAng) +
1i*sin((pi()/2)-PbInternalAng));
   PbIq= Ile* cos(PbInternalAng)* (cos(PbInternalAng) -
1i*sin(PbInternalAng));
   Ear=abs(VL/sqrt(3)-1i*Ile*Xl-Ile*Ra);
   Ife=interp1(Voc/sqrt(3),Ifoc,Ear,'pchip');
   Ifb=Ifoc(2)/Voc(2)/sqrt(3)*Ear;
   Xssd=(Xd-Xl)*Ifb/Ife+Xl;
   Xssq=Xq;
   Ef=abs(VL/sqrt(3)-1i*PbId*Xssd-1i*PbIq*Xssq-Ile*Ra);
   Ifl=interp1(Voc/sqrt(3),Ifoc,Ear,'pchip')*Ef/Ear;
   %----------------------0.8 lag PF point-------------------------------
   FI= (0.8-1i*0.6);
   FEf= Vt- 1i*FI*0.63517 - FI*0.0363905;
   FLoadAng= abs(angle(FEf));
   FInternalAng= abs(acos(0.8) - FLoadAng);
   Ialag= Pout(v)/sqrt(3)/VL/0.8;
   Ila=Ialag *(0.8-1i*0.6);
   if(acos(0.8) > FLoadAng)
   FIq= Ila* cos(FInternalAng)* (cos(FInternalAng)+1i*sin(FInternalAng));
   FId= Ila* sin(FInternalAng)* (cos((pi()/2)-FInternalAng)-
1i*sin((pi()/2)-FInternalAng));
   end
   if(acos(0.8) < FLoadAng)
   FIq= Ila* cos(FInternalAng)* (cos(FInternalAng)-1i*sin(FInternalAng));
   FId= Ila* sin(FInternalAng)* (cos((pi()/2)-
FInternalAng)+1i*sin((pi()/2)-FInternalAng));
   end
   Ear=abs(VL/sqrt(3)-1i*Ila*Xl-Ila*Ra);
   Ife=interp1(Voc/sqrt(3),Ifoc,Ear,'pchip');
   Ifb=Ifoc(2)/Voc(2)/sqrt(3)*Ear;
   Xssd=(Xd-Xl)*Ifb/Ife+Xl;
   Xssq=Xq;
   Ef=abs(VL/sqrt(3)-1i*FId*Xssd-1i*FIq*Xssq-Ila*Ra);
   Iflag=interp1(Voc/sqrt(3),Ifoc,Ear,'pchip')*Ef/Ear;
   %---------------------------------------------------------------------
FF=221.7510-Ifu;
plot(If+FF,Ia,Ifu+FF,Iau,'o',Ifl+FF,Ial,'*',Iflag+FF,Ialag,'x'); grid; hold
on;
end
title('V-curves for salient-pole synchronous motor');
xlabel('Field current, A'); ylabel('Stator current, A');
legend(['KW Increment. = ',num2str((Pout(2)-Pout(1))/1000)],'Unity PF',
'0.8 PF leading','0.8 PF lag',4);
hold off;
```

Appendix D

D.1 Ansys-RMxprt design sheet

THREE-PHASE SYNCHRONOUS MOTOR DESIGN	
File: Setup1.res	
GENERAL DATA	
Rated Power (kW):	5000
Rated Power Factor:	1
Power Factor Type:	Inductive
Rated Voltage (V):	3300
Winding Connection:	Wye
Number of Poles:	14
Frequency (Hz):	22.1667
Rated Speed (rpm):	190
Operating Temperature (C):	120
Friction Loss at Reference Speed (W):	30000
Windage Loss at Reference Speed (W):	0
Windage Loss at Reference Speed (W):	190
Exciter Efficiency (%):	98
Start Field Resistance (ohm):	0
Exciting Current (A):	241
STATOR DATA	
Number of Stator Slots:	147
Outer Diameter of Stator (mm):	1600
Inner Diameter of Stator (mm):	1302
Type of Stator Slot: 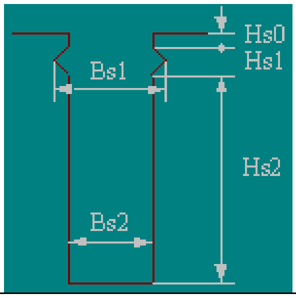	6
Stator Slot	

hs0 (mm):	1
hs1 (mm):	4
hs2 (mm):	52.3
bs1 (mm):	16.9
bs2 (mm):	15.05
Top Tooth Width (mm):	12.775
Bottom Tooth Width (mm):	15.224
Number of Sectors per Lamination:	7
Skew Width (slots):	0
Length of Stator Core (mm):	2340
Stacking Factor of Stator Core:	0.95
Type of Steel:	M19
Press board thickness (mm):	0
Magnetic press board	No
Number of Air Ducts:	26
Width of Air Ducts (mm):	9
STATOR-WINDING DATA	
End Length Adjustment (mm):	18
End-Coil Clearance (mm):	5
Number of Parallel Branches:	1
Type of Coils:	21
Coil Pitch:	9
Number of Conductors per Slot:	2
Number of Wires per Conductor:	8
Limited Wires per Coil Side:	4
in width direction	1
in thickness direction	4
Wire Width (mm):	4.9
Wire Thickness (mm):	4.85
Wire Wrap Thickness (mm):	0.02
Wire Direction in Slot:	Horizontal
Coil Wrap (mm):	0.2
Coil Width (mm):	5.32
Coil Height (mm):	19.88
Bottom Insulation (mm):	0
Wedge Thickness (mm):	4
Slot Liner Thickness (mm):	2.6
Layer Insulation (mm):	3

Slot Area (mm^2):	866.065
Slot Fill Factor (%):	42.6754
Stator Winding Factor:	0.931856
Wire Resistivity (ohm.mm^2/m):	0.0217
ROTOR DATA	
Minimum Air Gap (mm):	7.9
Inner Diameter (mm):	838
Length of Rotor (mm):	2340
Stacking Factor of Yoke:	0.95
Stacking Factor of Pole:	0.95
Type of Yoke Steel:	M19
Type of Pole Steel:	M19
Polar Arc Offset (mm):	203
Ratio of Max. to Min. Air Gap:	1.50546
Mechanical Pole Embrace:	0.732647
Pole-Shoe Width (mm):	209.2
Pole-Shoe Height (mm):	36
Pole-Body Width (mm):	136
Pole-Body Height (mm):	96
Second Air Gap (mm):	0
Magnetic Shaft:	No
FIELD-WINDING DATA	
Number of Parallel Branches:	1
Winding Type:	Edgewise Coil
Width of Wire (mm):	40
Thickness of Wire (mm):	1.5
Number of Turns per Pole:	44
Wire Wrap Thickness (mm):	0.4
Under-Pole-Shoe Insulation (mm):	2
Pole-Body-Side Insulation (mm):	2
Winding Control Width (mm):	40.4
Winding Control Height (mm):	88
Clearance between Windings (mm):	10
Inside Corner Radius (mm):	75
End Core-Coil Clearance (mm):	0
DAMPER DATA	
Number of Dampers per Pole:	4

Slot Pitch (mech. degrees):	4.98763
Center Slot Pitch (mech. degrees):	9.97526
Type of Damper Slot: 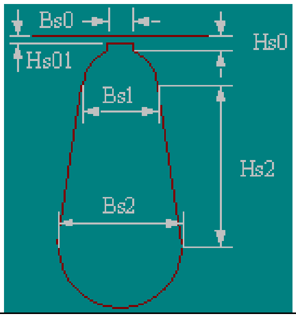	1
Damper Slot	
hs0 (mm):	2
hs2 (mm):	0
bs0 (mm):	1.8
bs1 (mm):	8.75
bs2 (mm):	8.75
Resistivity of Dampers	
at 75 Centigrade (ohm.mm^2/m):	0.0217391
End Ring Type:	0
Non-Magnetic End Press Board (mm):	40
WAVEFORM FACTORS	
Electrical Pole Embrace:	0.703465
Air-Gap Flux Total Harmonic	
Distortion at No-Load (%):	10.7356
Phase-Voltage Total Harmonic	
Distortion at No-Load (%):	4.92872
Line-Voltage Total Harmonic	
Distortion at No-Load (%):	0.18874
Phase-Voltage Total Harmonic	
Distortion at Full-Load (%)	15.9002
Line-Voltage Total Harmonic	
Distortion at Full-Load (%)	0.886758
MATERIAL CONSUMPTION	
Armature Wire Density (kg/m^3):	8900
Field Copper Density (kg/m^3):	8900
Damper Bar Material Density (kg/m^3):	8933
Damper Ring Material Density (kg/m^3):	8933

Armature Core Steel Density (kg/m^3):	7650
Rotor Pole Steel Density (kg/m^3):	7650
Rotor Yoke Steel Density (kg/m^3):	7650
Armature Copper Weight (kg):	1313.03
Field Copper Weight (kg):	1680.19
Damper Bar Material Weight (kg):	77.0178
Damper Ring Material Weight (kg):	129.224
Armature Core Steel Weight (kg):	8446.99
Rotor Pole Steel Weight (kg):	3075.09
Rotor Yoke Steel Weight (kg):	4626.13
Total Net Weight (kg):	19347.7
Armature Core Steel Consumption (kg):	15555.3
Rotor Core Steel Consumption (kg):	22198.9
UNSATURATED STEADY STATE PARAMETERS	
Armature Resistance R1 (ohm):	0.0363905
Armature Resistance at 20C (ohm):	0.0261396
Armature Leakage Reactance X1 (ohm):	0.148002
D-Axis Reactive Reactance Xad (ohm):	2.02177
Q-Axis Reactive Reactance Xaq (ohm):	1.2354
D-Axis Reactance X1+Xad (ohm):	2.16977
Q-Axis Reactance X1+Xaq (ohm):	1.3834
Field Winding Resistance Rf (ohm):	1.31251
Armature Resistance per Unit:	0.0167082
Armature Leakage Reactance per Unit:	0.0679532
D-Axis Reactive Reactance per Unit:	0.928269
Q-Axis Reactive Reactance per Unit:	0.567217
D-Axis Reactance per Unit:	0.996222
Q-Axis Reactance per Unit:	0.63517
Field Winding Resistance per Unit:	0.0056251
Base Voltage (V):	1905.26
Base Current (A):	874.773
Base Impedance (ohm):	2.178
NO-LOAD MAGNETIC DATA	
Stator-Teeth Flux Density (Tesla):	2.02677
Stator-Yoke Flux Density (Tesla):	1.1764

Pole-Shoe Flux Density (Tesla):	1.26537
Pole-Body Flux Density (Tesla):	1.65514
2nd Air-Gap Flux Density (Tesla):	1.65514
Rotor-Yoke Flux Density (Tesla):	1.16507
Air-Gap Flux Density (Tesla):	0.907081
Stator-Teeth Ampere Turns (A.T):	2386.84
Stator-Yoke Ampere Turns (A.T):	18.8613
Pole-Shoe Ampere Turns (A.T):	1.64146
Pole-Body Ampere Turns (A.T):	392.766
2nd Air-Gap Ampere Turns (A.T):	0
Rotor-Yoke Ampere Turns (A.T):	16.1848
Air-Gap Ampere Turns (A.T):	6940.75
No-Load Exciting Ampere Turns (A.T):	9757.04
No-Load Exciting Current (A):	221.751
Leakage-Flux Factor:	1.15922
Correction Factor for Magnetic	
Circuit Length of Stator Yoke:	0.7
Cogging Torque (N.m):	62.1381
FULL-LOAD DATA	
Induced Voltage per Unit with PF=0:	1.06808
Exciting Current with PF=0 (A):	475.969
D-Axis Ampere Turns with PF=0 (A.T):	6438.68
Power Factor Angle (degree):	-2.23991
Power Angle (degree):	22.4414
Induced Voltage per Unit:	0.987899
Total Exciting Ampere Turns (A.T):	10582.8
Armature Reactive Ampere Turns (A.T):	8075.59
D-Axis Armature Ampere Turns (A.T):	3937.03
Q-Axis Armature Ampere Turns (A.T):	3350.22
Phase Voltage (V):	1905.26
Phase Current (A):	917.051
Armature Thermal Load (A^2/mm^3):	329.855
Specific Electric Loading (A/mm):	65.9144

Armature Current Density (A/mm^2):	5.0043
Exciting Current (A):	240.519
Exciting Current Density (A/mm^2):	4.02304
Exciting Voltage (V):	315.685
Iron-Core Loss (W):	12634.3
Stator-Tooth Core Loss (W):	6542.27
Stator-Yoke Core Loss (W):	5930.36
Stator Surface Excess Loss (W):	0.0245747
Rotor Surface Excess Loss (W):	161.602
Mechanical Loss (W):	30000
Friction Loss (W):	25000
Windage Loss (W):	5000
Additional Loss (W):	25000
Copper Loss (W):	169289
Armature Copper Loss (W):	91811.3
Field Copper Loss (W):	75928.3
Exciter Loss (W):	1549.56
Total Loss (W):	236923
Input Power (kW):	5237.65
Output Power (kW):	5000.72
Efficiency (%):	95.4765
Shaft Torque (N.m):	251334
Apparent Power (kVA):	5241.65
Power Factor:	0.999236
TRANSIENT PARAMETERS & TIME CONSTANTS	
D-axis Damper Leakage Reactance (ohm):	0.385662
D-axis Damper Resistance (ohm):	0.500584
Q-axis Damper Leakage Reactance (ohm):	0.213952
Q-axis Damper Resistance (ohm):	0.277706
D-axis Transient Reactance (ohm):	0.513959
D-axis Subtransient Reactance (ohm):	0.335778
Q-axis Subtransient Reactance (ohm):	0.33037
Field Leakage Reactance (ohm):	0.446838
Negative-Sequence Reactance (ohm):	0.333052
Zero-Sequence Reactance (ohm):	0.148002
D-axis Damper Leakage Reactance per Unit:	0.177072

D-axis Damper Resistance per Unit:	0.229837
Q-axis Damper Leakage Reactance per Unit:	0.0982331
Q-axis Damper Resistance per Unit:	0.127505
D-axis Transient Reactance per Unit:	0.235977
D-axis Subtransient	
Reactance per Unit:	0.154168
Q-axis Subtransient	
Reactance per Unit:	0.151685
Field Leakage Reactance per Unit:	0.20516
Negative-Sequence Reactance per Unit:	0.152916
Zero-Sequence Reactance per Unit:	0.0679532
Field Winding Time Constant	
with Open-Circuit Armature (s):	1.44673
D-axis Transient Time Constant (s):	0.342689
D-axis Subtransient Time Constant	
with Open-Circuit Armature (s):	0.0107805
D-axis Subtransient	
Time Constant (s):	0.0070431
Q-axis Subtransient Time Constant	
with Open-Circuit Armature (s):	0.0374721
Q-axis Subtransient	
Time Constant (s):	0.0089487
Armature Time Constant (s):	0.0657119
Start Torque (N.m):	423740
Start Forward Phase Current (A):	4498.36
Start Backward Phase Current (A):	599.235
WINDING ARRANGEMENT	
The 3-phase, 2-layer winding can be arranged in 21 slots as below:	
AAAAZZZBBBBXXXCCCCYYY	
Angle per slot (elec. degrees):	17.1429
Phase-A axis (elec. degrees):	102.857
First slot center (elec. degrees):	0
The field winding can be arranged as below:	
	Turns Width Thickness
1th section:	44.0 40.00 1.50

Maximum number of turns per pole is:	44
TRANSIENT FEA INPUT DATA	
For Armature Winding:	
Number of Turns:	49
Parallel Branches:	1
Terminal Resistance (ohm):	0.0363905
End Leakage Inductance (H):	6.22E-05
For Pole Winding:	
Number of Turns:	616
Parallel Branches:	1
Terminal Resistance (ohm):	1.31251
End Leakage Inductance (H):	0.0093604
For Damper Winding:	
Bar Resistance (ohm):	0.0007996
End Ring Resistance (ohm):	0
End Ring Inductance (H):	0
End Ring Center Length Ratio:	0
End Ring Edge Length Ratio:	0
2D Equivalent Value:	
Equivalent Model Depth (mm):	2299.61
Equivalent Stator Stacking Factor:	0.870016
Equivalent Rotor Stacking Factor:	0.966685
Estimated Rotor Inertia (kg m^2):	4903.93

Appendix E

E.1 Demagnetization curves of Vacodym 677 HR – Vacuumschmelze GmbH & Co. KG

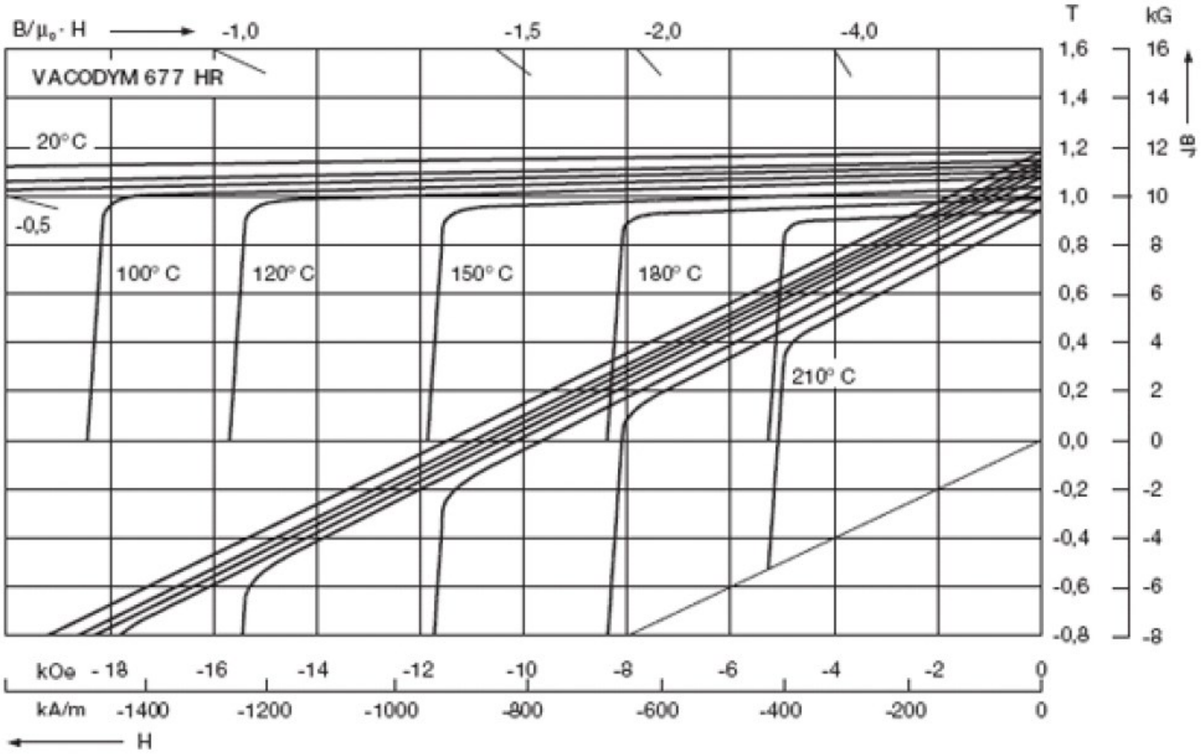

Source: Vacuumschmelze GmbH & Co. KG. (2015). VACODYM 677 HR. [Online] Available: http://www.vacuumschmelze.com/en/products/permanent-magnets-assemblies/permanent-magnets/nd-fe-b/vacodym/vacodym-677-hr.html

Appendix F

F.1 Test machine datasheet

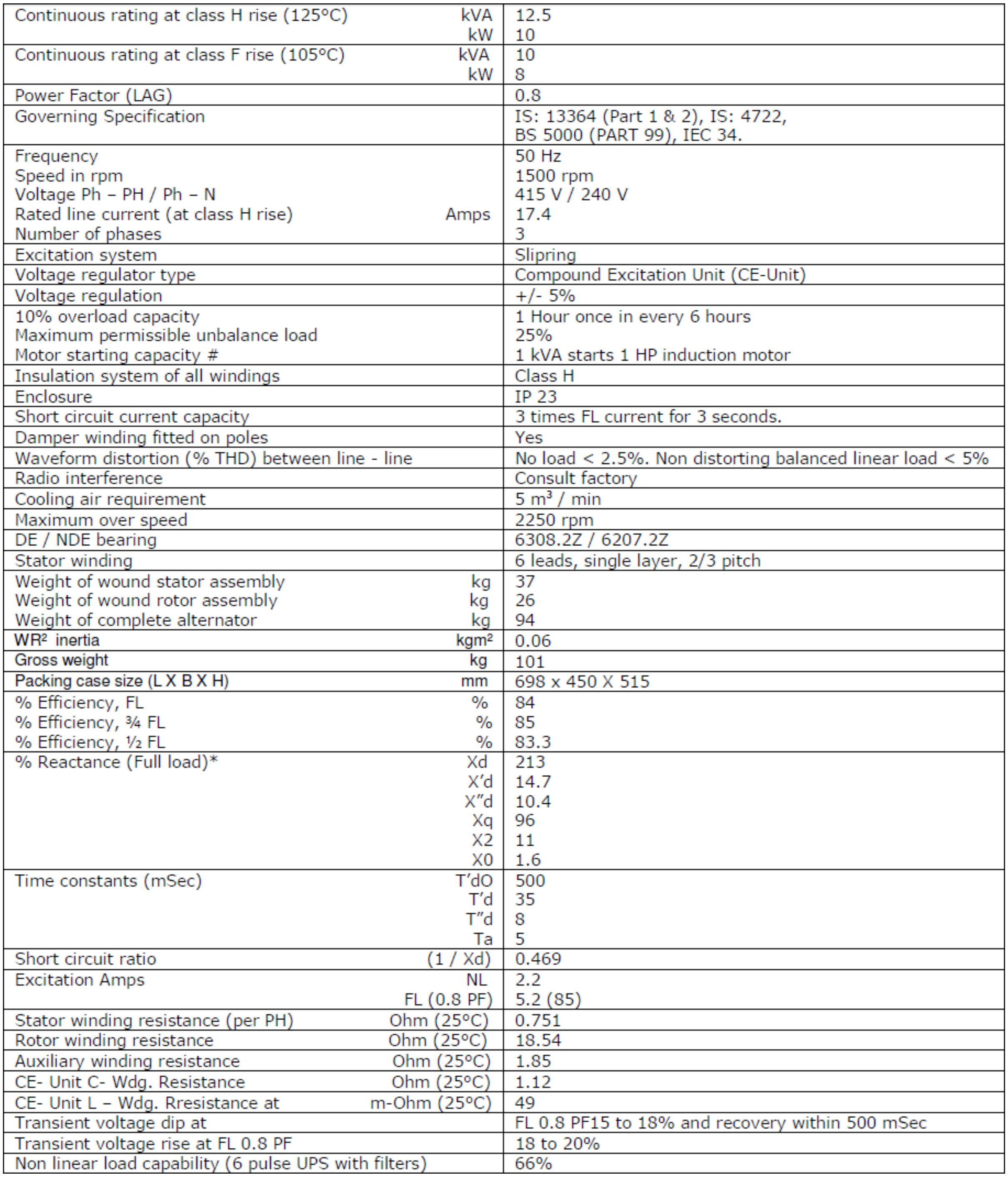

Continuous rating at class H rise (125°C)	kVA	12.5
	kW	10
Continuous rating at class F rise (105°C)	kVA	10
	kW	8
Power Factor (LAG)		0.8
Governing Specification		IS: 13364 (Part 1 & 2), IS: 4722, BS 5000 (PART 99), IEC 34.
Frequency		50 Hz
Speed in rpm		1500 rpm
Voltage Ph – PH / Ph – N		415 V / 240 V
Rated line current (at class H rise)	Amps	17.4
Number of phases		3
Excitation system		Slipring
Voltage regulator type		Compound Excitation Unit (CE-Unit)
Voltage regulation		+/- 5%
10% overload capacity		1 Hour once in every 6 hours
Maximum permissible unbalance load		25%
Motor starting capacity #		1 kVA starts 1 HP induction motor
Insulation system of all windings		Class H
Enclosure		IP 23
Short circuit current capacity		3 times FL current for 3 seconds.
Damper winding fitted on poles		Yes
Waveform distortion (% THD) between line - line		No load < 2.5%. Non distorting balanced linear load < 5%
Radio interference		Consult factory
Cooling air requirement		5 m^3 / min
Maximum over speed		2250 rpm
DE / NDE bearing		6308.2Z / 6207.2Z
Stator winding		6 leads, single layer, 2/3 pitch
Weight of wound stator assembly	kg	37
Weight of wound rotor assembly	kg	26
Weight of complete alternator	kg	94
WR^2 inertia	kgm^2	0.06
Gross weight	kg	101
Packing case size (L X B X H)	mm	698 x 450 X 515
% Efficiency, FL	%	84
% Efficiency, ¾ FL	%	85
% Efficiency, ½ FL	%	83.3
% Reactance (Full load)*	Xd	213
	X'd	14.7
	X"d	10.4
	Xq	96
	X2	11
	X0	1.6
Time constants (mSec)	T'dO	500
	T'd	35
	T"d	8
	Ta	5
Short circuit ratio	(1 / Xd)	0.469
Excitation Amps	NL	2.2
	FL (0.8 PF)	5.2 (85)
Stator winding resistance (per PH)	Ohm (25°C)	0.751
Rotor winding resistance	Ohm (25°C)	18.54
Auxiliary winding resistance	Ohm (25°C)	1.85
CE- Unit C- Wdg. Resistance	Ohm (25°C)	1.12
CE- Unit L – Wdg. Rresistance at	m-Ohm (25°C)	49
Transient voltage dip at		FL 0.8 PF15 to 18% and recovery within 500 mSec
Transient voltage rise at FL 0.8 PF		18 to 20%
Non linear load capability (6 pulse UPS with filters)		66%